LBL--28545

DE90 013871

Distribution of Metal and Adsorbed Guest Species in Zeolites

by

Bradley Floyd Chmelka

Lawrence Berkeley Laboratory
University of California
Berkeley, California 94720

This work was supported by the Director, Office of Energy Research, Office of Basic Energy Sciences, Materials Sciences Division of the U.S. Department of Energy under Contract No. DE-AC03-76SF00098.

Distribution of Metal and Adsorbed Guest Species in Zeolites

by

Bradley Floyd Chmelka

Abstract

Because of their high internal surface areas and molecular-size cavity dimensions, zeolites are used widely as catalysts, shape-selective supports, or adsorbents in a variety of important chemical processes. For metal-catalyzed reactions, active metal species must be dispersed to sites within the zeolite pores that are accessible to diffusing reactant molecules. The distribution of the metal, together with transport and adsorption of reactant molecules in zeolite powders, are crucial to ultimate catalyst performance. The nature of the metal or adsorbed guest distribution is known, however, to be dramatically dependent upon preparatory conditions. Our objective is to understand, at the molecular level, how preparatory treatments influence the distribution of guest species in zeolites, in order that macroscopic adsorption and reaction properties of these materials may be better understood.

The sensitivity of xenon to its adsorption environment makes ^{129}Xe NMR spectroscopy an important diagnostic probe of metal clustering and adsorbate distribution processes in zeolites. The utility of ^{129}Xe NMR depends on the mobility of the xenon atoms within the zeolite-guest system, together with the length scale of the sample heterogeneity being studied. In large pore zeolites containing dispersed guest species, such as Pt–NaY, ^{129}Xe NMR is insensitive to fine structural details at room temperature. Under these circumstances, a broad repertoire of experiments is required to elucidate microstructural features of the zeolite-guest system. Transmission electron microscopy, hydrogen chemisorption, Raman spectroscopy, temperature programmed reduction, and multiple-quantum NMR have been used, together with

^{129}Xe NMR, to obtain insight on the distribution and/or chemical identity of dispersed platinum species or aromatic molecules in NaY zeolite.

Where guest heterogeneities are large or mobility of the xenon is restricted, room-temperature ^{129}Xe NMR is a powerful tool for probing zeolite-guest structure. For example, a shrinking-core mass transport model, guided by ^{129}Xe NMR results, permits relative time scales to be established for diffusion of aromatic guests like hexamethylbenzene in NaY powders. Similarly, xenon atoms occluded in NaA zeolite have been studied using ^{129}Xe NMR to investigate directly the distribution and adsorption properties of molecules in confined, microporous environments. Correlating guest transport behavior and local adsorbate structure with the chemical reaction properties of zeolites is crucial to understanding the catalytic and adsorbent functions of this important class of materials.

Acknowledgements

What a time it's been.....rarely glamorous, but exciting and mind-expanding to the end. It is a privilege to be associated with the College of Chemistry and the people which comprise it. This applies in particular to the working relationships I have enjoyed with Professors Clayton Radke, Eugene Petersen, and Alexander Pines, which more than anything else, account for the enthusiasm I have toward my experience at Berkeley. I am grateful for the latitude and freedom that Professors Radke and Petersen granted me in pursuing topics and directions that went somewhat further afield than we expected. Their collective energy, guidance, perspective, and sense of humor (together with Clay's expertise in steering for the stern of a passing canoe) made for brisk, dynamic interaction. I count myself fortunate for the personal friendships that have evolved between us.

To Alex and my friends in the Pines' group, I extend my heartfelt appreciation. Ryong Ryoo, Shang-Bin Liu, and Count Louis Charles de Goublaye de Menorval gave me crucial guidance and encouragement at the beginning. David Shykind tolerated my quantum mechanics queries, and his questionable sense of tasteful humor was especially welcome in the post-midnight hours. The mass-piling theories and experiments of A.J. Shaka and Steve Rucker were influential in moderating my exercise philosophy, and I thank them for many a fine spot on the bench press. Dione Carmichael is a helpful and superb administrator. I benefited from enlightening discussions with past and current group members, particularly with Alon McCormick, Karl Mueller, John Pearson, Boqin Sun, Yue Wu, and Joe Zwanziger. It has been inspiring to participate in the exciting and dynamic atmosphere that extends from Alex' creative energy and contagious enthusiasm.

The scientific collaborations I have shared with other groups both inside and

outside the College have been highly rewarding. My thanks to Professor Alex Bell and his chemical engineering group, especially Greg Went and Rick Rosin, for their extended efforts in the Raman spectroscopy, temperature programmed reduction, and hydrogen chemisorption studies of metal-zeolite systems presented in Chapters 3 and 4. Roseann Csencsits in the Department of Material Science, and most recently at Digital Equipment Corp., Northborough, MA, performed the transmission and scanning electron microscopy experiments discussed in Chapters 3 and 5. Jonathan Stebbins (Department of Geology, Stanford University) provided invaluable guidance and expertise on inorganic mineral structures, whose partial preparation is discussed in Appendix G.

Many friends provided diversions crucial to my sanity's at least partial preservation: John Entrekin, noted last-place finisher with me in numerous feats of endurance (Markleeville and Lenzspitze come to mind, but things could have been worse...); Juan de Pablo, for sojourns in Mexico and a kindred spirit; Don Aumann, who has been on nearly as many outdoor trips as a legendary water bottle of mine; Laura Sanborn, whose political commentary is worthy of MacNeil and Lehrer; Jack Lewnard, with his enthusiasm for climbing high and his legacy of adventurous friends (replete with masochistic tendencies toward marathon slide viewing); George Bell, Jr. and Chris Treese, whose epic adventures in wild places continue to affirm that jeopardizing one's life can still be fun; the Tenants from Hell at the 1528 Club, an establishment noted for the levity of its parties and the bizarreness of its landlord (and probably visa-versa); the Red Menace, the Name Pendings, and the Chegs, a soccer and two softball teams in desperate need of managerial talent; and finally Nanine van Draanen, Joyce Prosser, Rick Rosin, and John Zielinski, whose friendships are irreplaceable.

I am grateful for the love, support, and encouragement of my parents and brother, and it is to them that I dedicate this work.

Contents

1 Introduction 1

2 Probing Metal Cluster Formation in Zeolites by ^{129}Xe NMR 9

2.1 Methods of Metal-Zeolite Preparation 9

2.2 Pulsed Fourier-Transform NMR 14

2.3 ^{129}Xe NMR Spectroscopy 20

2.4 Pt–NaY Sample Preparation 25

2.5 ^{129}Xe NMR Studies of Pt–NaY 32

2.6 Summary 36

3 Platinum Species Distributions in Pt–NaY 37

3.1 Abstract 37

3.2 Introduction 38

3.3 Calcination 39

3.4 Reduction 51

3.5 Reoxidation 57

3.6 Low Metal Loadings 66

3.7 Conclusions 66

4 The Chemistry of Pt-NaY Preparation 69

4.1 Abstract 69

4.2 Introduction 70

4.3 Experimental 71

4.4 Raman Spectroscopy Experiments 72

4.5 Temperature Programmed Reduction Studies 78

4.6 Summary of Results 82

5 Distributions of Aromatic Molecules in NaY Zeolite 85

5.1 Abstract 85

5.2 Introduction 86

5.3 Experimental 88

5.3.1 Sample preparation 88

5.3.2 NMR experiments 90

5.4 Macroscopic Adsorbate Distributions 90

5.4.1 HMB in NaY 91

5.4.2 TMB and Benzene in NaY 97

5.4.3 Heterogeneity Length Scales by ^{129}Xe NMR 102

5.5 Intracrystalline Adsorbate Distributions 109

5.5.1 Multiple-Quantum NMR Studies of Spin Clustering 109

5.5.2 Multiple-Quantum Data Analysis 112

5.6 Conclusions 116

6 Transport of Aromatic Molecules in NaY Zeolite Powders 118

6.1 Abstract 118

6.2 Introduction 119

6.3 Adsorbate Distributions by ^{129}Xe NMR 119
6.4 Modeling Adsorbate Transport in NaY 122
6.4.1 Sharp Adsorption Fronts 122
6.4.2 Effect of Co-adsorbed Guests 129
6.4.3 Guest Dispersal at Elevated Temperatures 132
6.5 Conclusions 132

7 Xenon Adsorption in NaA Zeolite **134**
7.1 Abstract 134
7.2 Introduction 135
7.3 Experimental 138
7.4 Results and Discussion 140
7.4.1 Xenon Distributions in NaA 140
7.4.2 Chemical Potential and Mobility of Xenon in NaA 144
7.4.3 Chemical Shift Analysis 148
7.5 Conclusions 153

8 Conclusion **156**

A Scattering Experiments **160**
A.1 Transmission Electron Microscopy Methods 160
A.2 NaY Crystallinity by X-ray Diffraction 162

B ^{129}Xe NMR of Pt–NaY **165**
B.1 Calcination Cooling Rate Effects 165
B.2 Pt–NaY Treatment Histories 167
B.3 Data Reproducibility 174
B.4 Dehydration of the NaY Support 174

C Divalent Metal Guests in NaY 178

D Xenon Adsorption in Zeolites 183

D.1 Xenon Adsorption in Y-type Zeolites 183

D.1.1 Experimental Procedures 183

D.1.2 Xenon Adsorption Data on NaY and Pt-NaY 188

D.2 Xenon Adsorption on CaA and Silica Gel 209

D.3 Thermodynamics of Adsorption 210

E Desorption and Reduction Studies of Pt-NaY 211

E.1 Temperature Programmed Decomposition of $Pt(NH_3)_4^{2+}$-NaX 211

E.2 Raman Spectrum of Reduced Pt-NaY 213

E.3 Temperature Programmed Reduction Studies of Pt-NaY 215

E.4 Hydrogen Chemisorption Measurements of Surface Platinum 230

E.4.1 Experimental Procedures 230

E.4.2 Hydrogen Chemisorption Data for 15 wt% Pt-NaY 233

F Transport of Adsorbed Guests in NaY 241

F.1 Liquid- Versus Vapor-Phase Guest Transport in NaY 241

F.1.1 Imbibition of Liquid Benzene 242

F.1.2 Vapor-Phase HMB Transport Experiment 247

F.2 HMB Diffusivity in NaY 251

F.2.1 Intercrystalline HMB Diffusivity in Macropores 251

F.2.2 Intracrystalline HMB Diffusivity in Micropores 252

F.3 Adsorption Capacity of HMB in NaY 255

F.4 Adsorption of Organic Guests on Faujasite-Type Zeolites 259

F.5 Proton NMR Spectra of HMB-NaY 261

G Synthesis of ^{17}O-Enriched Mineral Precursors **262**

G.1 Synthesis of $Si^{17}O_2$ 262

G.1.1 Method 1: Oxidation of Silicon Tetrachloride 262

G.1.2 Method 2: Oxidation of Silicon Metal 267

G.2 Synthesis of $Ca^{17}O$ 269

G.2.1 Synthesis of $Ca(^{17}OH)_2$ 269

G.2.2 Recovery of $H_2{}^{17}O$ 271

G.2.3 Decomposition of the Hydroxide to $Ca^{17}O$ 275

G.3 Synthesis of $Mg^{17}O$ 277

G.4 Uses of Precursor Materials 279

Bibliography **280**

List of Figures

1.1 Schematic diagram depicting possible locations of platinum atoms or clusters in NaY zeolite. 3

1.2 Length scales of adsorbate distribution heterogeneities by ^{129}Xe and multiple-quantum NMR. 5

1.3 Schematic diagram of xenon atoms occluded in a NaA zeolite α-cages. 7

2.1 Diagram of a single Y zeolite supercage with and without platinum guest species. 11

2.2 Schematic diagram depicting Pt–NaY preparation from nascent NaY zeolite. 13

2.3 Pulsed Fourier-Transform NMR. 19

2.4 Physisorbed ^{129}Xe as a probe of Y zeolite supercages. 22

2.5 Sensitivity of the ^{129}Xe nuclear resonance frequency to the average environment in Y zeolite supercages. 24

2.6 Xenon-129 NMR spectra of xenon adsorbed on 15 wt% $Pt(NH_3)_4^{2+}$–NaY following calcination at different temperatures. 26

2.7 Reactor for preparation of Pt–NaY catalyst samples. 28

2.8 Metal-zeolite sample preparation apparatus. 29

2.9 Pt–NaY sample cell for ^{129}Xe NMR and adsorption isotherm experiments. 31

2.10 Variation in ^{129}Xe chemical shift with the concentration of xenon adsorbed on 15 wt% $Pt(NH_3)_4^{2+}$–NaY zeolite samples calcined at different temperatures 473–673 K. 33

2.11 Variation in ^{129}Xe chemical shift with the concentration of xenon adsorbed on reduced 15 wt% Pt–NaY zeolite samples previously calcined at different temperatures. 35

3.1 Adsorption isotherms of xenon (T=295 K) on 15 wt% $Pt(NH_3)_4^{2+}$–NaY zeolite samples calcined at different temperatures. 40

3.2 Transmission electron micrographs of nascent NaY zeolite and 15 wt% $Pt(NH_3)_4^{2+}$-exchanged NaY. 41

3.3 Variation in ^{129}Xe chemical shift with the concentration of xenon adsorbed on 15 wt% $Pt(NH_3)_4^{2+}$–NaY zeolite samples calcined at different temperatures 473–873 K. 43

3.4 Transmission electron micrographs of 15 wt% Pt–NaY after calcination at 473 K and after reduction of the calcined catalyst at 673 K. . 44

3.5 Transmission electron micrographs of 15 wt% Pt–NaY after calcination at 573 K and after reduction of the calcined catalyst at 673 K. . 46

3.6 Transmission electron micrographs of 15 wt% Pt–NaY after calcination at 673 K and after reduction of the calcined catalyst at 673 K. . 47

3.7 Transmission electron micrographs of 15 wt% Pt–NaY after calcination at 773 K and after reduction of the calcined catalyst at 673 K. . 49

3.8 Transmission electron micrographs of 15 wt% Pt–NaY after calcination at 873 K and after reduction of the calcined catalyst at 673 K. . 50

3.9 Variation in ^{129}Xe chemical shift with the concentration of xenon adsorbed on reduced 15 wt% Pt–NaY zeolite samples previously calcined at different temperatures 473–873 K. 54

3.10 Increase in metal cluster density with zeolite particle thickness. Transmission electron micrograph of 15 wt% Pt–NaY after calcination at 873 K and subsequent reduction at 673 K. 56

3.11 Variation in ^{129}Xe chemical shift with the concentration of xenon adsorbed on 15 wt% Pt–NaY zeolite samples reoxidized by exposure of the reduced catalysts to oxygen gas at room temperature. 59

3.12 Variation in ^{129}Xe chemical shift with the concentration of xenon adsorbed on 15 wt% Pt–NaY zeolite samples reoxidized at elevated temperatures. 60

3.13 Schematic diagram depicting the effect of cluster size on platinum oxidation for different thermal treatments. 62

3.14 Transmission electron micrographs of 15 wt% Pt–NaY containing very large Pt clusters following reoxidation of the catalyst at 673 K. . . . 65

3.15 Variation in ^{129}Xe chemical shift with the concentration of xenon adsorbed on reduced Pt–NaY zeolite samples containing variable metal loadings. 67

4.1 Raman spectra of 15 wt% $Pt(NH_3)_4^{2+}$–NaY catalyst samples calcined in oxygen at different temperatures 578–873 K. 73

4.2 Raman spectra of compounds relevant to Pt–NaY preparation. 75

4.3 Temperature programmed reduction data for 15 wt% Pt–NaY samples calcined at different temperatures. 80

4.4 Summary of Pt–NaY preparation chemistry for different calcination conditions. 83

5.1 Scanning electron micrographs of the NaY zeolite used in organic guest adsorption/NMR experiments. 89

5.2 Room-temperature ^{129}Xe NMR spectra of xenon adsorbed on NaY zeolite with and without adsorbed hexamethylbenzene (HMB) guest species. 92

5.3 Room-temperature ^{129}Xe NMR spectra of xenon adsorbed on NaY zeolite containing a bulk loading of 0.5 HMB molecule per supercage introduced at 523 K. 93

5.4 Xenon-129 NMR spectra of xenon adsorbed on NaY zeolite containing 0.5, 0.7, and 0.9 HMB molecules per supercage. 95

5.5 Xenon-129 NMR spectra of xenon adsorbed on NaY zeolite containing 0.5 1,3,5-trimethylbenzene (TMB) molecules per supercage. 99

5.6 Xenon-129 NMR spectra of xenon adsorbed on NaY zeolite containing 0.5 benzene molecules per supercage. 101

5.7 Schematic diagrams of ^{129}Xe NMR spectra expected for different xenon mobilities in NaY zeolite containing 0.3 guest molecules/supercage. . 104

5.8 Room-temperature ^{129}Xe NMR spectra of xenon adsorbed on NaY zeolite containing a bulk loading of 0.3 HMB molecules per supercage adsorbed at 523 K. 106

5.9 Schematic diagrams of statistical and homogeneous distributions of guest molecules within zeolite cavities. 108

5.10 Proton multiple-quantum NMR spectra of 20.4 wt% HMB adsorbed on NaY zeolite at 573 K. 111

5.11 Gaussian fits to proton multiple-quantum NMR data of 20.4 wt% HMB adsorbed on NaY at 573 K. 113

5.12 Results of proton multiple-quantum NMR experiments for HMB loadings of 0.5, 1.0, and 2.0 molecules/supercage adsorbed on NaY zeolite at 573 K. 115

6.1 Room-temperature ^{129}Xe NMR spectra of xenon adsorbed on dehydrated NaY zeolite containing a bulk average of 0.5 HMB molecules per supercage adsorbed at 523 K and 573 K. 121

6.2 Room-temperature ^{129}Xe NMR spectrum of xenon adsorbed on partially hydrated NaY zeolite containing a bulk average of 0.5 HMB molecules per supercage adsorbed at 523 K. 123

6.3 Diagram of an axial HMB concentration profile arising from guest adsorption at 523 K in a packed bed of dehydrated NaY zeolite. . . . 127

6.4 Diagram of an axial HMB concentration profile arising from guest adsorption at 523 K in a packed bed of rehydrated NaY zeolite. . . . 131

7.1 Room-temperature ^{129}Xe NMR spectra of xenon occluded in NaA zeolite at 523 K at different loading pressures. 141

7.2 Binomial distribution plots of xenon occluded in NaA zeolite at 523 K at different loading pressures. 142

7.3 Variable-temperature ^{129}Xe NMR spectra of xenon occluded in NaA at 523 K and ca. 75 atm. 146

7.4 Density-dependence of the estimated condensation temperature of xenon occluded in NaA zeolite compared to that of bulk xenon gas. 147

7.5 Xenon-129 chemical shift plotted as a function of xenon density for xenon occluded in NaA α-cages and for bulk xenon gas. 150

A.1 Transmission electron micrograph showing micron-size Pt–NaY zeolite crystallites supported on a copper mesh sample grid. 161

A.2 X-ray diffraction data for commercial NaY zeolite. 162

A.3 X-ray diffraction data for commercial NaY zeolite accompanied by accepted standard values for peak intensities and positions. 164

B.1 The effect of cooling rate, as measured by variations in ^{129}Xe chemical shift, on 15 wt% $Pt(NH_3)_4^{2+}$–NaY zeolite samples calcined at different temperatures. 166

B.2 The effect of cooling rate, as measured by variations in ^{129}Xe linewidth, on 15 wt% $Pt(NH_3)_4^{2+}$–NaY zeolite samples calcined at different temperatures. 168

B.3 Treatment history of 15 wt% Pt–NaY initially calcined at 473 K: ^{129}Xe chemical shift data. 169

B.4 Treatment history of 15 wt% Pt–NaY initially calcined at 573 K: ^{129}Xe chemical shift data. 170

B.5 Treatment history of 15 wt% Pt–NaY initially calcined at 673 K: ^{129}Xe chemical shift data. 171

B.6 Treatment history of 15 wt% Pt–NaY initially calcined at 773 K: ^{129}Xe chemical shift data. 172

B.7 Treatment history of 15 wt% Pt–NaY initially calcined at 873 K: ^{129}Xe chemical shift data. 173

B.8 Reproducibility of Pt–NaY sample preparation procedures and ^{129}Xe NMR methods. 175

B.9 Variation in ^{129}Xe chemical shift with the concentration of xenon adsorbed on NaY samples dehydrated at 673 K and 873 K. 176

B.10 Adsorption isotherms of xenon (T=295 K) on NaY zeolite samples dehydrated at 673 K and 873 K. 177

C.1 Variation in ^{129}Xe chemical shift with the concentration of xenon adsorbed on dehydrated MgY, BaY and $Pt(NH_3)_4^{2+}$–NaY. 180

C.2 Adsorption isotherms of xenon (T=295 K) on CaY, MgY, and 15 wt% PtO–HY. 181

C.3 Transmission electron micrographs of 15 wt% $Pt(NH_3)_4^{2+}$–NaY after heating at 673 K under vacuum. 182

D.1 Apparatus for measuring xenon adsorption isotherms on Y zeolite samples. 184

D.2 Adsorption data for xenon on CaA zeolite and silica gel. 209

E.1 Temperature programmed decomposition data for $Pt(NH_3)_4^{2+}$–NaX. . 212

E.2 Raman spectrum of 15 wt% Pt–NaY, after chemisorption of hydrogen at 298 K following calcination at 773 K. 214

E.3 Schematic diagram of temperature programmed reduction apparatus. 216

E.4 Baseline-corrected TPR profile of 15 wt% Pt–NaY previously calcined at 473 K. 217

E.5 Time-dependent hydrogen consumption during temperature programmed reduction of 15 wt% Pt–NaY previously calcined at 473 K. 218

E.6 Time-dependent mass spectrometer traces for H_2, N_2, NH_3, and H_2O in the reactor effluent stream during temperature programmed reduction of 15 wt% Pt–NaY previously calcined at 473 K. 219

E.7 Baseline-corrected TPR profile of 15 wt% Pt–NaY previously calcined at 673 K. 220

E.8 Time-dependent hydrogen consumption during temperature programmed reduction of 15 wt% Pt–NaY previously calcined at 673 K. 221

E.9 Time-dependent mass spectrometer traces for H_2, N_2, NH_3, and H_2O in the reactor effluent stream during temperature programmed reduction of 15 wt% Pt–NaY previously calcined at 673 K. 222

E.10 Baseline-corrected TPR profile of 15 wt% Pt–NaY previously calcined at 773 K. 223

E.11 Time-dependent hydrogen consumption during temperature programmed reduction of 15 wt% Pt–NaY previously calcined at 773 K. 224

E.12 Time-dependent mass spectrometer traces for H_2, N_2, NH_3, and H_2O in the reactor effluent stream during temperature programmed reduction of 15 wt% Pt–NaY previously calcined at 773 K. 225

E.13 Baseline-corrected TPR profile of 15 wt% Pt–NaY previously calcined at 873 K. 226

E.14 Time-dependent hydrogen consumption during temperature programmed reduction of 15 wt% Pt–NaY previously calcined at 873 K. 227

E.15 Time-dependent mass spectrometer traces for H_2, N_2, NH_3, and H_2O in the reactor effluent stream during temperature programmed reduction of 15 wt% Pt–NaY previously calcined at 873 K. 228

E.16 Baseline-corrected TPR profile of 15 wt% Pt–NaY previously calcined at 873 K. Reproducibility of TPR results. 229

E.17 Vacuum/chemisorption manifold used for measurement of surface metal fractions in reduced, supported metal catalysts. 231

E.18 Room-temperature adsorption isotherms for hydrogen on reduced 15 wt% Pt–NaY previously calcined at 473 K. 234

E.19 Room-temperature adsorption isotherms for hydrogen on reduced 15 wt% Pt–NaY previously calcined at 573 K. 235
E.20 Room-temperature adsorption isotherms for hydrogen on reduced 15 wt% Pt–NaY previously calcined at 673 K. 236
E.21 Room-temperature adsorption isotherms for hydrogen on reduced 15 wt% Pt–NaY previously calcined at 773 K. 237
E.22 Room-temperature adsorption isotherms for hydrogen on reduced 15 wt% Pt–NaY previously calcined at 873 K. 238
E.23 Room-temperature adsorption isotherms for hydrogen on 15 wt% Pt–NaY reoxidized at 773 K, following calcination at 773 K and reduction at 673 K. 239
E.24 Room-temperature adsorption isotherms for hydrogen on 15 wt% Pt–NaY reoxidized at 873 K, following calcination at 873 K and reduction at 673 K. 240

F.1 (a) Dynamic force balance on a liquid thread in a cylindrical capillary tube. (b) A stationary macropore fluid distribution in thin capillaries resulting from mass-limited flow. 243
F.2 Mass-limited imbibition of liquid benzene at room temperature into a packed bed of hydrated NaY zeolite. 246
F.3 Sample preparation apparatus for demonstrating vapor-phase transport of HMB through NaY macropores. 249
F.4 Room-temperature ^{129}Xe NMR spectra of xenon adsorbed on dehydrated NaY zeolite demonstrating vapor-phase diffusion of HMB in the NaY macropores. 250

F.5 Temperature dependence of the self-diffusivity of benzene in NaX zeolite at a loading of 4.8 molecules per cavity. 254
F.6 Variation of the self-diffusivity of ethane (1.5 molecules/supercage) and n-butane (0.8 molecules/supercage) in NaX zeolite as a function of residual water concentration at 293 K. 256
F.7 Adsorption isotherms of benzene and n-heptane on NaY and CaY zeolites. 259
F.8 Adsorption isotherms of 1,3,5-triethylbenzene (TEB) on NaX zeolite at different temperatures. 260
F.9 Single-quantum ^1H NMR spectra of HMB adsorbed on NaY zeolite. . 261

G.1 Reactor apparatus for production of ^{17}O-enriched silicon dioxide. . . . 264
G.2 Bubbler apparatus for removing unreacted $SiCl_4$ from reactor exhaust gases. 266
G.3 Growth rates for silicon dioxide layers formed on (111)Si surface by reaction with dry oxygen gas. 268
G.4 Reaction apparatus for preparation of ^{17}O-enriched calcium hydroxide. 270
G.5 Vacuum manifold connections for recovery of $H_2{}^{17}O$. 272
G.6 $H_2{}^{17}O$ recovery trap for use during drying of solid hydroxide species. 273
G.7 Quartz cell used for decomposition of $Ca(^{17}OH)_2$ to $Ca^{17}O$ and $Mg(^{17}OH)_2$ to $Mg^{17}O$. 276

List of Tables

3.1 Accessible surface platinum in reduced Pt–NaY samples calcined at different temperatures. 52

3.2 Accessible surface platinum in reduced Pt–NaY samples following re-oxidation at elevated temperatures. 64

5.1 Some properties of benzene and related compounds. 98

7.1 Energetics of xenon adsorption on dealuminated NaY zeolite and quartz at 300 K. 154

A.1 Peaks in the x-ray diffraction spectrum of commercial NaY zeolite. . . 163

D.1 Index of Xe adsorption isotherm data. 189

D.2 Index of Xe adsorption isotherm data, continued. 190

Chapter 1

Introduction

Aluminosilicate zeolites have received a great deal of attention for their catalytic and adsorbent properties. As a class, zeolite crystal structures are characterized by an ordered, three-dimensional framework of AlO_4 and SiO_4 tetrahedra linked together through the sharing of oxygen atoms. This arrangement produces a high-porosity lattice comprised of cages and windows with sizes dependent on the particular type of zeolite [1,2]. Because of their high internal surface areas and molecular cage dimensions, zeolites are used widely as shape-selective catalysts and catalytic supports for a variety of industrially significant chemical processes [3,4,5]. For metal-catalyzed reactions, the active metal species must be dispersed to sites within the zeolite matrix which are accessible to the diffusing reactant molecules [5,6,7,8,9]. Transport and adsorption of reactant species, typicaliy organic molecules of moderate molecular weight, are crucial to the reaction process as well [5,6,7,8,9]. In both cases, the metal atoms or adsorbed atoms or molecules tend to congregate in isolated clusters within the zeolite pore spaces. Moreover, the nature of such distributions is known to depend dramatically upon preparatory treatments.

The objective of this research is to understand, at the molecular level, how

preparatory treatments influence the distributions of metal and adsorbed guest species in zeolites. We focus on NaY-supported platinum, hexamethylbenzene (HMB) adsorbed on NaY zeolite, and xenon occluded in NaA zeolite as representative systems for our investigation.

The performance of zeolite-supported metal catalysts is known to depend upon preparatory conditions which have a critical effect on metal atom mobility [5,6,10,11]. Migration of the metal species can result in undesirable redistribution of the metal to locations either outside the crystallites' internal pore spaces or to locations inaccessible to diffusing reactant species. Figure 1.1 illustrates the distribution possibilities for platinum species in NaY zeolite. The metal can aggregate, for example, into large, low surface-area clusters on the exterior surface of the micron-size NaY crystallites, as shown in Figure 1.1(a). Remaining entirely outside the zeolite cavities, the large aggregates represent a wasteful use of the precious metal catalyst. Conversely, Figure 1.1(b) depicts the metal guest in a catalytically desirable supercage site, accessible to diffusing reactant species through the 0.74 nm supercage apertures. Preparation of suitable Pt–NaY catalysts has relied on empirical recipes to produce reduced metal clusters in supercage locations where the highly-dispersed metal can be most effectively used. Under certain conditions (to be discussed in Chapters 3 and 4), the metal can penetrate the 0.22 nm windows of the sodalite cages where it becomes confined, as shown in Figure 1.1(c), in sites inaccessible to all but the smallest molecular species. Such migratory tendencies of the metal species are not well understood because the transformations undergone by metal guest species during their activation to the reduced state have not been firmly established. Through novel application of ^{129}Xe nuclear magnetic resonance (NMR) spectroscopy [Chapter 2], coupled with transmission electron microscopy (TEM), hydrogen chemisorp-

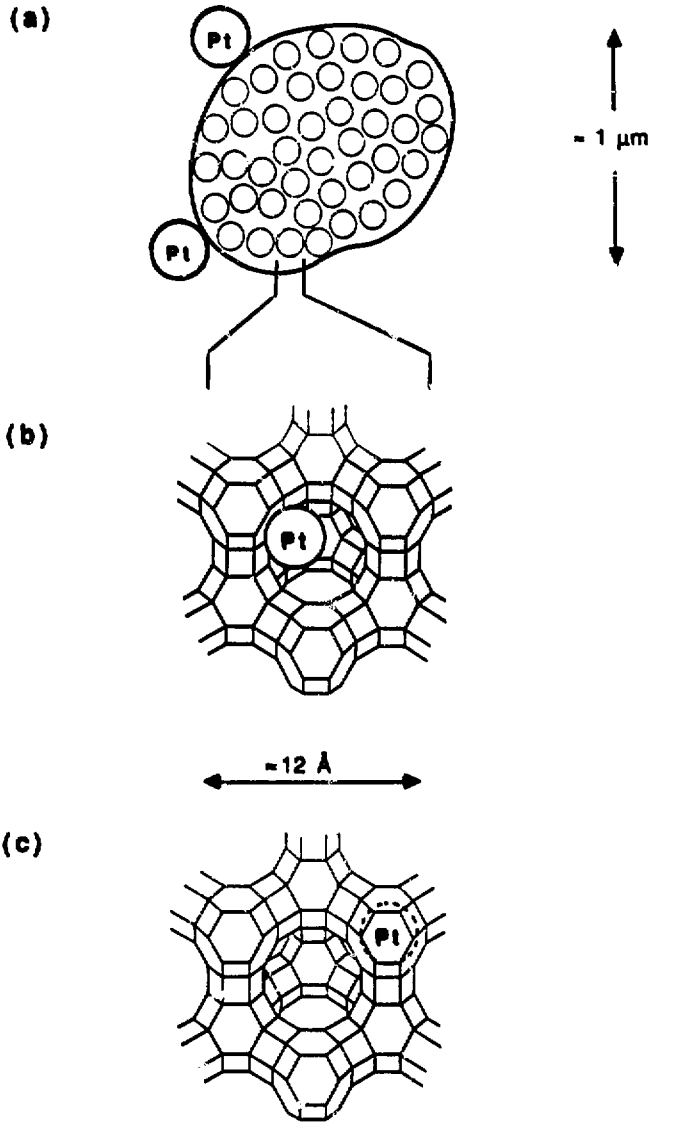

Figure 1.1: Schematic diagram depicting possible locations of platinum atoms or clusters in NaY zeolite: (a) platinum clusters on the exterior surface of a micron-size zeolite crystallite; (b) a platinum atom inside a NaY supercage; and (c) a platinum atom inside a NaY sodalite cavity.

tion, Raman spectroscopy, and temperature programmed reduction (TPR), we have uncovered the detailed chemistry of Pt–NaY catalyst preparation [Chapter 4] and its subsequent effect on metal distribution within the zeolite matrix [Chapters 3 and 4].

By their very nature, heterogeneous catalytic processes rely on molecular clustering at surface adsorption sites to promote chemical reactions. In probing the kinetics of such phenomena at the molecular level, it is imperative that the dynamics and distribution of adsorbed species be understood. Although the molecular dynamics of simple molecules, such as water, methane, and benzene, adsorbed in zeolite cavities have been investigated using NMR relaxation times, lineshape analyses, and NMR pulsed-field diffusion experiments, local structural information pertinent to adsorbate distribution is not available.

As a sensitive, non-reactive probe of supercage cavities within the crystalline zeolite matrix, ^{129}Xe NMR provides information on macroscopic adsorbate distribution heterogeneities in a packed sample volume. With ^{129}Xe NMR it is possible to distinguish, for example, between a packed bed possessing an axial adsorbate concentration gradient and one in which the adsorbate is dispersed homogeneously throughout the macroscopic volume. With knowledge of the zeolite particle size one can estimate the limiting length scale of the adsorbate distribution heterogeneities that can be probed by the ^{129}Xe NMR technique. This makes it possible to estimate the self-diffusivity of xenon atoms in the intracrystalline zeolite channels. Figure 1.2 illustrates that within single zeolite crystallites, microscopic heterogeneities in adsorbate distribution are distinguished from macroscopic axial concentration gradients by vastly different length scales. Unfortunately, detailed information on intracrystalline adsorbate distributions is not readily obtained using ^{129}Xe NMR spectroscopy. By probing local grouping of organic guest species into molecular clusters, however,

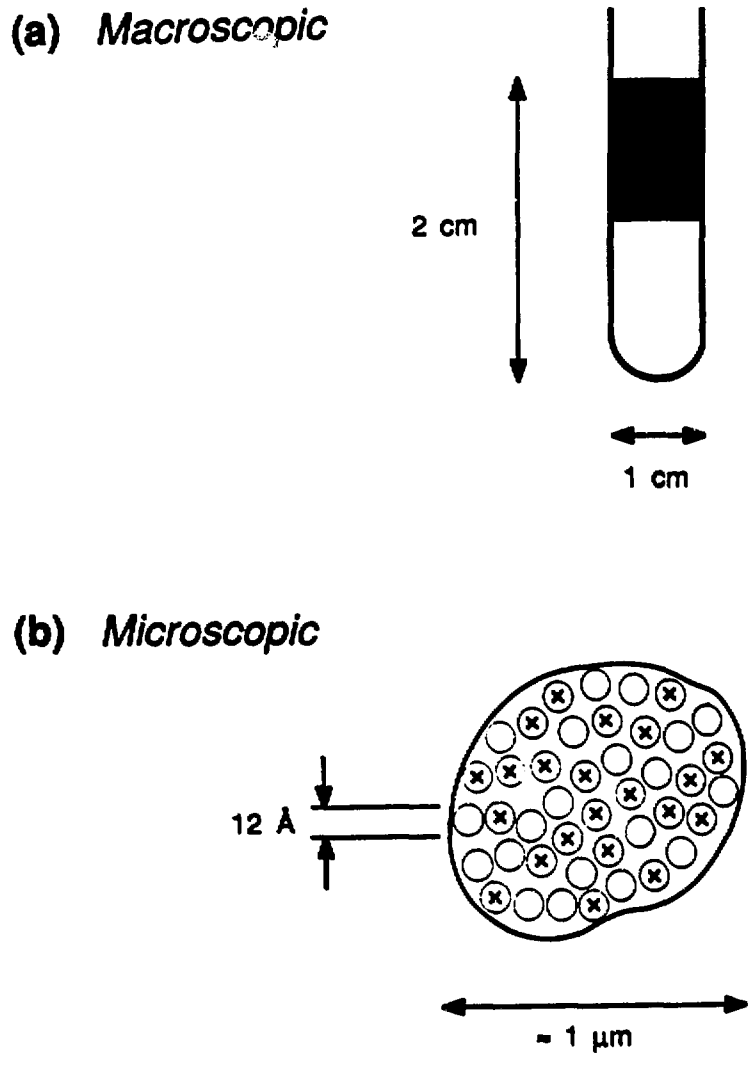

Figure 1.2: The length scales characteristic of adsorbate distribution heterogeneities are dependent upon sample thermal treatment. (a) Xenon-129 NMR can be used to probe macroscopic distribution heterogeneities, while (b) multiple-quantum NMR is sensitive to local structure within individual NaY zeolite supercages.

multiple-quantum (MQ) NMR spectroscopy can distinguish between homogeneous and statistical adsorbate distributions. In Chapters 5 and 6 we have employed a combination of ^{129}Xe and multiple-quantum NMR techniques, together with mass-transport modeling calculations, to obtain detailed information on the distributions of adsorbed aromatic guests in NaY zeolite.

Interactions of molecules inside micropores are crucial to the molecular-sieve function and adsorption properties of zeolites used in catalysis, chromatography, and separations applications. Using the 1.14-nm diameter α-cages of NaA zeolite as microscopic containers, intersorbate interactions in the proximity of a solid surface can be probed by confining and manipulating isolated molecular clusters inside zeolite pores. Heating dehydrated NaA zeolite under elevated xenon pressures allows the 0.44-nm diameter Xe atoms to penetrate the 0.42-nm (at 298 K) diameter windows of the NaA α-cages. Quenching the Xe/NaA system to room temperature produces a kinetically stable distribution of Xe atoms occluded within the zeolite cavities, as indicated schematically in Figure 1.3(a). Because the ^{129}Xe resonance frequency is very sensitive to both surface interactions and xenon density, ^{129}Xe NMR can be used to establish the relative distribution of α-cages containing different numbers of xenon atoms. Larger associations of xenon atoms in the α-cages produce ^{129}Xe peaks with progressively larger chemical shifts (higher resonant frequencies downfield) as shown in Figure 1.3(b). Chapter 7 demonstrates that the properties of xenon in microporous environments, differing in key respects from those of bulk xenon gas at comparable densities, allow the investigation of interactions responsible for the unique adsorption behavior induced by confinement effects in very small pores.

This thesis addresses the local structure of guest-zeolite systems by examining the distribution, chemistry, and transport of metal and adsorbed species in zeo-

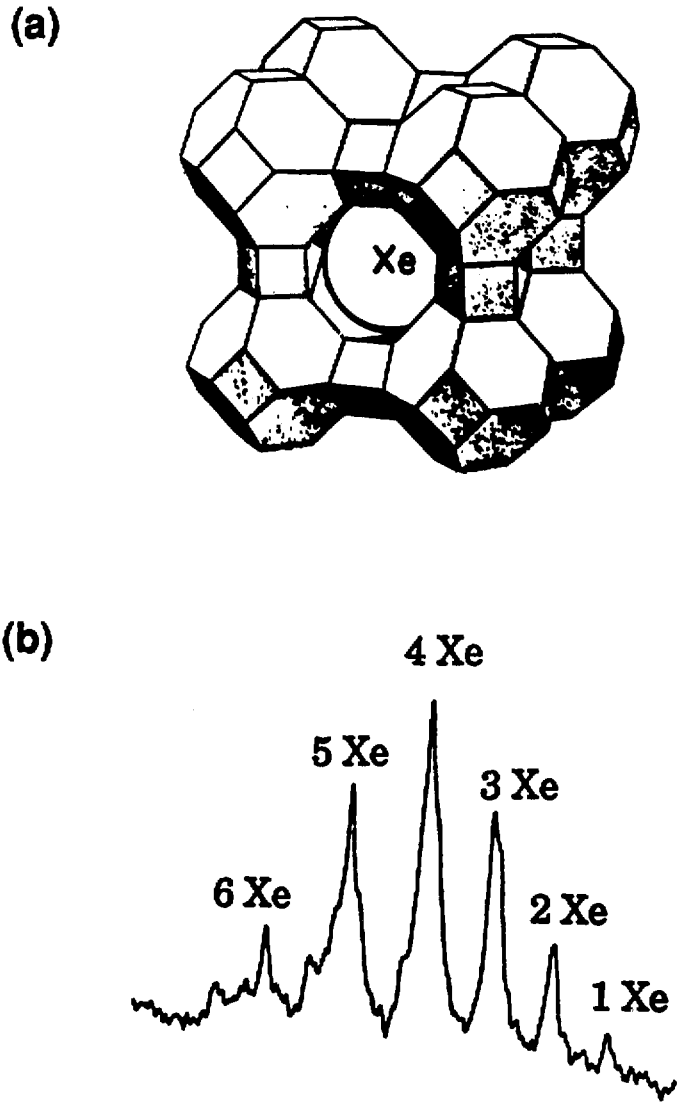

Figure 1.3: Xenon atoms occluded in a NaA α-cages (a) yield peaks in the NMR spectrum (b) that reflect the relative distribution of α-cages containing different numbers of xenon atoms.

lite cavities. Such microstructural information permits guest-guest and guest-lattice interactions to be probed at a molecular level from which macroscopic system properties may be better understood.

Chapter 2

Probing Metal Cluster Formation in Zeolites by ^{129}Xe NMR[1]

2.1 Methods of Metal-Zeolite Preparation

Introduction of catalytically active metals into the pore spaces of zeolites is desirable because of enhanced reaction activity and selectivity [3,4,11]. With internal void volumes of approximately 50% [1], large pore, faujasite-type zeolites such as NaY permit preparation of highly dispersed metal phases. Furthermore, zeolite Y has a silicon-to-aluminum ratio of 1.5–3.0 [1], so that the close proximity of Lewis or Brönsted acid centers to surface metal sites can provide unique, multifunctional catalytic behavior. Zeolite-supported platinum, for example, exhibits unique catalytic properties that are particularly useful in petroleum dewaxing reactions [12,13] or in reforming processes used to increase the octane number of gasoline feedstocks

[1]Presented, in part, at the American Institute of Chemical Engineers national meeting in New York City, November 1987. Portions have been previously published in *J. Amer. Chem. Soc.* 110, 4465 (1988).

[14,15,16,17,18,19]. In addition, Y zeolite-supported platinum has been used for hydrogenolysis of normal and isoparaffins [10,20], for aromatic ring cleavage reactions [21], and for hydrogenation of unsaturated olefins and aromatics [10,20,22].

Numerous means exist for introducing the metal species into the zeolite lattice. Standard impregnation procedures can be used which allow an anionic metal complex, such as aqueous chloroplatinic acid (H_2PtCl_6), to equilibrate within the zeolite pores. Subsequent low-temperature drying, calcination in oxygen, and reduction in hydrogen generate the catalytically active reduced metal.

$$H_2PtCl_6(aq) + [NaY] \xrightarrow{dry} \xrightarrow{O_2} \xrightarrow{H_2} [Pt^0 - NaY] + \text{other products}. \qquad (2.1)$$

Low affinity of the support for the negatively charged metal complex, however, leaves a substantial amount of the precious metal species behind in the bulk aqueous solution.

A more efficient way of introducing the metal into the NaY lattice exploits the favorable ion-exchange kinetics and equilibria for uptake of high-charge-density multivalent cations. A stoichiometric number of $(Al\text{–}O)^-Na^+$ sites on the framework readily exchange the Na^+ charge-balancing cations for multivalent species. For example, the 0.6 nm square-planar $Pt(NH_3)_4^{2+}$ cation adopts positions in the Y zeolite supercages which permit its charge to be shared between at least two of the anionic lattice sites. Nearly 100% of the metal-tetraammine complex in solution is taken up by the zeolite until all supercage sites are saturated. The primary advantage of this approach is the superior metal dispersion which can be obtained compared to the anion impregnation method [23]. As illustrated in Figure 2.1, careful calcination and reduction of the precious metal-exchanged zeolite can provide highly dispersed metal phases in NaY even at high metal loadings [24].

$$Pt(NH_3)_4Cl_2(aq) + [NaY] \xrightarrow{vac.} \xrightarrow{O_2} \xrightarrow{H_2} [Pt^0 - HY] + \text{other products}. \qquad (2.2)$$

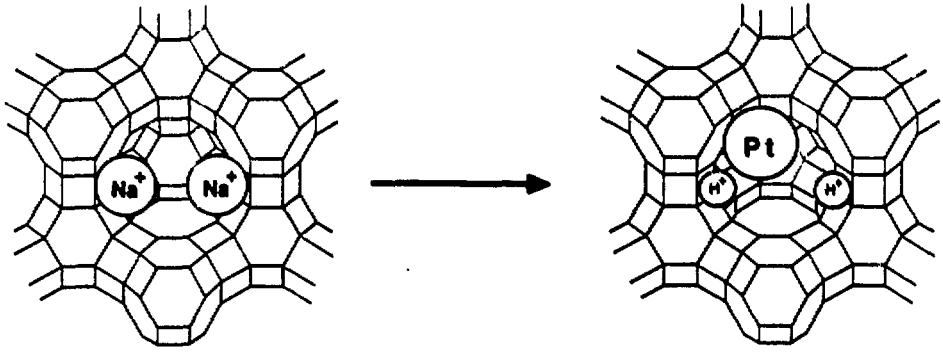

Figure 2.1: Diagram of a single 1.25-nm diameter NaY zeolite supercage. The vertices of the polygon structures represent silicon or aluminum atoms; bridging oxygen atoms are shown as black lines. For convenience of representation, only two of the four exchangeable Na^+ cations in the NaY supercage have been shown [1]. The objective of the catalyst preparation procedure is to introduce highly dispersed metal (e.g., platinum) into supercage locations accessible to diffusing reactant species.

More recent innovations use non-aqueous solvents or vapor-phase deposition of metal carbonyls [25] to introduce metal guests into zeolites. These methods have not, as yet, been applied on an industrial scale, but may become important in the future. For our studies, we focus on the importance of the calcination step to the preparation of highly dispersed metal-zeolite catalysts. We have chosen the popular ion-exchange procedure for initial introduction of the metal species into the zeolite. However, the characterization techniques we employ are suitable for studying metal introduced by the impregnation, non-aqueous solvent, or metal-carbonyl-vapor-deposition methods as well.

It is known that the method of preparation is important to the performance of zeolite-supported metal catalysts [6,26]. Homogeneous and reproducibly high metal dispersion can be achieved only through careful control of calcination and reduction conditions, since migration and agglomeration of cluster precursors can occur with subsequent loss of catalytic activity [10,24,27]. In spite of considerable research [11, 28,29,30,31,32,33,34], the transformations undergone by metal guest species during calcination and reduction have not been established, primarily due to difficulties in characterizing chemical intermediates which exist as cluster precursors. As shown in Figure 2.2, calcination of $Pt(NH_3)_4^{2+}$-exchanged NaY zeolite samples produces intermediate species whose identities and positions within the zeolite framework are strong functions of the thermal treatment imposed during preparatory treatments. Subsequent reduction of the intermediate species results in metal clusters whose sizes and locations are dependent upon the earlier calcination conditions. By using the ^{129}Xe NMR spectroscopy technique pioneered by Fraissard *et al.* [35,36,37,38,39] and Ripmeester [40] and applied to recent advantage by us and others [41,42,43,44,45], we gain insight into the detailed chemistry of metal-zeolite catalyst preparation. What

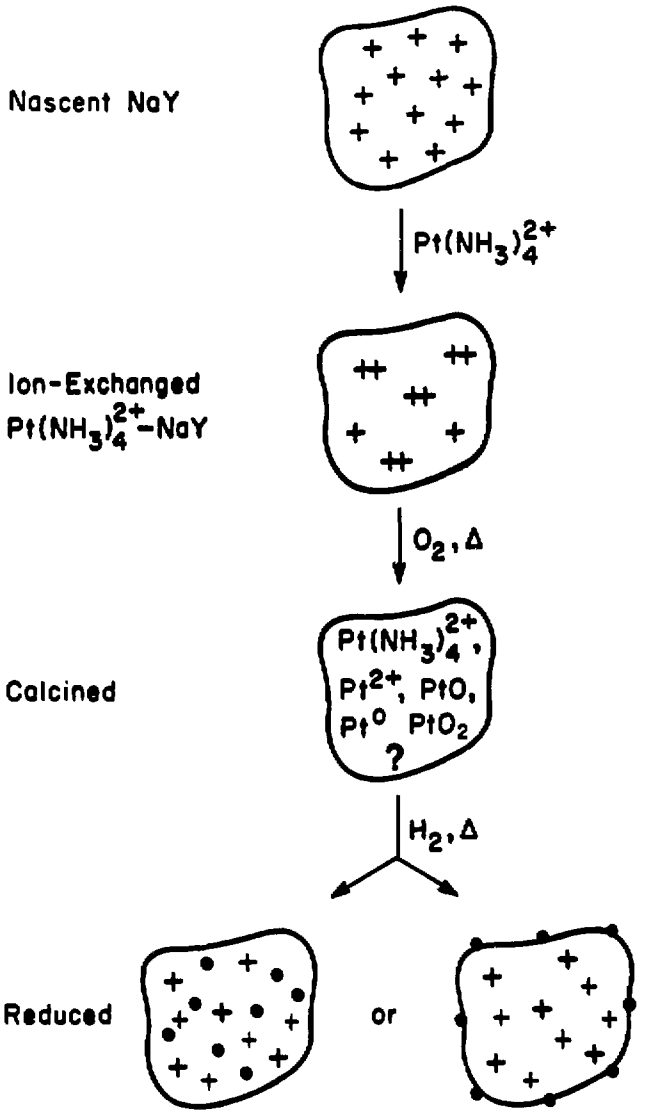

Figure 2.2: Schematic diagram depicting the preparation of Pt–NaY from the nascent NaY starting material. '+' and '++' represent Na^+ and $Pt(NH_3)_4^{2+}$ exchangeble cation species, respectively. Reduction of the calcined catalyst leads to different distributions of the metal phase (represented by the solid circles in the bottommost figures) depending upon the preparation history of the sample.

follows is a theoretical description of the "90°-pulse-and-acquire" method used in the ^{129}Xe NMR experiment.

2.2 Pulsed Fourier-Transform NMR

Nuclei with odd atomic mass or odd atomic number possess a net magnetic moment μ which will interact with an applied magnetic field. Consider an ensemble of such particles (dilute spin-$\frac{1}{2}$ ^{129}Xe nuclei, in our case) in the presence of the magnetic field typically used in NMR experiments:

$$\vec{H} = H_0\vec{z} + H_1(\vec{x}\cos\omega t - \vec{y}\sin\omega t)\,, \tag{2.3}$$

where H_0 is the magnitude of the static external field, H_1 is the magnitude of the magnetic component of the oscillatory pulsed-radiofrequency (rf) field at frequency ω, t is time, and $\vec{x}$, $\vec{y}$, and $\vec{z}$ are unit vectors in the laboratory frame of reference. Assume also that the nuclear spin Hamiltonian of the system is comprised only of contributions from interactions between the magnetic moment of the nuclei and the applied field $\vec{H}$ (the Zeeman interaction) and between the magnetic moment of the nuclei and polarized electron orbitals (the chemical shift interaction):

$$\mathcal{H} = \mathcal{H}_Z + \mathcal{H}_{cs}\,. \tag{2.4}$$

The Zeeman interaction has the general form

$$\mathcal{H}_Z = -\vec{\mu}\cdot\vec{H} = -\gamma\hbar\vec{I}\cdot\vec{H}\,, \tag{2.5}$$

where γ is the gyromagnetic ratio (a property of the particular nucleus under study), $\hbar$ is Planck's constant divided by 2π, and $\vec{I}$ is the net magnetization quantized in the z-direction. The Zeeman interaction splits the degeneracy of the $2I+1$ nuclear

energy levels by $\hbar\omega_0 = \hbar\gamma H_0$ (where ω_0 is the Larmor frequency). For a spin-$\frac{1}{2}$ system ($I = \frac{1}{2}$), a Boltzmann distribution exists between the populations N_1 and N_2 in the two energy states:

$$\frac{N_2}{N_1} = \exp\left(\frac{-\gamma\hbar H_0}{kT}\right). \tag{2.6}$$

Higher static fields lead to greater polarization of the spins and therefore to an increase in the sensitivity of the experiment (greater signal-to-noise).

The chemical shift interaction manifests electron shielding effects which alter the local magnetic field in the immediate vicinity of a given nucleus. Since the electronic environment of an atom is sensitive to bonding geometry or, in the case of physisorbed xenon, to surface or density effects, the chemical shift can be used as a diagnostic probe of nuclear, and hence chemical, environment. The chemical shift Hamiltonian has the form

$$\mathcal{H}_{cs} = -\vec{\mu}\cdot\vec{\sigma}\cdot\vec{H} = -\gamma\hbar\vec{I}\cdot\vec{\sigma}\cdot\vec{H}. \tag{2.7}$$

For liquids or gases in a static field directed along the z-axis, isotropic molecular motion averages the chemical shift tensor $\vec{\sigma}$ to an isotropic scalar value σ_z [46,47]. Thus, the nucleus under consideration experiences an effective static field of magnitude $H_{eff} = (1-\sigma_z)H_0$ in the z-direction as a result of electronic shielding effects.

For an ensemble of spin-$\frac{1}{2}$ particles in a field $\vec{H}$ the Hamiltonian therefore becomes

$$\mathcal{H}(t) = -\gamma\hbar(1-\sigma_z)H_0\hat{I}_z - \gamma\hbar H_1(\hat{I}_x\cos\omega t - \hat{I}_y\sin\omega t) \tag{2.8}$$

$$\mathcal{H}(t) = -\omega_{eff}\hbar\hat{I}_z - \gamma\hbar H_1(\hat{I}_x\cos\omega t - \hat{I}_y\sin\omega t), \tag{2.9}$$

where $\omega_{eff} = \gamma(1-\sigma_z)H_0$ and $\hat{I}_x$, $\hat{I}_y$, and $\hat{I}_z$ are the components of nuclear spin aligned along the respective Cartesian axes. The time-dependent Schrödinger equation

$$\mathcal{H}(t)|\psi(t)\rangle = i\hbar\frac{d}{dt}|\psi(t)\rangle \tag{2.10}$$

permits the evolution of the system to be followed as a function of time. The trajectory of the system is simplified considerably by performing a coordinate transformation into a frame of reference that rotates at angular frequency ω. We first identify the time-independent Hamiltonian which makes this transformation possible.

The time dependence in the second term of Equation 2.9 arises from rotating $\hat{I}_x$ about the z-axis as demonstrated below. For left-handed rotations,

$$e^{i\omega t\hat{I}_z}\,\hat{I}_x\,e^{-i\omega t\hat{I}_z} = \hat{U}(t)\,\hat{I}_x\,\hat{U}^\dagger(t), \tag{2.11}$$

where the time evolution operator

$$\hat{U}(t) = e^{i\omega t\hat{I}_z} \tag{2.12}$$

is unitary (that is, $\hat{U}\hat{U}^\dagger = 1$). For two arbitrary operators $\mathcal{A}$ and $\mathcal{B}$ which in general do not commute, it can be shown that

$$e^{\mathcal{A}}\mathcal{B}e^{-\mathcal{A}} = \sum_{n=0}^{\infty}\frac{1}{n!}[\mathcal{A},[\mathcal{A},\cdots[\mathcal{A},\mathcal{B}]]\cdots]_n\,, \tag{2.13}$$

so

$$e^{i\omega t\hat{I}_z}\,\hat{I}_x\,e^{-i\omega t\hat{I}_z} = \sum_{n=0}^{\infty}\frac{1}{n!}\left(\frac{i\omega t}{\hbar}\right)^n[\hat{I}_z,[\hat{I}_z,\cdots[\hat{I}_z,\hat{I}_x]]\cdots]_n\,. \tag{2.14}$$

But, using commutator identities, we know that

$$[\hat{I}_z,\hat{I}_x] = i\hbar\hat{I}_y\,, \tag{2.15}$$

$$[\hat{I}_z,[\hat{I}_z,\hat{I}_x]] = i\hbar[\hat{I}_z,\hat{I}_y] = \hbar^2\hat{I}_x\,, \tag{2.16}$$

and so on. From this it follows that

$$\hat{U}(t)\,\hat{I}_x\,\hat{U}^\dagger(t) = \hat{I}_x\sum_{n=0}^{\infty}\frac{-1^n(\omega t)^{2n}}{2n!} - \hat{I}_y\sum_{n=0}^{\infty}\frac{-1^n(\omega t)^{2n+1}}{(2n+1)!} \tag{2.17}$$

or

$$\hat{U}(t)\,\hat{I}_x\,\hat{U}^\dagger(t) = \hat{I}_x\cos\omega t - \hat{I}_y\sin\omega t \tag{2.18}$$

as expected. Recognizing that

$$e^{i\omega t \hat{I}_z}\,\hat{I}_x\,e^{-i\omega t \hat{I}_z} = \hat{I}_x\,, \tag{2.19}$$

permits Equation 2.9 to be rewritten as

$$\mathcal{H}(t) = e^{i\omega t \hat{I}_z}\left[-\omega_{eff}\hbar\hat{I}_z - \gamma\hbar H_1 \hat{I}_x\right] e^{-i\omega t \hat{I}_z} \tag{2.20}$$

$$\mathcal{H}(t) = \hat{\mathcal{U}}(t)\left[-\omega_{eff}\hbar\hat{I}_z - \gamma\hbar H_1 \hat{I}_x\right]\hat{\mathcal{U}}^{\dagger}(t)\,. \tag{2.21}$$

This allows us to define the time-independent Hamiltonian

$$\mathcal{H}_0 = \left[-\omega_{eff}\hbar\hat{I}_z - \gamma\hbar H_1 \hat{I}_x\right], \tag{2.22}$$

whereby

$$\mathcal{H}(t) = \hat{\mathcal{U}}(t)\,\mathcal{H}_0\,\hat{\mathcal{U}}^{\dagger}(t)\,. \tag{2.23}$$

Making the transformation into the rotating frame, we define $|\psi(t)\rangle_R$ so that

$$|\psi(t)\rangle = \hat{\mathcal{U}}(t)|\psi(t)\rangle_R \longrightarrow |\psi(t)\rangle_R = \hat{\mathcal{U}}^{\dagger}(t)|\psi(t)\rangle\,, \tag{2.24}$$

recalling that $\hat{\mathcal{U}}(t)$ is unitary. Expressing the time-dependent Schrödinger equation in terms of $|\psi(t)\rangle_R$ using Equations 2.10, 2.22, 2.23, and 2.24 yields

$$i\hbar\frac{d}{dt}|\psi(t)\rangle = i\hbar\frac{d}{dt}\left[\hat{\mathcal{U}}(t)|\psi(t)\rangle_R\right] \tag{2.25}$$

$$i\hbar\frac{d}{dt}|\psi(t)\rangle = i\hbar\frac{d}{dt}\left[e^{i\omega t\hat{I}_z}|\psi(t)\rangle_R\right] \tag{2.26}$$

$$i\hbar\frac{d}{dt}|\psi(t)\rangle = -\omega\hbar\hat{I}_z\hat{\mathcal{U}}(t)|\psi(t)\rangle_R + \hat{\mathcal{U}}(t)i\hbar\frac{d}{dt}|\psi(t)\rangle_R \tag{2.27}$$

and

$$\mathcal{H}(t)|\psi(t)\rangle = \hat{\mathcal{U}}(t)\,\mathcal{H}_0\,\overbrace{\hat{\mathcal{U}}^{\dagger}(t)\hat{\mathcal{U}}(t)}^{=1}\,|\psi(t)\rangle_R = \hat{\mathcal{U}}(t)\,\mathcal{H}_0\,|\psi(t)\rangle_R\,. \tag{2.28}$$

Substituting Equations 2.27 and 2.28 into Equation 2.10, we obtain

$$\hat{\mathcal{U}}(t)\,\mathcal{H}_0\,|\psi(t)\rangle_R = -\omega\hbar\hat{I}_z\hat{\mathcal{U}}(t)|\psi(t)\rangle_R + i\hbar\hat{\mathcal{U}}(t)\frac{d}{dt}|\psi(t)\rangle_R\,. \tag{2.29}$$

Since $\hat{I}_z$ and $\hat{U}(t)$ commute, Equation 2.29 can be rearranged and combined with Equation 2.22 to give

$$i\hbar\frac{d}{dt}|\psi(t)\rangle_R = (\mathcal{H}_0 + \omega\hbar\hat{I}_z)|\psi(t)\rangle_R \tag{2.30}$$

or equivalently

$$i\hbar\frac{d}{dt}|\psi(t)\rangle_R = \overbrace{[(\omega - \omega_{eff})\hbar\hat{I}_z - \gamma\hbar H_1\hat{I}_x]}^{\mathcal{H}\neq\mathcal{H}(t)}|\psi(t)\rangle_R. \tag{2.31}$$

The unitary transformation $\hat{U}(t)$ has, thus, changed the problem from one in the laboratory frame with a time-*dependent* Hamiltonian to one in a rotating frame with a time-*independent* Hamiltonian. Integrating Equation 2.31 yields the simplified expression for the behavior of the wavefunction in the rotating frame:

$$|\psi(t)\rangle_R = \exp\left\{-it[(\omega - \omega_{eff})\hat{I}_z - \gamma H_1\hat{I}_x]\right\}|\psi(0)\rangle_R. \tag{2.32}$$

Physically, the frequencies ω and ω_{eff} in Equation 2.32 represent the spectrometer carrier frequency (ω) and the resonance frequency (ω_{eff}) of each chemically distinct nucleus in the static field H_0. When $\omega = \omega_{eff}$, the $\hat{I}_z$ term disappears and Equation 2.32 reduces to

$$|\psi(t)\rangle_R = e^{i\gamma H_1 t\hat{I}_x}|\psi(0)\rangle_R \tag{2.33}$$

$$|\psi(t)\rangle_R = e^{i\theta\hat{I}_x}|\psi(0)\rangle_R, \tag{2.34}$$

where the exponential term corresponds to a rotation through an angle θ about the x'-axis in the rotating frame.

$$\theta = \gamma H_1 t \tag{2.35}$$

represents the flip angle of the spins in the rotating frame induced by the radiofrequency pulse $\vec{H}_1$ applied for a time t.

Manipulation of the spins experimentally is carried out as shown in Figure 2.3. The sample is placed inside a coil of copper wire which serves as both transmitter

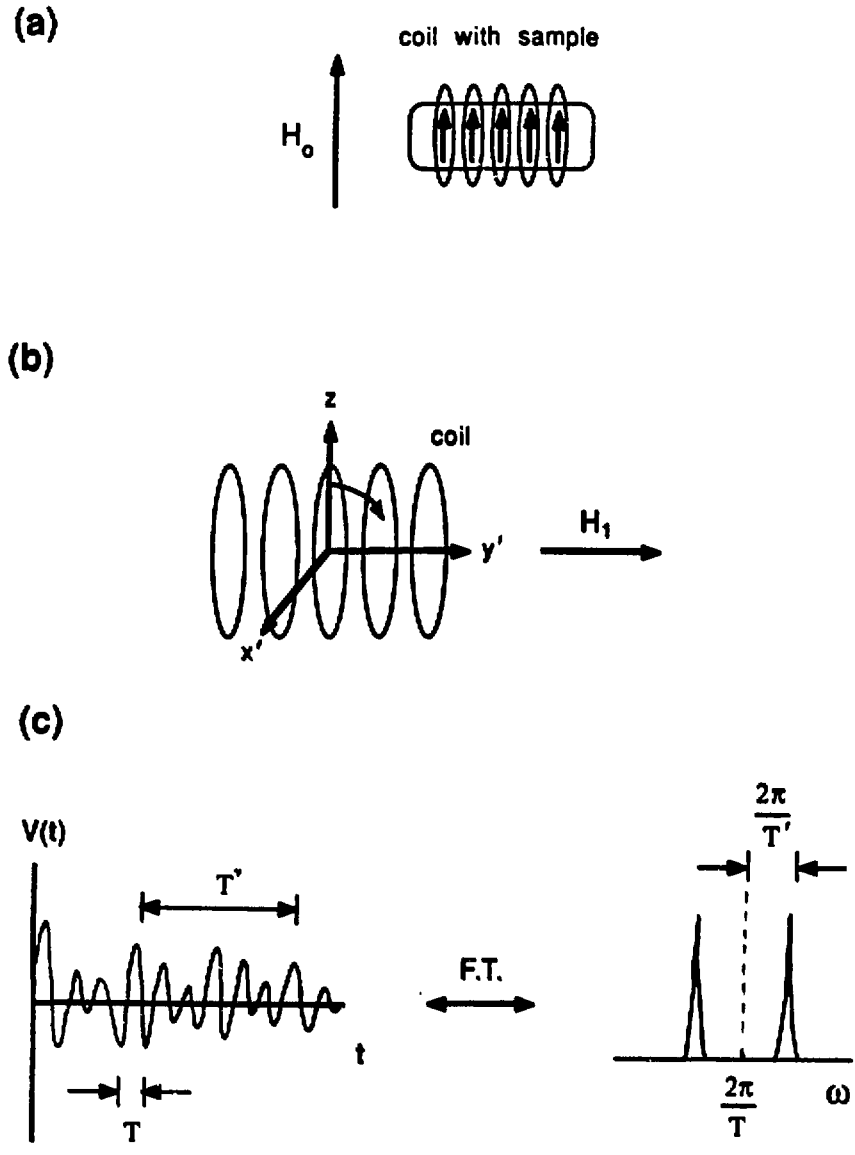

Figure 2.3: Pulsed Fourier-Transform NMR

of the $\vec{H}_1$ rf pulse and receiver of the voltage induced by the perturbed spin system as it returns to equilibrium in the laboratory frame. The coil itself is situated in an externally applied static field $\vec{H}_0$ [Fig. 2.3(a)] which initially polarizes the spin system along the z-axis in the direction of $\vec{H}_0$. Application of a pulse of radiofrequency radiation γH_1 through the transmitter coil for a time t causes the spins to rotate about the x'-axis in the rotating frame shown in Figure 2.3(b). The x'- and y'-axes rotate about the z-axis at the spectrometer carrier frequency ω. When the $\vec{H}_1$ field is turned off, an oscillating voltage (referred to as a 'free induction decay' or FID, for short) is induced in the receiver coil by the precessing spins, which gradually return to their equilibrium polarization along the z-axis in the presence of $\vec{H}_0$. Relaxation times T_1 (spin-lattice) and T_2 (spin-spin) describe the rapidity with which the spin system re-equilibrates in the direction of $\vec{H}_0$ (T_1) or dephases in the x'-y' plane (T_2). For systems in which only electron shielding effects are important, bonding or surface environments, which alter the electron distribution about a nucleus, change the resonant frequency ω_{eff}. As a result, the voltage induced in the receiver coil will contain as many superimposed FID's as there are chemically distinct types of a particular nuclei in the sample. For a material with two such species, for example the CH_3 and CH_2 protons in chloroethane (CH_3CH_2Cl), an interference pattern will be present in the FID resulting in two resolved peaks at discrete resonant frequencies in the Fourier-transformed NMR spectrum [Fig. 2.3(c)].

2.3 ^{129}Xe NMR Spectroscopy

Xenon-129 has a spin-$\frac{1}{2}$ nucleus (one unpaired neutron spin [48]) with a natural isotopic abundance of 26.4%. Its sensitivity of 2.1×10^{-2} relative to ^{1}H is an order of magnitude greater than that of ^{13}C used widely in NMR studies of organic molecules.

At room temperature, xenon exists as a monoatomic gas with a valence electron configuration that is completely filled (i.e., $5s^25p^6$). This results in a spherically symmetric electron distribution shielding the nucleus of an isolated xenon atom. Xenon's large electron cloud is easily polarized and thus serves as a sensitive probe of its environment. Interatomic interactions perturb the electron distribution about the xenon nucleus leading to large changes (called 'chemical shifts') in the ^{129}Xe nuclear resonance frequency. Jameson *et al.* have measured the resonant frequency of ^{129}Xe as a function of xenon density and in gas mixtures [49]. Perturbations arising from interactions with a solid surface can also give rise to shifts in the ^{129}Xe resonant frequency. This is illustrated in Figure 2.4 for a xenon atom physisorbed within a Y zeolite supercage cavity where interactions with the aluminosilicate lattice deshield the xenon nucleus. The splitting of the ^{129}Xe nuclear energy levels, and thus the magnitude of ω_{eff}, depend not only upon the external field $\vec{H}_0$, but on the deshielding which results from the collision-induced asymmetry of the electron distribution as well. Both contribute to the local field that establishes the ^{129}Xe nuclear resonance behavior observed.

Since atoms and molecules are dynamic species, the criterion of 'chemical distinctness' necessary for obtaining resolved spectra in isotropic phases requires some qualification. Assuming adequate sensitivity, resolved peaks are obtained in the NMR spectrum of an isotropic phase (i.e., a gas or a low viscosity liquid) only for species whose lifetimes are long with respect to the time scale of the NMR experiment. This is relevant to ^{129}Xe atoms interacting with the heterogeneous NaY zeolite lattice, where mean Xe residence times at individual surface sites are on the order of 10^{-9} s at room temperature [38,51]. Xenon exchange between adsorption sites within the NaY supercages is, thus, rapid with respect to the frequency splitting of ^{129}Xe in the

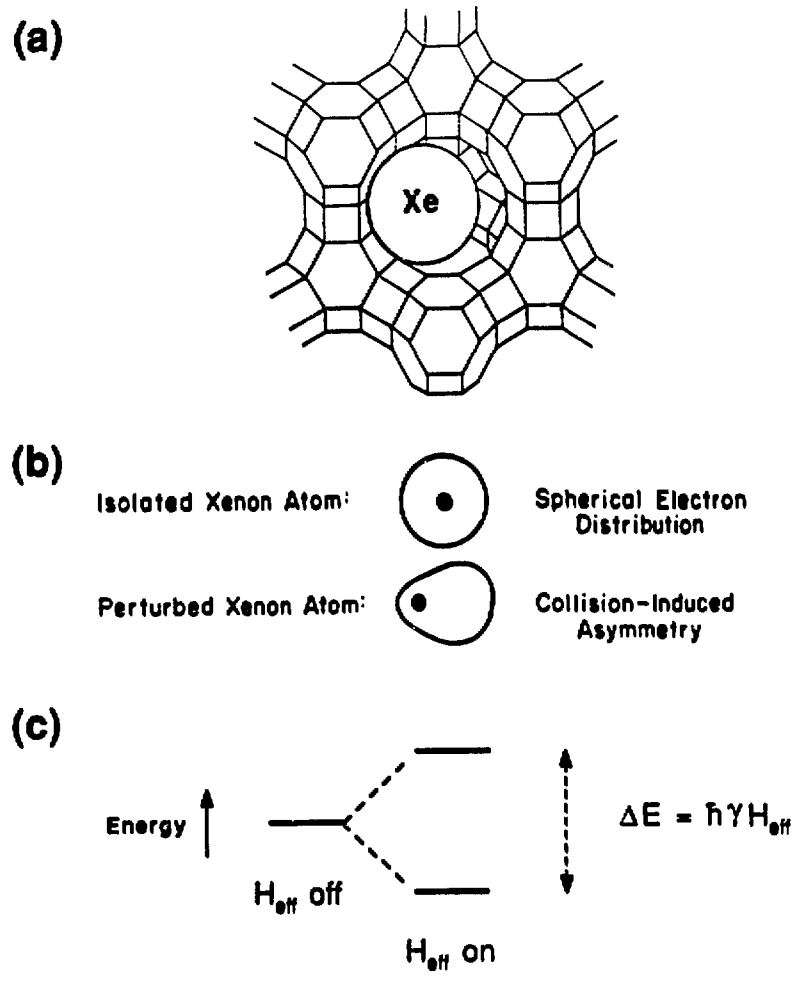

Figure 2.4: (a) Diagram of a xenon atom shown in the aperture of a Y-type zeolite supercage. The 0.44-nm diameter Xe atom is shown (to scale) alongside the 0.22 nm hexagonal window into the sodalite cages. (b) The xenon nucleus is maximally shielded when the electron distribution is spherically symmetric. Interatomic interactions perturb the electron distribution, deshielding the nucleus, so that H_{eff} is increased. (c) Under these circumstances, the ^{129}Xe resonant frequency becomes higher as the splitting between the nuclear energy levels increases.

different adsorption environments ($\approx 10^{-4}$ s) [52,53] [see Chapter 5]. The ^{129}Xe NMR technique therefore measures the mean ^{129}Xe resonant frequency, characteristic of an average supercage environment, over this period. For example, the two spectra in Figure 2.5 reveal single isotropically averaged peaks reflecting the rapid mobility of xenon probe atoms among the various distinct adsorption sites in different Y zeolite supercage environments. In Figure 2.5(a) xenon adsorbed in dehydrated NaY under an equilibrium atmosphere of 646 torr Xe resonates 98 ppm downfield from xenon gas at very low pressure. After ion-exchanging a bulk average of approximately 1.4 $Pt(NH_3)_4^{2+}$ cations per NaY supercage and dehydrating the sample at 473 K, the ^{129}Xe peak is shifted much farther downfield to 181 ppm as shown in Figure 2.5(b). Xenon-129 NMR, thus, cannot resolve individual intracrystalline NaY adsorption sites at room temperature, but it is very sensitive to the average environment in the Y zeolite supercages. Here, we exploit this sensitivity in studying the catalytic activation of NaY-supported platinum.

The preparation of metal-zeolite catalysts depends upon treatment conditions which alter the intracrystalline environment by affecting the identity and the location of metal guest species. The shielding of the ^{129}Xe nucleus is, in turn, dependent upon the intracrystalline structure of the zeolite-guest system so that changes in the metal guest can be followed by ^{129}Xe NMR. We report for the first time changes in the chemical environment of NaY-supported platinum guest species by monitoring shifts in the ^{129}Xe resonance signal induced by different chemical and thermal treatments. Calcination in oxygen at elevated temperatures, for example, decomposes the metal-tetraammine complex in $Pt(NH_3)_4^{2+}$-exchanged zeolite Y to an intermediate species (shown to be PtO in Chapter 4). Xenon-129 NMR data shown in Figure 2.6 reveal a substantial upfield shift in the single isotropic peak for xenon adsorbed in

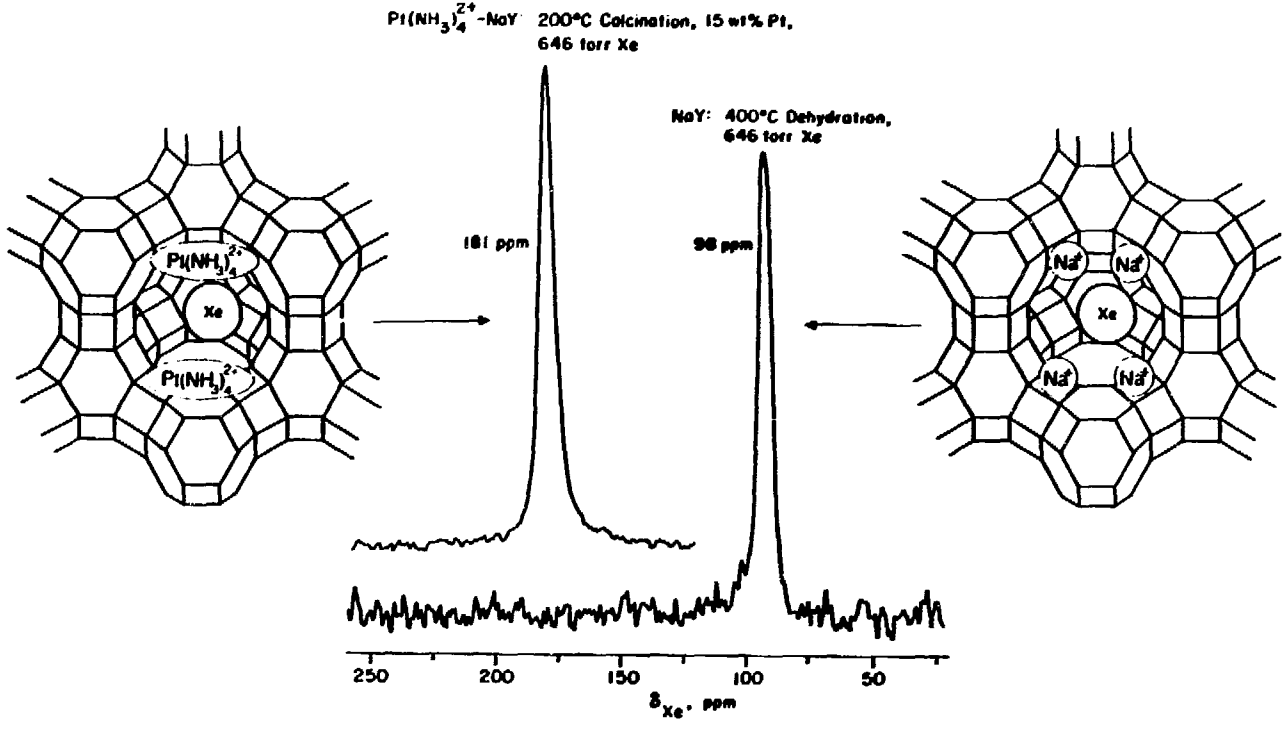

Figure 2.5: Sensitivity of the ^{129}Xe nuclear resonance frequency to the average environment in Y zeolite supercages.

$Pt(NH_3)_4^{2+}$–NaY zeolite samples calcined at different maximum temperatures. As noted above, the single peak in each spectrum arises from motional averaging of the many distinct physisorption sites and xenon–xenon interactions which a xenon atom encounters during each signal acquisition. Accordingly, the ^{129}Xe chemical shift reflects the intrinsic perturbations experienced at each site, weighted by the collisional probability with which each interaction occurs. The ^{129}Xe chemical shift data clearly indicate distinct chemical differences in the Pt–NaY samples resulting from different calcination treatments. For the specific case of adsorption under an equilibrium xenon pressure of 200 torr, the ^{129}Xe chemical shift moves farther upfield in $Pt(NH_3)_4^{2+}$–NaY samples calcined to progressively higher temperatures. The heavy metal loading (ca. 1.4 Pt atoms per supercage), coupled with enhanced xenon–Pt affinity [38], makes ^{129}Xe NMR particularly sensitive to the nature of the metal guest and accounts for the large chemical shifts reported in Figure 2.6.

2.4 Pt–NaY Sample Preparation

The heterogeneous local structure in the Y zeolite supercages requires that the interpretation of the ^{129}Xe NMR data be made with care. Shielding of the ^{129}Xe probe atoms is influenced by xenon density, the crystallinity and pore sizes of the host framework, the size, charge, and location of exchangeable cations, as well as the presence of metal or adsorbed guest species. Because the ^{129}Xe chemical shift is sensitive to all of these potential variables, extraction of chemical or structural information on a zeolite's intracrystalline environment requires careful attention to preparation of the sample and analysis of the NMR data.

Pt–NaY samples containing 15 wt% platinum were prepared by introducing the tetraammine salt, $Pt(NH_3)_4^{2+}$, into the zeolite lattice via the ion-exchange procedure

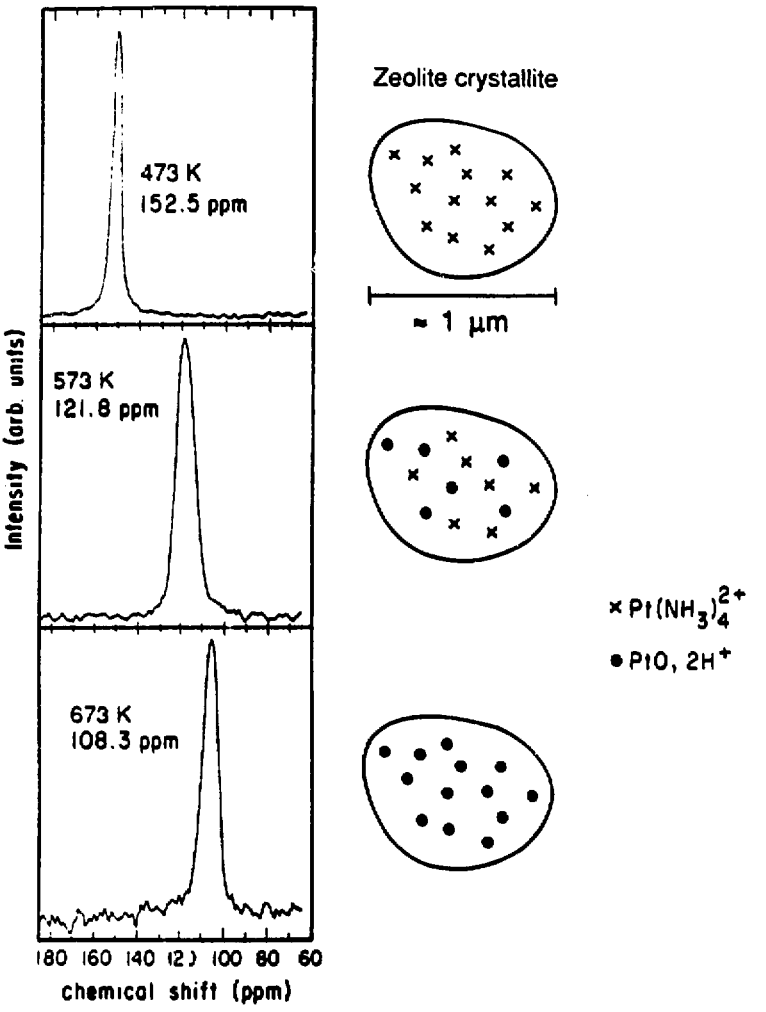

Figure 2.6: ^{129}Xe NMR spectra of xenon (200 torr equilibrium pressure, T=295 K) adsorbed on $Pt(NH_3)_4^{2+}$-NaY zeolite samples (ca. 15 wt% Pt) following calcination at 473 K, 573 K, and 673 K. Accompanying the spectra are schematic diagrams depicting chemical differences in the metal species produced by the different thermal treatments. Upon removal of the platinum species' cationic charge during calcination, the anionic charge on the zeolite lattice is balanced by H^+ or NH_4^+ produced during decomposition of the metal-tetraammine complex [50].

of Gallezot *et al.* [24]. To permit accurate determination of the zeolite mass, approximately 10 g of NaY zeolite was placed in a high-humidity environment overnight to ensure a water-saturated condition. The hydrated NaY was slurried in 500 cm^3 of deionized water, with the desired amount of $Pt(NH_3)_4Cl_2 \cdot H_2O$ then added to the vigorously stirred zeolite-water mixture. The ion-exchange process was allowed to equilibrate, under gentle refluxing, for 12 h at 373 K to achieve essentially 100% uptake of the divalent metal complex . The $Pt(NH_3)_4^{2+}$–NaY slurry was subsequently filtered in a 150 cm^3 Büchner funnel with a medium-grade fritted disk and rinsed twice with 100 cm^3 of 29% NH_4OH solution (Fisher Scientific Co.), to remove residual chloride ions, and twice more with 100 cm^3 of deionized water. The $Pt(NH_3)_4^{2+}$–NaY cake was dried overnight under house vacuum at 295 K.

Separate 0.5 g samples of the dried $Pt(NH_3)_4^{2+}$–NaY powder were charged separately to the reactor shown in Figure 2.7. The catalyst material was added through the long riser-tube prior to connecting the NMR sample cell via glassblowing methods. The $Pt(NH_3)_4^{2+}$–NaY sample rests on the lower fritted disk allowing the reactor to operate in upflow fashion to minimize channeling of the feed gas. The reactor was attached to the apparatus shown in Figure 2.8, downstream from the feed gas supply, and first flushed with helium gas. All feed gases were dried over three NaA-zeolite beds in series before being passed over the catalyst. Hydrogen used during reduction of previously calcined Pt–NaY was also passed through a chromate trap to remove residual oxygen. The volumetric flow of the feed gas was monitored by a downstream rotameter before being directed to a fume hood. The reactor was heated using a home-built 1 kW electric heater whose output was controlled by an Omega programmable temperature controller (Model CN-2010) with a thermocouple input from the reactor, positioned in the thermocouple well shown in Figure 2.7. During

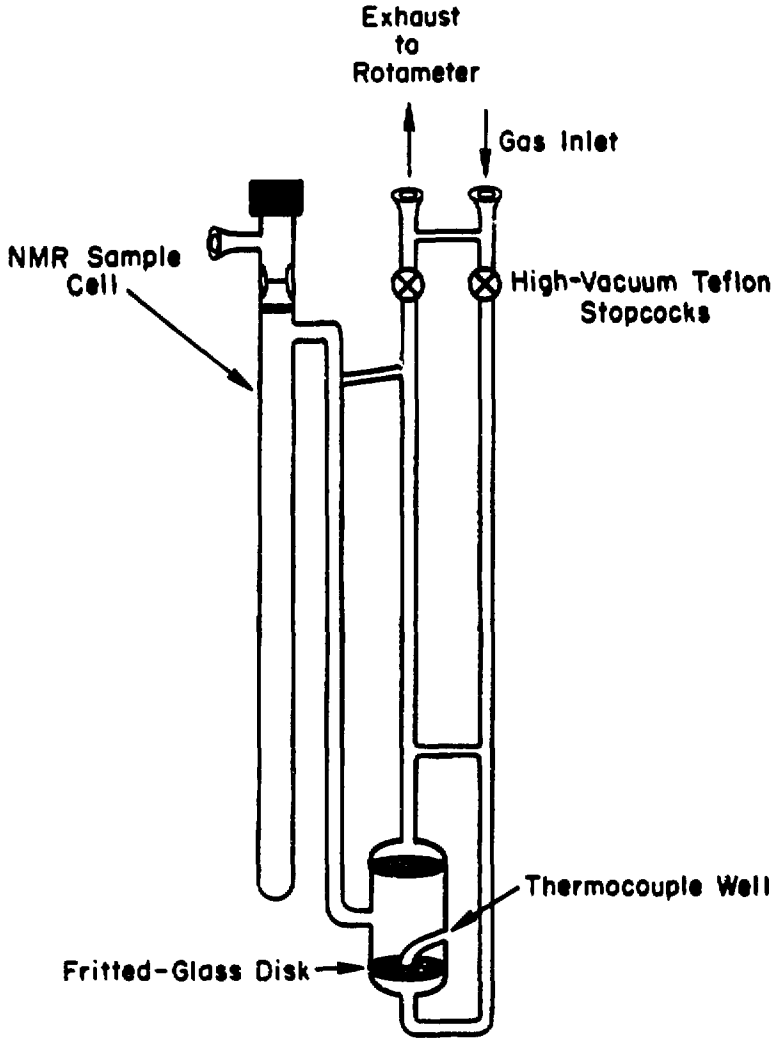

Figure 2.7: Catalyst preparation reactor used in calcination, reduction, and high-temperature reoxidation of Pt–NaY. The assembly is approximately 25 cm long.

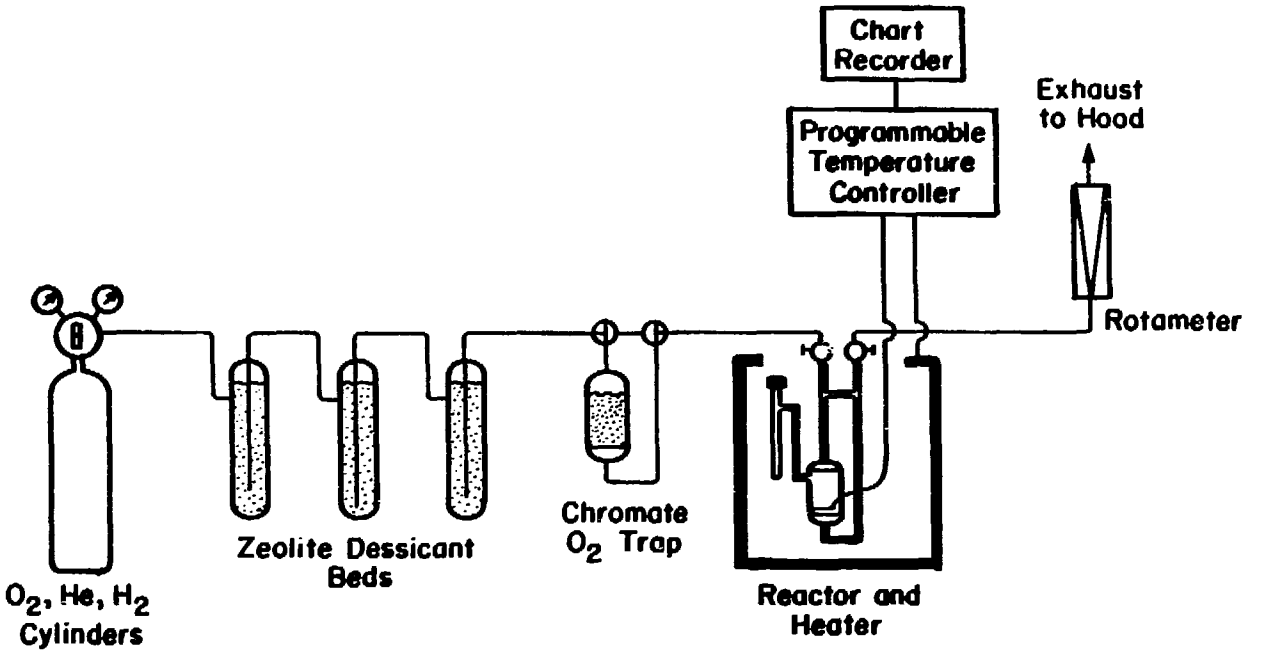

Figure 2.8: Metal-zeolite sample preparation apparatus.

calcination, the samples were heated at 11 K/h to maximum temperatures ranging from 473 K to 873 K in the presence of excess oxygen gas (15 cm^3/s). Upon reaching the upper temperature limit, the furnace was turned off, allowing the insulated reactor to cool to 298 K over a period of many hours.

After cooling, the reactor was again flushed with helium and disconnected from the apparatus shown in Figure 2.8. The calcined Pt–NaY catalyst material was then mechanically transferred via the riser-tube into the NMR cell, after which the cell was carefully sealed by glassblowing the sidearm shut. During the sealing operation the NMR cell containing the calcined Pt–NaY sample was disconnected from the reactor assembly near its attachment to the riser-tube. The NMR cell, shown in Figure 2.9, was fit with a coarse-grade fritted-glass disk and a Kontes high-vacuum stopcock to permit attachment to a vacuum rack for sample degassing and addition of xenon gas for ^{129}Xe NMR and adsorption isotherm experiments. After evacuation of the calcined Pt–NaY samples for 10 h at 295 K, xenon gas was introduced to various equilibrium pressures, guided by separate adsorption isotherm experiments [see Appendix D]. Xenon-129 NMR spectra of adsorbed xenon were obtained on a Bruker AM–400 spectrometer operating at 110.7 MHz. Typically, 2000 to 20000 signal acquisitions were accumulated for each spectrum with a recycle delay of 0.2 s between 90° pulses. Chemical shift measurements are precise to within 0.5 ppm and are expressed relative to xenon gas at very low pressure [37,49]. Xenon adsorption isotherms were measured for each calcined Pt–NaY sample and correlated with the NMR data.

Following the different calcination treatments and room-temperature ^{129}Xe NMR experiments, the same samples were recharged separately to the reactor assembly [Figs. 2.7 and 2.8] and reduced under identical conditions in purified flowing hy-

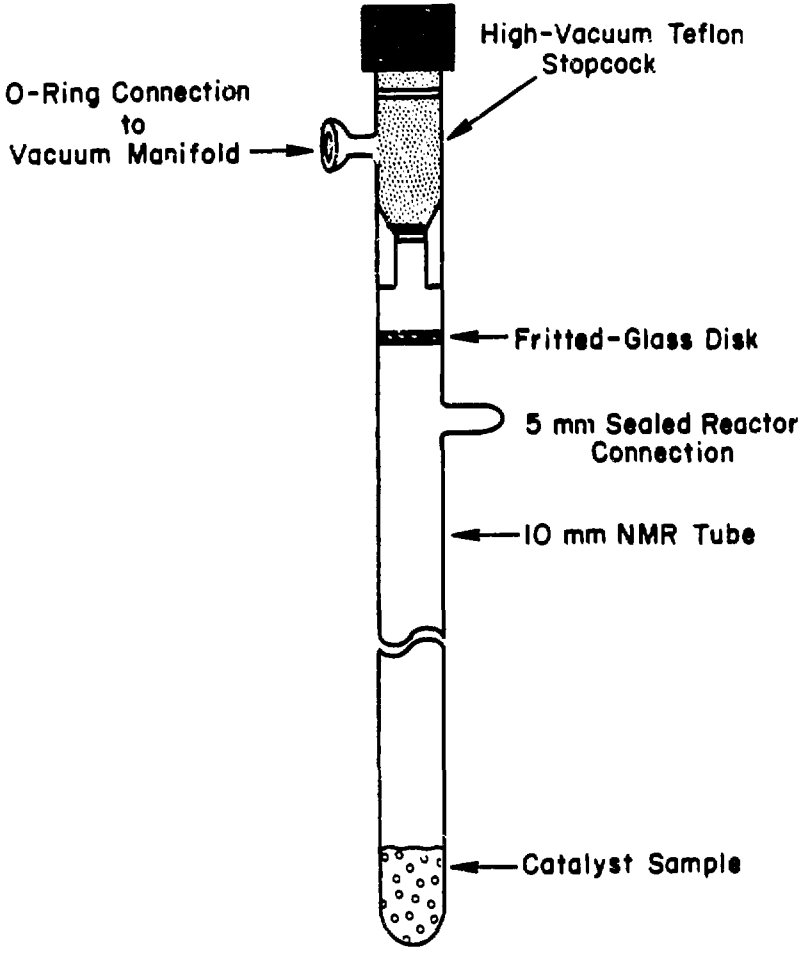

Figure 2.9: Pt–NaY sample cell used in ^{129}Xe NMR and adsorption isotherm experiments.

drogen (40 cm^3/s) for 4 h at 673 K. After sealing the samples in NMR cells once again, the reduced Pt–NaY catalysts were evacuated for 10 h at 673 K to desorb all chemisorbed hydrogen and then cooled to ambient temperature. Xenon-129 NMR spectra and adsorption isotherms were obtained on the various reduced and degassed Pt–NaY samples as outlined above, followed by separate hydrogen chemisorption measurements of accessible surface Pt [see Chapter 3 and Appendix E]. Next, two reoxidation procedures were employed: the first exposed the reduced, degassed Pt–NaY samples to dry oxygen gas (10 cm^3/s for 6 h) at room temperature followed by the second which reoxidized the samples under the same conditions used in their initial calcinations. Xenon-129 NMR and adsorption isotherm experiments were performed, as described above, following each of the reoxidation procedures. Appendix D contains adsorption isotherm data for all calcined, reduced, and reoxidized Pt–NaY samples studied.

2.5 ^{129}Xe NMR Studies of Pt–NaY

Calcination

Chemical changes induced during the calcination process are apparent in Figure 2.10, where ^{129}Xe chemical shift data are plotted as a function of adsorbed xenon concentration for samples calcined at temperatures of 473 K, 573 K, and 673 K. The data clearly demonstrate the sizable differences in ^{129}Xe chemical shift behavior observed for xenon adsorbed in samples possessing unique preparation histories. These chemical shift changes mirror a change in the average environment experienced by xenon atoms adsorbed within the supercages as a result of chemical changes undergone by the metal species during calcination. For more severe thermal treatments, the chemical shift of adsorbed ^{129}Xe decreases considerably for a given xenon uptake with the

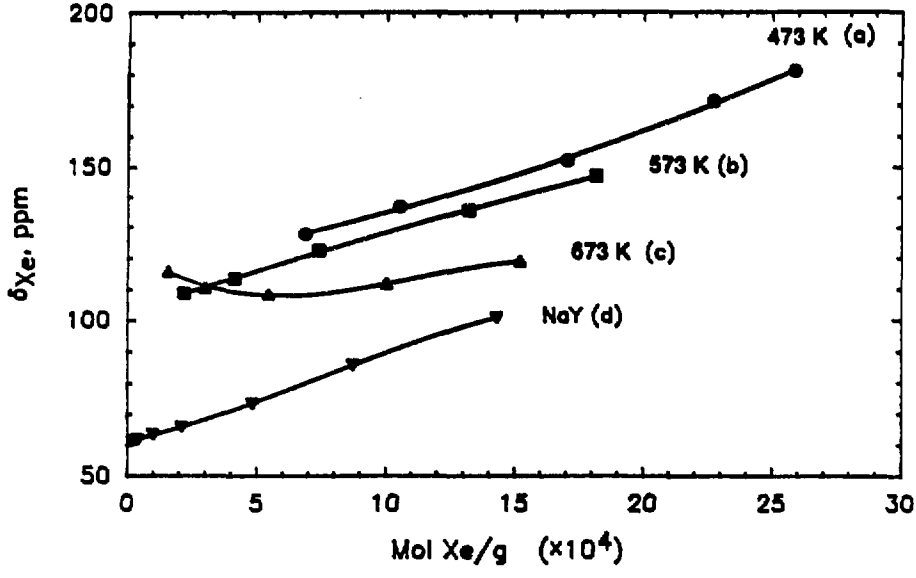

Figure 2.10: Variation in ^{129}Xe chemical shift with the concentration of xenon adsorbed (T=295 K) on 15 wt% $Pt(NH_3)_4^{2+}$–NaY zeolite samples calcined at different temperatures: (a) 473 K, (b) 573 K, and (c) 673 K. The ^{129}Xe resonance is isotropically averaged to a single peak in all spectra from which the above data are compiled [see Fig. 2.6]. The chemical shift of ^{129}Xe adsorbed on NaY zeolite dehydrated at 673 K is shown for reference purposes in curve (d).

functional form of the plots becoming more curved as well.

At 473 K, Figure 2.10(a), the mild calcination treatment dehydrates the $Pt(NH_3)_4^{2+}$-exchanged zeolite without significant decomposition of the tetraammine complex. At higher calcination temperatures, Figures 2.10(b–c), the tetraammine complex decomposes to a cluster precursor (shown in Chapter 4 to be PtO) in which the platinum is shielded from interaction with adsorbed xenon atoms. The ^{129}Xe NMR data indicate the extent to which this decomposition has progressed and rule out the presence of Pt^{2+} or autoreduced Pt as end products of the calcination process. Bare divalent cations and reduced metal species within zeolite supercages have previously been shown to have a much more pronounced effect on the chemical shift of the ^{129}Xe nuclear resonance frequency [36,39].

Reduction

Following reduction of the samples, ^{129}Xe NMR data in Figure 2.11 show a dramatic dependence on the temperature of the earlier calcination. de Menorval *et al.* have previously documented large downfield shifts of the ^{129}Xe NMR signal in the presence of bare platinum clusters [36]. In separate H_2-chemisorption experiments, we find that the downfield shifts in the ^{129}Xe chemical shift data correlate well with the amount of surface platinum accessible within the zeolite supercages [see Chapter 3]. Accordingly, Figure 2.11(c) reflects a large fraction of surface platinum metal, while in curves 2.11(a–b), the ^{129}Xe chemical shifts are substantially smaller, indicating smaller fractions of exposed platinum metal. For the 673 K reduction conditions imposed, ^{129}Xe NMR data indicate that formation of highly dispersed, NaY-supported platinum metal requires calcination at close to 673 K and progresses through a shielded precursor species following decomposition of the metal-tetraammine salt.

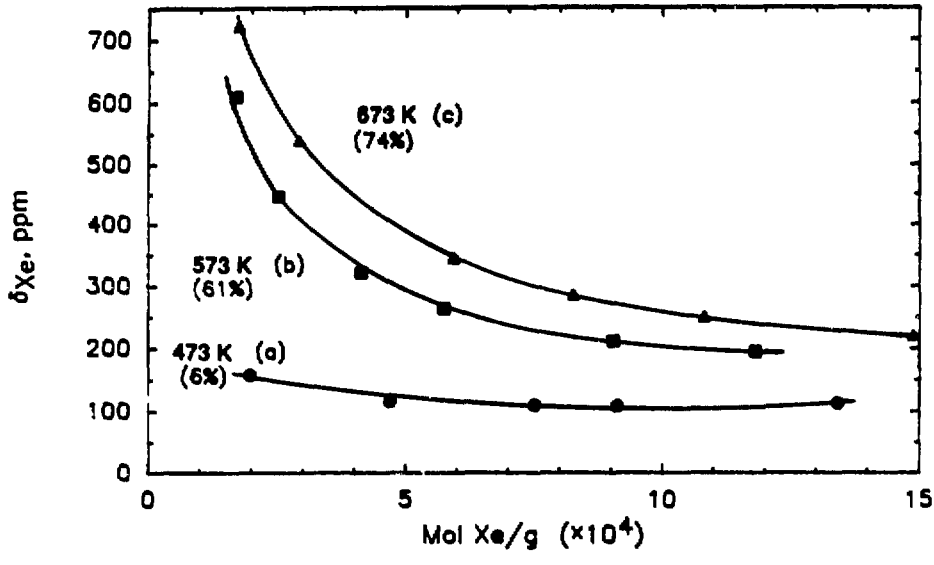

Figure 2.11: Variation in ^{129}Xe chemical shift with the concentration of xenon adsorbed (T=295 K) on reduced 15 wt% Pt-NaY zeolite samples previously calcined at different temperatures: (a) 473 K, (b) 573 K, and (c) 673 K. The percentage of surface platinum metal registered by hydrogen chemisorption experiments is shown in parentheses for each sample.

2.6 Summary

These new ^{129}Xe NMR experiments represent a unique means of investigating metal-zeolite catalyst preparation and provide important insight into the chemistry of the calcination process. The sensitivity of physisorbed xenon to the influence of the metal guest makes ^{129}Xe NMR spectroscopy an important diagnostic probe of metal-clustering phenomena in zeolitic media. In Chapters 3 and 4, the information provided by ^{129}Xe NMR will be combined with insight gained from TEM, Raman spectroscopy, and TPR to present a complete picture of the preparation and distribution of metal clusters in NaY zeolite.

Chapter 3

Platinum Species Distributions in Pt–NaY[1]

3.1 Abstract

Xenon-129 NMR spectroscopy, hydrogen chemisorption, and transmission electron microscopy are used to monitor the location and stability of metal clusters and cluster precursors as a function of calcination conditions for NaY zeolite-supported platinum catalysts. Our results indicate that for the 673 K reduction conditions imposed, the formation of highly dispersed platinum clusters within the Y zeolite matrix is best achieved by employing a calcination temperature close to 673 K. Incomplete decomposition of the ion-exchanged $Pt(NH_3)_4^{2+}$ complex during calcination at 473 K results in migration of nearly all platinum to the exterior surface of the zeolite crystallite during reduction. Calcination temperatures significantly above 673 K

[1] Presented in part at the European Conference on Structure and Reactivity of Surfaces, Trieste, Italy, 13 to 16 September 1988. Portions have been published in **Structure and Reactivity of Surfaces**, C. Morterra et al., eds., Elsevier: Amsterdam (1989) pp. 269–278.

induce decomposition of the shielded precursor species and subsequent migration of the metal into the sodalite cavities. Approximately 20% of the platinum confined within the sodalite cavities migrates back into the supercages during reduction at 673 K. After initial reduction of Pt–NaY, subsequent reoxidation, at temperatures up to 873 K, induces no additional agglomeration of the metal species.

3.2 Introduction

Preparatory treatments are critically important to the performance of zeolite-supported metal catalysts [6,26]. To achieve reproducibly high metal dispersion, the conditions of calcination and reduction must be carefully controlled [10,24,27], though the detailed chemical transformations undergone by the metal guests during these processes have been difficult to establish [30,33,34]. Recent studies have demonstrated the usefulness of ^{129}Xe NMR as a sensitive probe of the intracrystalline environment of molecular sieves [35,36,39,42,43,44,45,54,55,56,57,58,59]. Xenon's large spherically symmetric, polarizable electron cloud is extremely sensitive to its local environment as manifested by a chemical shift range of over 5000 ppm. As a result of xenon's chemical inertness, ^{129}Xe probe molecules undergo only physisorptive interactions within the interior pore spaces of the zeolite crystallites. Rapid diffusion through the zeolite's interior cavities at room temperature motionally averages the ^{129}Xe resonance signal, producing a single chemically-shifted peak. Correlating ^{129}Xe chemical shift data with catalyst preparatory treatments provides a convenient diagnostic probe of the metal clustering process. In particular, the distribution of metal guest species within NaY crystallites can be probed using ^{129}Xe NMR in conjunction with hydrogen chemisorption and transmission electron microscopy (TEM) experiments [60,61,62].

3.3 Calcination

Correlation of ^{129}Xe chemical shift measurements with adsorption isotherm data for Pt–NaY samples calcined at different temperatures provides insight on sample differences arising from unique catalyst preparation histories. As shown in Figure 3.1, the adsorption isotherm of xenon on Pt–NaY is a function of the catalyst's calcination treatment, making it necessary to account for variable xenon concentration within the different samples. Xenon-129 NMR is an effective probe of only the NaY-supercage environment, since a xenon atom's 0.44 nm atomic diameter is small enough to penetrate the 0.74 nm window into the supercage, but too large to enter the sodalite cages through the small 0.22 nm apertures of the six-membered oxygen rings. Changes observed in the xenon adsorption isotherm and in the ^{129}Xe chemical shift mirror changes in the average environment experienced by xenon atoms adsorbed within the supercages as a result of chemical changes undergone by the metal species during calcination.

For a metal loading of 15 wt% (dry basis), stoichiometric requirements dictate that a macroscopic average of 1.4 $Pt(NH_3)_4^{2+}$ cations are present per supercage within the uncalcined sample. The TEM micrographs in Figure 3.2 show the large scattering effect that the heavy metal loading has on the incident electron beam. (A description of TEM experimental methods is provided in Appendix A.1.) In Figure 3.2(a) the nascent NaY support is shown, with the closely spaced, parallel lattice fringes reflecting the zeolite's high crystallinity. Beam-damage to the particle is manifested by disappearance of this diffraction pattern during the experiment. The size of the rhomboids produced by the intersections of the non-parallel fringes correspond approximately to the dimensions of the zeolite Y supercages. In the $Pt(NH_3)_4^{2+}$–exchanged sample, the large number of metal scattering centers results in a mottled background

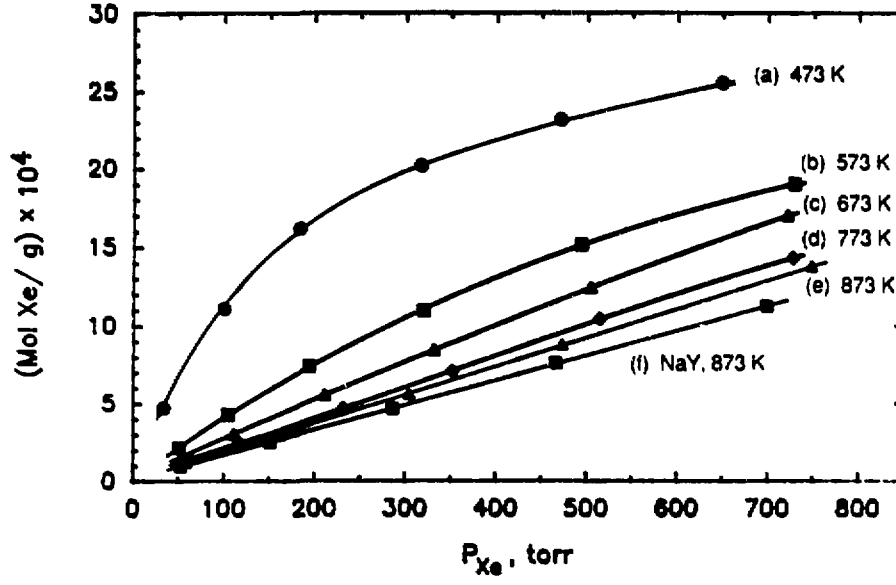

Figure 3.1: Adsorption isotherms of xenon (T=295 K) on 15 wt% $Pt(NH_3)_4^{2+}$–NaY zeolite samples calcined at different temperatures: (a) 473 K, (b) 573 K, (c) 673 K, (d) 773 K, (d) 873 K, (f) NaY dehydrated at 873 K.

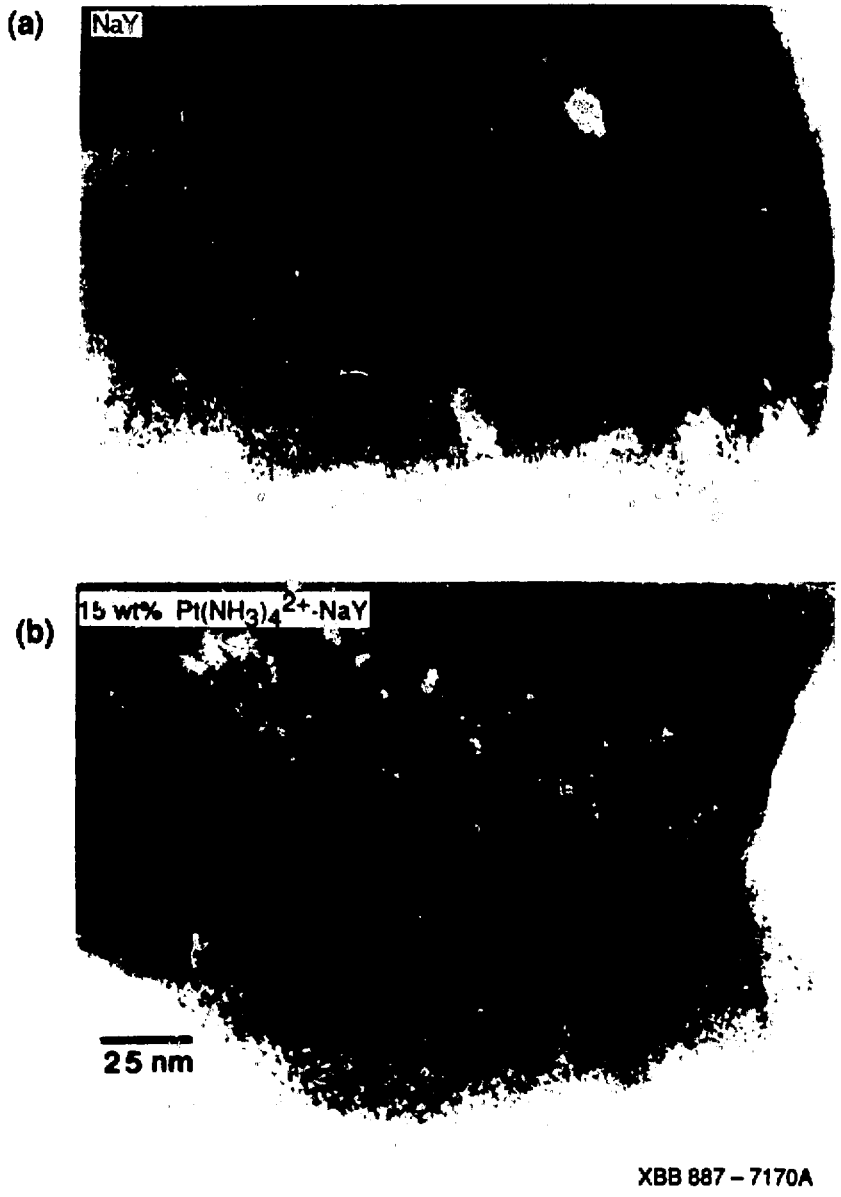

Figure 3.2: Transmission electron micrographs of (a) nascent NaY zeolite in the absence of precious metal guest species and (b) 15 wt% $Pt(NH_3)_4^{2+}$-NaY following ion-exchange and drying under vacuum at room temperature.

as seen in Figure 3.2(b). The crystallinity of the zeolite particle is preserved, but the lattice fringes are made less obvious by preferential scattering from the heavy Pt atoms. Accordingly, the mottled crystallite backgrounds in Figure 3.2(b) and in Figures 3.4–3.8 to follow, do not indicate the presence of very small aggregates.

Under very mild calcination conditions at 473 K, the ^{129}Xe NMR data in Figure 3.3(a) indicate that the zeolite matrix dehydrates without significant decomposition of the metal-tetraammine complex. The relatively large chemical shift observed for ^{129}Xe adsorbed on this sample, together with the high xenon uptake apparent in Figure 3.1(a), result from strong induced dipole interactions between xenon and the $Pt(NH_3)_4^{2+}$ complex. The divalent metal-tetraammine complex must be shared between two monovalent framework anion sites in the NaY supercages and, as a consequence, is readily accessible to the ^{129}Xe probe species. Fraissard *et al.* have reported large chemical shifts for ^{129}Xe adsorbed on Y zeolites exchanged with a large fraction of divalent alkaline earth cations [39]. Indeed, the chemical shift behavior we observe for xenon adsorbed on dehydrated $Pt(NH_3)_4^{2+}$–NaY is consistent with previously reported data for Ba^{2+}–NaY [39] [see Fig. C.1 in Appendix C]. The barium cation and the tetraammine platinum complex are both large divalent species possessing similar charge densities for which similar perturbation of the xenon probe atom is anticipated. Calcination at 473 K induces little detectable change in the $Pt(NH_3)_4^{2+}$–NaY material. The TEM micrograph in Figure 3.4(a), although at a slightly smaller magnification, is virtually identical to the micrograph of the uncalcined $Pt(NH_3)_4^{2+}$–NaY catalyst in Figure 3.2(b). In both of these samples the metal-tetraammine complex serves as the charge-balancing cation and therefore remains dispersed among the various ion-exchange sites of the zeolite supercages.

Under more severe calcination treatments at 573 K and 673 K, the catalyst mate-

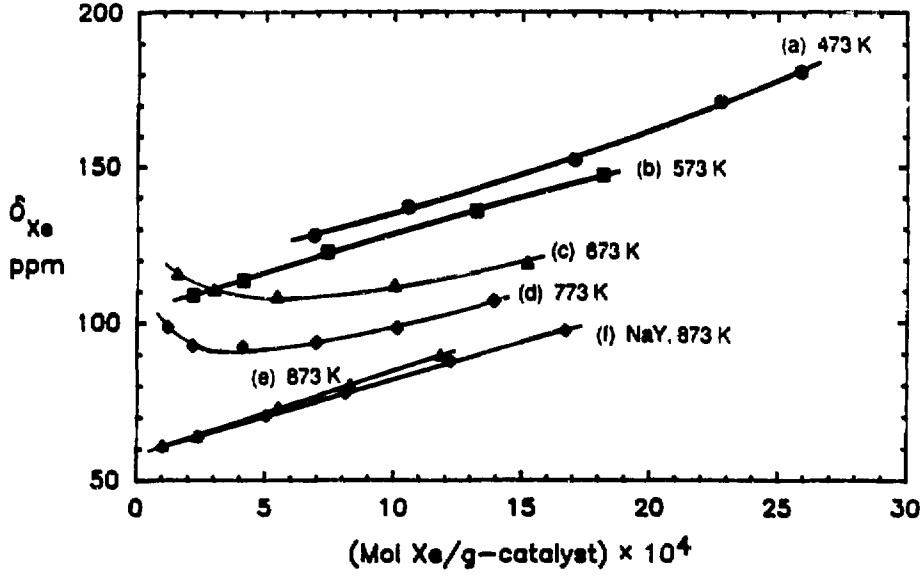

Figure 3.3: Variation in ^{129}Xe chemical shift with the concentration of xenon adsorbed (T=295 K) on 15 wt% $Pt(NH_3)_4^{2+}$–NaY zeolite samples calcined at different temperatures: (a) 473 K, (b) 573 K, (c) 673 K, (d) 773 K, (d) 873 K, (f) NaY dehydrated at 873 K. All samples were cooled under flowing oxygen to room temperature over a period of many hours. Different cooling rates can produce small, but measurable differences in calcined Pt–NaY [see Appendix B.1].

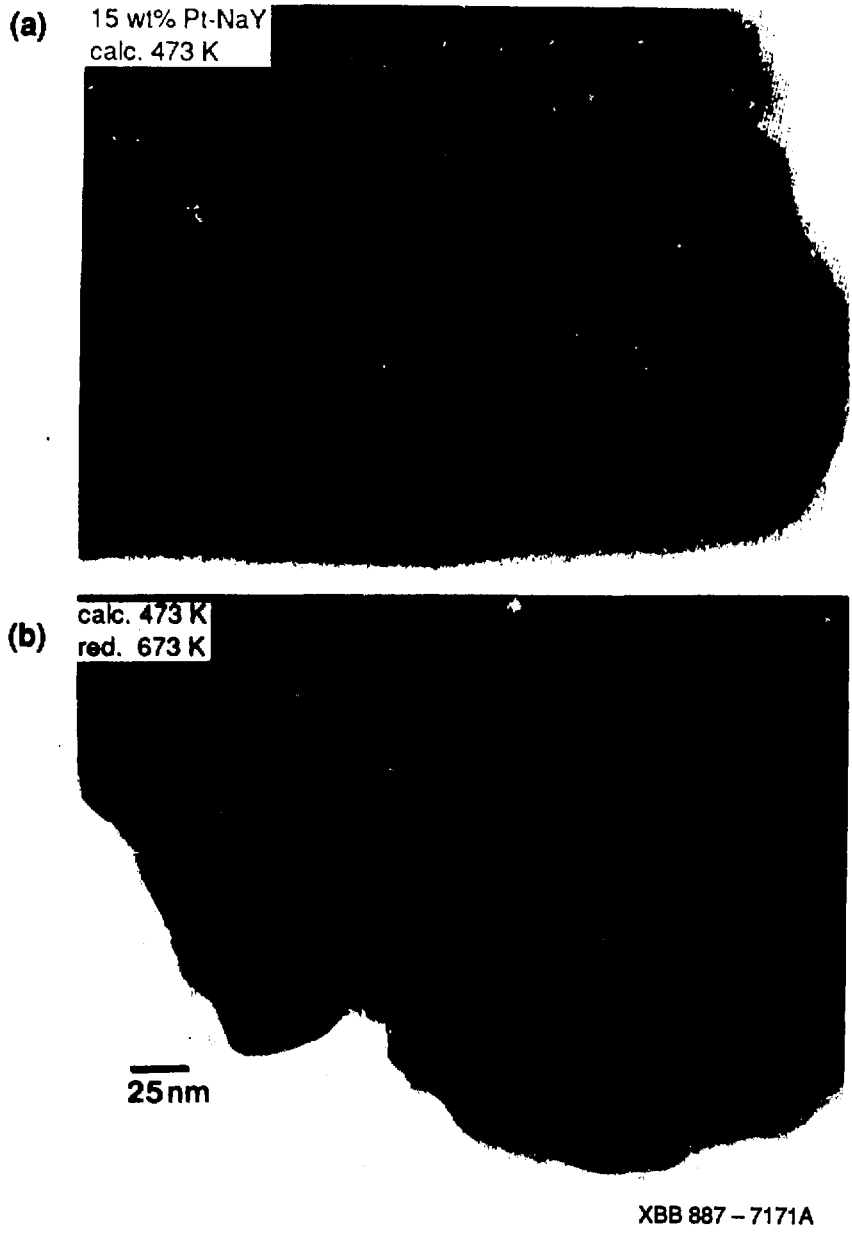

Figure 3.4: Transmission electron micrographs of 15 wt% Pt–NaY (a) after calcination of the $Pt(NH_3)_4^{2+}$–exchanged zeolite at 473 K and (b) after reduction of the calcined catalyst at 673 K.

rial changes color from white to dark gray as the metal complex decomposes [50,63]. In Figures 3.3(b–c), the diminished ^{129}Xe chemical shifts observed in samples calcined to 573 K and 673 K reflect decomposition of the tetraammine complex to a shielded metal intermediate located in the Y zeolite supercages. These results are consistent with temperature programmed desorption data of Exner *et al.* that document a dramatic increase in the rate of $Pt(NH_3)_4^{2+}$ decomposition in NaX zeolite in the vicinity of 573 K [see Fig. E.1 in Appendix E]. At calcination temperatures up to 673 K, our work and that of others [24,34] show that nearly all of the platinum is located in the supercages and is, therefore, accessible to the molecular xenon probe. Figures 3.1(a–c) demonstrate the need to account for differences in Xe/Pt–NaY adsorption to compare properly NMR data from the different samples. The decrease observed in the ^{129}Xe chemical shift is opposite to the behavior expected for Pt^{2+} or autoreduced $Pt^{(0)}$ calcination products in the supercages. A higher charge density or the existence of conduction electrons acts to perturb the local xenon field to a significantly greater extent, thereby producing a much larger ^{129}Xe chemical shift [36]. Large ^{129}Xe chemical shifts also occur in the presence of metal clusters covered with chemisorbed oxygen because xenon atoms are not completely shielded from interaction with the metallic core [58]. Our ^{129}Xe chemical shift data, therefore, indicate the extent to which the decomposition of the metal-tetraammine complex has progressed and reveal the shielded nature of the metal calcination product. The ^{129}Xe NMR results are consistent with TEM micrographs in Figures 3.5(a) and 3.6(a) of Pt–NaY samples calcined to 573 K and 673 K, though most of the calcination product species remains below the 3-nm resolution limit of the bright-field TEM technique. Separate Raman spectroscopy and temperature programmed reduction experiments suggest Pt^0 as the primary product of calcination at 673 K [see Chapter 4], with

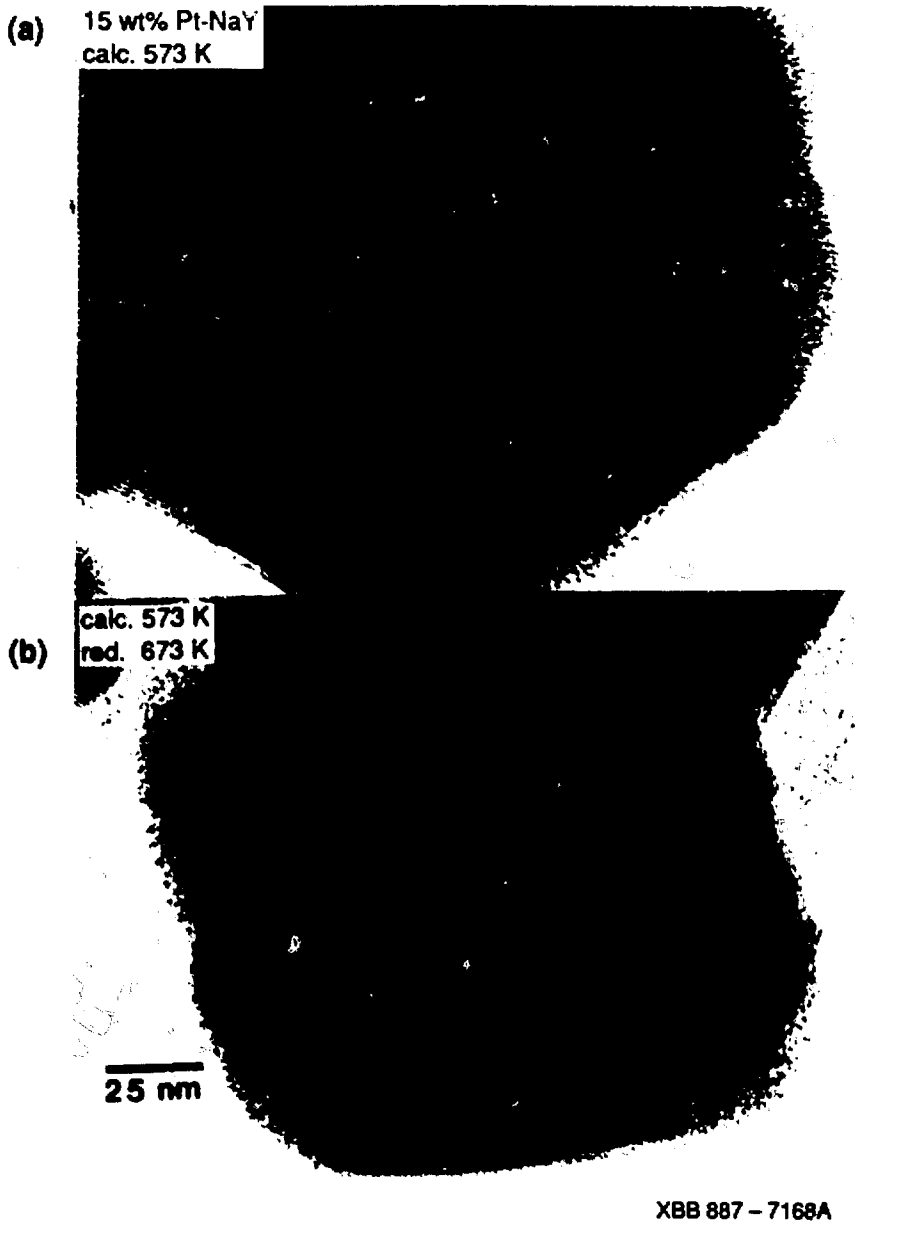

Figure 3.5: Transmission electron micrographs of 15 wt% Pt-NaY (a) after calcination of the $Pt(NH_3)_4^{2+}$-exchanged zeolite at 573 K and (b) after reduction of the calcined catalyst at 673 K.

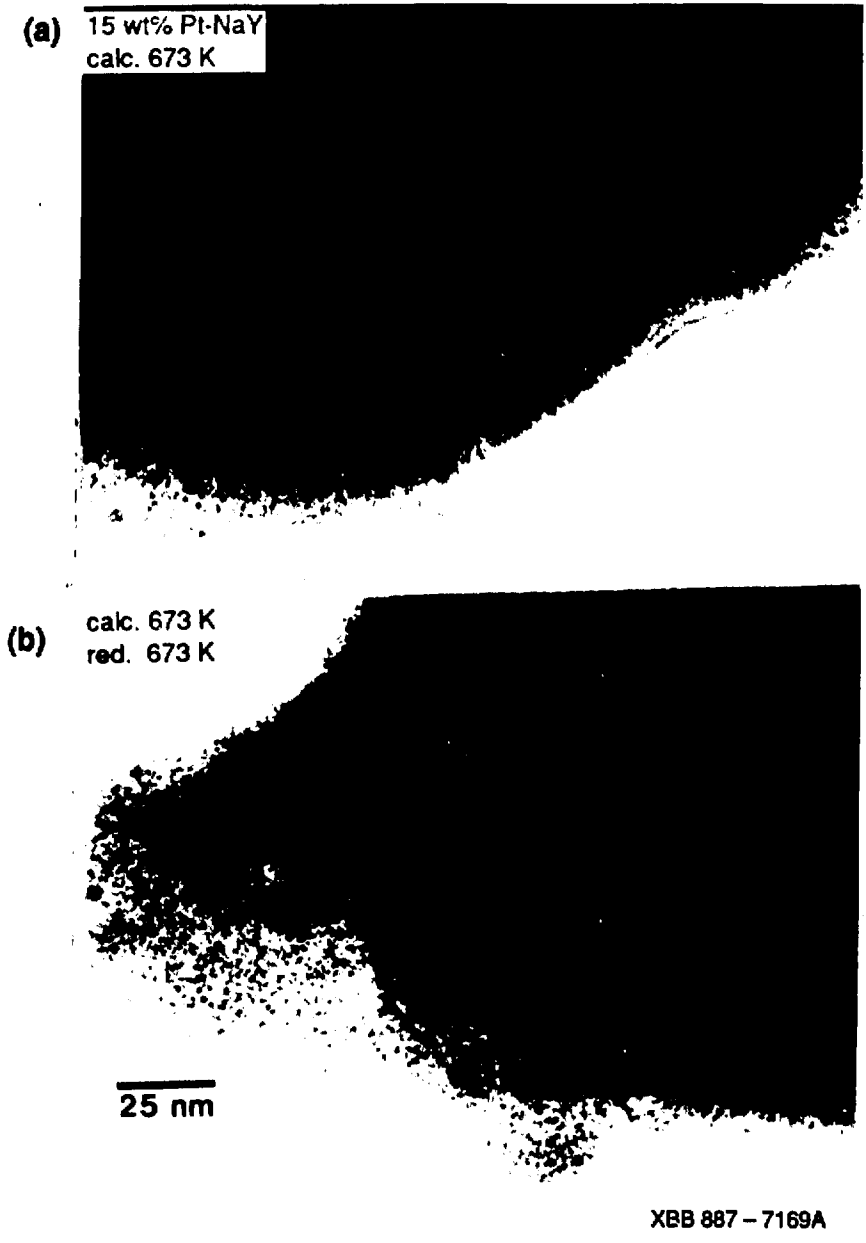

Figure 3.6: Transmission electron micrographs of 15 wt% Pt–NaY (a) after calcination of the $Pt(NH_3)_4^{2+}$–exchanged zeolite at 673 K and (b) after reduction of the calcined catalyst at 673 K.

both Figures 3.5(a) and 3.6(a) showing evidence of some large aggregate formation.

As shown in Figures 3.3(d–e), calcination of the catalyst samples at 773 K and 873 K produces additional change in the zeolite-supported metal species beyond the point where decomposition of the tetraammine complex has been completed. For samples calcined at 673 K and 773 K, little qualitative difference is observed in the shape of the ^{129}Xe chemical shift data as a function of the adsorbed xenon concentration [Figs. 3.3(c–d)]. However, the magnitude of the chemical shift registered at a given xenon uptake is substantially less for the sample treated at the higher temperature (773 K), and its gray coloration is significantly lighter. These observations indicate that some fraction of the metal species is inaccessible to the xenon probe following calcination at 773 K and imply partial platinum depopulation of supercage sites. Penetration of the metal species into sodalite cavities during calcination at elevated temperatures [60] is confirmed by combined application of TEM and ^{129}Xe NMR techniques. Following calcination at 773 K and 873 K, the TEM micrographs shown in Figures 3.7(a) and 3.8(a) reveal the absence of large clusters on the exterior of the zeolite crystallites, providing evidence that most Pt is intracrystalline and in aggregates less than the 3-nm bright field resolution limit.

The short-range nature of the metal perturbation on the local xenon magnetic field results in all metal species in the sodalite cages being invisible to the xenon probe. Removal of the metal guest from the NaY supercages, thus, diminishes the population of metal species accessible to the xenon probe atoms. In this situation, platinum–xenon interactions are less likely to occur leading to, on average, a more shielded ^{129}Xe nuclear environment in the supercages. As a result, in Figure 3.3(d) the downfield shift of the ^{129}Xe resonance at a given adsorbed xenon concentration is smaller in the sample calcined at 773 K, while the functional behavior is qualitatively

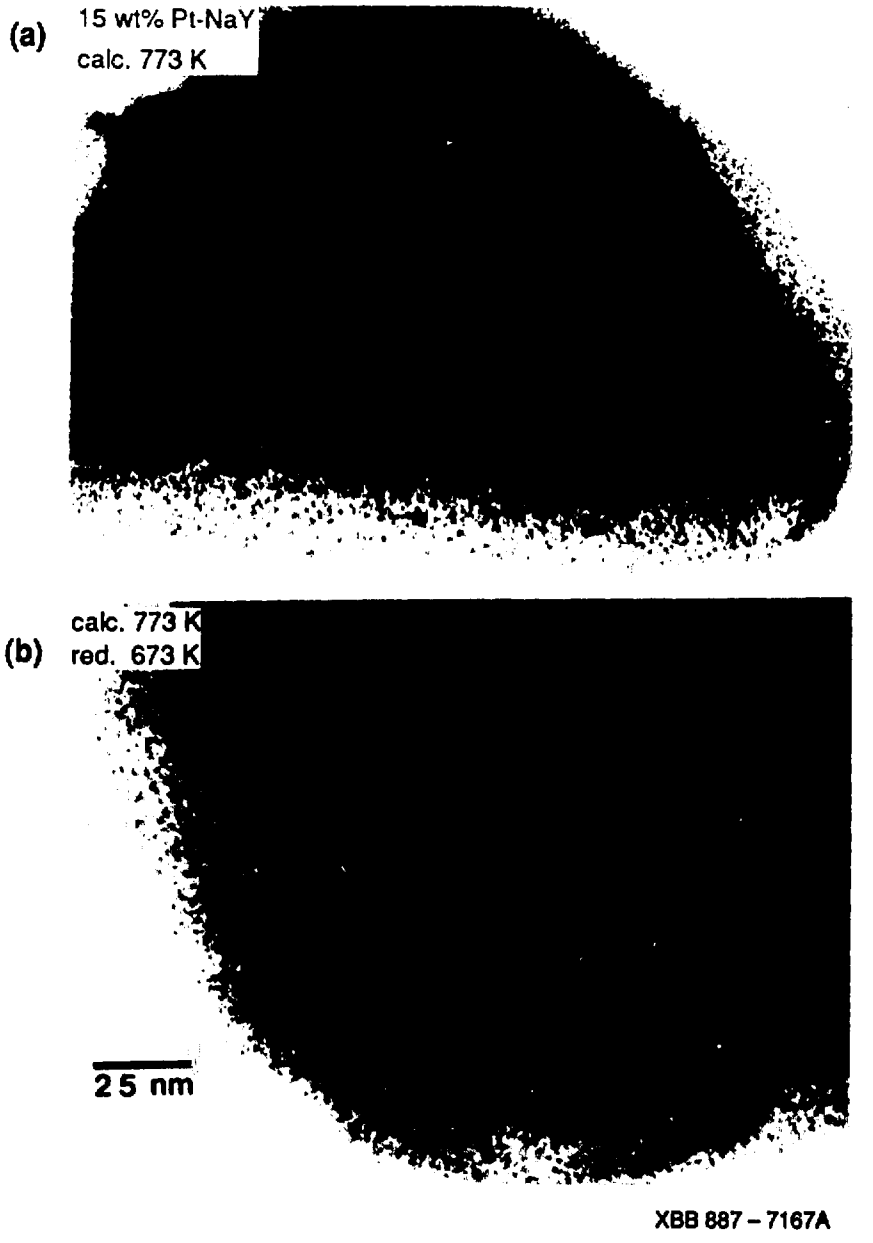

Figure 3.7: Transmission electron micrographs of 15 wt% Pt–NaY (a) after calcination of the $Pt(NH_3)_4^{2+}$-exchanged zeolite at 773 K and (b) after reduction of the calcined catalyst at 673 K.

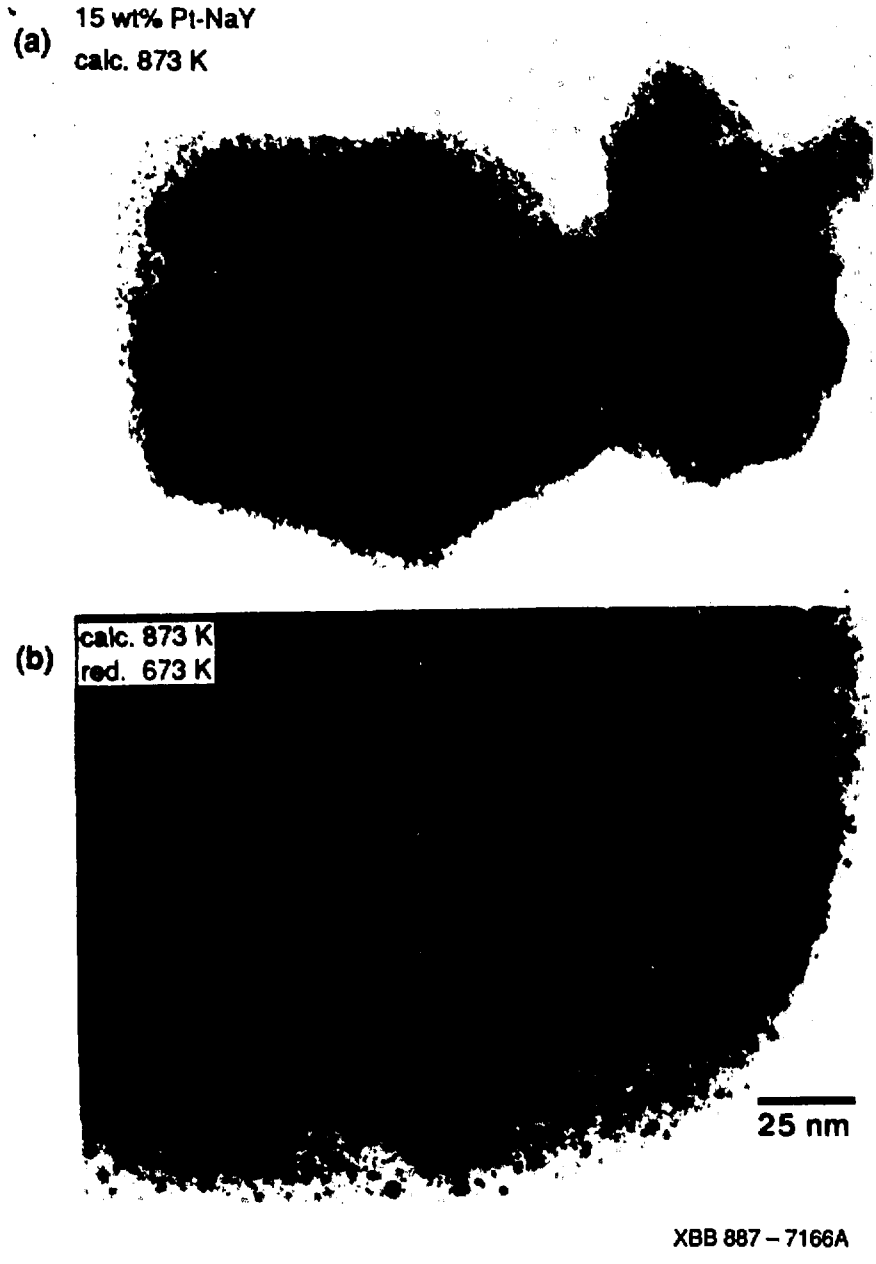

Figure 3.8: Transmission electron micrographs of 15 wt% Pt–NaY (a) after calcination of the $Pt(NH_3)_4^{2+}$-exchanged zeolite at 873 K and (b) after reduction of the calcined catalyst at 673 K.

unchanged from that observed for the sample calcined at 673 K. At 873 K, essentially complete penetration of the metal species into the sodalite cavities results in the adsorption of ^{129}Xe probe atoms into a supercage environment nearly identical to that of the nonmetal-loaded NaY support. Thus, as seen in Figures 3.3(e–f), ^{129}Xe NMR chemical shift data for the Pt–NaY sample calcined at 873 K nearly superimpose with those for the nascent NaY support material dehydrated at 873 K. The very light gray color of the sample calcined at 873 K is consistent with decomposition of the metal oxide [see Chapter 4] to Pt^{2+} species which migrate into the sodalite cages. Larger particles scatter light more effectively, so that the darkness of a Pt–NaY sample indicates the extent to which the metal species is clustered. The slight grayish cast of the 873 K calcined sample arises from the small number of undecomposed ca. 3 nm aggregates seen in Figure 3.8(a).

3.4 Reduction

After reduction of all the samples at 673 K, the fraction of surface platinum metal present within the supercages, shown in Table 3.1, has a large dependence on the temperature of the earlier calcination [see Section E.4 in Appendix E]. The nominal adsorption stoichiometry of 1 H/1 Pt permits the amount of accessible surface metal present in reduced Pt–NaY samples to be estimated from hydrogen uptake measurements [64,65,66]. Since the 0.29 nm kinetic diameter of the hydrogen molecule exceeds the 0.22 nm opening of the Y zeolite sodalite cage, the fraction of surface platinum reported in Table 3.1 reflects only that accessible (to both hydrogen and xenon) in the supercages at room temperature. From Figure 3.9, we find that the downfield shifts in the ^{129}Xe chemical shift data correlate well with the amount of surface platinum metal accessible to the xenon probe molecules within the zeolite

Table 3.1: Accessible surface platinum in reduced Pt-NaY samples calcined at different temperatures. Surface Pt in NaY supercages was determined from hydrogen chemisorption at 293 K [see Appendix E].

Sample	Calcination (K)	Reduction (K)	Fraction of surface Pt in supercages
a	473	673	0.08
b	573	673	0.61
c	673	673	0.74
d	773	673	0.42
e	873	673	0.15

supercages. Large downfield shifts in the ^{129}Xe resonance are observed when the quantity of dispersed platinum in the supercages is high. The maximum accessible surface Pt measured in the sample first calcined at 673 K agrees well with the maximum chemical shift perturbation of the ^{129}Xe resonance plotted in Figure 3.9(c). de Menorval *et al.* have previously documented large downfield shifts of the ^{129}Xe resonance signal in the presence of bare platinum clusters [36]. Conversely, the ^{129}Xe chemical shifts shown in Figures 3.9(a,b,d,e), are substantially smaller for a given xenon uptake due to diminished amounts of exposed platinum metal.

A distinguishing feature between aggregation of Pt into large clusters versus Pt penetration into sodalite cavities is the vastly different sizes characteristic of the metal species in the two cases. Transmission electron microscopy is capable of delineating between these two possible distributions and can, thus, determine the location of the inaccessible metal. For the Pt–NaY sample calcined at 473 K and reduced at 673 K, the TEM micrograph shown in Figure 3.4(b) reveals very large platinum clusters (ca. 40 nm) on the exterior of the micron-size zeolite crystallite that account for the low (8%) metal dispersion in Table 3.1(a). Most of the platinum present in this sample is in the form of very large agglomerates. A single 1-μm diameter Pt–NaY crystallite, for example, contains enough metal to produce about 20 clusters 40 nm in diameter (2×10^6 Pt atoms/cluster). This is consistent with the approximate number of such large clusters present on the exterior surface of the sample depicted in Figure 3.4(b) and more easily seen in Figure 3.14. Accordingly, xenon adsorbed in predominantly empty NaY cavities in the crystallites' interior accounts for the low ^{129}Xe chemical shift values observed in Figure 3.9(a). For the Pt–NaY samples calcined at 573 K and 673 K, more complete decomposition of the $Pt(NH_3)_4^{2+}$ complex has occurred, providing a greater amount of the preferred platinum oxide intermedi-

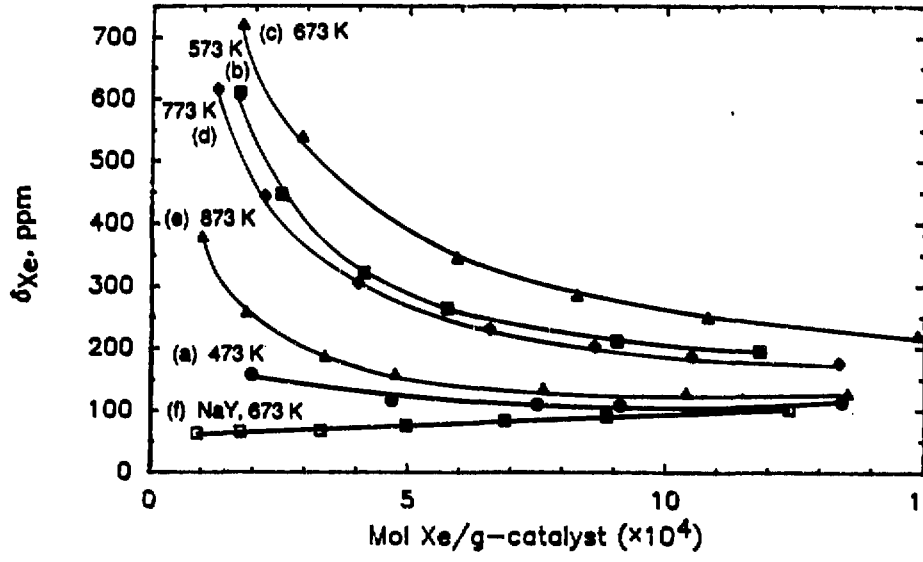

Figure 3.9: Variation in ^{129}Xe chemical shift with the concentration of adsorbed xenon (T=295 K) on reduced 15 wt% Pt–NaY zeolite samples previously calcined at different temperatures: (a) 473 K, (b) 573 K, (c) 673 K, (d) 773 K, (e) 873 K, (f) NaY dehydrated at 673 K.

ate necessary for producing high metal dispersion within the supercage cavities upon reduction. This is manifested by higher fractions of exposed Pt [Table 3.1(b–c)], by the absence of large aggregates on the crystallite surface [Figs. 3.5(b) and 3.6(b)], and by larger ^{129}Xe chemical shifts [Figs. 3.9(b–c)].

For the reduced Pt–NaY samples calcined at 773 K and 873 K, the lower fractions of accessible Pt [Table 3.1(d–e)] and smaller ^{129}Xe chemical shifts [Figs. 3.9(d–e)] are due mainly to penetration of the metal species (as Pt^{2+}) into the sodalite cages during the calcination treatment. Temperature programmed reduction data indicate that about two-thirds of the platinum species in the sodalite cavities are reduced at 673 K in hydrogen [see Chapter 4]. During reduction, some of the metal migrates from sodalite cage sites back into supercage environments, where it is accessible to both hydrogen and xenon. The small fractions of surface Pt [Table 3.1(d–e)] and low ^{129}Xe chemical shift values [Figs. 3.9(d–e)] suggest that reduction of Pt^{2+} in the sodalite cavities produces a migratory intermediate that tends to agglomerate in supercage sites.

Aggregation of platinum in the supercages under these circumstances is supported by the TEM micrographs shown in Figures 3.7(b) and 3.8(b) which reveal numerous reduced metal clusters larger than the 3-nm resolution limit of the bright field imaging technique. In the projected images provided by the TEM experiments, the contribution from metal clusters situated on the exterior zeolite surface to the observed cluster density is essentially independent of zeolite particle thickness. In Figure 3.10, however, no clusters are observed on the crystallite's periphery. Furthermore, the density of Pt clusters is greater in zones of greater crystallite thickness. This points to the occlusion of large Pt clusters within the zeolite matrix [60] and counters recent suggestions in the literature [67] that reduction at 673 K induces mi-

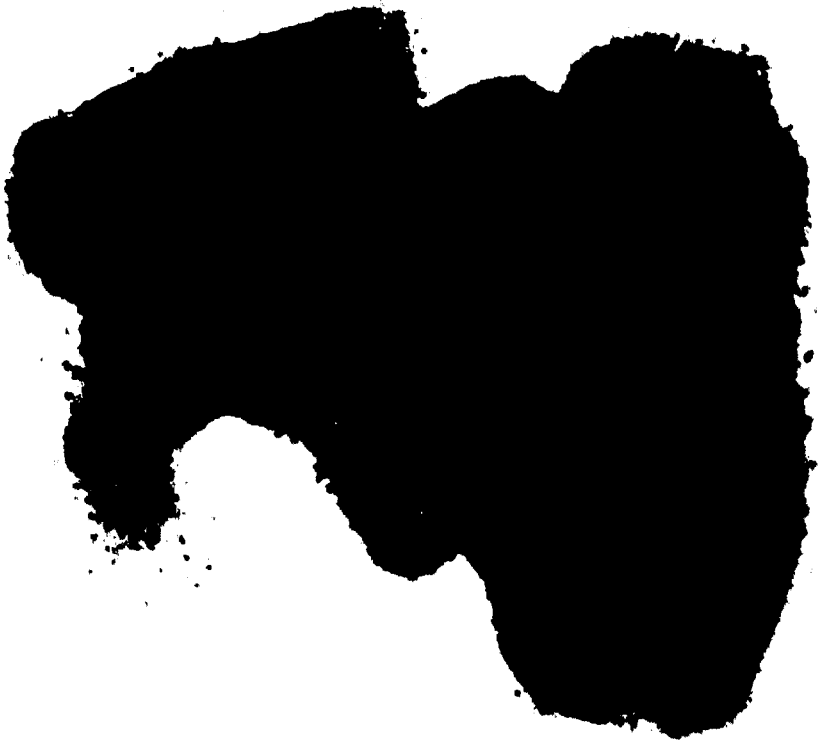

XBB 890 – 8739

Figure 3.10: Transmission electron micrograph of 15 wt% Pt–NaY following calcination at 873 K and subsequent reduction at 673 K. The particle shown is from the same sample depicted in Fig. 3.8(b), but at lower magnification.

gration of Pt atoms (0.27 nm diameter) from sodalite sites to the exterior crystallite surface before the metal agglomerates.

Structural damage, which may result from the growth of large metal clusters in the NaY supercages [68], does not affect the overall crystallinity of the framework [60]. Occlusion of a 3-nm Pt cluster in 15 wt% Pt-NaY, for example, may produce structural defects in two supercages, while 100 others in the immediate vicinity remain intact. Since enough metal exists in the 15 wt% Pt-NaY system to produce $3x10^5$ Pt clusters 3 nm in diameter (1200 Pt atoms/cluster) within each micron-size crystallite, most of the Pt is in the form of either small reduced metal clusters below the 3-nm TEM resolution limit or unreduced Pt^{2+} cations in the sodalite cages. Clearly from Figure 3.10 the number of Pt clusters observed in the 3-nm size range is significantly less than the maximum number possible. The low ^{129}Xe chemical shift measurements in Figure 3.3(e) and the low hydrogen uptake manifested in Table 3.1(e) indicate, moreover, the lack of an appreciable quantity of highly dispersed Pt in the supercages accompanying the large clusters. From this it is apparent that Pt present in the supercages is predominantly in the form of large clusters (corroborated by reoxidation experiments discussed below), though most of the metal remains in sodalite sites as one- to two-atom reduced species or as divalent platinum cations.

3.5 Reoxidation

The structure and reactivity of reduced metal clusters are known to be functions of aggregate size [69,70,71,72,73,74,75,76,77]. This directly affects the oxidative properties of dispersed platinum, which has been previously shown to exhibit size-dependent behavior [78,79]. An important issue is whether additional migration

of the Pt species occurs during reoxidation to increase the size and/or number of the larger clusters. Xenon-129 NMR, hydrogen chemisorption, and TEM can be used to probe changes in Pt–NaY systems induced by exposure to oxidizing conditions of differing severity.

Figures 3.11 and 3.12 display ^{129}Xe chemical shift data for xenon adsorbed on Pt–NaY systems following reoxidation at ambient and high temperature, respectively. The reoxidation treatments were performed, as described in Chapter 2, on the previously calcined and reduced Pt–NaY samples studied in sections 3.2 and 3.3 above. As shown in Figure 3.11, chemisorption of oxygen onto reduced Pt clusters at room temperature partially shields the ^{129}Xe probe atom from the conduction electrons of the metal cluster. Comparing Figures 3.9 and 3.11 shows that ^{129}Xe chemical shifts are substantially lower for a given xenon uptake following reoxidation of the catalyst at room temperature. As before, the relative magnitudes of the ^{129}Xe shifts correlate with the amount of Pt accessible to the xenon probe species within the NaY supercages. No migration of the metal is expected or observed during chemisorption of O_2 at 295 K [24,66].

Reoxidation of the Pt–NaY samples at elevated temperatures, however, affects the catalysts differently. In the samples possessing a preponderance of small clusters (namely those calcined at 573 K, 673 K, or 773 K), the ^{129}Xe chemical shifts are significantly smaller [Figs. 3.12(b–d)] than those measured in the samples chemisorbed with oxygen at room temperature [Figs. 3.11(b–d)]. Such is not the case for samples possessing a large fraction of large clusters in exterior and/or supercage sites accessible to both oxygen (0.28 nm kinetic diameter) and xenon, for which little or no additional shielding of the Pt species is observed. Comparing Figures 3.11(a,e) with Figures 3.12(a, e), for example, reveals very little change in the ^{129}Xe chemical

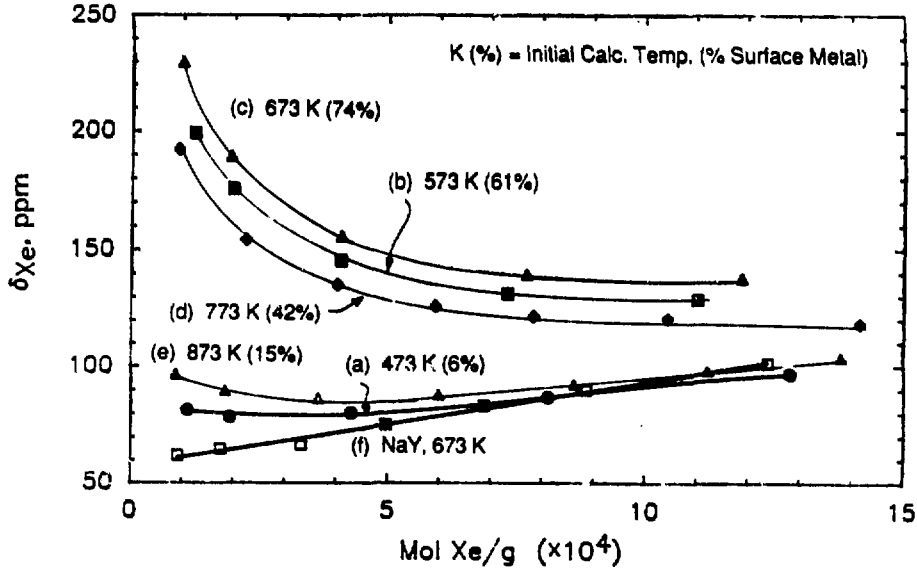

Figure 3.11: Variation in ^{129}Xe chemical shift with the concentration of xenon adsorbed (T=295 K) on 15 wt% Pt-NaY zeolite samples reoxidized by exposure of the reduced catalysts to oxygen gas at room temperature. The metal-zeolite samples were previously reduced at 673 K after calcination at different temperatures: (a) 473 K, (b) 573 K, (c) 673 K, (d) 773 K, (e) 873 K, (f) NaY dehydrated at 673 K. The percentage of surface Pt in the supercages (prior to reoxidation) is shown in parentheses for each sample.

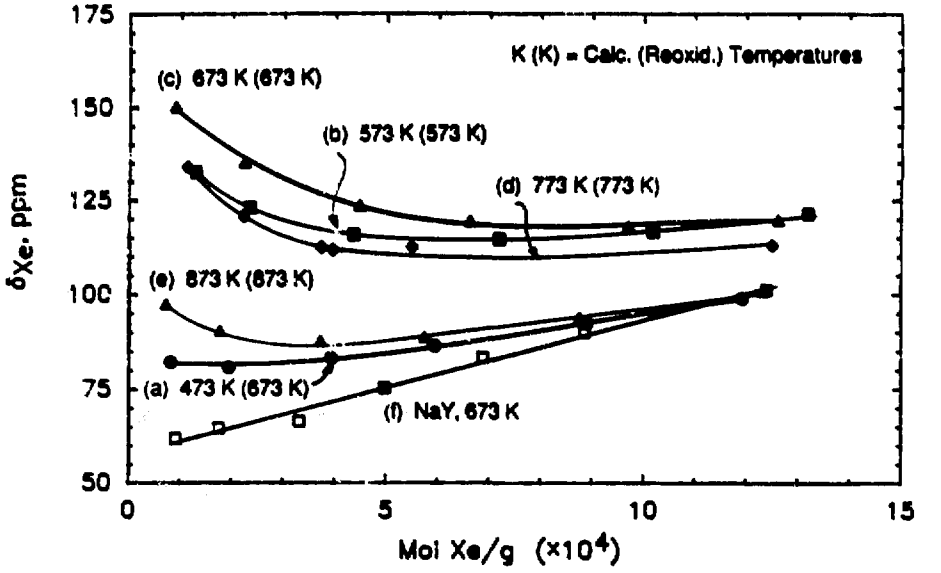

Figure 3.12: Variation in ^{129}Xe chemical shift with the concentration of xenon adsorbed (T=295 K) on 15 wt% Pt–NaY zeolite samples reoxidized at the temperatures of the catalysts' initial calcination (with the exception of sample (a) which was reoxidized at 673 K.) The metal-zeolite samples were previously reduced at 673 K after calcination at different temperatures: (a) 473 K, (b) 573 K, (c) 673 K, (d) 773 K, (e) 873 K, (f) NaY dehydrated at 673 K.

shift data for large cluster systems following high-temperature reoxidation of reduced samples initially calcined at 473 K and 873 K. These observations are more clearly seen in Figures B.3 and B.7 in Appendix B, where ^{129}Xe chemical shift data are presented as a function of treatment history for each Pt–NaY sample.

The cluster-size-dependent response of the catalyst to reoxidation at elevated temperatures can be understood in terms of the relative reactivities of the small and large metal particles. Small clusters of metal atoms are, in general, more reactive than large aggregates due to lower activation energy barriers to structural rearrangements [80,81]. As shown in Figure 3.13(a), small metal clusters are more readily oxidized than large particles [78,79], leading to more complete oxidation of highly dispersed metal at elevated temperatures. As more of the metal's conduction electrons become localized in covalent Pt–O bonds, Xe is shielded more effectively from the metal. This results in the lower ^{129}Xe shifts observed in Figures 3.12(b–d) associated with Pt–NaY samples reoxidized at high temperature, compared to ^{129}Xe shifts shown in Figures 3.11(b–d) for Pt–NaY systems reoxidized at room temperature.

For larger metal particles, hindered oxygen transport to reduced metal in the center of the clusters apparently prevents the oxidation process from proceeding to completion (during the 5–10 h reoxidation times employed in this study.) Formation of a thin oxide layer at a metal phase interface is known to passivate large clusters or thick films leading to incomplete oxidation of the metal [82]. As depicted in Figure 3.13(b), a diffusion-limited oxidation process at the relatively low temperatures employed here would result in a substantial portion of the metal remaining in the reduced state beneath a thin layer of PtO on the cluster periphery. Little additional shielding would be expected between the metal guest and the ^{129}Xe probe species under these circumstances. This is consistent with experimental observations in Fig-

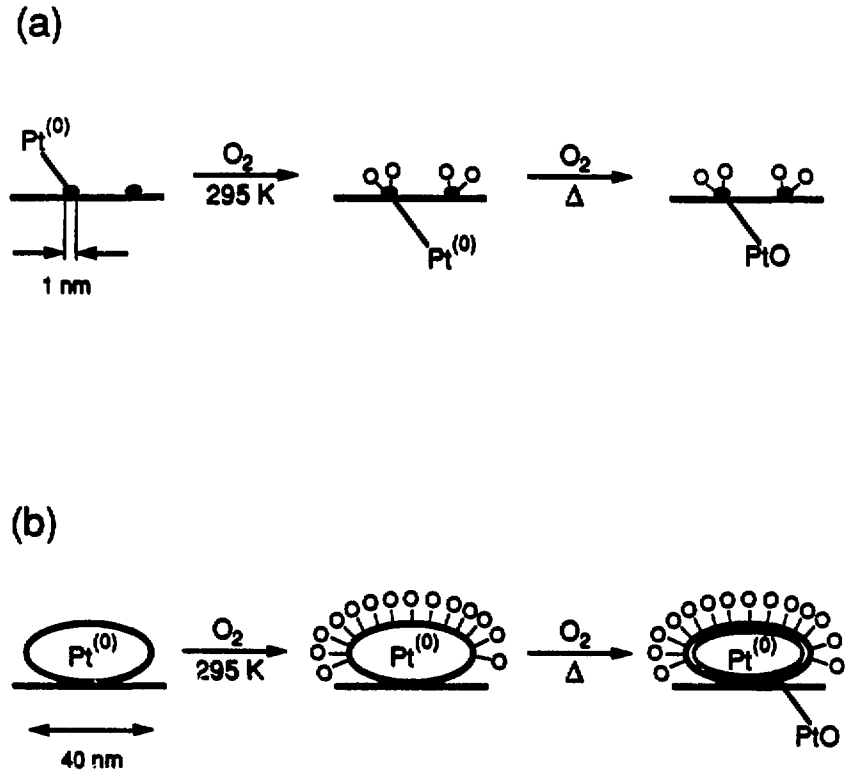

Figure 3.13: Schematic diagram depicting the effect of cluster size on platinum oxidation under different thermal conditions: (a) 1 nm Pt particles and (b) 40 nm Pt particles. The diameters of the reduced clusters reflect the approximate particle sizes obtained following reduction of samples initially calcined at 673 K and 473 K, respectively.

ures 3.11(a,e), 3.12(a,e), B.3, and B.7 which reveal that the ^{129}Xe shifts measured after the ambient and high-temperature reoxidation treatments are nearly identical.

The stability of zeolite-supported metal clusters to cyclic oxidation and reduction can be studied using hydrogen chemisorption and TEM. In Table 3.2, for example, the fraction of surface platinum metal present in the NaY supercages is unchanged (within ± 3% experimental error) in Pt–NaY samples reoxidized at the temperatures of the catalysts' initial calcination [see Table 3.1 for comparison, and also Section E.4 in Appendix E.] This indicates that after initial reduction at 673 K, reduced and ionic platinum species remain stably bound in sodalite sites both during treatment in oxygen at elevated temperatures and during multiple reductions at 673 K. After numerous reductions of samples initially calcined at 773 K and 873 K, the non-migratory character of unreduced Pt^{2+} species remaining in the sodalite cages is consistent with an equilibrium-limited reduction process at 673 K. Xenon-129 NMR and H_2 chemisorption experiments demonstrate that reoxidation of Pt–NaY systems at temperatures up at 873 K does not alter the surface area of the metal in the Y zeolite supercages.

TEM micrographs of very large cluster Pt–NaY systems, such as that shown in Figure 3.14, indicate that reoxidation at 673 K has little effect on the size or number of large of large metal particles present. Though loss of metal crystallinity has been reported for large Pt particles supported on SiO_2 or γ-Al_2O_3 during reoxidation at elevated temperatures [83], we see no evidence of this in Figure 3.14. The highly crystalline metal clusters visible in Figure 3.14(b) reveal little deterioration in the crystallinity of Y zeolite-supported Pt as a result of reoxidation at 673 K. No additional migration of the metal species apparently occurs as result of the high temperature oxygen–hydrogen titration processes employed in this study.

Table 3.2: Accessible surface platinum in reduced Pt–NaY samples following reoxidation at the temperatures used in the catalysts' initial calcination. Surface Pt in NaY supercages was determined from hydrogen chemisorption at 293 K [see Appendix E].

Sample	Reoxidation (K)	Reduction (K)	Fraction of surface Pt in supercages
c′	673	673	0.76
d′	773	673	0.43
e′	873	673	0.15

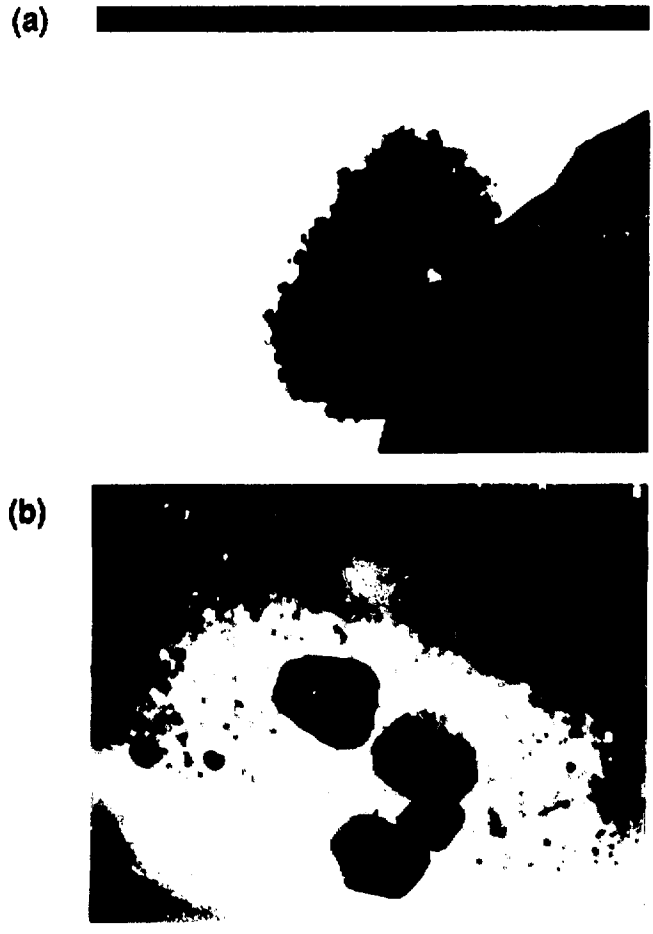

Figure 3.14: Transmission electron micrographs of 15 wt% Pt–NaY containing very large clusters following reoxidation of the catalyst at 673 K. The sample was initially calcined at 473 K and reduced at 673 K prior to the reoxidation treatment. (a) Low magnification view (x52,000) showing ca. 40 nm Pt clusters on the exterior surface of a single crystallite. The dark feature on the right is a portion of the Cu grid. (b) High magnification view (x380,000) showing the crystallinity of some of the larger Pt clusters.

3.6 Low Metal Loadings

Since ^{129}Xe NMR relies on changes in chemical shift to reflect changes in metal-guest chemistry or distribution, the technique requires a sufficient concentration the of metal species to produce measurably different ^{129}Xe shifts in samples subjected to different preparatory treatments. The sensitivity of the ^{129}Xe probe to highly dispersed, reduced metal permits lower, more industrially realistic metal loadings to be studied. Figure 3.15, for example, shows the effect of diminished platinum loadings on the ^{129}Xe chemical shift in Pt-NaY calcined and reduced at 673 K. Loadings down to 0.5 wt% Pt produce discernible shifts in the ^{129}Xe resonance at low adsorbed xenon concentrations. Unfortunately, low sensitivity of the ^{129}Xe shift to shielded metal species, such as the PtO calcination product, is troublesome at low metal guest loadings. In these cases, use of enriched ^{129}Xe (available as 80% ^{129}Xe from Isotec Inc.) can enhance the technique's sensitivity to the metal species by permitting studies at low Xe uptakes where Xe–metal interactions predominate.

3.7 Conclusions

Our results indicate that for the 673 K reduction conditions imposed, the formation of highly dispersed platinum clusters within the Y zeolite matrix is best achieved by employing a calcination temperature close to 673 K. Below this temperature, incomplete decomposition of the $Pt(NH_3)_4^{2+}$ complex during calcination results in migration of nearly all the platinum to the exterior surfaces of the NaY crystallites during reduction. Calcination at temperatures significantly above 673 K induces decomposition of the shielded precursor species (shown in Chapter 4 to be platinum oxide) and migration of the metal into the sodalite cavites. During reduction at

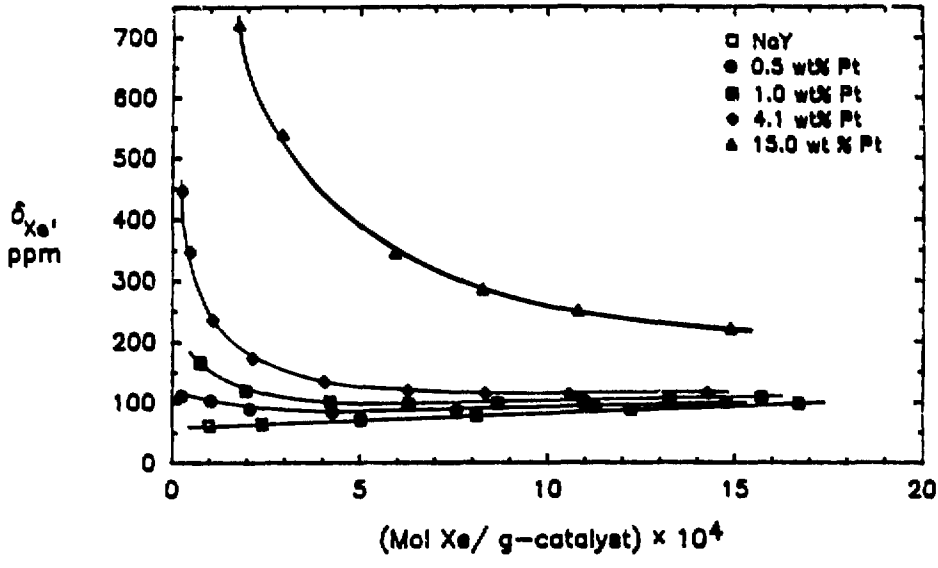

Figure 3.15: Variation in ^{129}Xe chemical shift with the concentration of xenon adsorbed (T=295 K) on reduced Pt-NaY zeolite samples containing variable metal loadings. The samples were calcined at 673 K before being reduced at 673 K.

673 K, a substantial amount of the platinum confined within the sodalite cavities migrates back into the supercages where it forms low surface-area aggregates. After initial reduction of Pt–NaY, subsequent reoxidation at 873 K does not induce or abet additional agglomeration of the metal species into larger clusters. The cluster size-dependent response of the Pt–NaY systems to reoxidation treatment is consistent with the greater reactivities expected for small metal particles compared to larger aggregates.

The sensitivity of physisorbed xenon to the influence of metal species makes ^{129}Xe NMR spectroscopy an important diagnostic probe of the metal clustering process in zeolites. Hydrogen chemisorption and transmission electron microscopy provide complementary information which correlates well with the ^{129}Xe NMR results. The combination of these techniques permit the influence of catalyst treatment conditions on metal guest distribution and stability to be established.

Chapter 4

The Chemistry of Pt-NaY Preparation[1]

4.1 Abstract

Raman spectroscopy and temperature programmed reduction experiments establish the chemical intermediates important to the formation of highly dispersed platinum clusters on a NaY zeolite support. Calcination at 673 K decomposes the ion-exchanged $Pt(NH_3)_4^{2+}$-NaY starting material to $PtO/2H^+$-NaY which, upon reduction at 673 K, yields optimum metal dispersion in the NaY supercage cavities. Calcination at temperatures above ca. 773 K induces decomposition of PtO to yield Pt^{2+} cations which occupy sodalite cage sites. Migratory tendencies of the metal during reduction of cationic precursors $Pt(NH_3)_4^{2+}$ and Pt^{2+} contribute to diminished metal dispersion in catalysts calcined at temperatures significantly below or

[1]Presented in part at the Eighth International Zeolite Conference, Amsterdam, 10 to 14 July 1989. Portions have also been published in Zeolites: Facts, Figures, Future, P.A. Jacobs and R.A. van Santen, eds., Elsevier: Amsterdam (1989) pp. 995-1005.

above 673 K, respectively.

4.2 Introduction

Chapter 3 discussed the calcination dependence of platinum species distributions in NaY zeolite using ^{129}Xe NMR spectroscopy, hydrogen chemisorption, and transmission electron microscopy (TEM). These techniques are sensitive probes of the location of metal clusters and cluster precursors within the zeolite matrix and provide insight into factors important in the preparation of dispersed metal catalysts. Our ^{129}Xe NMR spectroscopy experiments, in particular, demonstrate the existence of a shielded platinum intermediate formed during calcination at 673 K. Upon reduction at 673 K, this shielded precursor species yields highly dispersed platinum metal clusters located in the supercages of the Y zeolite lattice [84]. Likely candidates for the identity of the calcination product species are the two forms of platinum oxide Pt(II)O and Pt(IV)O_2, which can be distinguished based on differences in their Raman spectra and reduction stoichiometries. The possible existence of $PtOH^+$ as a primary product of calcination is ruled out by ^{129}Xe NMR and TEM results discussed in Appendix C. Raman spectroscopy is a sensitive probe of oxide phases and is capable of delineating between monomeric species and bulk structures [85]. Temperature programmed reduction (TPR) experiments complement the Raman studies by providing quantitative information on the distribution of the phases and on the average oxidation state of the metal. In this study, we use Raman spectroscopy and TPR to identify calcination product species which exist as precursors to zeolite-supported, dispersed metal clusters.

4.3 Experimental

Fifteen weight-percent (dry basis) $Pt(NH_3)_4^{2+}$–NaY catalyst samples were prepared by introducing the platinum tetraammine cation $Pt(NH_3)_4^{2+}$ into the zeolite lattice via the ion-exchange procedure of Gallezot *et al.* [24]. For the Raman measurements, 0.5 g of the 15 wt% $Pt(NH_3)_4^{2+}$–NaY catalyst material was pelletized under 100 MPa pressure into a 13-mm diameter pellet of 1-mm thickness. The sample was heated in purified, flowing oxygen to 473 K at a heating rate of 50 K/h and subjected to a 4 h soak before the Raman spectra were acquired. Raman spectra were taken under flowing oxygen using the 488.0 nm line of an argon ion laser (Spectra Physics, Model 165) with 50 mW of power at the sample. Spectra were recorded from 200 cm^{-1} to 1200 cm^{-1}, with a resolution of 6 cm^{-1}. Following completion of the Raman acquisition, the sample was heated under the conditions described above to a new maximum temperature of 578 K. Another Raman spectrum was then acquired, with the procedure repeated in $\approx$ 100 K increments to a calcination temperature of 873 K. After calcination at 773 K and 873 K, the sample was cooled and the Raman spectra acquired at 673 K to minimize thermal broadening.

Temperature programmed reduction experiments were performed on separate 15 wt% $Pt(NH_3)_4^{2+}$–NaY catalyst samples calcined at 473 K, 673 K, 773 K, and 873 K. Each sample was heated in purified flowing oxygen at 47 K/h to its respective calcination temperature where it was soaked for 5 h before being cooled to room temperature and then evacuated for 0.25 h. After further cooling to 123 K in flowing argon, a continuous flow of 9800 ppm hydrogen gas in an argon carrier, also at 123 K, was directed over the sample. Hydrogen consumption and ammonia evolution were monitored directly using a downstream mass spectrometer as the temperature was ramped from 123 K to 1073 K at 20 K/min.

4.4 Raman Spectroscopy Experiments

Raman spectroscopy can delineate between different chemical species by correlating differences in characteristic molecular vibration frequencies. In Figure 4.1 we show Raman spectra for 15 wt% $Pt(NH_3)_4^{2+}$-NaY catalyst samples calcined at different temperatures. Fluorescence was severe in the sample treated at 473 K preventing meaningful analysis of the $Pt(NH_3)_4^{2+}$ precursor state. After treatment at 578 K, the Raman spectrum of Figure 4.1(a) reveals a complicated series of vibrations with resolvable bands at 498 and 625 cm^{-1} and a broad feature at 700–1000 cm^{-1}. Because of the mild calcination treatment, Figure 4.1(a) contains contributions from the metal-tetraammine complex and various products from the metal complex' partial decomposition, in addition to the Y zeolite support [59,84]. The sensitivity of the complex' decomposition rate to small differences in temperature (on the order of a few degrees Kelvin) can lead to measurable differences in the extents of calcination near 573 K [63] [see Fig. E.1 in Appendix E]. However, as the calcination temperature is increased to 673 K, the $Pt(NH_3)_4^{2+}$ complex is completely decomposed [84], yielding the simplified spectrum in Figure 4.1(b). Here the spectrum reveals well-defined peaks at 492, 610, and 626 cm^{-1}, with the latter possessing a shoulder feature at approximately 632 cm^{-1}. The broad band at 700–1000 cm^{-1} has entirely disappeared in Figure 4.1(b). Similar features are present in the sample calcined at 773 K [Fig. 4.1(c)], but the sharp peaks at 610 and 626 cm^{-1} have diminished in intensity relative to the band at 500 cm^{-1}. A small peak at 290 cm^{-1} is also noticeable in Figure 4.1(c). At 873 K, the sharp peak at 610 cm^{-1} has completely disappeared, leaving only the bands centered at 507 and 632 cm^{-1} in Figure 4.1(d). The peak at 630 cm^{-1} is now less intense than the band at 507 cm^{-1} while the intensities of bands at 290 and 820 cm^{-1} have increased.

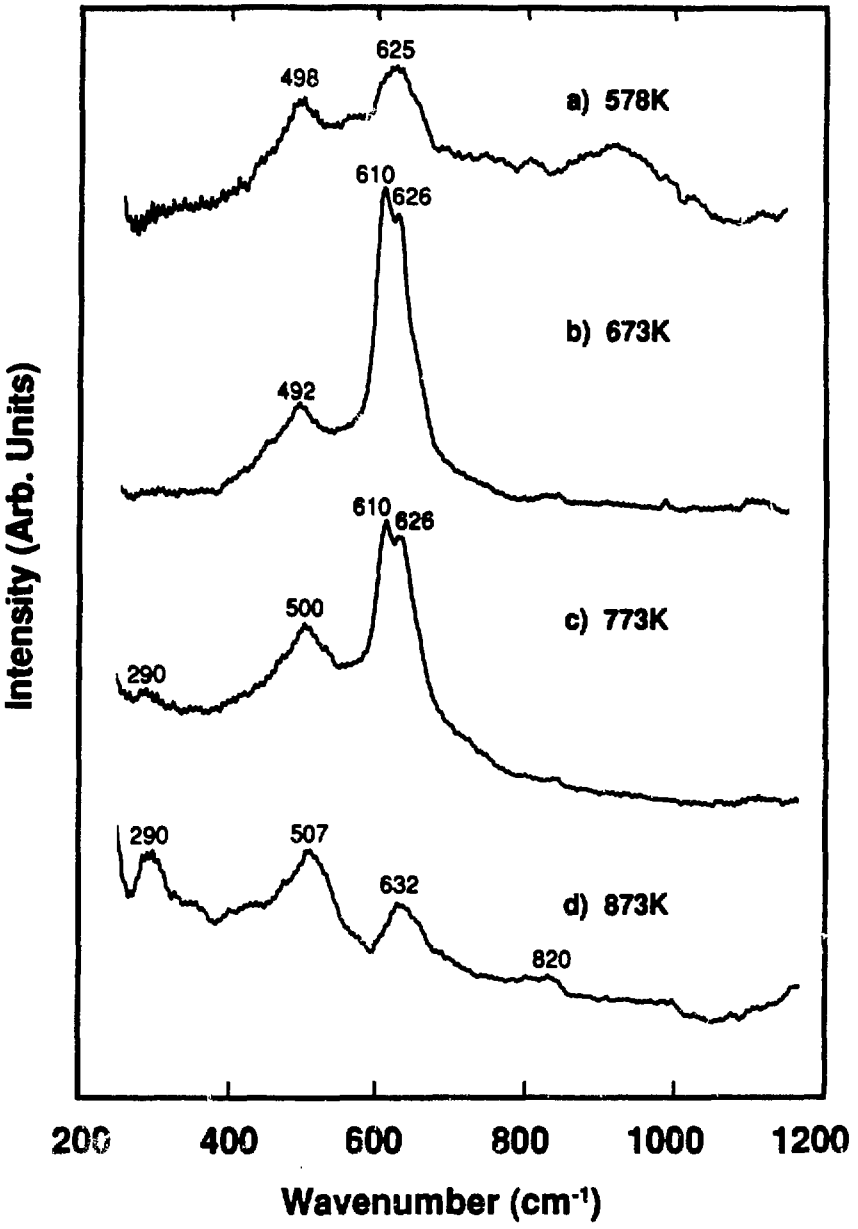

Figure 4.1: Raman spectra of 15 wt% $Pt(NH_3)_4^{2+}$-NaY catalyst samples calcined in oxygen at different temperatures: (a) 578 K, (b) 673 K, (c) 773 K, and (d) 873 K.

Identifying the species which give rise to these vibrational patterns is aided by correlation with previous ^{129}Xe NMR and hydrogen chemisorption experiments [59, 84] and by comparison with Raman spectra of standard compounds whose chemical identities are known. The band at ca. 500 cm^{-1}, for example, can be assigned to the Y zeolite support as it agrees with the 499 cm^{-1} peak observed in Figure 4.2(a) for the nascent NaY support material. The spectrum in Figure 4.2(a) is in good agreement with Roozeboom *et al.* [86] and Dutta *et al.* [87] who have published similar spectra for the solid-phase NaY zeolite support. Small calcination-induced changes in the position of the zeolite framework band in Figures 4.1(a–d) (492–507 cm^{-1}) reflect the sensitivity of the aluminosilicate lattice to the chemical nature of the metal guest. Experiments by Gallezot *et al.* [24] on platinum-loaded NaY zeolites indicate that the structural integrity of the macroscopic framework remains intact below 1173 K, with the matrix collapsing into an amorphous phase above this temperature.

The product of the platinum tetraammine calcination can be inferred from Raman experiments on reoxidized Pt–NaY samples through consideration of the adsorption/reaction behavior of oxygen with reduced Pt–NaY. The stoichiometry for oxygen chemisorption on zeolite-supported platinum at room temperature has been shown to vary from 0.5 to 1.0 mole of atomic oxygen per mole of surface Pt, depending on metal cluster size [24,66]. Significantly, the 632 cm^{-1} peak in Figures 4.1(b–d), after disappearing upon exposure to molecular hydrogen at room temperature [see Fig. E.2 in Appendix E], is regenerated in Figure 4.2(b) at precisely the same location following reoxidation of the reduced platinum at 773 K and subsequent cooling to 298 K. Because the 610–630 cm^{-1} bands in the Raman spectra of the calcined and reoxidized Pt–NaY samples [Figs. 4.1(b–d), 4.2(b)] are at substantially different positions than those observed for bulk PtO_2 at 511 and 555 cm^{-1} [Fig. 4.2(c)], the

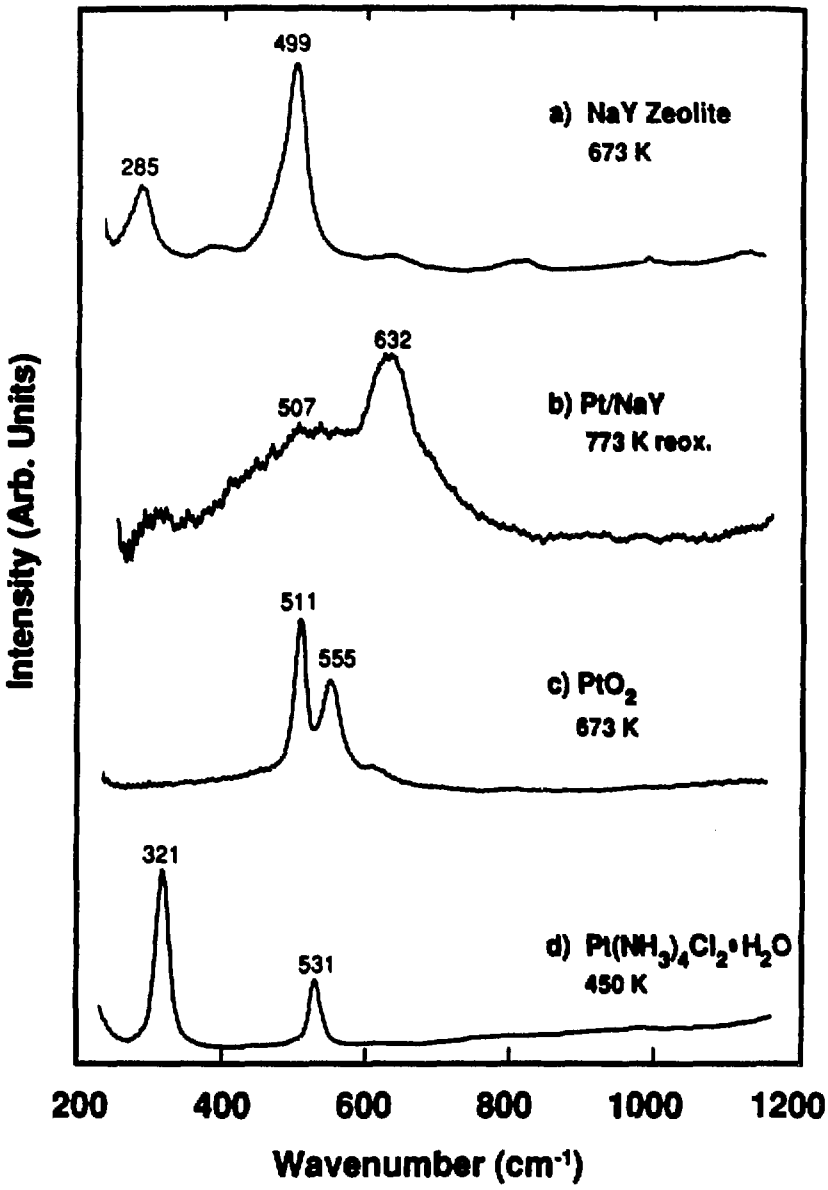

Figure 4.2: Raman spectra of standard compounds: (a) NaY zeolite support, T = 673 K; (b) Pt-NaY reoxidized at 773 K (following calcination at 773 K and reduction at 673 K), T = 298 K; (c) PtO_2, T = 673 K; and (d) $Pt(NH_3)_4Cl_2 \cdot H_2O$, T = 450 K.

most likely calcination product candidate at 673 K is the monoxide species, PtO. Indeed, reference Raman data for other Group VIII metal oxides such as PdO [88] show bands for the metal-oxygen stretch at ca. 650 cm^{-1}, consistent with the assignment of features at 610, 626, and 632 cm^{-1} to PtO.

The relatively simple features in the Raman spectra of the $Pt(NH_3)_4Cl_2 \cdot H_2O$ bulk standard compound in Figure 4.2(d) provide a basis for interpreting the Raman data of the partially calcined catalyst sample in Figure 4.1(a). First, we note that the zeolite framework band is quite visible at 498 cm^{-1} as a shoulder on the dominant peak at 625 cm^{-1}. After ion-exchange into the zeolite, the $Pt(NH_3)_4^{2+}$ cation retains its nominal D_{4h} symmetry, but has relinquished the two chlorine ligands occupying apex positions above the square-planar tetraammine configuration. The two prominent bands at 321 cm^{-1} and 531 cm^{-1} in the Raman spectrum of $Pt(NH_3)_4Cl_2 \cdot H_2O$ [Fig. 4.2(d)] are identified as Pt–Cl and Pt–N stretching modes, respectively based on very strong bands assigned to these vibrations in the closely related compound trans-$[Pt(NH_3)_4Cl_2]Cl_2$ [89]. As expected, the Pt–Cl vibrations at 321 cm^{-1} are completely absent in the Raman spectra of the ion-exchanged/calcined catalyst samples shown in Figures 4.1(a–d). However, the Pt–N band observed in the bulk tetraammine salt at 531 cm^{-1} in Figure 4.2(d) can be observed in the incompletely calcined catalyst as a broad feature between the 498 cm^{-1} framework band and the 625 cm^{-1} metal oxide band, thus, confirming the existence of a substantial quantity of the undecomposed metal complex following calcination at 573 K [59,84]. The broad features in Figure 4.1(a) from 700–1000 cm^{-1} are unassigned, but are probably due to modes of the partially decomposed platinum tetraammine complex and/or ammonia adsorbed on the zeolite support. The complicated structure of Figure 4.1(a) provides evidence of the large role played by the zeolite support in the decomposition of the

tetraammine complex. The origins of the two peaks at 511 and 555 cm^{-1} in the previously unreported Raman spectrum of bulk PtO_2 [Fig. 4.2(c)] are uncertain, but are due possibly to different vibrational modes or to separate phases of the metal dioxide [90].

The dominant peak at 625 cm^{-1} in Figure 4.1(a) is present in Raman spectra 4.1(b–d) as well, but with variable intensity relative to the framework band. In Figure 4.1(b), the only bands which survive calcination at 673 K are the framework peak at ca. 500 cm^{-1} and peak(s) at ca. 610–630 cm^{-1} corresponding to the metal oxide species. The substantial increase in the intensities of PtO bands in the Raman spectrum acquired at 673 K compared with those observed at 573 K is consistent with our ^{129}Xe NMR results which indicate complete decomposition of the $Pt(NH_3)_4^{2+}$ species to a shielded product (located in the supercages) during calcination at 673 K [84]. The sharp band at 610 cm^{-1} observable in Figures 4.1(b–c) arises most likely from small PtO aggregates possessing homogeneous scattering sites, whereas the broader band centered at 632 cm^{-1} is probably due to isolated PtO species which are expected to have a more inhomogeneous scattering character [91].

Higher calcination temperatures of 773 K and 873 K leave the positions of the 610, 626, and 632 cm^{-1} peaks unchanged as illustrated in Figures 4.1(c–d). However, the PtO peak diminishes in intensity relative to the zeolite lattice peak. This is consistent with thermal decomposition of the metal oxide intermediate into Pt^{2+} cations above 773 K, according to the reaction

$$PtO{-}2H^{+}Y \xrightarrow{>773\,K} Pt^{2+}{-}2Y + H_2O\,(g), \qquad (4.1)$$

which allows the platinum species to enter the sodalite cavities as previously documented by us [84] and others [24,34]. The highly-charged Pt^{2+} cation (0.148 nm) establishes a more stable energetic configuration within a sodalite cavity at the ex-

pense of two sodalite Na^+ cations which exchange into the vacated supercage cation sites. Mobility of the Pt^{2+} cations within the Y zeolite cavities is expected to be relatively high, based on diffusivity data available for Mg^{2+} ($D_{MgY} \approx 10^{-12}$ m^2/s at 773 K) [92], whose charge density is very similar to that of the divalent platinum cation. In the confined environment of the sodalite cage, the highly charged transition metal cations are in closer proximity to the anionic charges of the lattice than would be possible in a supercage location. Essentially all of the divalent Pt^{2+} species resulting from decomposition of the PtO intermediate occupy sodalite sites where the respective charges can be more effectively neutralized. The small peaks at 290 cm^{-1} and 820 cm^{-1} are unassigned, though the former may arise from the zeolite lattice as there is a small band at this position in the Raman spectrum of the bulk NaY standard in Figure 4.2(a), while the latter is probably a weak band from the quartz cell [93]. Our observation of PtO decomposition over the temperature range 773 to 873 K is consistent with decomposition temperatures of PtO published elsewhere [24,34,94]. The dramatically reduced intensity of the PtO peak in Figure 4.1(d), following calcination at 873 K, corroborates our ^{129}Xe NMR and H_2 chemisorption results which indicate essentially complete decomposition of the PtO intermediate and subsequent population of sodalite cage sites by nearly all of the metal present [84].

4.5 Temperature Programmed Reduction Studies

TPR experiments performed on 15 wt% Pt–NaY samples calcined at different temperatures quantitatively support the identification of the PtO calcination inter-

mediate. We observe in all catalyst samples consumption of ca. 1 mole of molecular hydrogen per mole of platinum guest, in agreement with data published previously by Park *et al.* [95] for Pt–NaY samples calcined between 473 and 723 K. In most instances, reduction occurs over a wide (ca. 600 K) temperature range. In Figure 4.3(a), reduction of the undecomposed $Pt(NH_3)_4^{2+}$ complex in the sample calcined at 473 K consumes 1.3 moles of H_2 and is accompanied by substantial evolution of ammonia at 523 K which suggests the following reaction:

$$Pt(NH_3)_4^{2+}{-}2Y + H_2 \xrightarrow{523\ K} Pt^0{-}2H^+Y + 4NH_3\,(g). \qquad (4.2)$$

The TPR peak at 483 K in Figure 4.3(a) is not accompanied by evolution of NH_3 and can be attributed to reduction of some PtO formed in the supercages during incomplete calcination at 473 K. Decomposition of $Pt(NH_3)_4^{2+}$ in hydrogen over the temperature range 573–673 K is in agreement with the temperature programmed decomposition data of Reagan *et al.* [50] and Exner *et al.* [63]. The massive migration of platinum to the exterior of the zeolite crystallite during reduction of the undecomposed metal-tetraammine complex [84] is consistent with the formation of a mobile metal hydride species, $Pt(NH_3)_2H_2$, as suggested by Dalla-Betta and Boudart [10].

In Figure 4.3(b), reduction of the PtO species produced during calcination at 673 K similarly consumes 1.0 mole of H_2 for each mole of Pt present with little evolution of ammonia. This confirms the existence of Pt(II) species in the zeolite supercages following complete decomposition of the metal-tetraammine complex. Reduction of PtO occupying supercage locations is complete below 673 K, with the reaction proceeding as

$$PtO{-}2H^+Y + H_2 \xrightarrow{673\ K} Pt^0{-}2H^+Y + H_2O\,(g). \qquad (4.3)$$

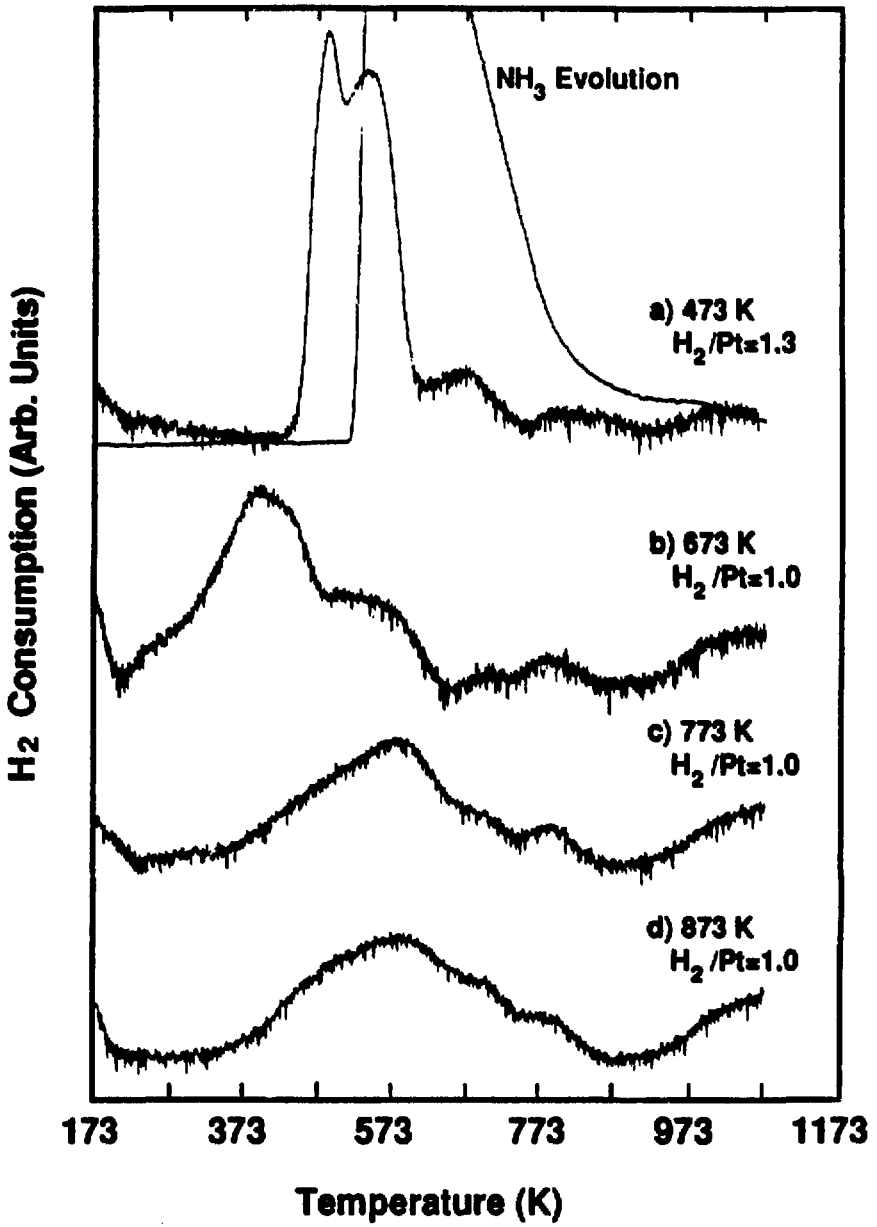

Figure 4.3: Temperature programmed reduction data for 15 wt% Pt–NaY samples calcined at different temperatures: (a) 473 K, (b) 673 K, (c) 773 K, and (d) 873 K. Moles of H_2 consumed per mole of Pt are shown for each curve.

Adsorption of the effluent water by the stainless steel TPR apparatus axially disperses the H_2O species, obscuring its detection by the downstream mass spectrometer [see Appendix E]. The TPR spectrum has broadened from that observed in Figure 4.3(a), reflecting the more heterogeneous distribution of metal environments which exist as a result of clustering of the PtO precursor species [84].

Pt-NaY samples calcined at 773 K and 873 K both consume 1.0 mole of H_2 per mole of Pt, though as shown in Figures 4.3(c-d), the broad dominant features occur at substantially higher reduction temperatures in comparison to those for Pt-NaY samples calcined at lower temperatures [Figs. 4.3(a-b)]. The total quantity of hydrogen consumed during the reduction of the 773 K and 873 K calcined samples is the same as that observed for samples calcined at 573 K and 673 K, for which all Pt is accessible in supercage sites. All platinum species are, therefore, capable of being reduced, including Pt^{2+} cations confined within the sodalite cavities which follow the reaction

$$Pt^{2+}-2Y + H_2 \xrightarrow{>673\,K} Pt^0-2H^+Y. \qquad (4.4)$$

Reduction of Pt^{2+} in sodalite sites occurs only if the 0.29 nm-diameter H_2 molecules or smaller dissociated hydrogen species penetrate the potential barrier imposed by the nominal 0.22-nm six-membered oxygen ring entrance into the sodalite cavities. Lattice vibrations, which increase in amplitude at higher temperatures, produce fluctuating bond lengths between framework atoms comprising the sodalite aperture. At room temperature, hydrogen diffusion past this barrier is very slow, but at reduction temperatures above 673 K it occurs more readily. Spillover of dissociated hydrogen from reduced Pt clusters in the supercages may, also, contribute to the reduction of sodalite cage Pt^{2+} species. While our data do not permit identification of the dominant reducing agent(s) within the sodalite cages, it is clear that diffusion of

a hydrogenic species through the sodalite aperture represents the rate-determining step for reduction of Pt^{2+} cations confined to sodalite locations.

From Figure 4.3(c–d), our results indicate that reduction of Pt^{2+} cations in the sodalite cages is not complete until approximately 823 K. At reduction temperatures above 953 K, we observe in Figures 4.3(a–d) what are believed to be early indications of damage to the structural integrity of the zeolite matrix. Cleavage of some lattice oxygen bonds are thought to result in the consumption of hydrogen as surface hydroxyl groups are formed. Low surface-metal fractions observed in samples calcined at 773 K and 873 K and reduced at 673 K [84] are due to incomplete reduction of platinum in sodalite cage locations and to Pt aggregation in supercages as a result of metal movement out of the sodalite cavities during reduction. The TPR data are corroborated by ^{129}Xe NMR, hydrogen chemisorption, and TEM experiments which we have previously reported [84].

4.6 Summary of Results

Figure 4.4 summarizes the preparation chemistry and resulting platinum distributions for various calcination and reduction treatments used in activating 15 wt% Pt-NaY catalyst [59,84,96]. The platinum guest is introduced initially into the lattice by ion-exchanging the divalent tetraammine cation $Pt(NH_3)_4^{2+}$ for two Na^+ cations in the nascent support material. The $\approx$ 0.6 nm $Pt(NH_3)_4^{2+}$ complex occupies only supercage locations [Fig. 1.1(b)] within the ion-exchanged zeolite, being too large to penetrate the 0.22 nm windows of the sodalite cavities. Under mild calcination conditions at 473 K, the $Pt(NH_3)_4^{2+}$–exchanged zeolite dehydrates without significant decomposition of the tetraammine complex. Coulombic interactions with the lattice keep the divalent complex dispersed within the supercages. Reduction of this sample

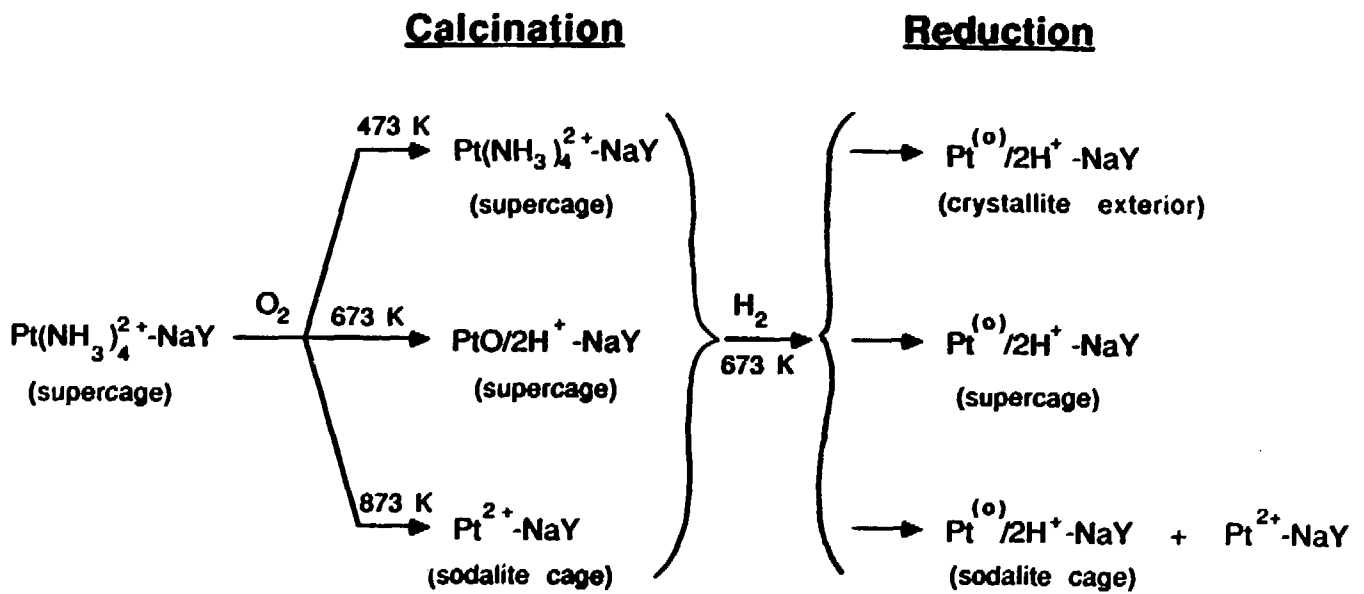

Figure 4.4: Summary of Pt–NaY preparation chemistry for different calcination conditions. The locations of the metal species within the zeolite lattice are indicated in parentheses.

to the metallic state at 673 K induces migration of the metal species to the exterior of the crystallites as depicted schematically in Figure 1.1(a). High metal mobility results in the exodus and subsequent aggregation of the platinum into very large, catalytically undesirable clusters ca. 40 nm in diameter.

If calcination is undertaken at 673 K, the tetraammine complex decomposes to essentially non-migratory PtO species which remain in supercage locations. Following reduction of this material at 673 K, highly-dispersed platinum occupies supercage sites [Fig. 1.1(b)], providing high metal surface area and accessibility to reactant species. Finally, calcination at 873 K decomposes the PtO intermediate, producing Pt^{2+} species which occupy sodalite cages inaccessible to xenon and molecular hydrogen at room temperature. Penetration of Pt^{2+} cations into the sodalite cavities increases the temperature necessary for complete reduction of platinum in these sites. Xenon-129 NMR, H_2 chemisorption, and TEM experiments provide independent and corroborative data on the locations of the metal species [Chapter 3], while ^{129}Xe NMR, Raman spectroscopy, and TPR experiments independently support the identification of the PtO and Pt^{2+} precursor species. These results establish that calcination at 673 K and subsequent reduction also at 673 K provide optimal conditions for preparation of our highly-dispersed, NaY-supported 15 wt% platinum catalysts.

Chapter 5

Distributions of Aromatic Molecules in NaY Zeolite

5.1 Abstract

The distribution of adsorbed molecules in zeolites has been studied using ^{129}Xe and multiple-quantum NMR. Local and macroscopic arrangements of benzene, 1,3,5-trimethylbenzene, and hexamethylbenzene (HMB) molecules among the cavities of NaY zeolite samples have been investigated. Xenon-129 NMR, a sensitive probe of distributions of molecules in zeolite particles, demonstrates the importance of sample heat treatment in distributing an adsorbate homogeneously throughout a collection of zeolite particles. NaY samples containing organic guests adsorbed at low temperatures produce multiple or broad xenon lines characteristic of macroscopic (i.e. interparticle) adsorbate concentration gradients. After thorough heat treatment at higher temperatures, the xenon spectrum collapses to a single sharp line, consistent with a macroscopically-uniform distribution. For HMB adsorbed in NaY, "counting" hydrogen clusters by multiple-quantum NMR reveals intraparticle HMB distributions

consistent with one molecule per cavity at low loadings (average bulk loading $\leq$ one molecule per cavity) and two molecules per cavity at higher loadings. The relationship between molecular distribution and physical properties of the guest species is discussed.

5.2 Introduction

Zeolites possess unique chemical and structural properties that make them important in numerous industrial applications. Because of their high internal surface areas and molecular-size cage dimensions, zeolites are used widely as shape-selective catalysts or adsorbents in a variety of industrially significant chemical processes [1,2]. Transport and adsorption of reactant species within the porous zeolite matrix are particularly crucial to the molecular-sieve function of these materials. Heterogeneous catalytic processes, for example, rely on molecular clustering and orientation at surface adsorption sites to promote chemical reactions. The diffusivity and adsorption kinetics of reactant guest molecules in zeolites are known, however, to be highly dependent on treatment conditions which have a dramatic effect on the distribution of guest molecules within the porous matrix. In probing the kinetics of such phenomena at the molecular level, it is imperative that the distribution and dynamic behavior of adsorbed species be understood in porous materials.

Hydrocarbons adsorbed on zeolites have been extensively studied by X-ray scattering [97], infrared spectroscopy [98], and neutron diffraction [99] which, if taken together, provide insight into the distribution, mobility, and orientation of organic guest species. Applications of NMR techniques to the study of zeolites are widespread and are reviewed in numerous texts [46,100,101]. Although the molecular dynamics of simple molecules, such as water, methane, and benzene, adsorbed in zeolite cavities

have been investigated using NMR relaxation times [102,103,104], lineshape analyses [105,106,107], and pulsed field-gradient experiments [108], local structural information pertinent to adsorbate distribution is not easily obtained. Important questions remain with regard to the uniformity, site occupancy, and preparatory-treatment dependence of adsorbate distributions in zeolite cavities.

To address these issues, we have employed a combination of ^{129}Xe and proton multiple-quantum NMR to obtain detailed information on the distributions of adsorbed organic molecules in NaY zeolite. By virtue of a ^{129}Xe chemical shift range that exceeds 5000 ppm, slight variations in local environment can have a profound influence on the ^{129}Xe resonance frequency. Fraissard and coworkers [109,110], Ripmeester [40], Pines *et al.* [59,111] and others [42,43,44,112] have successfully applied ^{129}Xe NMR to the study of ordered porous materials, such as zeolites and clathrates, with and without guest species. Multiple-quantum (MQ) NMR spectroscopy [113] provides a convenient way of determining the size of hydrogen clusters [114] within isolated NaY supercages from which organic guest occupancies of the zeolite cavities can be inferred.

In a preliminary communication [41], we applied ^{129}Xe and multiple-quantum NMR techniques to the study of NaY zeolite samples containing adsorbed hexamethylbenzene (HMB). These experiments demonstrated the importance of sample heat treatment in the distribution of organic guest species within NaY zeolite cavities. Here, we present a complete account of this work, and extend the study to distributions of adsorbed benzene and 1,3,5-trimethylbenzene (TMB) in NaY zeolite. These particular molecules were chosen because their kinetic diameters, 0.58 nm for benzene, 0.75 nm for TMB, and 0.82 nm for HMB, are comparable to the 0.74 nm supercage aperture of NaY at room temperature [1]. The relevance of molecular size,

mobility, and phase properties to the transport and adsorption of organic guests can therefore be investigated. The combination of ^{129}Xe and multiple-quantum NMR comprehensively characterizes the distributions of these adsorbate species, not only among a collection of sample particles, but also within individual NaY zeolite particles as well.

5.3 Experimental

5.3.1 Sample preparation

All zeolite samples were prepared in 10-mm NMR tubes [Fig. 2.9] connected to a vacuum apparatus through a Kontes high-vacuum stopcock. NaY zeolite was synthesized according to the procedure of Breck [1], with crystallinity confirmed by x-ray diffraction studies. As shown in Figure 5.1, separate scanning electron microscopy experiments establish NaY crystallite grain diameters of 1–2 μm. Before addition of the adsorbate species, the NaY samples were dehydrated in the sample tubes by heating at 673 K under vacuum (ca. 10^{-5} torr) overnight. After dehydration, a known amount of organic adsorbate was introduced to the zeolite at room temperature to achieve the bulk loading desired. Adsorbate loadings were calculated from mass balances utilizing NaY supercage density and the masses of zeolite and organic guest materials. Benzene was introduced to NaY zeolite samples at room temperature by allowing benzene vapor to diffuse into the bed under evacuated conditions. Liquid TMB and solid HMB were stored at 273 K in a sidearm of the sample tube during dehydration and subsequently introduced mechanically under vacuum to the top of the zeolite sample volume. Without delay, the samples were placed in a furnace equipped with a programmable temperature controller, heated for a known period of

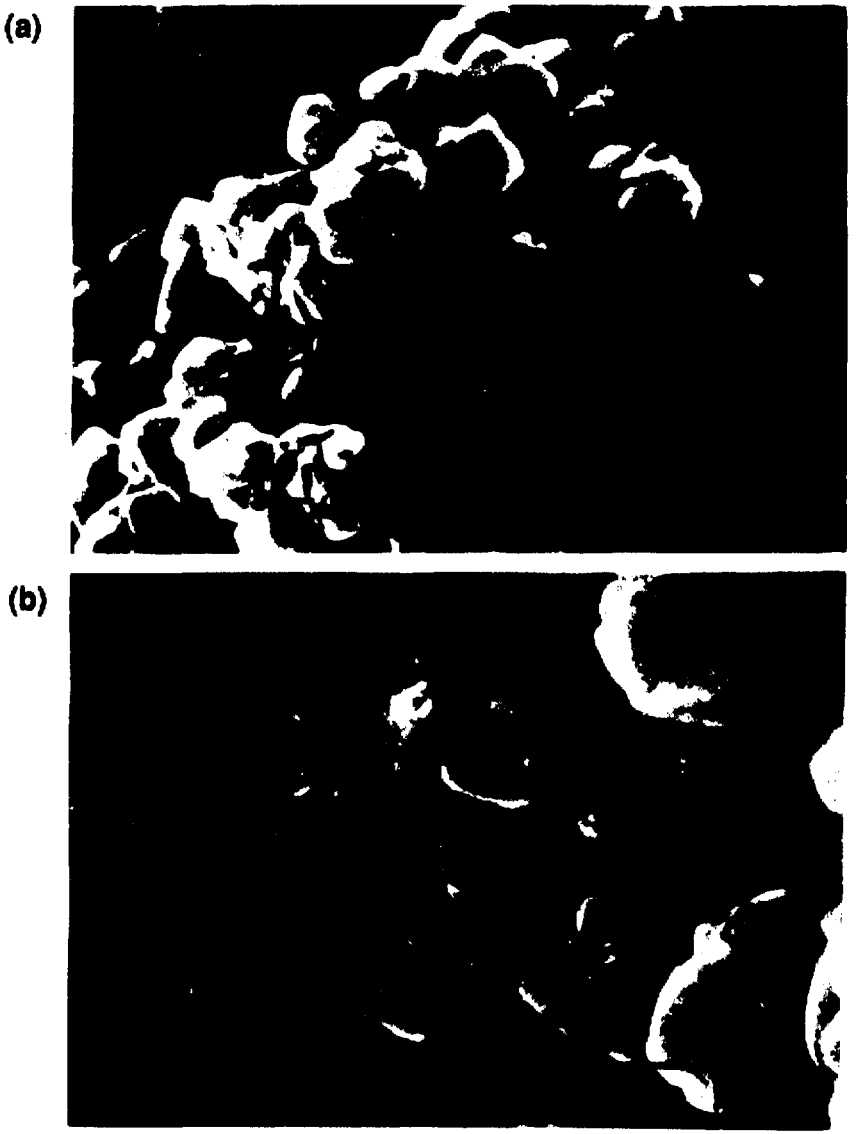

Figure 5.1: Scanning electron micrographs of the NaY zeolite used in adsorption/NMR experiments of aromatic guest species distribution: (a) Low (x10,000) and (b) high (x20,000) magnification views of micron-size NaY crystallites. The corrugated features reflect intergrowth of zeolite crystals during synthesis.

time, and cooled to room temperature over a period of many hours. Xenon gas was then introduced into each sample at room temperature and allowed to equilibrate to a pressure of $\approx$ 300 torr.

5.3.2 NMR experiments

Room temperature ^{129}Xe NMR spectra were obtained on Nicolet and Bruker spectrometers operating a 49.8 MHz and 110.0 MHz, respectively. Each acquisition typically consisted of 2000–4000 free induction decay scans with a delay of 0.2 s between 90° pulses. The experiments employed a sweep width of 41667 Hz with a digitizing time of 12 μs. All ^{129}Xe chemical shift values are referenced to the ^{129}Xe signal of xenon gas at very low pressure [37] and are believed accurate to 0.5 ppm. Proton multiple-quantum NMR data were obtained using a phase cycling technique [114] on a home-built spectrometer operating at 179 MHz. Long excitation-time multiple-quantum intensities were fit to a Gaussian curve according to statistical arguments described elsewhere [115]. The effective cluster size N is obtained from the standard deviation of the Gaussian fit, taken equal to $\sqrt{N/2}$.

5.4 Macroscopic Adsorbate Distributions

As a sensitive, non-reactive probe of supercage cavities within the crystalline zeolite matrix, room temperature ^{129}Xe NMR provides information on interparticle adsorbate distribution heterogeneities in polycrystalline NaY samples. Physisorption within the zeolite matrix perturbs a xenon atom's spherical, polarizable electron cloud, producing a shift in the ^{129}Xe resonant frequency in an externally applied magnetic field. In NaY zeolite, the 0.44 nm xenon atom easily penetrates the 0.74 nm window into the supercages, thereby serving as an indirect probe of guest molecules

adsorbed in supercage sites. The room-temperature ^{129}Xe NMR spectrum of xenon adsorbed on dehydrated NaY zeolite is shown in Figure 5.2(a). The single line at 78 ppm agrees with that found previously by Ito and Fraissard for xenon adsorbed on NaY at an equilibrium xenon pressure of 300 torr [35]. The large downfield shift in the ^{129}Xe resonance manifests the deshielding experienced by xenon nuclei due to collisions between ^{129}Xe atoms and the NaY cage walls and other xenon atoms. Figure 5.2(b) displays a ^{129}Xe NMR spectrum containing a single peak at 109 ppm corresponding to xenon adsorbed on dehydrated NaY zeolite loaded with an average of 1.0 HMB molecule/supercage. As demonstrated in our preliminary communication [41] and recently by Gedeon *et al.* [116], sample heat treatment plays a crucial role in controlling the distribution of the adsorbed guest molecules within the zeolite sample volume.

5.4.1 HMB in NaY

It is possible, using ^{129}Xe NMR, to distinguish between a packed bed of zeolite crystallites possessing an axial adsorbate concentration gradient and one in which the adsorbate is dispersed homogeneously throughout the macroscopic sample volume. This is accomplished by exploiting the different perturbations experienced by xenon atoms diffusing through zeolite environments containing different guest loadings. By monitoring the chemical shift of physisorbed ^{129}Xe, distinct zones of guest molecule adsorption can be identified within NaY zeolite samples. Figure 5.3, for example, displays ^{129}Xe spectra of xenon adsorbed at 295 K on dehydrated NaY containing, on average, one molecule of HMB for every two supercage cavities present in the bulk sample (denoted hereafter as 0.5 HMB/cavity.) Placement of the receiver coil about the lower region of the sample volume results in the single ^{129}Xe peak at 78 ppm

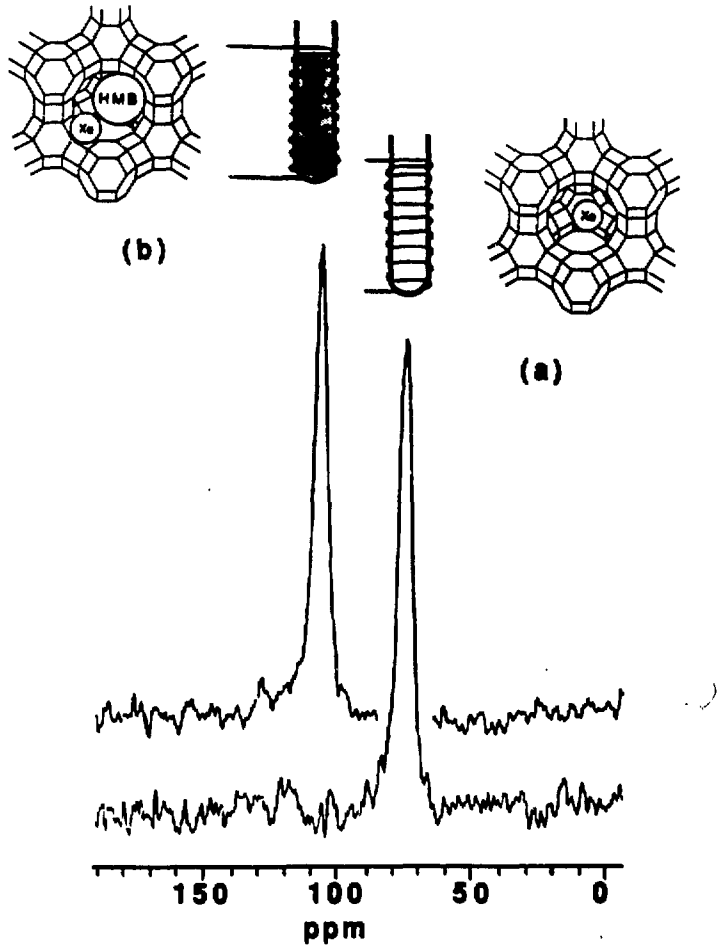

Figure 5.2: Room-temperature ^{129}Xe NMR spectra of xenon (300 torr equilibrium pressure) adsorbed on NaY zeolite with and without adsorbed HMB guest species. Schematic diagrams of NaY zeolite samples in 10 mm NMR tubes are shown above the spectra. Shading reflects the presence of adsorbed guests in supercage environments. The receiver coil is shown to indicate the approximate sample volume probed by the NMR experiment. (a) The ^{129}Xe chemical shift, δ_{xe}, is 78 ppm in dehydrated NaY containing no guest species. (b) δ_{xe} = 109 ppm in dehydrated NaY containing, on average, 1 HMB molecule/supercage adsorbed at 523 K.

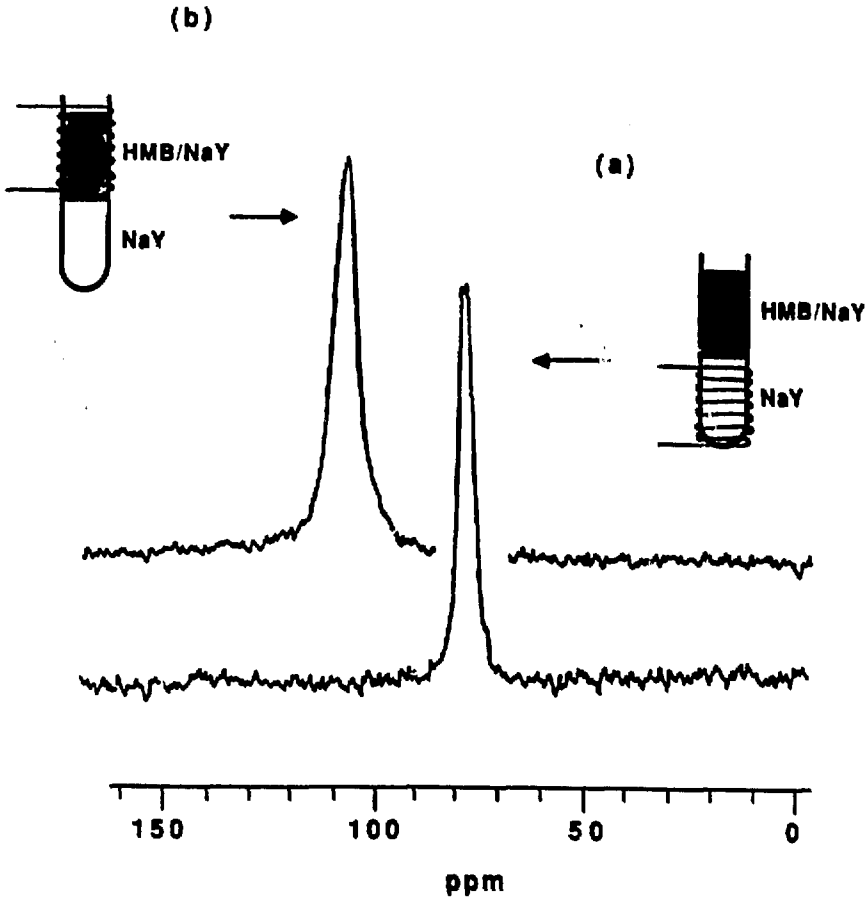

Figure 5.3: Room-temperature ^{129}Xe NMR spectra of xenon (300 torr equilibrium pressure) adsorbed on NaY zeolite containing a bulk loading of 0.5 HMB molecules per supercage. The HMB was adsorbed onto the zeolite by heating at 523 K for 2 h. (The adsorbate distribution remains unaffected by longer heating periods.) Different zones of the zeolite bed can be probed by varying the position of the receiver coil relative to sample: (a) δ_{xe} = 78 ppm near the bottom of the sample, while (b) δ_{xe} = 109 ppm in the uppermost region.

shown in Figure 5.3(a). From comparison with Figure 5.2(a), this corresponds to xenon adsorbed in NaY supercage cavities devoid of HMB guests. Conversely, placement of the receiver coil about the uppermost region of the sample volume results in a single ^{129}Xe peak at 109 ppm [Fig. 5.3(b)] corresponding to xenon adsorbed in supercages containing HMB guests. The identical ^{129}Xe chemical shift values observed in Figures 5.2(b) and 5.3(b) indicate the existence of a single HMB molecule per supercage in the upper region of the NaY zeolite bed.

This methodology can be extended to sample volumes containing different adsorbate loadings and/or different adsorbate guest species. Figure 5.4 depicts ^{129}Xe NMR spectra for different loadings of HMB introduced into the NaY matrix at 523 K and then redistributed at 573 K. In Figure 5.4(a), the two peaks at 109 and 78 ppm correspond to distinct adsorption zones with and without HMB guest species adsorbed in NaY supercage cavities. The chemical shifts of these peaks are identical with those in Figure 5.2 for NaY samples loaded with one and zero HMB molecules per NaY supercage, respectively. It is clear, therefore, that zeolite particles in the upper region of the sample volume contain one HMB molecule per supercage, whereas those in the lower region are devoid of adsorbed guests. The well-resolved peaks indicate close to a step-change in HMB concentration near the midpoint of the sample volume's longitudinal axis. The nearly equal peak areas reflect a nearly equal number of xenon adsorption sites in the two regions, as expected for an average bulk loading of 0.5 HMB/cavity. Upon reheating this sample to 573 K for 4 h, the discrete lines in Figure 5.4(a) collapse to the single peak in Figure 5.4(d) at 94 ppm. This is consistent with dispersal of HMB throughout the sample volume and indicates a macroscopically uniform guest distribution. In this situation, xenon atoms diffusing rapidly from one supercage to another encounter equal numbers of empty and

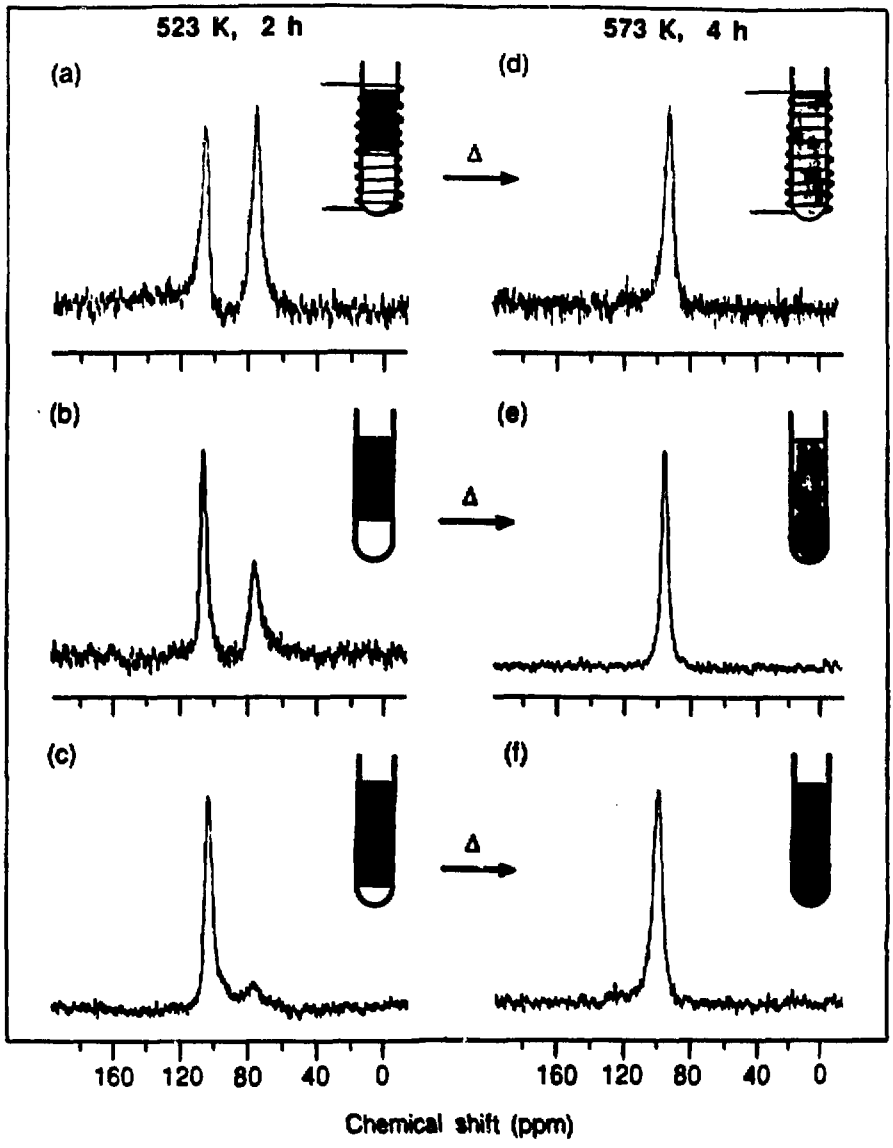

Figure 5.4: Xenon-129 NMR spectra of xenon (300 torr equilibrium pressure) adsorbed on NaY zeolite containing (a) 0.5, (b) 0.7, and (c) 0.9 HMB molecules per supercage. The samples in (a)–(c) were all initially heated at 523 K for 2 h. Spectra (d)–(f) were obtained after reheating the respective samples at 573 K for 4 h.

HMB-occupied cavities; hence, the 94-ppm chemical shift is the expected arithmetic average of ^{129}Xe shift values in the presence of only empty NaY cavities (78 ppm) or only cavities with one HMB guest (109 ppm).

Similar results are obtained for samples containing higher adsorbed guest loadings, as shown in Figures 5.4(b), 5.4(c), 5.4(e), and 5.4(f). As the overall adsorbate loading increases, the intensity of the line arising from xenon adsorbed in the presence of one HMB guest at 109 ppm increases relative to that from xenon adsorbed in empty NaY supercages at 78 ppm [Figs. 5.4(a-c)]. After a 2 h heat treatment at 523 K, a bulk loading of 0.7 HMB/NaY supercage yields ^{129}Xe peaks at 109 and 78 ppm [Fig. 5.4(b)] with relative areas of approximately 0.7 and 0.3, respectively. These data are consistent with one HMB/supercage in the upper 70% of the zeolite sample volume, with the remainder being devoid of adsorbed molecular species. Further heating of this sample for 4 h at 573 K disperses the organic guests throughout the macroscopic sample volume, yielding the single ^{129}Xe peak at 98 ppm in Figure 5.4(e). The peak location is again very close to the average of the ^{129}Xe resonance signals with and without HMB present, weighted by the respective bed fractions of the two zones.

Similarly, a bulk loading of 0.9 HMB/NaY supercage after thermal treatment at 523 K yields the ^{129}Xe spectrum shown in Figure 5.4(c) with peaks at 109 and 78 ppm. Again, the relative areas of the two peaks, approximately 0.9 and 0.1, reflect the proportions of the macroscopic sample volume with and without an HMB guest adsorbed in the NaY supercages. After thermal treatment at 573 K, the two peaks collapse in Figure 5.4(f) as before to a single peak at 102 ppm near the expected weighted-average location.

5.4.2 TMB and Benzene in NaY

Introduction of chemically similar 1,3,5-trimethylbenzene (TMB) and benzene into the NaY supercage network yields results which are consistent with the above discussion. Table 5.1 demonstrates that the melting and boiling points of TMB and benzene are significantly lower than those of HMB. Accordingly, less severe thermal treatments are necessary to effect transport and subsequent adsorption of the guest species within the sample volume. Elevated guest concentrations in the macropores between zeolite particles induce dispersal of the guest species through the bed at temperatures lower than those studied for HMB.

Figure 5.5 displays ^{129}Xe NMR spectra of NaY zeolite samples containing a bulk average of approximately 0.5 TMB molecule/supercage adsorbed under progressively more severe thermal conditions. After initial heat treatment at 323 K for 0.5 h, two distinct lines of roughly equal intensity are observed at 116 and 78 ppm in the ^{129}Xe spectrum of Figure 5.5(a). Again, the peak at 78 ppm is attributed to the ^{129}Xe chemical shift in empty NaY supercages, while that at 116 ppm is from ^{129}Xe in cavities containing one TMB guest. A loading of 0.5 TMB molecules per cavity produces peaks of roughly equal intensity because one-half of the NaY supercages are empty and the other half contain one molecule of TMB. This corresponds to an axial TMB concentration gradient in the zeolite bed analogous to that for the HMB/NaY system shown in Figure 5.4(a).

Further heating of this sample for 1 h at 413 K yields a broad ^{129}Xe peak at 105 ppm with a noticeable shoulder at about 78 ppm [Fig. 5.5(b)]. The broadness of the spectrum reflects an intermediate adsorbate distribution somewhere between the sharp macroscopic heterogeneity of Figure 5.5(a) and the homogeneous guest dispersion of Figure 5.5(c). At 413 K, desorption of TMB from supercage sites

Table 5.1: Some properties of benzene and related compounds.

		Kinetic Diameter, nm	Normal Melting Point, K	Normal Boiling Point, K
Benzene		0.58	279	353
1,3,5-Trimethylbenzene	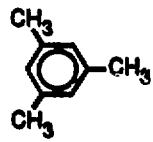	0.75	318	438
Hexamethylbenzene	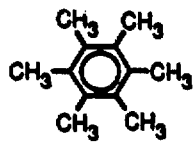	0.82	440	538

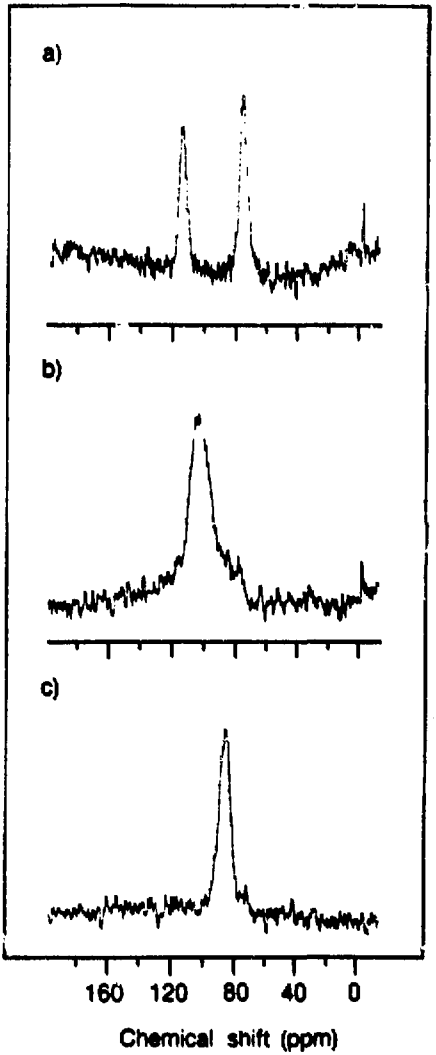

Figure 5.5: Xenon-129 NMR spectra of xenon (300 torr equilibrium pressure) adsorbed on dehydrated NaY zeolite containing 0.5 TMB molecules per supercage. (a) Sample heated at 323 K for 0.5 h. (b) Same sample heated again at 413 K for 1 h and (c) after further heating at 523 K for 2 h. The xenon gas peak at ≈ 0 ppm is seen in both (a) and (b).

in the upper portion of the zeolite bed allows the guest species to diffuse into the lower reaches of the sample volume. After additional heat treatment at 523 K for 2 h, Figure 5.5(c) reveals a single sharp line at 88 ppm which indicates complete dispersal of TMB throughout the macroscopic sample volume. These observations are consistent with the ^{129}Xe NMR data in Figure 5.4 for the HMB/NaY system.

From the arguments presented above, we expect a similar thermal treatment-dependence for benzene introduced into polycrystalline NaY zeolite. Figure 5.6(a) depicts the ^{129}Xe NMR spectrum for a NaY sample containing 0.5 benzene molecules per supercage chemisorbed at room temperature. A high concentration of benzene in the macropores between NaY crystallites results in substantial benzene transport to the lower reaches of the bed, even at room temperature [see Chapter 6 and Appendix F]. The non-zero signal intensity between peaks observed at 106 ppm and 78 ppm indicates that the macroscopic sample heterogeneity is not a sharp front as before. Instead, the data reflect an ensemble of particles that contain a gradually decreasing number of benzene molecules across a diffuse boundary between adsorption zones with and without organic guest species. The peak at 78 ppm is assigned unambiguously to xenon atoms in the empty NaY zeolite cavities, as in Figure 5.2(a). The remaining two peaks at 86 and 106 ppm arise from the xenon atoms in the NaY cavities containing one or more benzene molecules, respectively. After heating the sample at 423 K for 1 h the multiple peaks of Figure 5.6(a) collapse to a single resonance at 89 ppm [Fig. 5.6(b)]. Further heating at 473 K for 1 h, results in a slightly narrower line at 87 ppm [Fig. 5.6(c)]. Apart from the small difference in ^{129}Xe peak locations in Figures 5.6(b) and 5.6(c), the chemical shifts are near the weighted-average value expected from the spectrum in Figure 5.6(a). Above 473 K, dispersal of benzene guests throughout the sample volume is consistent with thermal

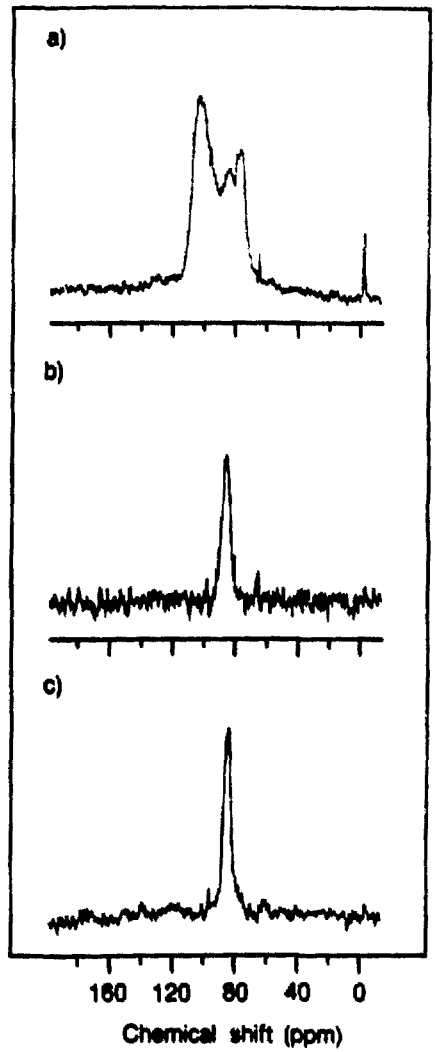

Figure 5.6: Xenon-129 NMR spectra of xenon (300 torr equilibrium pressure) adsorbed on NaY zeolite containing 0.5 benzene molecules per supercage. (a) Benzene adsorbed on dehydrated NaY at 298 K. The narrow peak at $\approx$ 0 ppm arises from gaseous xenon in the interstitial voids between zeolite particles. (b) The same sample heated at 423 K for 1 h and (c) after further heating at 473 K for 1 h.

desorption experiments of Fominykh *et al.* which document benzene desorption from NaX-zeolite at 468 K [117]. Subsequent sample heating at 533 K for 2 h yields a spectrum identical to Figure 5.6(c). Samples containing 1.5 benzene molecules per cavity behaved similarly.

5.4.3 Heterogeneity Length Scales by ^{129}Xe NMR

Because the length scale of the zeolite guest heterogeneity is important to the utility of the ^{129}Xe NMR technique, establishing the mobility of xenon probe atoms during the experiment is crucial to the distribution-heterogeneity measurement. For samples that possess fewer than one guest molecule per supercage, some cavities contain guest molecules while others do not. One might, therefore, expect to observe two or more ^{129}Xe NMR signals corresponding to cavities with or without adsorbed guest species. At 298 K and 300 torr, the mean free path of gaseous xenon is calculated from kinetic theory to be approximately 142 nm. Within the 1.25-nm diameter NaY supercages, therefore, the use of bulk transport properties ($D \approx 10^{-5}$ m^2/s [118]) overestimates the mobility of the xenon probe species.

The macroscopic guest distribution heterogeneities in Figures 5.4(a–c) produce two well-resolved peaks reflecting slow exchange of xenon between the two adsorption environments. The relevant time scale in these experiments is the reciprocal frequency separation of the ^{129}Xe peaks corresponding to xenon adsorption sites in NaY supercages with and without HMB [119,120]. In Figure 5.4(a), for example, ^{129}Xe resonances in the two environments are separated by 31 ppm (3400 Hz) for which an exchange time of 290 μs results. (Note that the digitizing time must be less than the exchange time to sample the data properly during acquisition.) We define the length scale of a particular distribution heterogeneity to be the mean dis-

tance between supercages with and without an adsorbed guest. In Figures 5.3 and 5.4(a–c), the distances separating supercages with and without HMB are large, so that jumps between these environments occur on a time scale which is slow with respect to 290 μs [52,53]. On the other hand, microscopic guest distribution heterogeneities resulting from heat treatment of HMB/NaY samples at 573 K produce a single peak, as shown in Figures 5.4(d–f). Rapid xenon exchange between adjacent supercages with and without HMB averages the contributions from the two environments. Jumps between the different sites occur significantly faster than 290 μs, since little broadening is observed.

The issue, then, centers on the magnitude of the heterogeneity length scales that can be probed in NaY zeolite by the ^{129}Xe NMR technique. To address the issue of xenon mobility in NaY, we consider two limiting cases corresponding to diffusion of a xenon probe atom within a single crystallite or among several crystallites during the NMR experiment. Figure 5.7 depicts anticipated ^{129}Xe NMR spectra for these two possibilities: first, in the presence of an axial HMB concentration gradient and, second, after thorough mixing of the particles to render the sample volume homogeneous in macroscopic terms. Irreversible adsorption of HMB at room temperature dictates that the adsorbed guest population of each crystallite is the same prior to and after physical mixing, only the relative particle positions within the bed are changed. Suppose that xenon atoms diffuse too slowly to probe more than an average supercage environment within a single micron-size zeolite particle. Such xenon atoms occupy only one crystallite on the time scale of the NMR experiment and, therefore, must be indifferent to the adsorbed guest loadings in adjacent particles. Consequently, as shown in Figure 5.7(a), physical mixing of a zeolite sample containing a macroscopically heterogeneous adsorbate distribution should not alter the

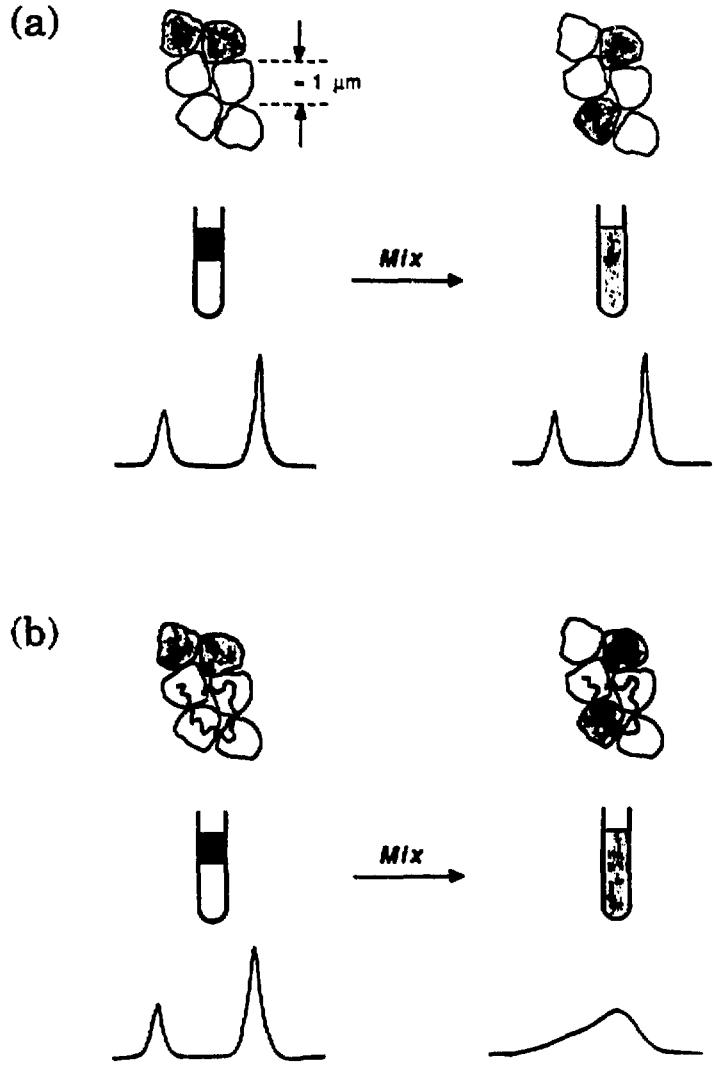

Figure 5.7: Schematic diagrams of ^{129}Xe NMR spectra expected for different xenon mobilities in NaY zeolite containing 0.3 guest molecules per supercage. A xenon atom diffuses (a) within a single crystallite or (b) among several adjacent crystallites on the time scale of the NMR experiment. Shading indicates that the particles are occupied by adsorbed guest species.

^{129}Xe NMR spectrum in any way.

Conversely, if xenon atoms diffuse rapidly enough to visit many particles on the time scale of the NMR experiment, a more macroscopic averaging of the resonance signal is expected. As illustrated in Figure 5.7(b), the ^{129}Xe NMR technique would be then capable of resolving adsorbate distribution heterogeneities with length scales no smaller than several crystallite diameters. The xenon atoms in such circumstances would be sensitive to the adsorbed guest loadings of adjacent crystallites whose placement in the bed is disturbed by the mixing process. As a consequence of physically mixing the bed, the ^{129}Xe NMR spectrum would thus collapse to the single peak shown in Figure 5.7(b). Rapid xenon exchange among many particles containing different HMB loadings would average the ^{129}Xe resonance from an ensemble of particles in close proximity to one another. This situation is similar to a thermally-mixed HMB/NaY system in that the respective distribution heterogeneities are unresolved as a result of high xenon mobility within the samples [Figs. 5.4(d–f)].

Xenon mobility in HMB/NaY can be experimentally established by the sample mixing procedure discussed above. Because the macroscopic HMB distribution heterogeneities arising from chemisorption of HMB in NaY at 523 K are large [Figs. 5.4(a–c)], exchange is slow between adsorption zones with and without HMB. Physically mixing the zeolite particles in such a sample alters the bed character by reducing the heterogeneity length s[illegible] to that of a single crystallite diameter. Xenon-129 NMR data shown in Figure 5.8, for NaY zeolite containing 0.3 HMB/supercage adsorbed at 523 K, reveal that thorough mixing of the NaY particles within the sample produces little change in the ^{129}Xe spectrum from that obtained in the presence of a macroscopic axial distribution of HMB. This clearly indicates that xenon exchange between crystallites is slow compared to the 290 μs exchange time between adsorp-

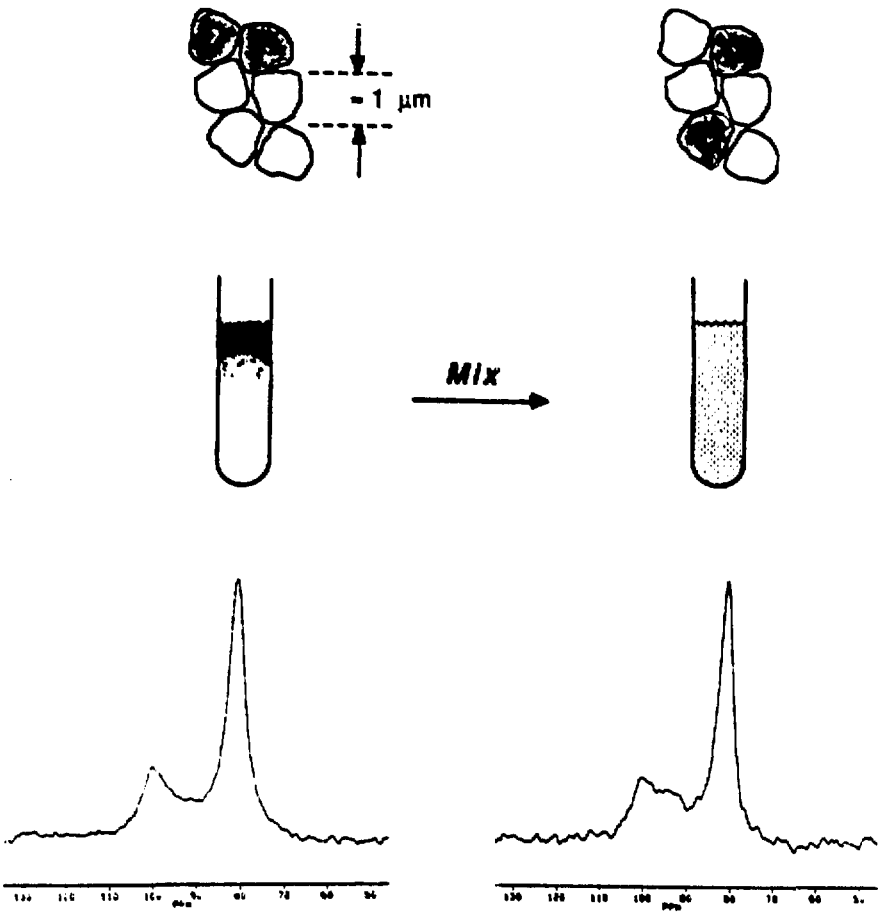

Figure 5.8: Room-temperature ^{129}Xe NMR spectra of xenon (300 torr equilibrium pressure) adsorbed on partially hydrated NaY zeolite containing a bulk loading of 0.3 HMB molecules per supercage adsorbed at 523 K for 2 h. Spectra were acquired before and after thorough physical mixing of the sample.

tion environments. Since Figures 5.4(d–f) reflect rapid xenon exchange among many adjacent supercages, we have bounded xenon mobility to occur within approximately one crystallite on the time scale of the NMR experiment. When either multiple or broad ^{129}Xe lines are observed, the length scales of the sample's heterogeneities must be, consequently, larger than one NaY crystallite diameter. The ^{129}Xe peaks in these regions are resolved or broadened due to slow exchange between the adsorption zones reflecting, thereby, the macroscopic nature of the heterogeneous guest distribution. It is clear that ^{129}Xe NMR is, thus, capable of resolving heterogeneous distributions of molecular species in NaY zeolite, providing the length scales of the heterogeneities are larger than approximately 1 μm.

With the characteristic length, l, and time, t, of the xenon exchange process known in NaY, a diffusivity calculation permits the mobility of the sorbed ^{129}Xe probe to be made more quantitative. Using Einstein's equation [121]

$$< l(t)^2 > = 6 D_{Xe} t$$

with t = 290 μs and $l(t)$ = 1 μm, we estimate the self-diffusivity of xenon in NaY zeolite, D_{Xe}, to be 6x10^{-10} m^2/s. This value is consistent with measurements by Kärger and Pfeifer for other diffusing gases in NaY using NMR pulsed field-gradient techniques [121]. It is two orders-of-magnitude smaller than the diffusivity predicted by the Knudsen correlation based on mean-free-path arguments alone [122].

For heterogeneities characterized by length scales significantly smaller than 1 μm, detailed information on intracrystalline guest distributions is, unfortunately, not readily obtained using ^{129}Xe NMR spectroscopy. The single peaks present in the ^{129}Xe spectra of Figures 5.4(d–f), for instance, are consistent with both of the intracrystalline distributions shown in Figure 5.9. The length scales of the adsorbate distribution heterogeneities in the two cases are both very small compared to indi-

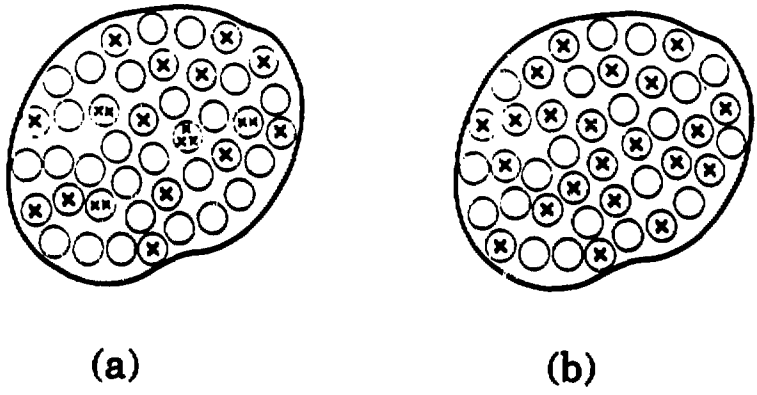

Figure 5.9: Schematic diagrams of possible guest molecule distributions within zeolite cavities when the average loading is less than one molecule per cavity. The open circles represent empty zeolite cavities and the guest molecules are indicated by the symbol X. (a) Statistical distribution of adsorbed guest molecules in zeolite supercage cavities. (b) Homogeneous dispersion in which each zeolite supercage contains at most one adsorbed guest molecule.

vidual NaY crystallite diameters. At room temperature, fast hopping of the xenon atoms among the cavities with and without guest molecules averages the ^{129}Xe chemical shift values of the two possible adsorption environments. To examine smaller adsorbate distribution length scales, we use multiple-quantum NMR to assess proton cluster sizes in the NaY cavities.

5.5 Intracrystalline Adsorbate Distributions

As discussed above, dispersal of adsorbed HMB guests throughout the sample volume results in much smaller heterogeneity length scales than can be distinguished by the highly mobile ^{129}Xe probe species at room temperature. Adsorption of 0.5 HMB molecules per NaY supercage at 573 K, for instance, results in a nominal heterogeneity length scale on the order of 1 nm, the distance between adjacent supercages in the NaY matrix. Also, at this temperature, the kinetic barrier to chemisorption of at least a second HMB molecule in each supercage is surmounted, so that clustering of guest species may occur [41]. By establishing the number of adsorbed organic molecules residing in NaY supercages, multiple-quantum NMR probes guest distribution heterogeneities on a molecular scale.

5.5.1 Multiple-Quantum NMR Studies of Spin Clustering

The multiple-quantum 'counting' experiment is sensitive to the average size of homonuclear dipole-dipole coupled spin networks in a given sample [113,114]. The two intracrystalline guest distributions of Figure 5.9 are distinguished by the degree to which the adsorbed guest species are clustered in NaY supercages. In Figure 5.9(a), the adsorbate is statistically dispersed, with some cavities containing two or perhaps three molecules, though the bulk average remains 0.5 guest/supercage.

This is in contrast to the homogeneous guest dispersion shown in Figure 5.9(b), where, for an identical 0.5 guest/supercage bulk loading, only one adsorbed molecule is present in each occupied supercage. Implementing the multiple-quantum experiment requires sufficient isolation of a spin system such that intercluster interactions are much weaker than intracluster couplings. This is true for certain adsorbed organic molecules in NaY supercages, where the size of the proton spin system isolated within a given cavity depends on the number of organic guests clustered therein. Each HMB molecule, for example, contributes 18 hydrogen atoms to the spin system within a particular supercage. These proton spins are in close proximity to other HMB molecules adsorbed within the same supercage, permitting the protons to become dipole coupled to one another after a sufficiently long period of excitation.

Multiple-quantum NMR determines the number of homonuclear dipole-dipole coupled spins in a finite cluster by measuring the response of the coupled spins to radiofrequency (rf) excitation as a function of the excitation time [41]. In this study, the clustering of HMB within NaY supercages has been examined as a function of adsorbate concentration. HMB loadings of 5.1 wt%, 10.2 wt%, and 20.4 wt% were used, corresponding to bulk averages of approximately one-half, one, and two HMB molecules/NaY supercage, respectively. As shown for 20.4 wt% HMB/NaY in Figures 5.10(a–c), higher order multiple-quantum intensities increase with lengthening rf excitation times as more spins coherently interact through their dipolar couplings. Weaker dipolar couplings become effective at longer excitation times, until ultimately all of the spins within a cluster are interacting with one another. In a zeolite, a natural limit exists on the size of a dipolar-coupled spin system due to physical isolation of the adsorbate molecules in different cavities. As the excitation time is increased under such circumstances, n-quantum peak intensities approach constant values with

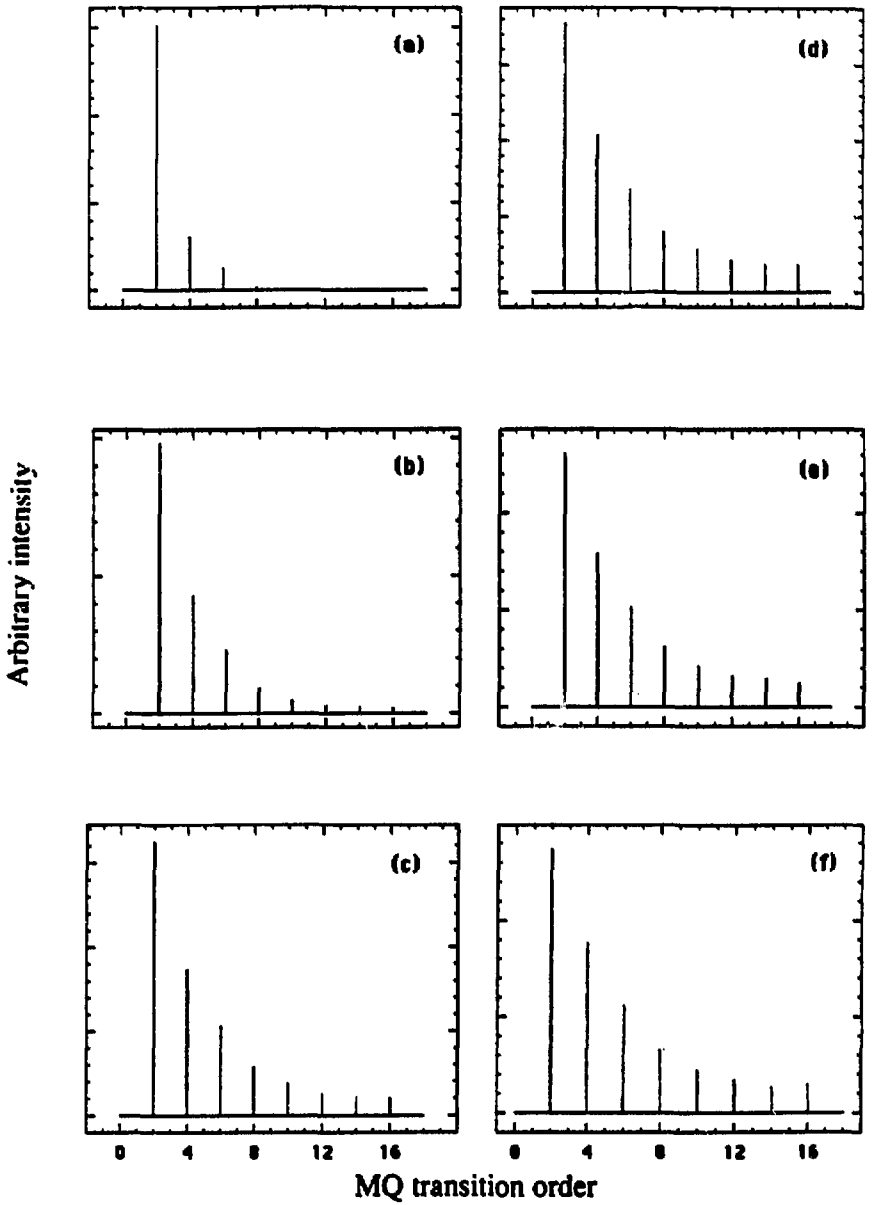

Figure 5.10: Proton multiple-quantum NMR spectra of 20.4 wt% HMB adsorbed on NaY zeolite at 573 K. The spectra were acquired at different radiofrequency excitation times: (a) 132 μs, (b) 264 μs, (c) 396 μs, (d) 528 μs, (e) 660 μs, and (f) 792 μs.

respect to the total signal intensity [Figs. 5.10(d–f)], reflecting the limited spin network size of the isolated guest species.

5.5.2 Multiple-Quantum Data Analysis

The number of adsorbed guest molecules within the NaY cavities can be determined by measuring the size of a spin system using multiple-quantum NMR. For a given excitation time, the resulting MQ spectrum [e.g., Fig. 5.10], can be fit in the statistical limit to a Gaussian curve with a standard deviation of $\sqrt{N/2}$, where N is the spin network size [115]. We observe for protons on adsorbed molecules that the two-quantum signal decays more slowly than the intensities of higher order transitions. The two-quantum peak in the multiple-quantum spectra of adsorbed HMB is consequently more intense than that predicted by the Gaussian model derived from statistical arguments [115]. Inclusion of the two-quantum transition yields a poor fit to the data and may result in erroneous measurements of the spin network size N. All necessary clustering information is retained, however, in the higher order data, providing a sufficient number of points remain to yield a meaningful curve fit.

Neglecting the two-quantum transition, Figure 5.11(a) displays the Gaussian fit to the multiple-quantum results for 20.4 wt% HMB in NaY. The discrepancy between curve 5.11(a) and the data is still appreciable, because finite MQ peak intensities exist for higher-order transitions. This solid-lattice-like behavior can probably be attributed to a small amount of residual, unadsorbed solid HMB located in the pore spaces between the micron-sized crystallites. The bulk-like material contains an essentially infinite lattice of dipole-dipole coupled protons, yielding MQ spectra whose peak intensities are best fit by a Gaussian function much broader than that associated with HMB molecules isolated in NaY supercages. Since the contribution

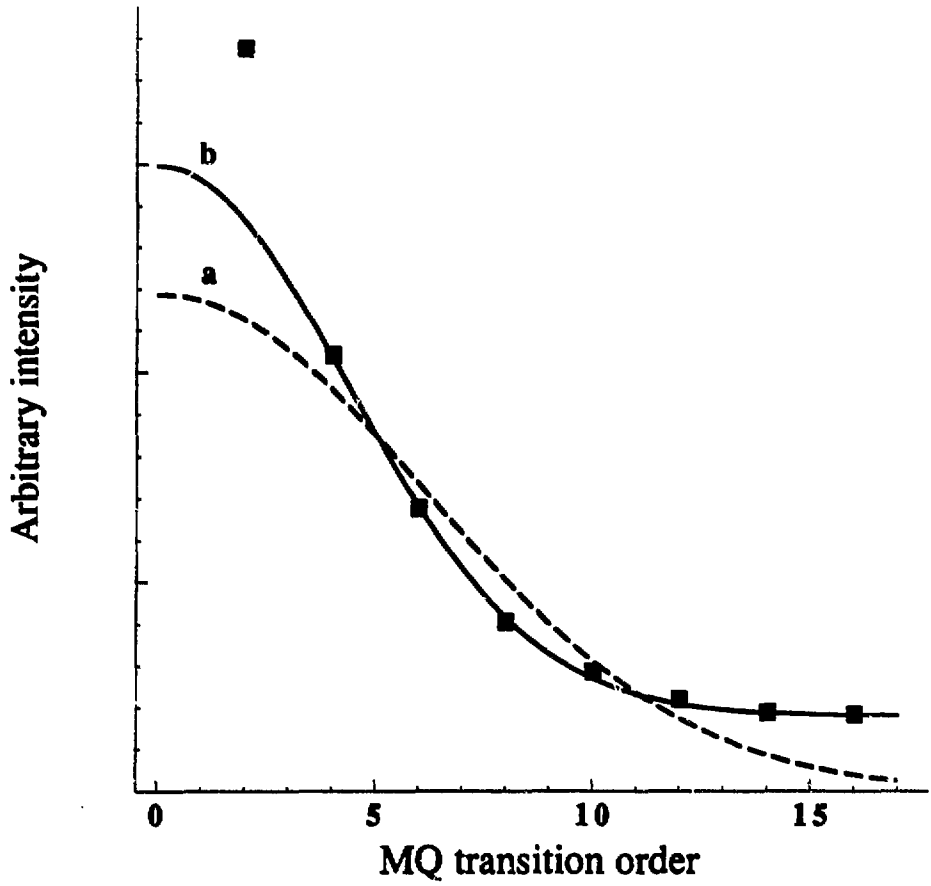

Figure 5.11: Gaussian fits to the proton multiple-quantum NMR data of Figure 5.10(d) for 20.4 wt% HMB adsorbed on NaY at 573 K. Each point represents the measured n-quantum peak intensity associated with a particular n-quantum transition. The data were acquired with a radiofrequency excitation time of 528 μs.

from solid HMB masks clustering information on HMB adsorbed within the NaY cavities, it is desirable to discount its influence. A baseline correction effectively eliminates the contribution of bulk HMB to the multiple-quantum signal by recalibrating the intensity scale to zero at the highest transition orders. Curve 5.11(b) is a baseline-corrected Gaussian fit that demonstrates good agreement with the data.

If the resulting spin network size N is plotted as a function of radiofrequency excitation time, cluster sizes for various macroscopically uniform adsorbate loadings can be determined. For NaY samples containing 5.1 wt% and 10.2 wt% HMB, the Gaussian-fit values for N in Figure 5.12 approach maximum spin network sizes N_{max} of about 23 and 24 spins, respectively. The nearly overlapping MQ data for these samples suggest similar spin clustering behavior and, thus, similar local distribution of adsorbed HMB guest species. Values of $N_{max} \approx 23$ or 24 compare favorably with the number of protons on a single molecule of HMB (18 hydrogen atoms) and correspond to a local distribution of about one HMB molecule per supercage cavity. It appears that some cavities may possess two adsorbed guests, as reflected by the somewhat elevated proton count measured by the multiple-quantum experiment. Nonetheless, if a statistical distribution of guests existed within the NaY cavities, many spin systems of 36 and 54 protons might be present, corresponding to two and three HMB molecules/NaY supercage, respectively. In this situation, a much broader Gaussian function would be required to fit the distribution of MQ peak intensities. Significantly higher limiting cluster sizes would result for 5.1 wt% and 10.2 wt% HMB loadings, contrary to experimental data on the 0.5 and 1.0 HMB/supercage bulk loaded samples. At HMB loadings above 10.2 wt%, more supercages accept a second adsorbed guest molecule. For 20.4 wt% HMB/NaY, the limiting cluster size is measured to be $N_{max} \approx 38$, consistent with an occupancy of two HMB

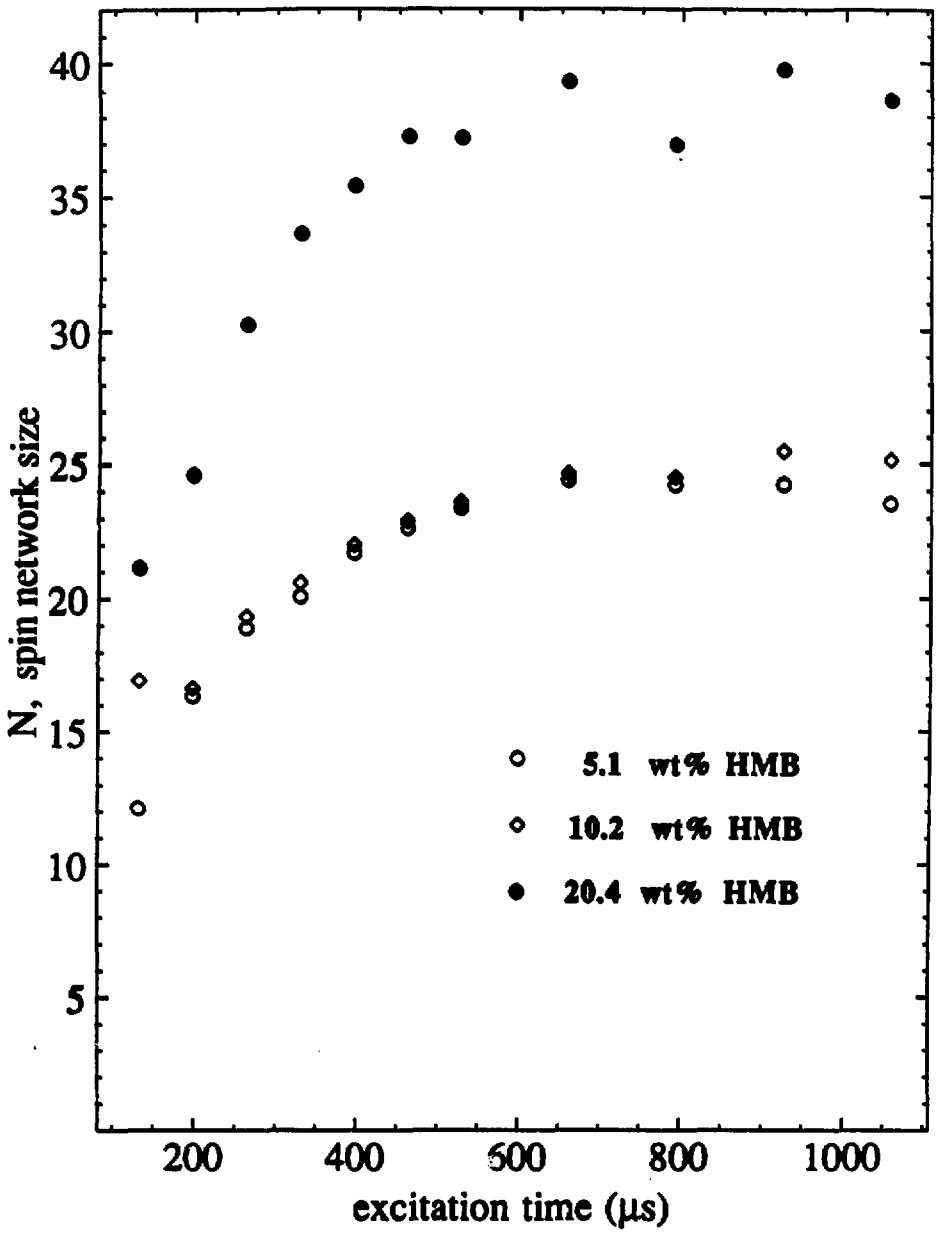

Figure 5.12: Results of proton multiple-quantum NMR experiments for HMB adsorbed on NaY zeolite at 573 K.

guests/supercage. Despite apparent pairing of some adsorbed guests at loadings of 5.1 wt% and 10.2 wt% HMB, the MQ data of Figure 5.12 show the HMB guests to be dispersed in an essentially homogeneous manner throughout the NaY matrix, as depicted in Figure 5.9(b).

5.6 Conclusions

From our ^{129}Xe NMR investigation, it is clear that extensive thermal treatment is required to disperse guest molecules adsorbed in the supercage cavities throughout a macroscopic sample volume. Although the present study does not define a precise temperature or duration of thermal treatment required, certain criteria emerge. These criteria are related to the physical properties of the guest molecule, such as molecular weight, vapor pressure, kinetic diameter, diffusivity, and to the nature of the guest molecules' interactions with the NaY matrix. At higher temperatures, elevated vapor-phase concentrations of the adsorbing species in the macropores permit guest molecules to diffuse farther into the zeolite bed. Room-temperature ^{129}Xe NMR is a convenient means of studying heterogeneous distributions of HMB in NaY, providing the heterogeneity length scales are larger than about 1 μm. Such situations may lend themselves to NMR chemical shift imaging methods in which a linear magnetic field gradient might be used to image xenon profiles in samples possessing macroscopic adsorbate heterogeneities.

The suitability of multiple-quantum NMR spectroscopy for probing adsorbate distributions in catalysis is due primarily to the technique's relative immunity to obstacles posed by the heterogeneous nature of the HMB/NaY system. Counting the number of proton spins in clusters of chemisorbed organic species yields information on their spatial distributions and, thus, about microstructural features of the

adsorption sites themselves. Because of the central importance of these sites to the reaction process, multiple-quantum NMR represents a potentially valuable means by which a catalyst's microscopic adsorbate structure can be correlated with its chemical reaction properties. Such information, used in conjunction with the macroscopic adsorbate distributions measured by ^{129}Xe NMR spectroscopy, is key to characterizing intracrystalline mass transport and adsorption of reactant species within zeolitic catalysts.

Chapter 6

Transport of Aromatic Molecules in NaY Zeolite Powders

6.1 Abstract

Xenon-129 NMR is used to probe macroscopic distributions of aromatic molecules adsorbed in a packed bed of 1 μm NaY zeolite particles. Relative rates of guest transport through pores of different size play a unique role in the axial distribution of aromatic molecules, such as hexamethylbenzene (HMB), in a zeolite powder. Xenon-129 NMR spectra show that a sharp HMB adsorption front advances through a bed of dehydrated NaY crystallites at 523 K, whereas at 573 K or in the presence of co-adsorbed water, HMB species disperse through the bed without forming a sharp boundary between adsorption zones. Using a shrinking-core model to describe axial penetration of the bed by vapor-phase guest species, we establish the criteria necessary for formation of a sharp adsorption front, namely that guest transport must be controlled by diffusion in the macropores and that a pseudo steady-state condition must apply to the front's advance within the bed. This permits the adsorption

process to be modeled quantitatively, yielding estimates for the intracrystalline diffusivities of HMB in dehydrated and partially hydrated NaY zeolite of 10^{-13} m^2/s and 10^{-15} m^2/s, respectively, at 523 K. Xenon-129 NMR is a powerful tool for probing adsorbed guest distribution in zeolites, allowing relative time scales to be established for transport of molecular guests in NaY powders.

6.2 Introduction

Transport and adsorption properties of reactant species in small pores are important to the performance of heterogeneous catalysts. The mobility of molecular guests establishes reactant accessibility to active sites within the porous matrix and, in so doing, affects species distribution within the catalyst particles. Distributions of adsorbed guest molecules in zeolite cavities are known, for instance, to be dependent on catalyst treatment conditions [98,116,123,124]. Recently, we have studied the distributions of organic adsorbates, namely benzene, 1,3,5-trimethylbenzene (TMB), and hexamethylbenzene (HMB) in NaY zeolite by ^{129}Xe and multiple-quantum nuclear magnetic resonance spectroscopy (NMR) [41,111,125]. In this chapter, we model quantitatively the distribution of hexamethylbenzene (HMB) in NaY zeolite to establish the transport mechanisms responsible for the macroscopic adsorbate concentration profiles observed.

6.3 Adsorbate Distributions by ^{129}Xe NMR

As a sensitive, non-reactive probe of supercage cavities within the crystalline zeolite matrix, room-temperature ^{129}Xe NMR spectroscopy provides information on interparticle adsorbate heterogeneities in NaY powders. By monitoring the chemi-

cal shift of physisorbed ^{129}Xe, distinct regions containing different concentrations of adsorbed guests can be identified within NaY zeolite samples. Using sample preparation methods and NMR procedures described elsewhere [125], ^{129}Xe NMR data in Figure 6.1(a) indicate a sharp, axial HMB adsorption front in a packed bed of micron-size NaY crystallites. In this experiment a limited amount of liquid HMB (0.5 HMB molecules per supercage) was brought into contact with the zeolite powder and held at 523 K for 2 h. The two NMR peaks at 109 ppm and 78 ppm in Figure 6.1(a) correspond to ^{129}Xe physisorbed at ambient temperatures in adsorption zones with and without HMB guest species. Xenon exchange is slow between macroscopic zones containing different HMB loadings within the NaY zeolite supercages. The time scale of the exchange process is on the order of 10^{-4} s, so that the ^{129}Xe probe species averages the adsorbate loading within approximately one NaY crystallite (1 μm diameter) at room temperature [125] [see Chapter 5]. The well-resolved peaks, therefore, indicate essentially a step-change in HMB concentration near the midpoint of the sample volume's longitudinal axis, with the nearly equal peak areas reflecting nearly equal numbers of xenon adsorption sites in the two regions. This is consistent with an average bulk loading of 0.5 HMB/cavity distributed so that the upper 50% of the bed contains one HMB molecule in nearly every supercage, while the lower 50% is devoid of adsorbed guests.

In contrast, no sharp adsorption front exists for HMB adsorbed at higher temperatures or for HMB in a bed of partially hydrated NaY zeolite. Thus, after reheating the dehydrated HMB/NaY sample of Figure 6.1(a) to 573 K for 4 h, the two discrete peaks collapse to a single line at 94 ppm in Figure 6.1(b). This is consistent with dispersal of HMB throughout the sample volume and indicates a macroscopically uniform guest distribution [125]. The presence of co-adsorbed water provides a dis-

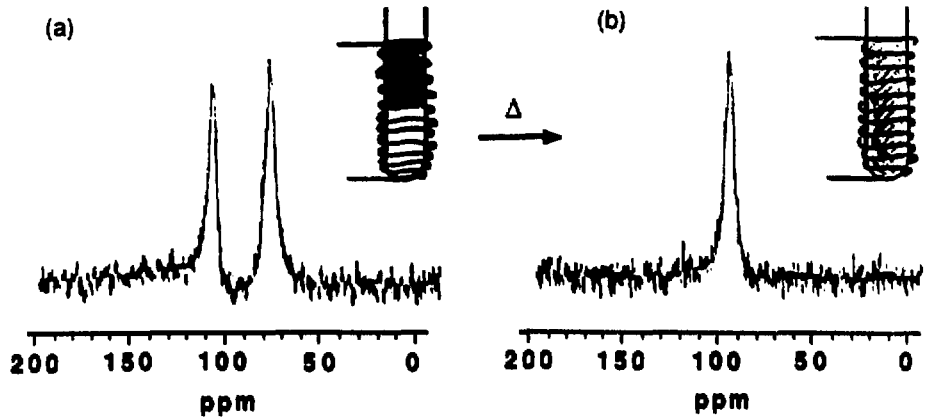

Figure 6.1: Room-temperature ^{129}Xe NMR spectra of xenon (300 torr equilibrium pressure) adsorbed on dehydrated NaY zeolite containing a bulk average of 0.5 HMB molecules per supercage. (a) After heating the zeolite sample at 523 K for 2 h, two well-resolved peaks are observed corresponding to macroscopically distinct adsorption regions within the bed. The peak at 109 ppm arises from ^{129}Xe in supercage environments containing one adsorbed HMB guest molecule. The peak at 78 ppm is due to ^{129}Xe in empty NaY supercages. (b) After reheating the sample at 573 K for 4 h, the two peaks coalesce to a single peak at 94 ppm reflecting complete dispersal of the HMB guests throughout the macroscopic sample volume. Schematic diagrams of NaY zeolite samples in 10 mm NMR tubes accompany the spectra. The receiver coil is shown to indicate the approximate sample volume probed by the NMR experiment. Shading reflects the concentration of adsorbed HMB guests in supercage environments.

persive influence in the HMB distribution as well. The nonzero ^{129}Xe signal intensity between peaks at 78 and 90 ppm in Figure 6.2 reflects a macroscopic distribution of NaY particles containing a range of different HMB loadings (0–1 HMB/supercage) near the boundary between distinct adsorption zones. Our objective is to elucidate the transport mechanism(s) responsible for the adsorbate distributions observed.

6.4 Modeling Adsorbate Transport in NaY

6.4.1 Sharp Adsorption Fronts

Modeling guest transport effects in porous solids is crucial to understanding guest/lattice interactions which influence the distribution of organic adsorbates in zeolites. Ruckenstein *et al.* have modeled the sorption behavior of solids with bidisperse pore structures, somewhat similar to the packed bed of NaY crystallites considered here, and established the criteria necessary for identifying rate-limiting features of guest transport in these systems [126]. The distribution of adsorbed guest species in a zeolite packed bed depends on the adsorption properties of the system, together with the relative transport rates of the guest species in the interstitial void spaces between the micron-size crystallites (NaY macropores) and in the supercages and windows within individual zeolite crystallites (NaY micropores.) Xenon-129 NMR provides a particularly useful means of probing adsorbed guest distributions in zeolites from which it is possible to estimate the relative time scales associated with adsorbed guest transport in bidispersed NaY pore systems.

At 523 K, the sharp HMB adsorption front observed in Figure 6.1(a) might arise from liquid- and/or vapor-phase transport of HMB in the macropores, but this issue is easily resolved. Calculation and experimental observation of imbibition rates of liquid

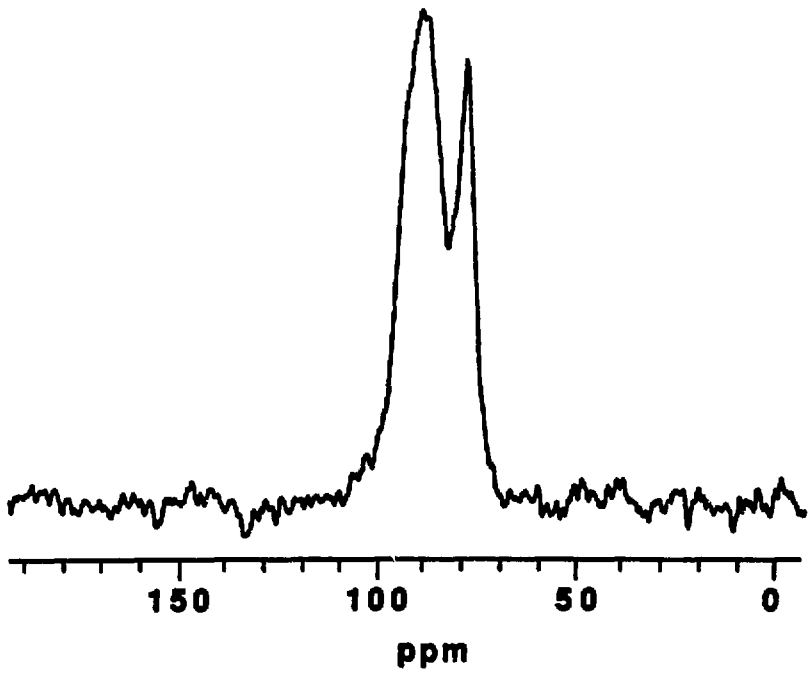

Figure 6.2: Room-temperature ^{129}Xe NMR spectrum of xenon (300 torr equilibrium pressure) adsorbed on partially hydrated NaY zeolite containing a bulk average of 0.5 HMB molecules per supercage. The sample was dehydrated at 723 K for 5 h and then rehydrated uniformly to ≈ 25% of maximum NaY water content. HMB was added to the top of [illegible]ed and the system heated at 523 K for 2 h. The peak corresponding to the adsorption zone with HMB is shifted to 90 ppm, 19 ppm upfield from its 109 ppm location in dehydrated NaY. The presence of co-adsorbed water leads to a more shielded adsorption environment for ^{129}Xe probe species in the NaY supercages containing HMB guest species.

benzene axially into the zeolite powder reveal rapid capillary flow [see Appendix F.1]. However, the limited quantities of bulk organic adsorbate used in our experiments are so small that less than 7% of the NaY packed bed comes in contact with liquid-phase adsorbate during the chemisorption process [see Appendix F.1]. Accordingly, intercrystalline mass transport occurs predominantly by diffusion of vapor-phase HMB molecules through the interstitial macropores separating the NaY crystallites. Vapor-phase diffusion of HMB is confirmed experimentally by ^{129}Xe NMR data from HMB/NaY samples prepared at 473 K in the absence of direct contact between the zeolite bed and liquid adsorbate. As shown in Figure F.4 in Appendix F, a sharp adsorption front is produced in a packed bed of dehydrated NaY crystallites by uptake of vapor-phase HMB from the macropores.

The criteria for forming sharp boundaries between adsorption zones in NaY powders are established by a shrinking-core model applied to the bed as a whole. Three characteristic times exist for guest distribution in a packed bed:

t_{micro}, the time required for guest diffusion within a single NaY crystallite;

t_{macro}, the time required for guest diffusion in the bed's macropores;

and t_f, the time required for advance of the adsorption front through the bed.

As discussed in detail below, both a pseudo steady-state condition and macropore-controlled diffusion must exist such that

$$t_f >> t_{macro} >> t_{micro} . \tag{6.1}$$

These criteria are necessary and sufficient conditions for the formation of a sharp adsorption front by adsorbed guest species in a packed bed of NaY zeolite crystallites.

To explain the sharp boundary between adsorption zones indicated by Figures 6.1(a) and F.4, we postulate that HMB molecules adsorb strongly from the vapor

state onto the exterior surfaces of the NaY crystallites and migrate rapidly into interior cavities. In our nomenclature, strong adsorption refers to a high adsorption capacity by the zeolite support. Mobility of adsorbed molecules through the nominal 0.8 nm windows from one supercage to another is permitted and, furthermore, is necessary to explain the absence of pore-mouth blocking effects which would otherwise be severe for the large 0.82-nm diameter HMB molecules. Moreover, at temperatures near 523 K, migration of strongly adsorbed organic guests within a crystallite must occur much faster than the rate at which the molecules diffuse in the gas phase through interparticle macropores to nascent crystallites. Transport of HMB in the intracrystalline micropores will be fast compared to that in the macropores when $t_{macro} \gg t_{micro}$ [126], or equivalently

$$\frac{x_f^2}{D_{macro}} >> \frac{d_p^2}{D_{micro}}. \tag{6.2}$$

where d_p is the mean diameter of a NaY crystallite, x_f is the length of the adsorbate contact zone in the NaY packed bed, D_{micro} is the intracrystalline diffusivity of HMB within the micropores of a single crystallite, and D_{macro} is the intercrystalline diffusivity of HMB through the macropores between NaY crystallites. For the conditions of this experiment, $d_p = 1$ μm, $x_f = 1$ cm, $D_{macro} \approx 10^{-5}$ m^2/s [see Appendix F.2], allowing a lower bound on the intracrystalline diffusivity of the guest to be established. According to Ruckenstein *et al.* diffusion-limited transport in the macropores occurs when

$$\frac{x_f^2}{D_{macro}} > 100 \frac{d_p^2}{D_{micro}}, \tag{6.3}$$

yielding $D_{micro} > 10^{-13}$ m^2/s for HMB in dehydrated NaY at 523 K. This result is comparable to diffusivity data recently published for benzene in NaY [186].

Particles held at 523 K for 2 h apparently sustain a kinetic barrier to adsorption of more than one HMB molecule per cavity [see Appendix F.2]. As a result, HMB

molecules preferentially adsorb onto unsaturated particles possessing a bulk loading of less than one HMB/supercage. After all supercages in a given 1-μm particle have been loaded with a single HMB guest, subsequent vapor-phase HMB molecules diffuse past this saturated crystallite to the next unsaturated particle where they adsorb strongly and migrate rapidly into the crystallite's interior. Ultimately, the liquid HMB reservoir at the top of the bed is exhausted as all of the bulk organic material evaporates, diffuses, and chemisorbs as a mass-limited shock wave represented schematically in Figure 6.3(a). A linear vapor-phase HMB gradient exists within the intercrystalline macropores of the HMB-saturated zone [Fig. 6.3(b)] because of a pseudo steady-state condition which arises when $t_f \gg t_{macro}$ [127]. In this situation, the HMB concentration in the micropores of individual, dehydrated NaY crystallites may be considered to be essentially uniform throughout the micron-size particles. A material balance based on such a pseudo steady-state, shrinking-core treatment [127] yields

$$\frac{\phi D_{macro} C_o}{x_f} = \alpha \frac{dx_f}{dt}, \tag{6.4}$$

where x_f is the distance traveled by the guest adsorption front along the bed axis, ϕ is the void fraction of the bed's macropores, C_o is the vapor-phase concentration of HMB in equilibrium with the liquid reservoir at the top of the bed, and α is the adsorption capacity of the intracrystalline cavities expressed as moles of adsorbate per total bed volume. The adsorption capacity α of the micropores (i.e. the NaY supercages) for aromatic guests is substantially greater than the capacity of the exterior crystallite surfaces, based on surface-area scaling arguments discussed in Appendix F.3. We have assumed that α is constant for this treatment, consistent with the highly nonlinear adsorption isotherms for compounds such as benzene, n-heptane, and 1,3,5-triethylbenzene on faujasite-type zeolites [1,128,129] [see Appendix F.4].

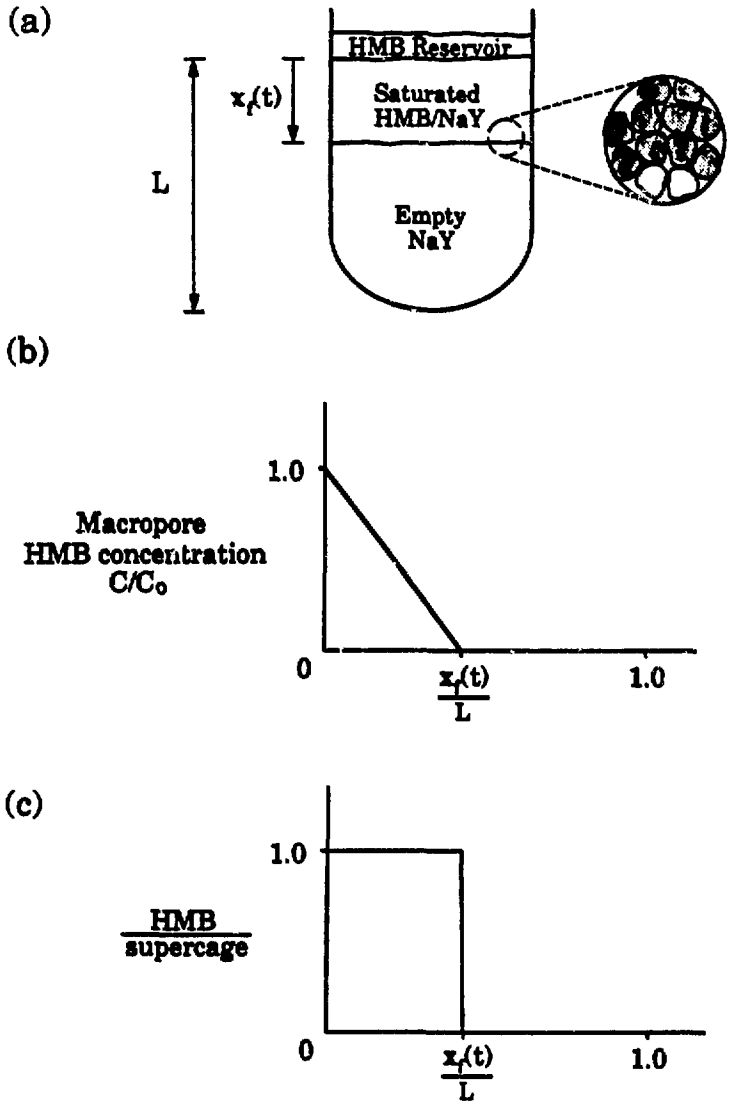

Figure 6.3: (a) Diagram of an axial HMB concentration profile arising from adsorption at 523 K in a packed bed of dehydrated NaY zeolite. The inset depicts the sharp boundary separating zones with and without adsorbed HMB. (b) Macropore HMB concentration plotted as a function of dimensionless distance from the top of the NaY bed. (c) Intracrystalline HMB loading in dehydrated NaY micropores plotted as a function of dimensionless distance from the top of the bed.

Equation 6.4 can be integrated to predict the time-dependent advance of an adsorption front through the zeolite bed:

$$t_f = \frac{x_f^2 \alpha}{2\phi C_o D_{macro}} . \tag{6.5}$$

The pseudo steady-state criterion, $t_f \gg t_{macro}$, can subsequently be expressed as

$$\frac{\alpha}{\phi C_o} >> 1 , \tag{6.6}$$

or more specifically [127,130,131,132,133]

$$\frac{\alpha}{\phi C_o} > 10^3 . \tag{6.7}$$

For dehydrated NaY zeolite containing a bulk loading of 0.5 HMB/supercage chemisorbed at 523 K, the adsorption front in NaY penetrates axially to the midpoint of the bed [Fig. 6.3(c)], thus accounting for the two well-resolved ^{129}Xe peaks in Figure 6.1(a). For $x_f = 1$ cm of contacted bed length, $\alpha = 4.4\text{x}10^{-4}$ $\frac{\text{mol HMB}}{\text{cm}^3 \text{ bed}}$ [see Appendix F.3], $\phi \approx 0.5$ $\frac{\text{cm}^3 \text{ NaY}}{\text{cm}^3 \text{ bed}}$, $C_o = 2.3\text{x}10^{-6}$ $\frac{\text{mol}}{\text{cm}^3}$ [see Appendix F.2], and $D_{macro} = 1.9\text{x}10^{-5}$ $\frac{\text{m}^2}{\text{s}}$ [see Appendix F.2], we calculate $\alpha(\phi C_o)^{-1} \approx 770$ and $t_f = 15$ min. These results are supported by separate experimental measurements on HMB/NaY samples held 5–10 minutes at 523 K, which indicate axial transport times of approximately 10 min.

The mass-limited nature of the adsorption front's progression is confirmed by Figures 5.4(a–c) in Chapter 5. As the overall guest loading is increased from 0.5 to 0.9 HMB molecules per supercage at 523 K, the larger adsorbate reservoir supplies the additional mass of HMB necessary for deeper axial penetration of the front into the bed. The fractions of the zeolite beds saturated with one HMB guest molecule per supercage, determined from the integrated peak areas of the ^{129}Xe spectra in Figures 5.4(a–c), once again agree with the overall bulk guest loadings of

the respective samples. These observations hold true as well for adsorption of 1,3,5-trimethylbenzene (TMB) in NaY at 323 K, which also establishes a sharp adsorption front for a loading of 0.5 TMB/supercage, as shown in Figure 5.5(a). While the axial HMB gradients correspond to systems far from thermodynamic equilibrium, such guest distributions are observed to be kinetically stable at room temperature over a period of many months. In general, the existence of a sharp adsorption boundary in a packed zeolite bed is anticipated when adsorption capacities are high for guest species possessing low vapor pressures and high intracrystalline mobilities in very small particles.

6.4.2 Effect of Co-adsorbed Guests

The rate of intracrystalline HMB transport in the NaY micropores is dramatically reduced in the presence of even a small amount of previously adsorbed species such as water [121]. By creating more crowded supercage environments, sorbed water obstructs migration of HMB guests within the NaY micropores. In this situation, the additional transport resistance can invalidate the condition of rapid intracrystalline transport, so that adsorbed HMB molecules migrate more slowly from the exterior crystallite surface to empty supercages in the particle interior. Intracrystalline transport of HMB in the micropores may, thus, proceed at a rate which is comparable to intercrystalline vapor-phase diffusion of HMB to the exterior surfaces of the NaY particles. Consequently, $t_{macro} \approx t_{micro}$, or

$$\frac{x_f^2}{D_{macro}} \approx \frac{d_p^2}{D_{micro}}, \tag{6.8}$$

so that a shrinking-core treatment is no longer a valid model. As before [Eq. 6.3], D_{micro} is now estimated to be no larger than 10^{-15} m^2/s for HMB in 25% rehydrated NaY (5 H_2O/supercage [116]). Thus, the diffusivity of HMB in NaY decreases by at

least two orders of magnitude in the presence of co-adsorbed water. This is consistent with diffusivity data of Kärger and Pfeifer for low molecular weight hydrocarbons in partially hydrated NaY zeolite [121] [see Appendix F.2].

As in the case of the dehydrated HMB/NaY system discussed above, vapor-phase HMB molecules diffuse through the bed macropores until the HMB species adsorb on an unsaturated crystallite surface. The reduced intracrystalline mobility of HMB in partially hydrated NaY, however, results in substantially slower HMB migration into the zeolite particle interiors. A saturated surface region likely exists on the periphery of the NaY crystallites which retain center cores devoid of adsorbed HMB guests. In this situation, vapor-phase HMB molecules in the macropores perceive a saturated surface region in many partially hydrated crystallites that lack fully saturated interiors. The vapor-phase species diffuse through the macropores between NaY particles until contact is finally made with an unsaturated NaY crystallite *surface*. Under such conditions, crystallites near the boundary between fully saturated and fully unsaturated regions of the bed possess a distribution of HMB loadings, as depicted schematically in Figure 6.4. Intracrystalline adsorbate distributions in particles near the boundary likely evidence intraparticle shrinking-core behavior [127,134,135]. The room-temperature ^{129}Xe NMR technique, however, averages adsorbate distribution information within approximately one NaY crystallite [see Chapter 5], so that *intra*crystalline adsorbate concentration profiles are not accessible in this study. Nonetheless, the ^{129}Xe NMR data of Figure 6.2 confirm that no sharp *macroscopic* adsorption front exists within the NaY packed bed. Such a macroscopic distribution of particles containing different HMB loadings is consistent with hindered intracrystalline transport of the HMB guests due to the presence of co-adsorbed water. The shrinking-core model becomes an invalid description of the

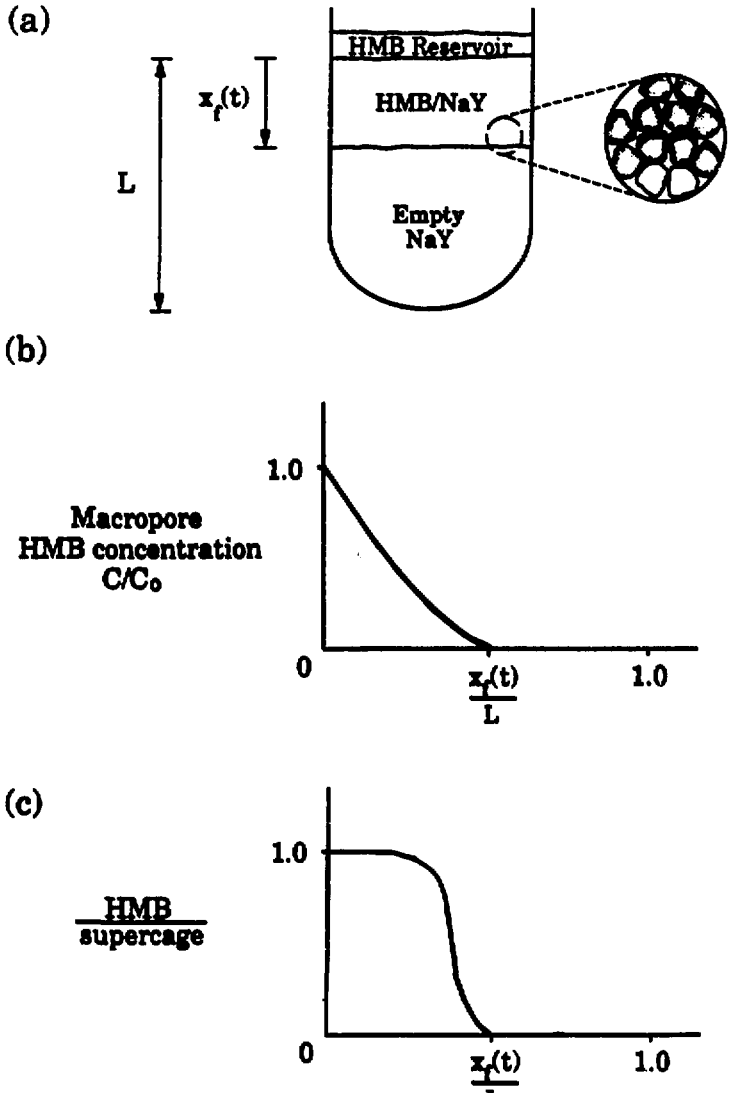

Figure 6.4: (a) Diagram of an axial HMB concentration profile arising from adsorption at 523 K in a packed bed of rehydrated NaY zeolite. The inset depicts the indistinct boundary separating zones with and without adsorbed HMB. (b) Macropore HMB concentration plotted as a function of dimensionless distance from the top of the NaY bed. (c) Intracrystalline HMB loading in rehydrated NaY micropores plotted as a function of dimensionless distance from the top of the bed.

chemisorption process in NaY powders when guest transport in the macropores and micropores occur at comparable rates ($t_{macro} \approx t_{micro}$).

6.4.3 Guest Dispersal at Elevated Temperatures

Chemisorption at higher temperatures increases the macropore concentration of the adsorbing species both by increasing the vapor pressure of the imbibed bulk liquid and by increasing the desorption rate of previously sorbed guest molecules. Under these circumstances, a more homogeneous macroscopic distribution of adsorbed guests will be produced within the zeolite bed. At 573 K, for example, $\alpha(\phi C_o)^{-1} \approx 140$ [see Appendix F.3]. The shrinking-core model is thus inappropriate, since $\frac{\alpha}{\phi C_o}$ is no longer sufficiently large to justify a pseudo steady-state treatment (i.e., $t_f \approx t_{macro}$) [127]. In the situation illustrated in Figure 6.1(b), HMB is dispersed throughout the sample volume, so that a sharp boundary between distinct macroscopic adsorption zones no longer exists. Similarly, high guest concentrations in the macropores account for the diffuse boundary between benzene/NaY adsorption zones observed in Figure 5.6(a) and also for dispersal of preadsorbed HMB/NaY in Figures 5.4 and 6.1. These data are consistent with adsorption isotherms for 1,3,5-triethylbenzene on NaY that demonstrate substantially lower guest uptake at elevated temperatures where kinetic effects are unimportant [1,128,129] [see Appendix F.4].

6.5 Conclusions

Transport of aromatic molecules, such as HMB, into a packed bed of micron-size NaY crystallites occurs by vapor-phase diffusion to exterior particle surfaces. HMB species adsorb strongly on NaY at temperatures below 523 K, migrating to interior

supercages until all cavities contain approximately one molecular guest. The existence of a sharp adsorption front is predicated on an adsorption capacity that is large compared to the vapor-phase concentration of the diffusing organic material, coupled with rapid intracrystalline transport of adsorbed guest molecules. These two criteria specify an axial shrinking-core description of HMB diffusion in dehydrated NaY zeolite powder. The relative magnitudes of *intra*crystalline and vapor-phase (*inter*crystalline) guest transport rates, together with relative guest concentrations in the micropores and in the macropores, establish whether shrinking-core behavior will be observed. In the absence of co-adsorbed guests which hinder intracrystalline HMB transport, rapid migration of strongly adsorbed HMB within NaY micropores, relative to vapor-phase diffusion of HMB through the bed's macropores, produces a sharply defined adsorption front in a dehydrated NaY zeolite bed at 523 K. However, in the presence of a co-adsorbed species such as water or at temperatures where the macropore guest concentration becomes important, no sharp adsorption front exists. Xenon-129 NMR is a sensitive means of monitoring the macroscopic distributions of adsorbed guests in NaY zeolite produced by chemisorption at different temperatures. The adsorbate distribution information obtained from ^{129}Xe NMR complements the theoretical insight provided by the shrinking-core model. The result is a more quantitative description of molecular adsorption and transport processes in zeolites.

Chapter 7

Xenon Adsorption in NaA Zeolite[1]

7.1 Abstract

Xenon atoms occluded in the α-cages of NaA zeolite have been studied using ^{129}Xe NMR spectroscopy to probe directly the distribution and adsorption properties of molecules in confined, microporous environments. The powerful ^{129}Xe NMR technique is sensitive to subtle changes in xenon environment, permitting relative populations of α-cages containing different numbers of xenon guests to be determined. On the basis of ^{129}Xe NMR spectra, the distribution of xenon among NaA α-cages is shown to exhibit a marked dependence on the pressure at which the xenon guests are introduced. Loading pressures less than about 100 atm produce xenon–cage occupancies which can be described by a binomial distribution. Loading pressures near

[1]Presented, in part, at the Eighth International Zeolite Conference, Amsterdam, 10 to 14 July 1989, and also at the American Institute of Chemical Engineers national meeting in San Francisco, November 1989.

200 atm, however, produce xenon–cage occupancies which deviate appreciably from those predicted by binomial statistics.

Xenon-129 NMR spectra recorded at 200 K reveal that, for the same density, xenon atoms in the NaA α-cages experience diminished mobility, resembling condensation-like phenomena, at higher temperatures than in the bulk gas. The chemical potential of adsorbed xenon can thus be investigated experimentally as a function of both temperature and guest density. The density dependences of the ^{129}Xe chemical shift in Xe/NaA and in bulk xenon gas show that Xe–Xe interactions in the proximity of the NaA cage wall are important in α-cages containing more than five xenon guests. This trend is linked to entropic effects which may enhance xenon adsorption in the confined environment of the NaA α-cages.

7.2 Introduction

The behavior of a gas inside micropores is crucial to the use of molecular sieves in adsorption, catalysis, chromatography, and bulk gas separations. However, a quantitative understanding of the phenomena that account for the extraordinary properties of zeolites remains lacking. Zeolites can have high sorption capacities and catalytic activities that are difficult to predict from zeolite chemistry and structure. For example, though the adsorption capacity and equilibrium coefficient are proportional to the crystal density to first order, they also vary with aluminum content and pore structure [2]. The enthalpy and entropy of adsorption can be a complicated and often non-monotonic function of the loading [136,137,138,139,140] and of the zeolite structure [141] as well. In addition, the diffusion of molecules remains poorly understood as a function of the composition and structure of both the zeolite and the diffusing guest species.

There is currently no complete theory of adsorption that accounts for the sorption behavior observed in zeolites. Such a theory must include the effects of surface heterogeneities, intersorbate interactions, steric effects, and a host of intermolecular interactions. Molecular interactions that affect adsorption in zeolites have been reviewed by Barrer [2], Ruthven [142], and others [1,143]; several researchers are working on atomistic theories of adsorption of simple molecules in zeolites [138,144,145,146,147,148,149,150]. They have attained some degree of success at predicting Henry's constants and heats of adsorption at very low coverage, but difficulties arise in predicting the intermolecular potential even for a bulk gas [151].

Recent work has revealed a number of mechanisms that can account for the sorption properties of zeolites. Rabo, for example, suggests considering the zeolite-sorbate interaction as analogous to solvent-solute interactions [152], while Bezus *et al.* [144] and Anderson [137] show that the interaction energy of a sorbed molecule is a strong function of the adsorption site. Derouane and coworkers have, moreover, calculated that the heat of adsorption can be enhanced in a zeolite pore through increased contact between a sorbed molecule and a wall with high curvature, giving rise to the concept of "confinement catalysis" [112,153]. Recent molecular simulations support such a perspective by revealing anomalies in the behavior of simple molecules from confinement effects near a solid surface. Monte Carlo and molecular dynamics calculations indicate that surprisingly dense arrangements of guest molecules exist in layers parallel to the surface. In such circumstances, the confined guest species possess an average density which exceeds that of the bulk fluid [154,155,156,157]. Data from which specific interactions can be unambiguously quantified, however, remain inadequate. Experiments are required which can quantify sorbent-sorbate

and intersorbate interactions and to verify adsorption calculations for simple systems.

Xenon-129 NMR spectroscopy has been used to study gas-phase interactions [49,158,159,160], to study zeolite [161,162] and clathrate [163] structures, and to characterize guest species [39,42,43,59,111], such as metal clusters, adsorbed organics, and exchangeable cations, within the zeolite matrix. Xenon is a spherically symmetric, relatively inert atom which has a NMR-active, spin-$\frac{1}{2}$ isotope (^{129}Xe) with 26.4% natural abundance. Interactions with other molecules, electric field gradients, or surfaces perturb the xenon electron cloud producing a van der Waals chemical shift in the ^{129}Xe nuclear resonance frequency [164]. In this study, we use ^{129}Xe NMR to estimate the condensation temperature of xenon in a confined environment and to probe interactions between adsorbed Xe guests and a solid surface as a function of xenon density within the pores.

Preparation-dependent properties of adsorbate mobility and local structure have been studied for small, strongly sorbed hydrocarbon molecules in A-type zeolites [97,123,124,165,166]. Bakaev has used statistical mechanics arguments to predict the time-averaged distribution of mobile sorbate molecules in zeolites from which equilibrium cage occupancies can be obtained. The results indicate a statistical distribution of guests in zeolite cages which are expected to be sensitive to temperature, intermolecular potentials, and sorption capacity [167]. The exchange of xenon between cages is fast enough in large pore zeolites, such as those with faujasite structures, to produce coalescence of the ^{129}Xe resonances into a single resonance signal [see Chapter 5]. Xenon-129 NMR measurements in large pore zeolites, therefore, provide information on the average xenon density within many cavities over time. As a result, local fluctuations in guest cage occupancy are difficult to characterize. To study situations in which cage occupancies of adsorbed guests are well-defined it

is necessary to halt sorbate transport between the cavities.

NaA zeolite provides a confining matrix which permits the properties of occluded xenon atoms to be compared with those characteristic of bulk xenon gas. A zeolite matrix can trap clusters of gaseous atoms and molecules in its void space if the molecular diameter of the guest slightly exceeds the pore diameter of the zeolite at room temperature. For example, 0.44 nm diameter xenon atoms can be introduced into NaA zeolite, which has a nominal window diameter of 0.42 nm at room temperature, by heating the zeolite to 523 K in the presence of xenon gas. Subsequent cooling of the Xe/NaA system to room temperature traps the xenon guest species inside the 1.14 nm diameter α-cages of the NaA framework. The ^{129}Xe chemical shift is sensitive to interactions experienced by adsorbed xenon atoms and has been used to distinguish different populations of xenon in NaA cavities [45]. Since the ^{129}Xe chemical shift is dominated by the van der Waals contribution [164], it should be possible to investigate adsorbate interactions in the cages to gain insight into the behavior of these molecular assemblies [49,168]. The use of NaA as a confining matrix allows precise determination of the number of xenon atoms in a given cage from the ^{129}Xe NMR spectrum. This permits the behavior of xenon inside the α-cage to be compared with xenon in the bulk gas of the same effective density. Such a comparison cannot be made when xenon exchange between cages is rapid, since the distribution of the local xenon densities among the cavities cannot be instantaneously known.

7.3 Experimental

NaA zeolite samples were dehydrated by heating at 673 K under vacuum (ca. 10^{-5} torr) for 10 h in a 1-cm diameter stainless steel bomb. After cooling the zeolite to room temperature, approximately 2 atm xenon gas (a natural abundance mixture

of isotopes) was introduced to the bomb at 298 K using a standard vacuum rack apparatus. High xenon loading pressures (up to 200 atm at 298 K) were achieved by first condensing the gas in the bomb assembly (immersed in a liquid-nitrogen bath), isolating the bomb from the vacuum rack, and then re-expanding the xenon gas into the small 10-cm^3 bomb volume. All loading pressure measurements were made at 298 K unless otherwise noted. The zeolite samples in the bomb were heated to 523 K, permitting xenon atoms to penetrate the expanded NaA α-cage network. The samples were subsequently quenched by immersion of the bomb in an ice-water bath, resulting in the occlusion of xenon atoms in the NaA α-cages. Quenching rates were varied from about 0.2–2 K/s with no detectable effect on the xenon distribution in samples otherwise treated identically. The pressure and temperature decreased simultaneously in the constant volume bomb as the sample was quenched. Transient effects which might alter the xenon guest distribution during the quenching process tend to offset one another, since adsorption is favored by low temperatures and high pressures. Consequently, the xenon population in the NaA α-cages probably retains a distribution close to that existing at equilibrium during adsorption at high temperature.

After quenching, the Xe/NaA samples were sealed in glass ampoules under dry nitrogen to prevent contamination by atmospheric moisture. Co-adsorbed water diminishes the ability of the NaA matrix to confine the occluded xenon guests, permitting xenon atoms to escape the α-cage network. Xenon-129 NMR spectra were obtained on a Bruker AM-400 spectrometer operating at 110 MHz, using 5000 to 10000 scans. Since the spin-lattice relaxation time (T_1) of ^{129}Xe in these samples is 2–3 s, a recycle delay of 10–15 s was used. The effects of co-adsorbed nitrogen gas on the ^{129}Xe shift have been shown to be small [169]. Chemical shifts are referenced

to xenon gas at very low pressure [37].

7.4 Results and Discussion

7.4.1 Xenon Distributions in NaA

Figure 7.1 shows ^{129}Xe spectra of NaA samples after occlusion of xenon atoms within the zeolite matrix. The ^{129}Xe nucleus becomes less shielded with increasing guest density, so that multiple peaks are observed in a single Xe/NaA sample. Each peak corresponds to a ^{129}Xe signal in α-cages containing a different number of occluded xenon atoms. The distribution of xenon in these different cage environments can be determined from the relative areas of the peaks in the ^{129}Xe NMR spectrum. As illustrated in Figure 7.1, xenon occupancy of the NaA α-cages is a sensitive function of the xenon loading pressure. The mean xenon population increases monotonically as the loading pressure is increased, with the variance of the population distribution in the α-cages first increasing and then decreasing as a loading limit is apparently approached.

As shown in Figure 7.2, xenon occupancy of NaA α-cages can be described by a binomial distribution when loading pressures are less than about 100 atm. A binomial occupancy of N_s sites is defined by [170]

$$f_n = \frac{N_s!}{n!(N_s-n)!} p^n (1-p)^{N_s-n}, \tag{7.1}$$

where f_n is the normalized number of NaA α-cages possessing n xenon guests, p is the probability that a xenon atom will occupy a given cage site, and N_s is the xenon saturation capacity of a single NaA α-cage. The cage occupancies f_n can be measured for xenon occluded in NaA zeolite (for $n > 0$) by integrating the peaks in the ^{129}Xe NMR spectrum [e.g. Fig. 7.1]. Experimentally determined occupancies

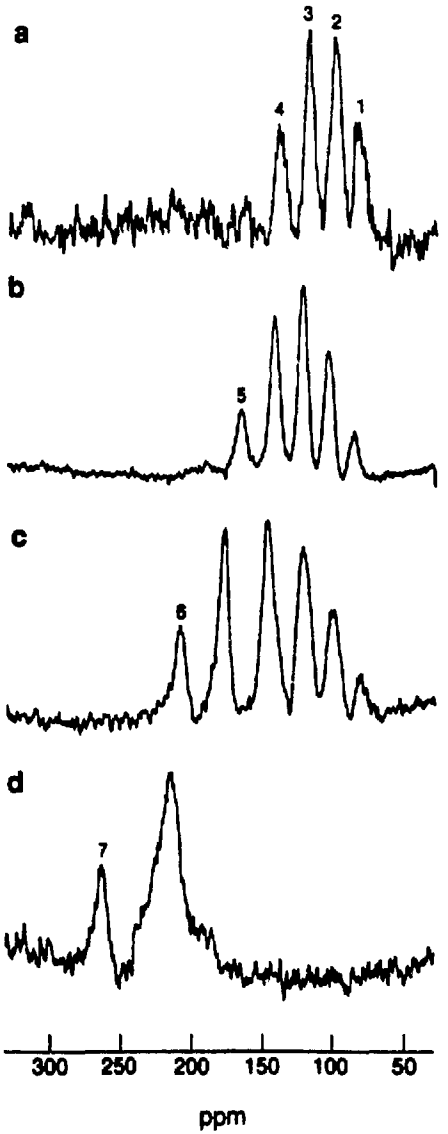

Figure 7.1: Room-temperature ^{129}Xe NMR spectra of xenon occluded in NaA zeolite at different loading pressures: (a) 30 atm, (b) 50 atm, (c) 75 atm, and (d) 200 atm. Each peak corresponds to a ^{129}Xe signal from xenon in α-cages containing different numbers of occluded Xe atoms (indicated by the numbers above the respective peaks.) The chemical shift is referenced to xenon gas at very low pressure.

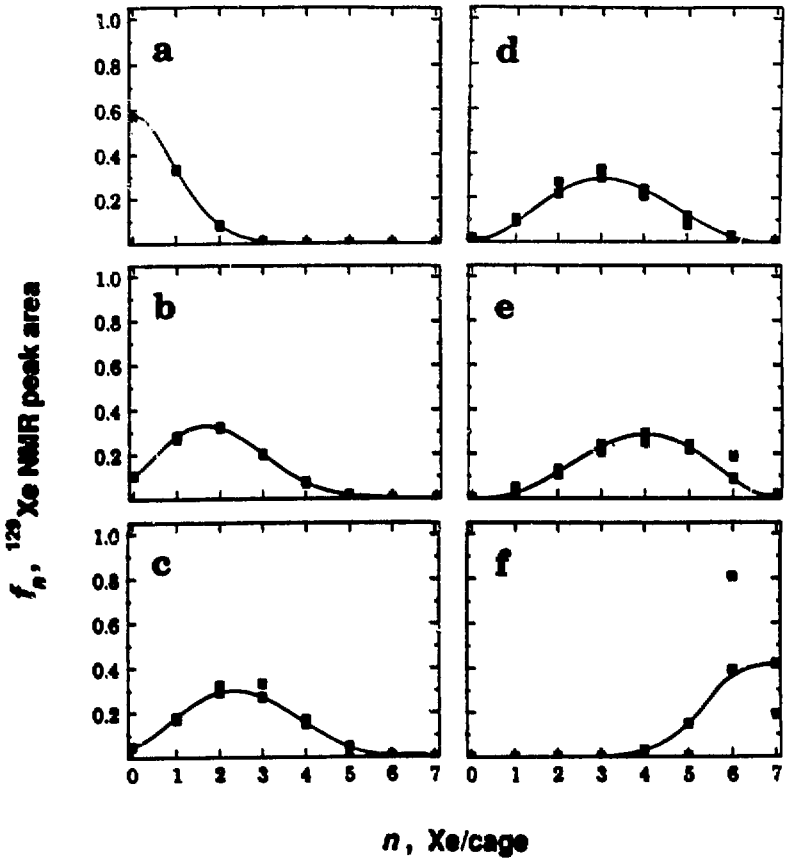

Figure 7.2: Plots of normalized ^{129}Xe NMR peak areas, f_n, (filled squares) versus the number of xenon atoms occluded in an ensemble of NaA α-cages at different loading pressures: (a) 1 atm, (b) 10 atm, (c) 30 atm, (d) 50 atm, (e) 75 atm, and (f) 200 atm. Accompanying the data are values for f_n (open squares) computed using Equations 7.1 and 7.2 for a binomial distribution of xenon in the α-cages, assuming a saturation capacity of 7 Xe atoms per cage. The curves represent polynomial best-fits through the calculated values of f_n. Plots (a)-(b) are from unpublished data provided by L.C. de Menorval, M.G. Samant, and M. Boudart, Stanford University (pressure measurements at 523 K). Plots (c)-(f) are from the ^{129}Xe NMR spectra shown in Figure 7.1.

f_n are plotted in Figures 7.2(a–f) for Xe/NaA samples subjected to different xenon loading pressures. The mean xenon loading per cage $\langle n \rangle$ is readily determined from the relative ^{129}Xe peak areas in each NMR spectrum, permitting the probability p to be computed using [170]:

$$p = \frac{\langle n \rangle}{N_s}. \tag{7.2}$$

The saturation capacity N_s is, therefore, the only adjustable parameter in Equation 7.1. For $5 < N_s < 15$, the best binomial fits to the data are obtained using $N_s = 7$, based on a criterion minimizing the sum of the squares of the deviations between experimental f_n measurements and the calculated binomial distribution values. The cage occupancies f_n are not a strong functions of N_s over this interval, but the ^{129}Xe NMR spectrum in Figure 7.1(d) supports $N_s = 7$ Xe atoms/α-cage. When compared with data in references [137] and [171], the value of seven for N_s suggests that the xenon sorption capacity scales with available surface area for quartz, dealuminated NaY zeolite, and NaA zeolite. For comparison, body-centered cubic packing of spherical xenon atoms (the densest possible arrangement) would result in a maximum loading of approximately 15 Xe/cage which is not supported by our results.

As illustrated in Figures 7.2(a–e), agreement between ^{129}Xe NMR experiments and binomial statistics theory is excellent for Xe/NaA systems loaded at xenon pressures below approximately 100 atm. As the loading pressure is increased, the maxima of the plots shift to higher values of n, reflecting larger mean xenon guest populations in the NaA α-cages. This trend continues until the energetics become unfavorable for adding another xenon atom to an α-cage already crowded with previously occluded xenon guests, apparently when loadings of $\approx 7 \frac{Xe}{cage}$ are approached. As shown in Figure 7.2(f), however, loading pressures near 200 atm lead to xenon–cage

occupancies that deviate appreciably from the distribution predicted by binomial statistics. Changes in the adsorption isotherm of xenon on NaA probably account for the anomalous distribution of xenon in this high pressure regime, where the finite size of the atoms may become important. To probe further the interactions responsible for the sorption behavior of guest molecules in micropores, the thermodynamics of the adsorption process will now be considered.

7.4.2 Chemical Potential and Mobility of Xenon in NaA

Certain sorbent and catalytic properties of zeolites may be related to enhancement of an adsorbed species' equivalent bulk chemical potential (i.e., the bulk chemical potential evaluated at the average guest density in the zeolite pores) over that of the bulk material. It has been suggested, for example, that the high activity of zeolites in such reactions as catalytic cracking may be partly attributed to a high "effective concentration" of species in the micropores [152]. In this case, an enhanced equivalent bulk chemical potential of the adsorbed reactants may result in a shift in the reaction equilibrium inside the zeolite pore spaces. Probing the chemical potential of sorbed and occluded molecules is, consequently, crucial to understanding adsorption and reaction phenomena in microporous environments.

The equivalent bulk chemical potential of an occluded gas, $\mu(\langle\rho\rangle)$, corresponding to the mean guest density $\langle\rho\rangle$ within a given microscopic container, can be investigated by determining the temperature of the guest species' transition to a nominally condensed phase. An increase in the temperature at which condensation occurs indicates an increase in the equivalent bulk chemical potential $\mu(\langle\rho\rangle)$ of the occluded guest [173]. We ascribe this increase primarily to enhancement of the average guest density within the the NaA α-cages due to interactions with the zeolite cage wall.

Figure 7.3 shows ^{129}Xe NMR spectra of xenon occluded in the NaA matrix as the temperature is lowered. The ^{129}Xe signals arising from xenon in the most crowded cages broaden at higher temperatures than do those associated with xenon in less dense cage environments. Though condensation of xenon inside the NaA α-cages is not observed directly, broadening of the ^{129}Xe resonance as the temperature is lowered indicates decreased mobility of the xenon guest. Correlation times of xenon motion in NaA cavities can be estimated using reference [52]. For a frequency separation of 40 ppm between different Xe adsorption sites (estimated from the width of broadened Xe/NaA peaks at low temperature), we calculate a correlation time of $\approx 10^{-6}$ s. Within the 1.14 nm α-cages, this means that the average speed of a Xe atom is on the order of 10^{-3} m/s. For comparison, we note that the mean molecular speed of an ideal gas at 200 K is about 180 m/s and that of a liquid is on the order of 10 m/s. It is reasonable to suggest, therefore, that diminished xenon mobility, reflected by broadening of the ^{129}Xe lineshape, indicates a transition to a condensed, solid-like phase within the NaA cavities.

Figure 7.4 shows that the temperature at which xenon occluded in the NaA α-cages becomes solid-like is greater than that for bulk xenon at the same density. The condensation point of bulk xenon gas shown in Figure 7.4 is determined using the Clausius-Clapeyron equation from data in reference [174]. The data indicate both that xenon's equivalent bulk chemical potential is enhanced in the NaA α-cage and that NMR offers a means to ascertain the degree of this enhancement. Note that the estimated condensation temperature of Xe/NaA, as measured by ^{129}Xe NMR, increases with xenon density in the α-cages at a rate higher than that predicted for the bulk gas by the Clausius-Clapeyron equation. Our objective is to determine whether this increased rate can be ascribed to the interactions experienced by xenon

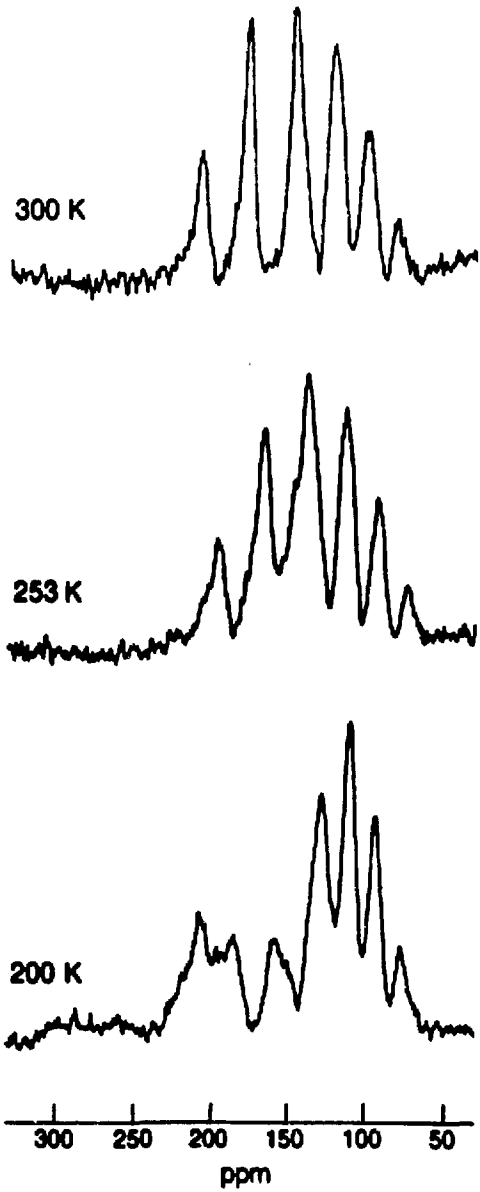

Figure 7.3: Variable temperature ^{129}Xe NMR spectra of xenon occluded in NaA. Broadening of the peaks indicates decreased xenon mobility within the α-cages. (Loading pressure = 75 atm)

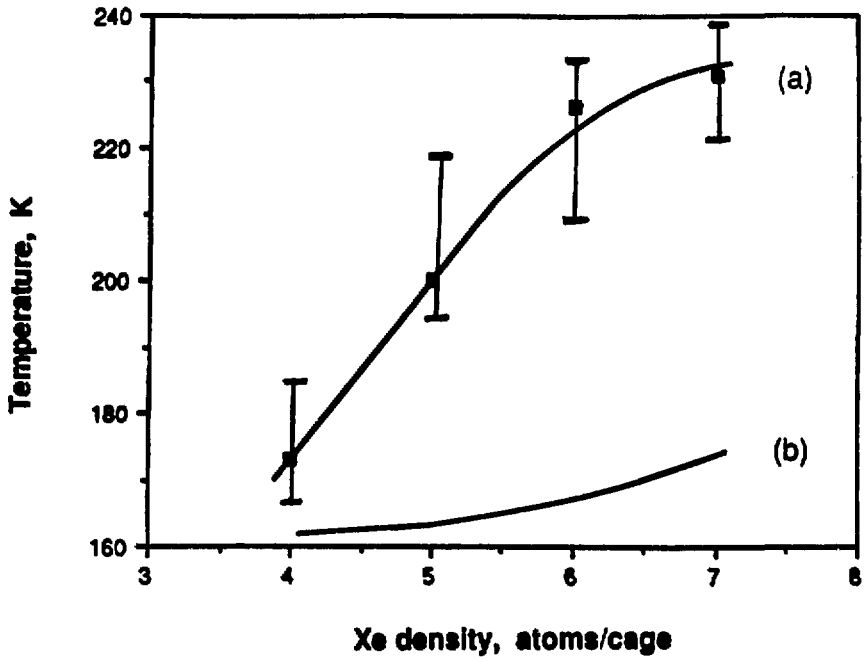

Figure 7.4: (a) Density-dependence of the estimated condensation temperature of xenon occluded in NaA zeolite. The condensation temperature is estimated from the onset of spectral broadening observed for the various ^{129}Xe peaks during variable temperature ^{129}Xe NMR experiments. Broadening occurs in the more densely loaded cavities first. (b) The freezing point of bulk xenon plotted as a function of xenon density. High pressure volumetric data [158] was used to compensate for Xe nonideality at high pressures.The density is expressed as the number of xenon atoms in a volume equivalent to the NaA α-cage.

atoms within the NaA matrix.

7.4.3 Chemical Shift Analysis

Measurement of the ^{129}Xe chemical shift permits the interactions between individual xenon atoms or between xenon atoms and the cage wall to be investigated directly. For spherically symmetric, monoatomic gases the chemical shift is dominated by the van der Waals shift, which arises from fluctuating electric fields induced when the gas molecules interact with their environment [164]. The chemical shift δ of ^{129}Xe in NaA α-cage environments results from the exchange-averaged shifts of a xenon atom in free space, a xenon atom interacting with other Xe atoms, and a xenon atom interacting with the NaA cage wall:

$$\begin{aligned} \delta \;=\; & \delta_o P_o + [\delta_{2xe} P_{2xe} + \delta_{3xe} P_{3xe} + \delta_{4xe} P_{4xe} + ...] + \\ & [\delta_{xe-wall} P_{xe-wall} + \delta_{2xe-wall} P_{2xe-wall} + ...] \end{aligned} \tag{7.3}$$

where δ_o is the intrinsic chemical shift of a single xenon atom in free space (taken to be zero by convention); δ_{2xe}, δ_{3xe}, and δ_{4xe} are the intrinsic shifts of one xenon atom interacting with one, two, or three other xenon atoms, respectively; $\delta_{xe-wall}$ and $\delta_{2xe-wall}$ are the intrinsic shifts of one xenon atom in contact with the zeolite cage wall or with the wall *and* a second Xe atom, respectively; and P_n are the probabilities that a xenon atom experiences each of these various interactions. In general, δ_{2xe}, δ_{3xe}, δ_{4xe}, and $\delta_{2xe-wall}$ are virial coefficients that account for multibody interactions between xenon atoms in cavities containing more than one xenon guest. $\delta_{xe-wall}$ and $\delta_{2xe-wall}$ are associated with the van der Waals interaction of the xenon with an aluminosilicate wall of specified curvature and aluminum content [112,153,168]. Some studies have included an extra term to account for the electrostatic effects of cations

or metals, but this term is negligible for NaA and is, more generally, important only if the shift increases as the xenon density within the cavities approaches zero [175].

The ^{129}Xe chemical shift of xenon distributed in NaA α-cages is shown in Figure 7.5. The error bars are due to variations among samples, most likely from co-adsorbed H_2O. The ^{129}Xe chemical shift of xenon occluded in NaA increases at an increasing rate as the xenon density becomes greater: a trend which has also been observed in zeolites L, ZSM-5, and erionite [175]. This behavior is in contrast to that observed for the bulk gas, also shown in Figure 7.5, permitting investigation of xenon confinement effects in NaA cavities. At room temperature, the virial expansion approach of Jameson *et al.* is suitable for four-body interactions up to approximately 250 atm [49]. While the bulk gas shift also increases with density, the rate of increase diminishes with increasing xenon concentration. Any 'bulk gas' contribution to the ^{129}Xe shift in NaA is accounted for by the xenon-xenon interaction terms $\delta_{nxe}P_{nxe}$. We conclude from Figure 7.5 that the zeolite cage causes xenon to experience interactions which are different from those in the bulk gas.

It is possible to deduce the nature of these interactions through analysis of the ^{129}Xe chemical shift. As given by Equation 7.3, the chemical shift of each ^{129}Xe peak in Figure 7.1 represents a weighted average of the intrinsic shifts arising from a xenon atom's interaction with the various adsorption environments in a single NaA α-cage. The nonlinear chemical shift behavior at high xenon loadings [Fig. 7.5(a)] must be explained by increases in the intrinsic shifts $\delta_{xe-wall}$ and $\delta_{2xe-wall}$ at the wall and/or by increases in the probabilities $P_{xe-wall}$ and $P_{2xe-wall}$ with which those interactions occur. The terms $\delta_{xe-wall}$ and $\delta_{2xe-wall}$, however, can be functions of loading only if the sites at which xenon atoms adsorb change with loading. Atomistic calculations [137] suggest that the zeolite surface is heterogeneous, with the four-oxyen ring

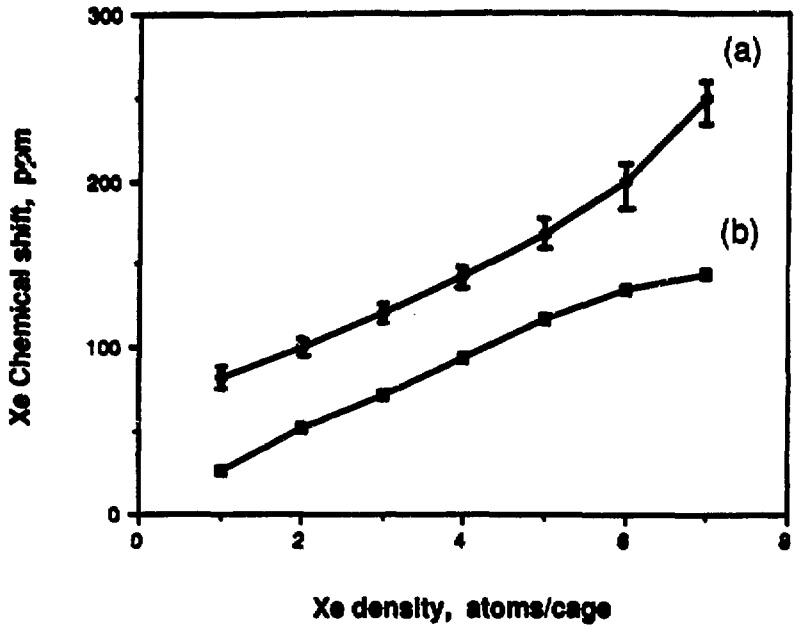

Figure 7.5: ^{129}Xe chemical shift plotted as a function of xenon density (a) for xenon occluded in NaA α-cages and (b) for bulk xenon gas. The density is expressed as the number of xenon atoms in a volume equivalent to the NaA α-cage. Values for bulk xenon gas are taken from reference [49](a).

providing the most stable adsorption site for xenon. Preferential adsorption at favored sites, however, is unlikely to govern the ^{129}Xe shift in NaA for two reasons. First, should xenon populate weaker adsorption sites at higher loadings, the chemical shift should decrease rather than increase, contrary to experimental observation [Fig. 7.5(a)]. Secondly, Monte Carlo and molecular dynamics calculations show that the mobility of small molecules in a single cage is quite high at room temperature with no significant sorption site preference [150,176].

In other studies, the influence of the zeolite cage wall on the ^{129}Xe chemical shift

$$[\delta_{xe-wall} P_{xe-wall} + \delta_{2xe-wall} P_{2xe-wall} + ...], \tag{7.4}$$

has been assumed to be constant with xenon density (that is, $P_{xe-wall}$ is constant and $P_{2xe-wall}$ is much less than unity) [35,177]. This is a valid assumption at flat walls, in large pores, or at low guest loadings, where the probability of multibody Xe–Xe interactions at the wall is small. It is not necessarily true, however, in the confined NaA pore spaces (the α-cage is only 2.5 times larger than the diameter of the xenon guest) at the high loadings imposed here. Even when local xenon densities are high, the interaction energy of a xenon atom with the NaA-cage wall greatly exceeds that between individual xenon atoms and also the translational energy of a xenon atom at room temperature. The heat of xenon adsorption in NaA is 5.4 kcal/mol [142], so that the probability of a xenon atom being free of the wall is only about 0.01% at 298 K. Furthermore, Rybolt *et al.* [149] calculate that the depth of the Lennard-Jones interaction potential well is approximately 75kT for xenon in contact with an aluminosilicate wall. For comparison, Aziz and Slayman[151] report that the depth of the xenon-xenon potential well is only 1kT. The affinity of guest species for the zeolite surface has been documented by Cohen de Lara *et al.* [176] who have used molecular dynamics simulations to show that methane, a molecule with dimensions

similar to those of xenon, remains near the cage wall at room temperature. From this we infer that $P_{Xe-wall}$ is near unity at low guest loadings.

At high guest loadings, the confinement of multiple xenon atoms in a single α-cage results in more frequent interaction between the xenon guests, a situation enhanced by the preference of the xenon atoms for positions in close proximity to the wall. The probability that a single xenon atom will be free to interact alone with the cage wall is substantially diminished when many xenon atoms are present in a given cavity. This is manifested by an increase in the probability of multibody Xe interactions at the wall, $P_{2Xe-wall}$, which occurs at the expense of $P_{Xe-wall}$. We conclude therefore that Xe–Xe interactions in the proximity of the NaA cage wall, as measured by $P_{2Xe-wall}$, become important at high xenon loadings (> 5 Xe/cage) and in so doing account for the non-bulk ^{129}Xe chemical shift behavior observed in Figure 7.5.

It is possible that Xe–Xe–wall interactions in the cage are amplified by the confinement effects demonstrated by van Megen and Snook [154] and others [155,156,157]. For example, the confinement of fluid molecules may produce concentric laminae of high density within a few molecular diameters of the wall. Vanderlick *et al.* [156] have shown using molecular dynamics calculations that these effects cause striation of the fluid in slit-pore models for hard sphere, non-attractive fluids as well as for Lennard-Jones fluids. Moreover, Magda *et al.* [155] indicate that adsorption can be enhanced by confinement effects, since the average density in a pore is a sensitive function of the pore width (for diameters from two to five times the molecular diameter.)

Confinement, furthermore, can cause the entropy of guest species adsorption to be more favorable in a micropore relative to that on a flat surface. Israelachvili has discussed how guest interactions in a confined pore can lead to a less ordered adsor-

bate configuration (and low "solvation forces") [157], in agreement with adsorption entropy measurements and calculations for zeolites and large pore sorbents [137,171]. The adsorption equilibrium coefficient K at constant pressure is related to the concentration of adsorbed xenon n and the heat and entropy of xenon adsorption, ΔH and ΔS respectively, by

$$\ln n \propto \ln K = \frac{-\Delta H}{RT} + \frac{\Delta S}{R} . \tag{7.5}$$

Data in Table 7.1 reflect similar heats of adsorption for xenon on quartz and on dealuminated NaY zeolite, as do adsorption isotherms for xenon on silica gel and CaA zeolite [see Fig. D.2 in Appendix D] [178]. Since the heats of xenon adsorption are similar on a variety of silicate sorbents, the high adsorption equilibrium coefficient in zeolites might be ascribed to entropic effects. Enthalpic and entropic contributions to the adsorption equilibrium coefficient K of xenon on dealuminated NaY and quartz are shown in Table 7.1. The entropic contribution to xenon adsorption is substantially less negative (more favorable for adsorption) in NaY than on quartz. Such observations are consistent with previously mentioned confinement effects which may give rise to sorbed molecular assemblies of diminished order [157]. Some supporting evidence for this can be found from adsorption studies of xenon on NaX [179], in which the calculated heat capacity suggests the formation of a phase less ordered than expected for adsorption on a flat surface.

7.5 Conclusions

Xenon-129 NMR spectra of xenon occluded in NaA zeolite reveal guest distributions which exhibit a sensitive dependence on xenon loading pressure. For loading pressures less than about 100 atm, the xenon distribution agrees closely with that

Table 7.1: Energetics of xenon adsorption on dealuminated NaY zeolite and quartz at 300 K. The values for quartz were calculated from data in the literature in the manner described by Anderson [137].

Sorbent	$\frac{\Delta H}{RT}$	$\frac{\Delta S}{R}$ Expt.	$\frac{\Delta S}{R}$ Theory
Dealuminated NaY Zeolite	-7.17[a]	-3.62[a]	-3.93[b]
Quartz	-8.75[c]	-17.06[c]	

a) Anderson, M.W. et al., *J. Chem. Soc., Farad. Trans. 1*, 82, 2851 (1986).
b) Kiselev, A.V. and Du, P.Q., *J. Chem. Soc., Farad. Trans. 2*, 77, 1 (1981).
c) Ahrens-Botzong, V.R. et al., *Ber. Bunsen Gesell.*, 76(5), 460 (1972)

predicted by binomial statistics and indicates a saturation capacity of approximately 7 Xe atoms/α-cage. The observed xenon distribution deviates from the binomial description at loading pressures near 200 atm, though ^{129}Xe NMR results support a maximum loading of 7 Xe/cage. Broadening of ^{129}Xe lineshapes at 200 K indicates diminished mobility of occluded xenon at temperatures much higher than would be observed for bulk xenon. Variation of the ^{129}Xe chemical shift with the number of guest atoms trapped inside a NaA α-cage allows a quantitative measurement of the interactions responsible for the enhanced equivalent bulk chemical potential of adsorbed xenon. Xenon–xenon interactions in the proximity of the NaA cage wall may be augmented by confinement effects which can be used to rationalize heightened entropic contributions to the xenon adsorption equilibrium coefficient. Xenon-129 NMR provides a sensitive, direct means of probing Xe guest interactions in NaA α-cages, providing experimental data which complement recent results from rapidly developing theories of molecular adsorption in zeolites.

Chapter 8

Conclusions

There are two major themes unifying this work. The central one is the pursuit of microstructural information pertaining to the distribution of guest species among the intracrystalline cavities of zeolites. The other, to be discussed first, is the pervasiveness of the ^{129}Xe NMR technique in providing insight on the issue of zeolite-guest structure. High mobility of the xenon probe species makes room-temperature ^{129}Xe NMR a popular characterization tool in the study of zeolites and other porous solids, but accounts for its most critical limitation as well. The burgeoning use of ^{129}Xe NMR is due, to a large extent, to its motionally averaged signal for which conventional NMR detection techniques are suitable. Motional averaging, however, often obscures local structural information by limiting spectral resolution to situations in which guest distribution heterogeneities are large compared to the rate of xenon exchange between different, site-averaged adsorption environments. Careful attention to sample preparation and knowledge of relevant guest/zeolite heterogeneity length scales are necessary to benefit from the diagnostic capabilities of the ^{129}Xe NMR technique.

The utility of ^{129}Xe NMR, thus, depends on the mobility of the xenon species

within the zeolite-guest system, together with the length scale of the sample heterogeneity being studied. When the heterogeneity length scale is short relative to the distance diffused by a xenon atom on the time scale of the NMR experiment, the ^{129}Xe technique cannot resolve specific structural details because the information is averaged by fast xenon exchange between discrete adsorption sites. This situation exists in large pore zeolite systems, such as Pt–NaY and HMB/NaY, where the microstructure of the dispersed metal or adsorbed guest species is beyond the resolution range of the ^{129}Xe probe at room temperature. Under these circumstances, ^{129}Xe NMR is used most profitably in conjunction with other physical and chemical methods to characterize zeolite-guest structural features. Transmission electron microscopy, hydrogen chemisorption, Raman spectroscopy, and temperature programmed reduction, for example, provide insight on the location and chemical identity of metal guest species which complement results obtained from ^{129}Xe NMR [Chapters 3 and 4].

For hydrocarbon molecules adsorbed on zeolites, multiple-quantum NMR provides microstructural information on the size of isolated dipole-dipole coupled spin systems permitting guest occupancy of NaY supercages to be determined [Chapter 5]. As shown in Chapter 5, a xenon atom diffuses within roughly one micron-size NaY crystallite on the time scale of a room-temperature NMR experiment. Consequently, at 298 K ^{129}Xe NMR is incapable of resolving structural heterogeneities with length scales smaller than about one crystallite diameter in a collection of NaY zeolite particles. Local guest structure can have an important influence on the averaged ^{129}Xe signal in zeolites, but generally such information is obscured by rapid xenon exchange among numerous intracrystalline adsorption sites.

For ^{129}Xe NMR to resolve structural features within a zeolite-guest system, xenon exchange between different adsorption environments must be slow relative to the

splitting between the respective ^{129}Xe resonance frequencies. This is the case, for example, in a packed zeolite bed possessing a macroscopic adsorbate concentration gradient such as observed in HMB/NaY samples following chemisorption of the organic guest at 523 K [Chapter 5]. A simple dual porosity model for HMB transport in NaY and adsorbate distribution data provided by ^{129}Xe NMR permit the relative rates of *intra*crystalline and *inter*crystalline HMB diffusion to be established [Chapter 6]. As a second example, xenon atoms occluded in NaA zeolite possess greatly diminished intracrystalline mobilities (i.e., exchange between α-cages is slow), thus, allowing study of structural features with much shorter length scales. The distribution of xenon atoms among NaA α-cages can be measured as a function loading pressure, permitting the xenon/α-cage saturation capacity to be estimated and confinement effects on adsorbed species to be studied [Chapter 7].

Under such circumstances, xenon guest atoms serve as sensitive, direct probes of local adsorption environments. Similarly, ^{129}Xe NMR experiments performed on condensed phases at reduced temperatures have promise for diminishing the mobility of xenon probe species even in large pore zeolite systems. Though adoption of more sophisticated NMR methods will be required to remove anisotropic broadening effects prevalent in solid xenon phases, determining the local structure of specific adsorption sites appears to be an accessible objective.

The purpose of our experimental agenda has been to understand how preparatory treatments influence the distribution of guest species in zeolites. In attacking this problem, diverse experimental methods have been used, motivated by the need for a molecular understanding of the chemistry and transport effects governing guest interactions and mobilities in zeolites. Such effects are crucial to the performance of heterogeneous catalysts and fundamental to the behavior of molecules at solid sur-

faces. In particular, we have elucidated the chemistry of the activation process(es) responsible for platinum distributions observed in NaY zeolite. Although specific to Pt–NaY, the results are pertinent to other Group VIII metals dispersed on hydrophilic zeolite supports. The combination of experimental methods employed here is, furthermore, directly amenable to the study of other metal-zeolite systems. Reaction studies which can correlate catalyst performance with a detailed understanding of metal guest structure will disclose further the effect of preparatory conditions on catalytically-active metal species. Similarly, spatial distributions of adsorbed guests in zeolites are important for the insight gained regarding diffusion of reactant species in confined pore spaces, together with microstructural features of the intracrystalline adsorption environments. Correlating guest transport behavior and local adsorbate structure with the chemical reaction properties of zeolites is crucial to understanding the catalytic function(s) of these materials. Proper characterization of the interactions governing guest species reaction, mass transport, and adsorption in zeolites requires an interdisciplinary perspective. The spectroscopic tools of modern physical chemistry now permit engineering problems such as these to be approached and scrutinized at a molecular level from which macroscopic system properties may ultimately be better understood.

Appendix A

Scattering Experiments

A.1 Transmission Electron Microscopy Methods

Selected bright field TEM experiments were performed on calcined and reduced Pt–NaY samples to characterize visually catalyst features larger than about 3 nm. All TEM data were acquired using a JEOL 200CX microscope with a top entry holder and a high resolution pole piece at the National Center for Electron Microscopy at Lawrence Berkeley National Laboratory. Powdered Pt–NaY specimens were suspended in 200 proof ethanol and sonicated for several minutes to break up large aggregates of the micron-size zeolite crystallites. A drop of the suspension was placed on a holey carbon film [Fig. A.1] supported on a copper mesh grid, which was subsequently dried in air prior to TEM analysis. The microscope was operated at its maximum accelerating voltage, 200 KeV, to minimize electron beam-induced damage of the zeolite [180,181].

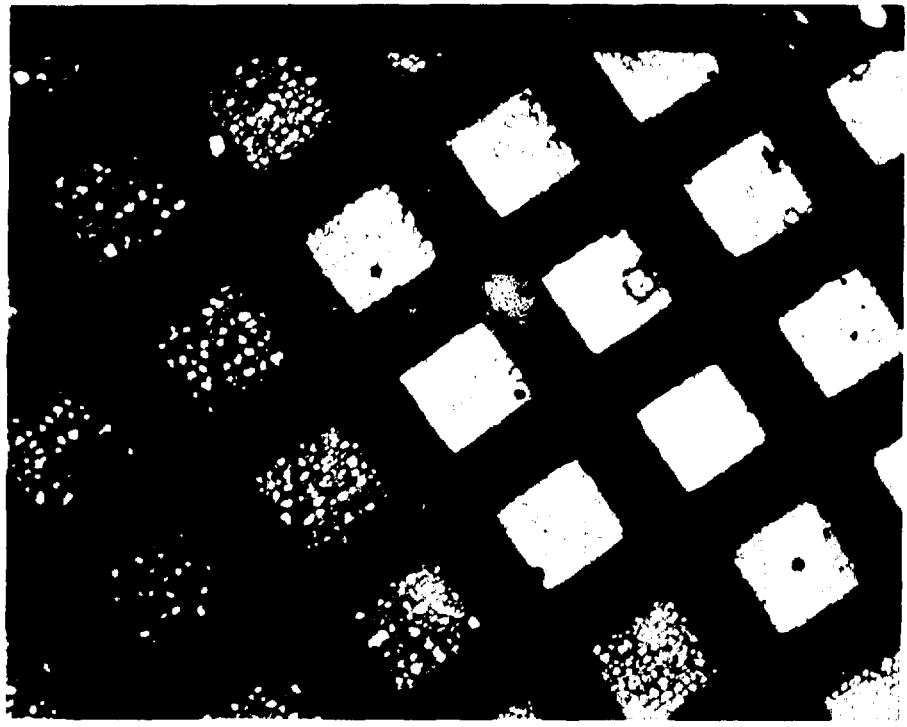

XBB 890 – 8725

Figure A.1: Low magnification (x2 ,000) transmission electron micrograph showing micron-size Pt-NaY zeolite crystallites supported on the copper mesh sample grid. The holey carbon film is visible overlaying the Cu mesh in the 40 μm gaps between the wire strands.

A.2 NaY Crystallinity by X-ray Diffraction

Figure A.2 shows X-ray diffraction data obtained for the commercial NaY zeolite (Union Carbide LZY-52, lot #968084061002-S) using a Siemens Diffrac-11 X-ray diffractometer at Lawrence Berkeley Laboratory. Peaks are tabulated in Table A.1 over the range $5° < 2\theta < 77°$. For scattering angles 2θ between 5° and 35°, the data show close agreement with standard book values for NaY, as shown in Figure A.3.

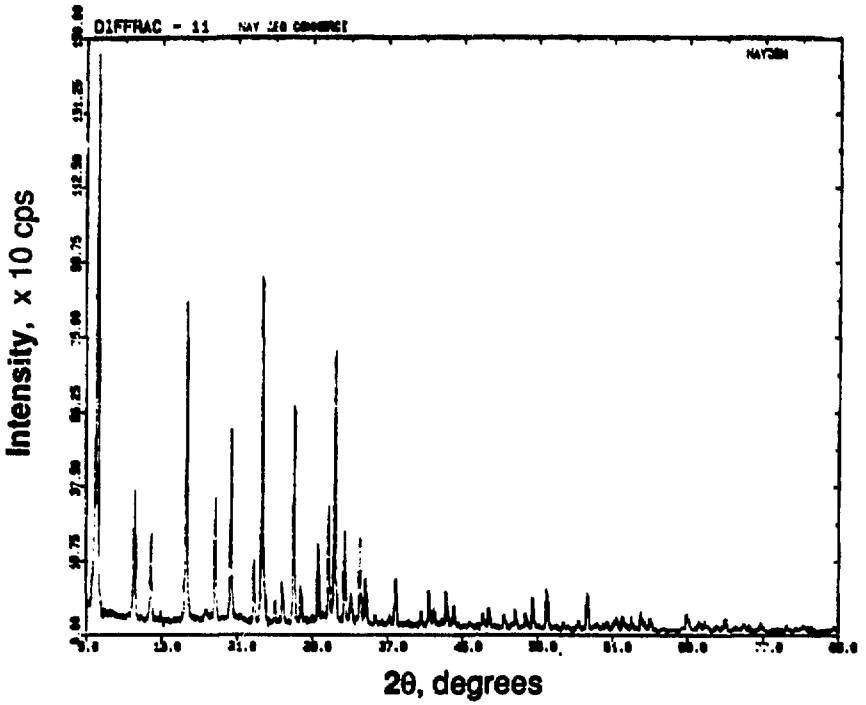

Figure A.2: X-ray diffraction data for commercial NaY zeolite: Union Carbide LZY-52, lot #968084061002-S.

Table A.1: Peaks in the x-ray diffraction spectrum of commercial NaY zeolite: Union Carbide LZY-52, lot#968084061002-S.

NO	2THETA	D	INTEG.I (%)	INTEG.I	MAX.I	FWHM
1	6.173	14.3057	100.0	11434.	1727.	0.331
2	10.117	8.7359	19.4	2215.	445.	0.249
3	11.864	7.4538	10.8	1237.	296.	0.209
4	13.841	6.8887	1.2	139.	43.	0.161
5	15.624	5.6670	37.5	4289.	1080.	0.199
6	17.638	5.0244	2.4	271.	41.	0.327
7	18.663	4.7506	15.3	1744.	421.	0.207
8	20.332	4.3643	21.3	2433.	643.	0.189
9	22.775	3.9014	7.7	883.	219.	0.202
10	23.626	3.7628	44.5	5091.	1175.	0.217
11	24.973	3.5627	2.5	284.	79.	0.179
12	25.758	3.4559	4.9	561.	141.	0.199
13	27.026	3.2966	26.0	2974.	740.	0.201
14	27.744	3.2129	4.3	496.	124.	0.200
15	29.617	3.0138	8.4	961.	258.	0.186
16	30.783	2.9069	13.3	1516.	374.	0.203
17	31.381	2.8483	33.0	3775.	911.	0.207
18	32.437	2.7580	10.3	1179.	308.	0.191
19	33.059	2.7075	4.9	560.	105.	0.268
20	34.079	2.6287	9.5	1084.	277.	0.195
21	34.477	2.5988	6.5	742.	155.	0.239
22	35.643	2.5169	1.6	180.	34.	0.265
23	37.167	2.4171	1.3	149.	39.	0.190
24	37.880	2.3733	7.9	900.	160.	0.281
25	40.546	2.2232	2.2	250.	53.	0.234
26	41.384	2.1801	5.0	575.	121.	0.237
27	41.898	2.1545	2.7	303.	57.	0.264
28	43.202	2.0924	4.7	541.	118.	0.229
29	44.010	2.0558	3.2	371.	71.	0.262
30	45.730	1.9824	1.9	213.	27.	0.400
31	47.145	1.9262	3.1	355.	57.	0.310
32	47.764	1.9027	2.8	322.	66.	0.244
33	49.383	1.8440	3.1	352.	47.	0.373
34	50.557	1.8039	2.9	330.	64.	0.258
35	51.735	1.7656	2.9	335.	53.	0.314
36	52.410	1.7444	4.9	555.	108.	0.287
37	53.951	1.6982	5.9	679.	135.	0.252
38	55.719	1.6484	1.5	173.	29.	0.302
39	57.359	1.6051	1.6	189.	33.	0.289
40	58.263	1.5823	5.4	622.	122.	0.254
41	59.310	1.5569	1.2	142.	23.	0.313
42	60.327	1.5330	1.6	181.	29.	0.306
43	61.386	1.5091	2.9	334.	45.	0.374
44	61.995	1.4957	1.6	183.	49.	0.188
45	62.985	1.4746	1.0	120.	46.	0.130
46	64.001	1.4536	2.6	297.	63.	0.237
47	64.995	1.4337	2.0	224.	38.	0.291
48	68.881	1.3620	1.9	221.	52.	0.212
49	73.030	1.2946	2.2	257.	41.	0.316
50	74.907	1.2667	1.4	159.	24.	0.331
51	76.723	1.2412	2.0	225.	31.	0.359

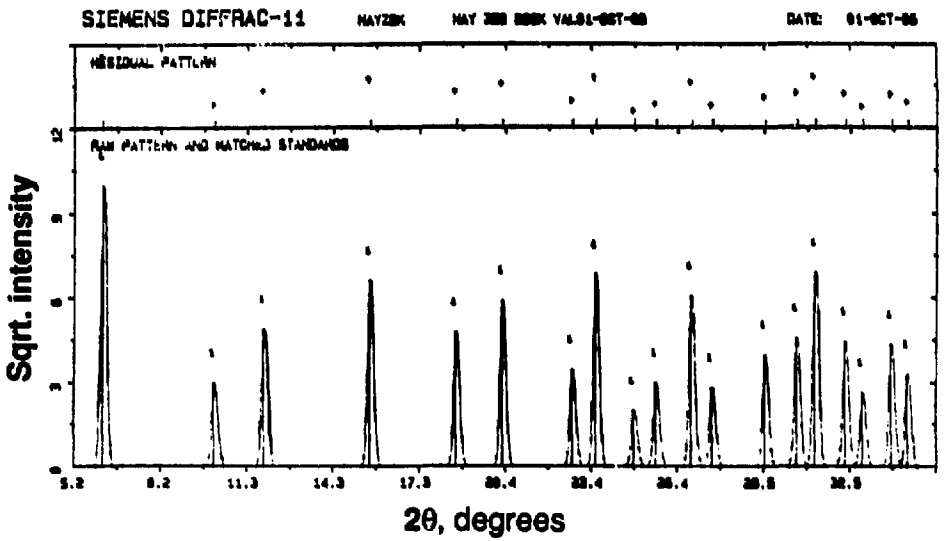

Figure A.3: X-ray diffraction data for commercial NaY zeolite accompanied by accepted standard values for peak intensities and positions as indicated by the lines and overhead daggers.

Appendix B

^{129}Xe NMR of Pt–NaY

B.1 Calcination Cooling Rate Effects

The rate at which the Pt–NaY system is cooled following calcination is important when reactions involving the metal species are kinetically limited. The kinetic effects are manifested by the lower ^{129}Xe chemical shifts registered in calcined Pt–NaY samples cooled slowly to ambient temperature compared to those that were rapidly quenched. From Figure B.1 it is apparent that kinetic limitations exist during decomposition of the metal-tetraammine complex. The ^{129}Xe chemical shift in samples calcined at 473 K and 573 K, for example, exhibit cooling rate dependences consistent with more complete decomposition of the $Pt(NH_3)_4^{2+}$ complex in samples held at elevated temperatures for a longer time. Since the PtO calcination product [see Chapter 4] produces a more shielded supercage environment for the adsorbed xenon, slow cooling of the samples yields diminished ^{129}Xe shift values. Decomposition of the tetraammine complex is completed during calcination at 673 K and 773 K, afterwhich no further cooling rate dependence is observed. Subsequent decomposition of the PtO intermediate at higher temperatures, thus, proceeds as an equilibrium

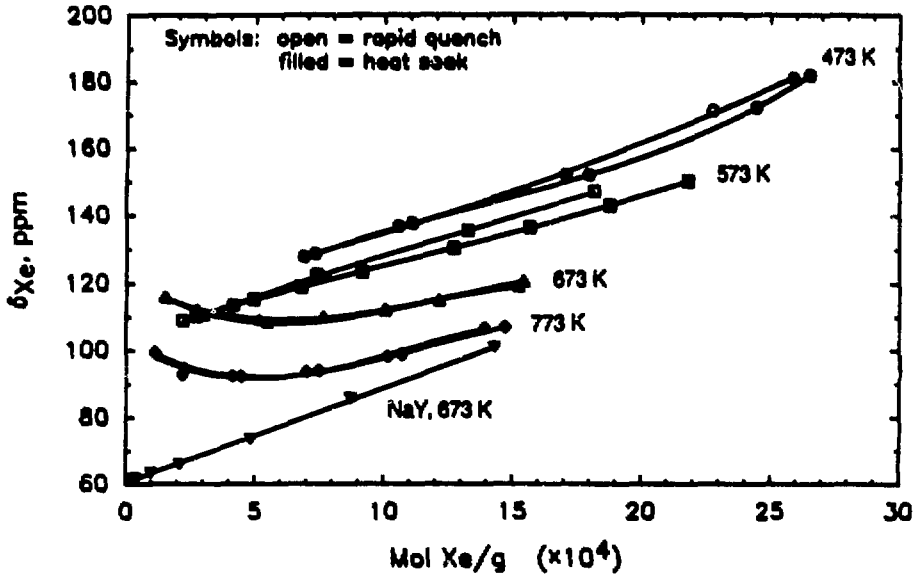

Figure B.1: Variation in ^{129}Xe chemical shift with the concentration of xenon adsorbed (T=295 K) on 15 wt% $Pt(NH_3)_4^{2+}$-NaY zeolite samples calcined at different temperatures. The effect of cooling rate on the calcined Pt-NaY samples is shown.

limited reaction.

Fast exchange of xenon among different Pt–NaY adsorption sites averages the shielding perturbations which xenon atoms experience on the time scale of the NMR experiment. High xenon mobility results in a single peak at the isotropic chemical shift for all Pt–NaY samples investigated here. The width of the ^{129}Xe peak depends on the distribution and homogeneity of adsorption sites within a sample, weighted by the time spent in each adsorption environment. Thus, like the ^{129}Xe chemical shift, the ^{129}Xe linewidth varies with sample preparation treatment as shown for the calcined Pt–NaY systems in Figure B.2. Differences are apparent in the functional form of the linewidth data for the various calcination treatments. The data also reflect the influence of the cooling rate on the character of the calcined sample, particularly at 573 K. Because the ^{129}Xe linewidth is much less sensitive than the ^{129}Xe chemical shift to differences between samples, the linewidth data are generally less useful for diagnostic purposes.

B.2 Pt–NaY Treatment Histories

As discussed at length in Chapter 3, the chemical shift of ^{129}Xe adsorbed on Pt–NaY is dependent upon sample treatment history. Previous emphasis was placed on the differences between *different* Pt–NaY samples after specific oxidation, reduction, or reoxidation procedures. In Figures B.3–B.7, the ^{129}Xe NMR chemical shift data are replotted as a family of curves for individual samples subjected to a sequence of different treatment conditions.

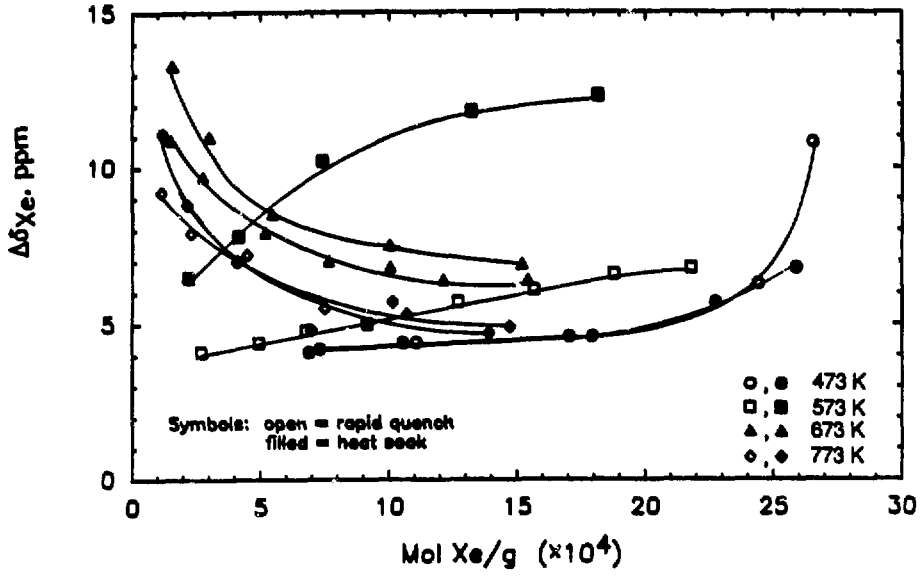

Figure B.2: Variation in ^{129}Xe linewidth with the concentration of xenon adsorbed (T=295 K) on 15 wt% $Pt(NH_3)_4^{2+}$–NaY zeolite samples calcined at different temperatures. The effect of cooling rate on the calcined Pt–NaY samples is shown.

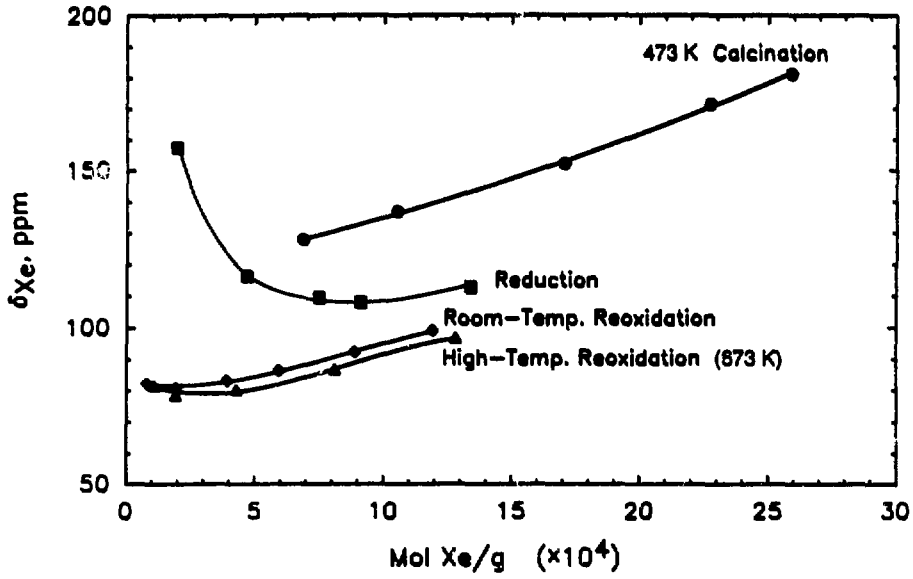

Figure B.3: Variation in ^{129}Xe chemical shift with the concentration of xenon adsorbed (T=295 K) on 15 wt% Pt–NaY after each of the following treatments: initial calcination at 473 K, reduction at 673 K, chemisorption of oxygen at 295 K, and reoxidation at 673 K.

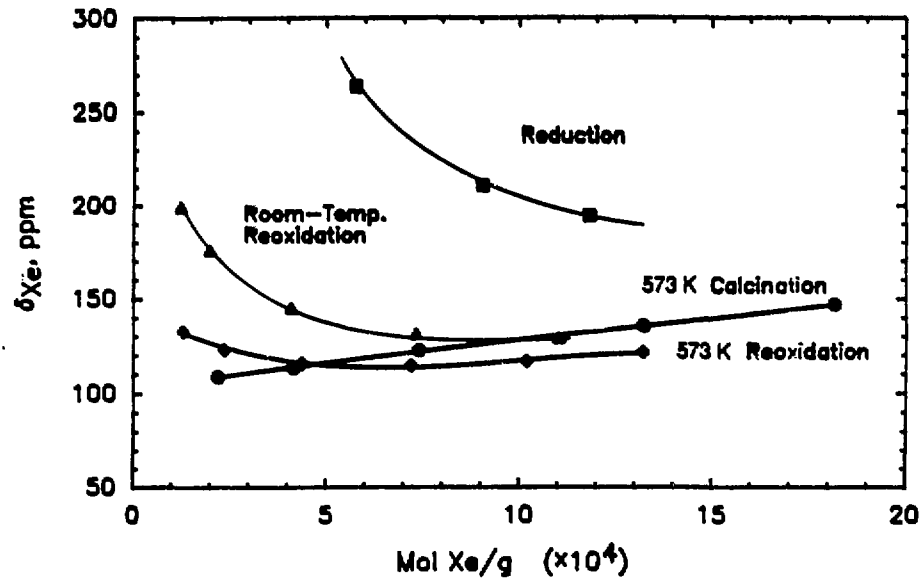

Figure B.4: Variation in ^{129}Xe chemical shift with the concentration of xenon adsorbed (T=295 K) on 15 wt% Pt–NaY after each of the following treatments: initial calcination at 573 K, reduction at 673 K, chemisorption of oxygen at 295 K, and reoxidation at 573 K.

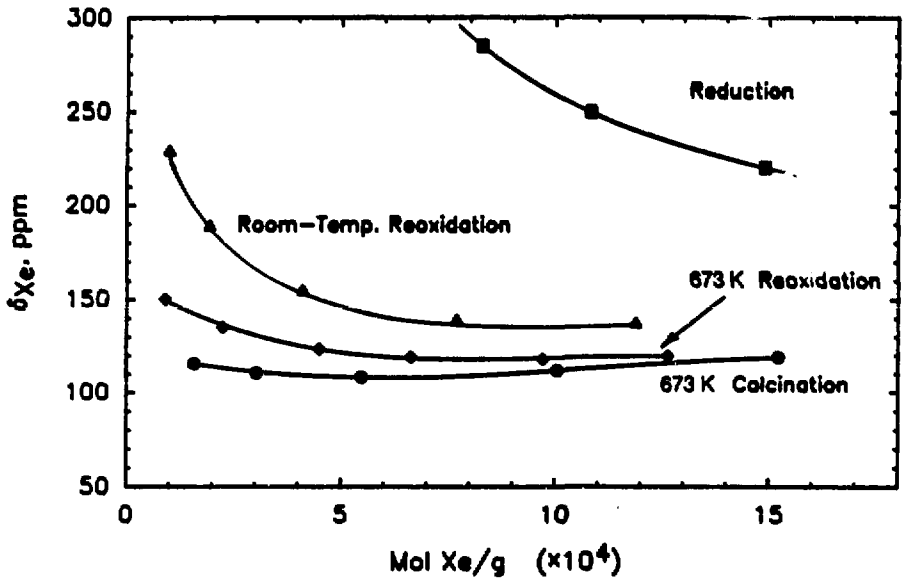

Figure B.5: Variation in ^{129}Xe chemical shift with the concentration of xenon adsorbed (T=295 K) on 15 wt% Pt-NaY after each of the following treatments: initial calcination at 673 K, reduction at 673 K, chemisorption of oxygen at 295 K, and reoxidation at 673 K.

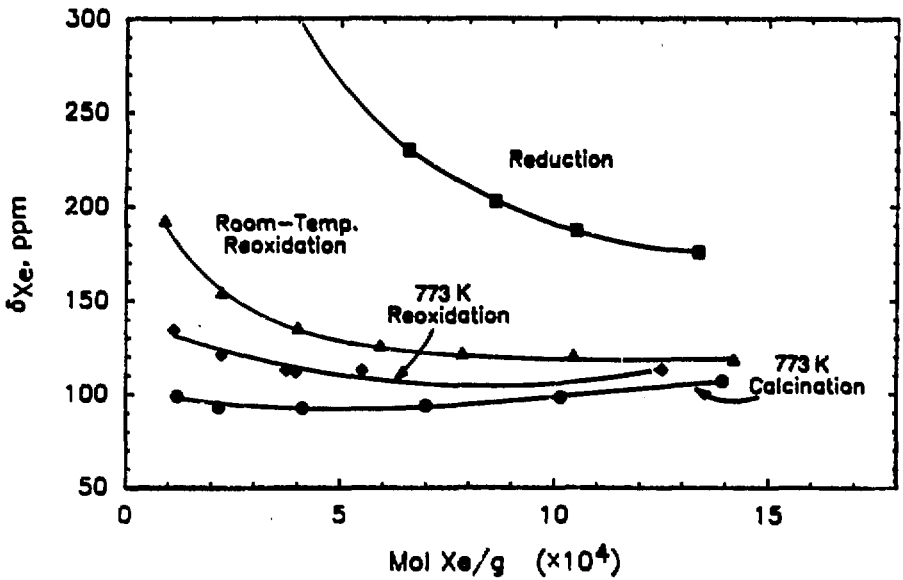

Figure B.6: Variation in ^{129}Xe chemical shift with the concentration of xenon adsorbed (T=295 K) on 15 wt% Pt–NaY after each of the following treatments: initial calcination at 773 K, reduction at 673 K, chemisorption of oxygen at 295 K, and reoxidation at 773 K.

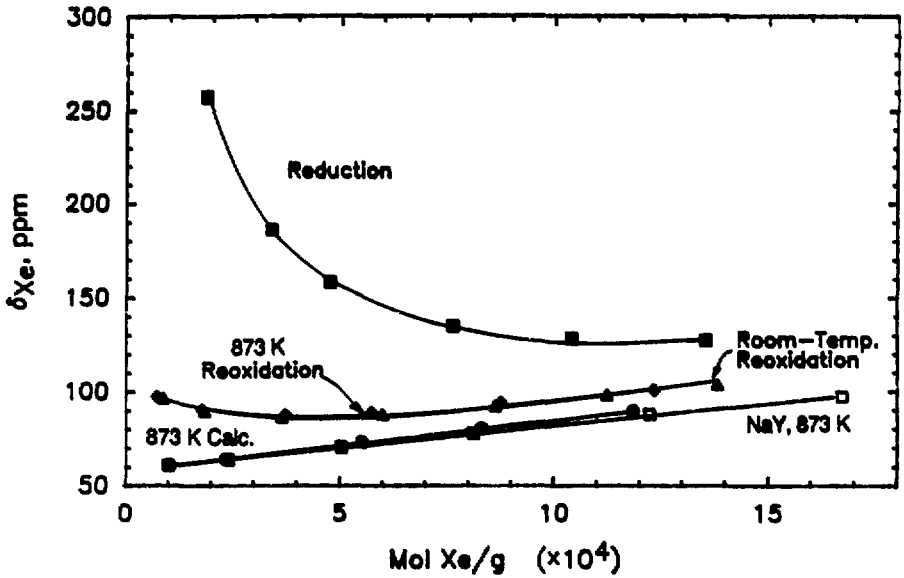

Figure B.7: Variation in ^{129}Xe chemical shift with the concentration of xenon adsorbed (T=295 K) on 15 wt% Pt-NaY after each of the following treatments: initial calcination at 873 K, reduction at 673 K, chemisorption of oxygen at 295 K, and reoxidation at 873 K.

B.3 Data Reproducibility

Figure B.8 demonstrates the reproducibility of the sample preparation procedures and the ^{129}Xe NMR methods. Different batches of 15 wt% $Pt(NH_3)_4^{2+}$–NaY zeolite samples were ion-exchanged separately and then calcined at 673 K as described in Chapter 2. The ^{129}Xe chemical shift data for the two samples are in good agreement.

B.4 Dehydration of the NaY Support

Though dehydration of NaY is thought to be complete after in vacuo heating overnight at 673 K [1,35,43], the ^{129}Xe NMR data in Figure B.9 indicate significant changes in the NaY support as a result of more severe thermal treatment at 873 K. These changes are reflected also in greater xenon adsorption on NaY heated to 873 K as shown in Figure B.10. The lower ^{129}Xe chemical shift values in NaY treated at 873 K is due likely to desorption of strongly adsorbed water from the zeolite supercages, providing more spacious adsorption environments for the xenon probe species.

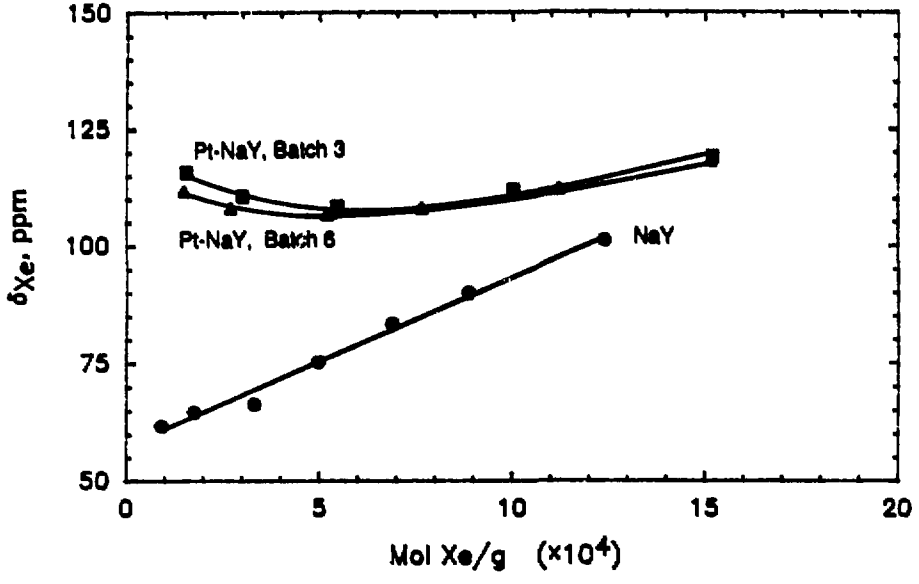

Figure B.8: Variation in ^{129}Xe chemical shift with the concentration of xenon adsorbed (T=295 K) on 15 wt% Pt-NaY samples calcined at 673 K. The catalysts were prepared in separate ion-exhange/calcination procedures to test reproducibility of the treatment methods and the NMR data. The ^{129}Xe chemical shift of xenon adsorbed or dehydrated NaY is shown for reference purposes.

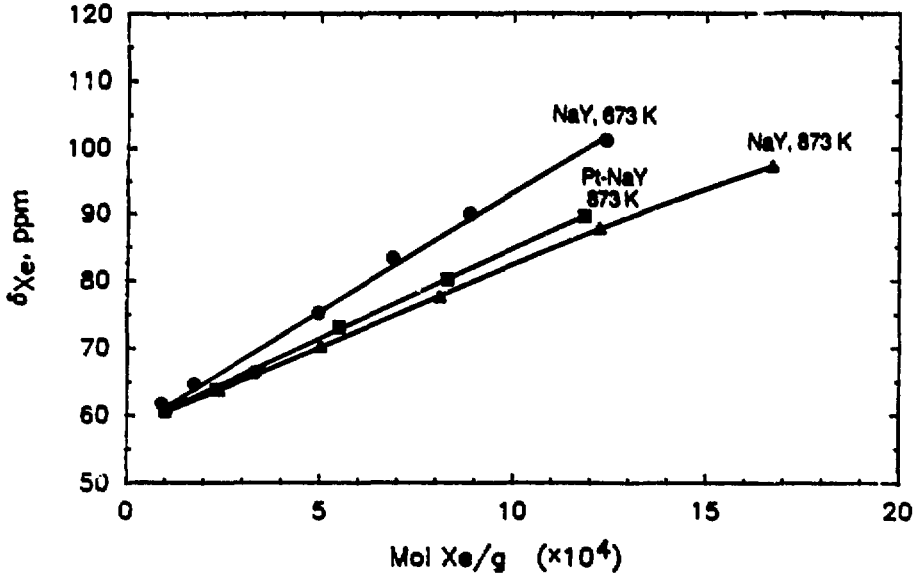

Figure B.9: Variation in ^{129}Xe chemical shift with the concentration of xenon adsorbed (T=295 K) on NaY samples dehydrated at 673 K and 873 K. The ^{129}Xe chemical shift of xenon adsorbed on 15 wt% Pt–NaY samples calcined at 873 K is shown for reference purposes.

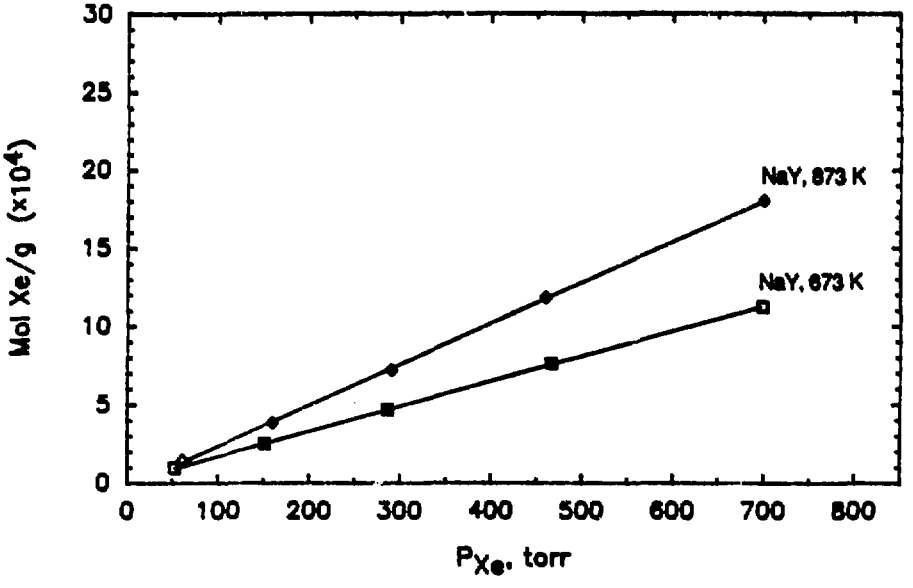

Figure B.10: Adsorption isotherms of xenon (T=295 K) on NaY zeolite samples dehydrated at 673 K and 873 K.

Appendix C

Divalent Metal Guests in NaY

Small divalent cations, such as Ca^{2+} and Mg^{2+}, have high charge densities that may dissociate intrazeolitic water according to the reaction [182]

$$M^{2+}(OH_2)_n \rightleftharpoons MOH^+ + H^+, \qquad (C.1)$$

where M represents a divalent metal species. Under such circumstances, the anionic charges on the Y zeolite lattice are balanced, by a partially hydrolyzed metal cation and by a Brönsted proton. Larger divalent species, such as $Pt(NH_3)_4^{2+}$ and Ba^{2+}, possess lower charge densities that are less apt to induce hydrolysis. For these species, therefore, the equilibrium lies farther to the left, requiring single divalent cations to be shared between two anionic lattice sites. Infrared spectoscopy studies and zeolite acidity measurements [182] support this view, which has ramifications to the behavior of xenon adsorbed on Y zeolites containing divalent guests . Since the shielding of the xenon probe atoms is a function of the local electrostatic fields produced by the exchangeable cations, xenon uptake by the zeolite and the ^{129}Xe chemical shift will be affected by the distribution and charge density of the charge-balancing species and other guests present. In Figure C.1 the high ^{129}Xe chemical shifts registered for xenon adsorbed on dehydrated Y zeolite samples containing

$Pt(NH_3)_4^{2+}$ and Ba^{2+}, for example, indicate the less shielded nature of the non-hydrolyzed cations. On the other hand, the low ^{129}Xe shifts for xenon adsorbed on $Mg_{0.71}Y$ are consistent with formation of $MgOH^+$ [182], since unshielded Mg^{2+} is expected to produce a high local field and thus a large ^{129}Xe shift as a result of its high charge density. Figure C.2 shows similar xenon adsorption behaviors in dehydrated Y zeolites containing magnesium ($MgOH^+$) and calcined platinum (PtO) guests. In Figure C.1 the comparable chemical shifts of ^{129}Xe adsorbed on the $Mg_{0.71}Y$ and PtO–HY samples indicate that the electrostatic environment of the zeolite supercages is much the same in the two cases. Based on charge-density arguments alone, one might expect the formation of $PtOH^+$ species according to Equation C.1, since Pt^{2+} and Mg^{2+} are very similar in size (0.148 nm and 0.142 nm respectively.) An ionic species such as $PtOH^+$, however, would necessarily occupy discrete ion-exchange sites on the lattice to maintain effectively the electrical neutrality of the system. Following calcination at 673 K, the clustering of the metal species observed in TEM micrographs [Chapter 3] rules out $PtOH^+$ as a candidate for the primary product of calcination.

Moreover, darkening of the Pt–NaY sample during in vacuo heating at 673 K is consistent with the formation of PtO aggregates. (CaY and MgY samples dehydrated under identical conditions are white.) In the absence of flowing oxygen, it likely that interstitial water in Y zeolite's hydrophilic cavities serves as the oxidizing agent. The large number of clusters visible above the 3-nm TEM resolution limit in Figure C.3 indicates more migratory character on the part of the metal species during in vacuo heating than when calcination is undertaken in flowing oxygen [10].

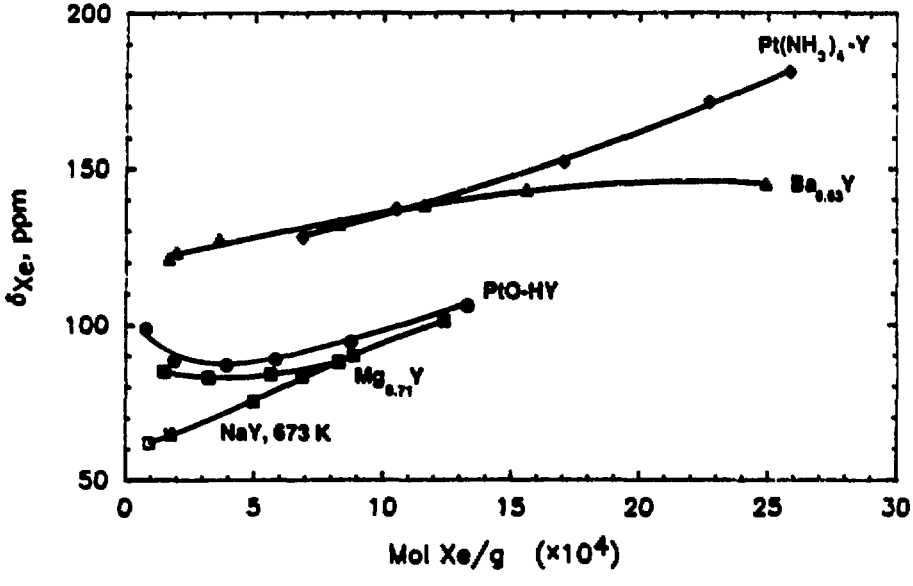

Figure C.1: Variation in ^{129}Xe chemical shift with the concentration of xenon adsorbed (T=295 K) on dehydrated Y zeolites containing different divalent metal guests. The $Mg_{0.71}Y$ and $Ba_{0.63}Y$ materials were dehydrated in vacuo at 673 K for 8 h, while the $Pt(NH_3)_4^{2+}$-NaY sample was dehydrated in flowing oxygen at 473 K as described in Chapter 2. The data for $Mg_{0.71}Y$ and $Ba_{0.63}Y$ are taken from reference [39]. The ^{129}Xe chemical shift of xenon adsorbed on dehydrated NaY is shown for reference purposes.

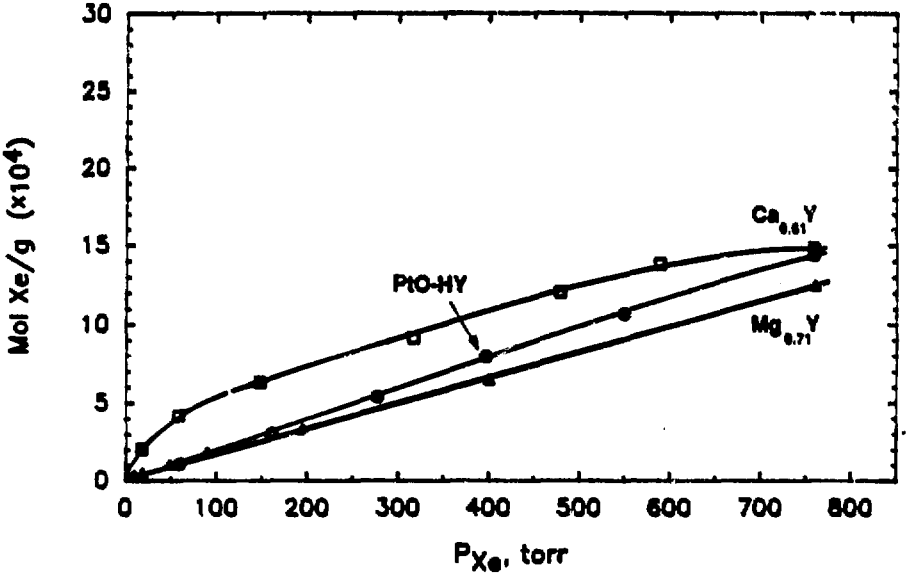

Figure C.2: Adsorption isotherms of xenon (T=295 K) on $Ca_{0.61}Y$ [35], $Mg_{0.71}Y$ [39], and 15 wt% PtO–HY samples. The $Ca_{0.61}Y$ and $Mg_{0.71}Y$ materials were dehydrated in vacuo at 673 K for 8 h, while the PtO–HY sample was calcined in flowing oxygen at 673 K as described in Chapter 2.

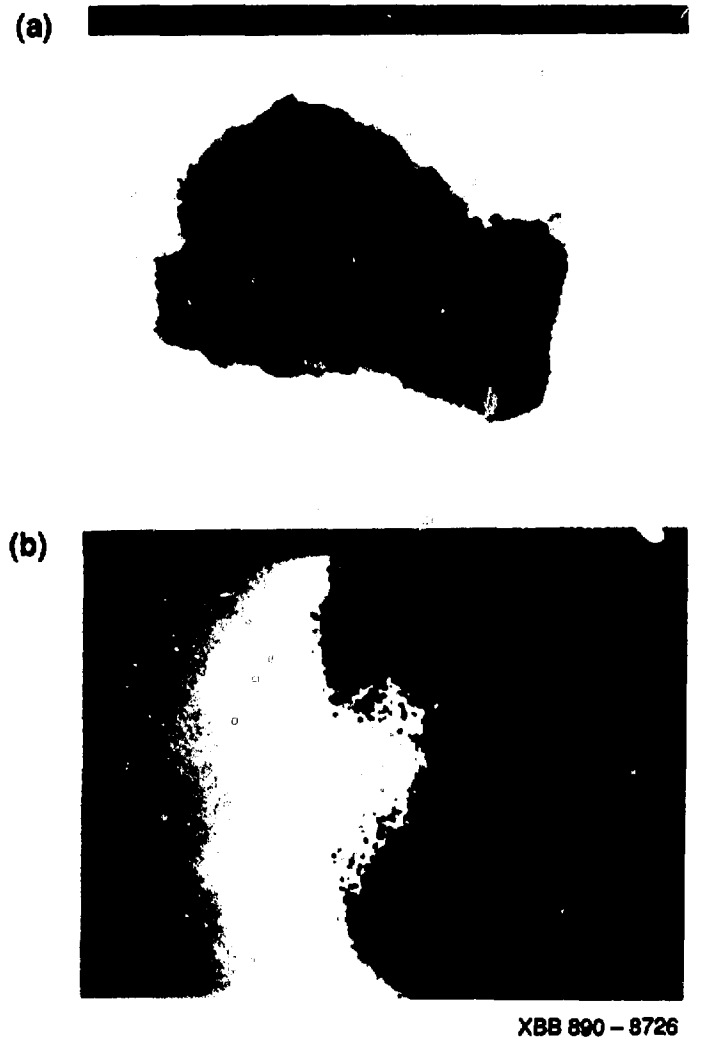

Figure C.3: Transmission electron micrographs of 15 wt% $Pt(NH_3)_4^{2+}$-NaY after heating to 673 K under vacuum: (a) A low magnification view (x52,000) of a single zeolite crystallite and (b) a high magnification view (x200,000) showing evidence of metal aggregates (probably PtO).

Appendix D

Xenon Adsorption on Zeolites

D.1 Xenon Adsorption on Y-type Zeolites

D.1.1 Experimental Procedures

Room-temperature adsorption isotherms of xenon in Y zeolites are required to correlate ^{129}Xe NMR chemical shift data with the concentration of xenon adsorbed on the samples. The amount of xenon adsorbed on a surface is determined by subtracting the xenon mass in the gaseous sample atmosphere at equilibrium from the total mass of xenon charged to the system. For the procedural discussion which follows, refer to the adsorption apparatus diagrammed in Figure D.1.

Sample Volume Measurements with Helium

The bulb volume V_0 is known to be 55.76 cm^3 from separate H_2O mass/volume measurements. Xenon uptake experiments require volumes V_1 (bounded by the pressure gauge and stopcocks 1, 2, 3, and 5), V_2 (bounded by stopcocks 3 and 4) and V_3 (in the sample cell below stopcock 4) to be known precisely. Xenon behaves as an ideal

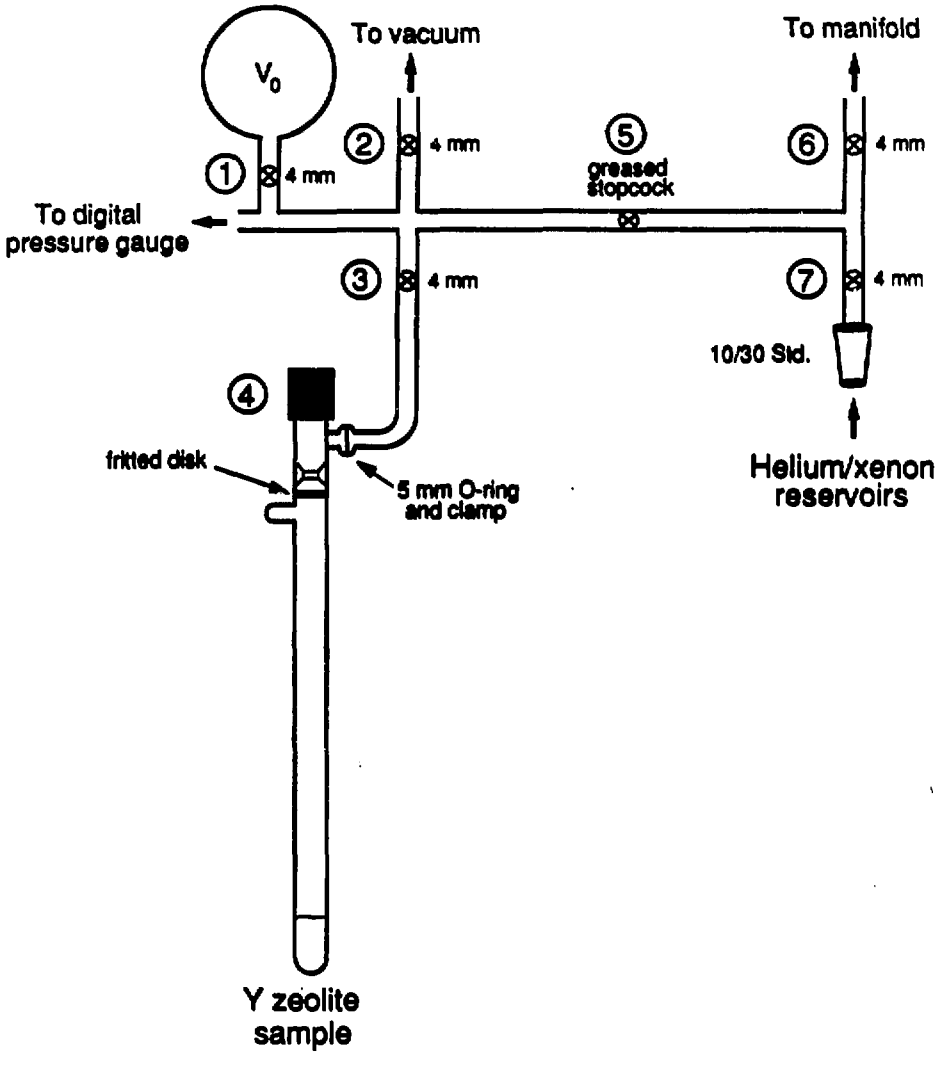

Figure D.1: Apparatus for measuring xenon adsorption isotherms in Y zeolite samples.

gas at pressures on the order of 1 atm or less [49], permitting V_1, V_2, and V_3 to be determined easily from measurement of helium pressure in these regions.

1. With all stopcocks initially closed, evacuate the manifold and bulb V_0 shown in Figure D.1 by opening stopcocks 1, 2, and 5.

2. Purge all air from the helium loading hose by flowing ultrahigh purity (UHP) helium gas (99.999+% He) for 5 minutes.

3. Close stopcock 2 and open stopcock 7 to charge $\approx$ 1 atm He to the adsorption apparatus.

4. Since some air will unavoidably enter the system as a result of the non-purged volume between stopcock 7 and the He hose connection, it is necessary to re-evacuate the apparatus to remove all contaminant gases. Close stopcock 7 to isolate the apparatus from the helium source. Open stopcock 2 to evacuate the system. Repeat the fill/purge cycle four times.

5. With the apparatus evacuated after the final fill/purge cycle, close stopcock 2 and then open stopcock 7 to charge $\approx$ 1 atm UHP helium gas to the system. Close stopcock 7.

6. Close stopcock 1 to isolate UHP helium in bulb volume V_0. Record the pressure measured by the digital gauge.

7. Open stopcock 2 to evacuate the manifold. Disconnect and store the helium loading assembly. Close stopcock 5.

8. Open stopcock 3 to evacuate volume V_2.

9. Open stopcock 4 to evacuate sample cell volume V_3. Outgas to ca. 10^{-5} torr.

10. Close stopcocks 4, 3, and 2 (sequentially in the order listed.)

11. Open stopcock 1. Record He pressure P_{01} in volume ($V_0 + V_1$). Record the ambient temperature.

12. Open stopcock 3. Record He pressure P_{012} in volume ($V_0 + V_1 + V_2$).

13. Open stopcock 4. Record He pressure P_{0123} in volume ($V_0 + V_1 + V_2 + V_3$). Since He does not adsorb on the zeolite sample, no equilibration time is required between helium addition and measurement of the system pressure.

14. Close stopcock 1 and record the new pressure P_0.

15. Open stopcock 2 to re-evacuate volumes V_1, V_2, and V_3 to ca. 10^{-5} torr.

16. Repeat steps 10–13 at different He pressures to obtain a series of redundant volume measurements from which mean values of the respective volumes can be computed.

17. Open stopcocks 1, 2, 3, and 4 to remove all helium from the adsorption apparatus. (Stopcocks 5, 6, and 7 remain closed.) Outgas to ca. 10^{-5} torr, then close stopcock 4 to isolate the sample.

Xenon Adsorption Measurements

Liquid nitrogen readily condenses xenon (normal melting and boiling points of 161 K and 163 K, respectively), allowing xenon to be manipulated easily to desired regions of the adsorption apparatus. Taking care to prevent contamination by air or moisture, essentially all of the xenon used during the adsorption isotherm experiments can be recovered for reuse. Make certain a xenon trap (immersed in a liquid nitrogen bath at 77 K) is installed between the vacuum pumps and the adsorption apparatus

to prevent loss of Xe in the event of accidental xenon evacuation into the vacuum line.

1. Continuing from step 17 above, attach a valved Xe reservoir to the port beneath stopcock 7.

2. Open stopcocks 1, 2, 3, 5, and 7 to evacuate the manifold to the Xe reservoir valve (not shown). Stopcocks 4 and 6 remain closed.

3. Close stopcock 2 to isolate the manifold from the vacuum line.

4. Close stopcock 5, and then open stopcock 7 to charge Xe gas to the isolated, right-half of the manifold.

5. Slowly charge xenon gas to the left-half of the manifold by slowly opening stopcock 5. (The greased stopcock permits Xe flow to be throttled carefully.) Close stopcock 5. Record Xe pressure P_{01} in volume $(V_0 + V_1)$. Record the ambient temperature.

6. Open stopcock 3. Record Xe pressure P_{012} in volume $(V_0 + V_1 + V_2)$.

7. Open stopcock 4. Allow approximately 20 minutes for the adsorption process to equilibrate, then record Xe pressure P_{0123} in volume $(V_0 + V_1 + V_2 + V_3)$.

8. Close stopcock 4 to isolate Xe in the sample cell.

9. Using liquid nitrogen, condense all xenon remaining in the manifold back into the main Xe reservoir beneath stopcock 7. When the xenon pressure in the manifold has dropped to approximately zero torr, close stopcocks 3 and 5, and remove the liquid nitrogen bath from the Xe reservoir.

10. Repeat steps 5–9 at progressively higher Xe pressures until $P_{0123} \approx 1$ atm at equilibrium.

11. The total moles of xenon, n^{ads}_{0123}, adsorbed on the zeolite sample can be computed at each equilibrium loading pressure P_{0123} using the ideal gas law and a xenon mass balance:

$$n^{ads}_{0123,i} = \left(n_{3,i-1} + n^{ads}_{0123,i-1} + \frac{(n_{01} + n_{012})_i}{2} \right) - n_{0123,i}, \qquad (D.1)$$

where i represents a given equilibrium pressure measurement,

n_3 is the moles of xenon in the atmosphere of volume V_3,

n_{01} is the moles of xenon in the atmosphere of volume $(V_0 + V_1)$,

n_{012} is the moles of xenon in the atmosphere of volume $(V_0 + V_1 + V_2)$,

and n_{0123} is the moles of xenon in the atmosphere of volume $(V_0 + V_1 + V_2 + V_3)$.

D.1.2 Xenon Adsorption Data on NaY and Pt–NaY

Room-temperature adsorption isotherms are presented for xenon on dehydrated NaY and Pt–NaY zeolites after modification by different thermal, oxidation, reduction, and/or reoxidation treatments. Tables D.1 and D.2 list the adsorption data which follow.

Table D.1: Index of Xe adsorption isotherm data.

Isotherm	Sample description
1	NaY dehydrated under vacuum at 673 K
2	NaY dehydrated under vacuum at 873 K
3	15 wt% $Pt(NH_3)_4^{2+}$–NaY heated under vacuum to 673 K
4	15 wt% $Pt(NH_3)_4^{2+}$–NaY calcined at 473 K, slow cool
5	15 wt% $Pt(NH_3)_4^{2+}$–NaY calcined at 473 K, fast cool
6	sample 4 reduced at 673 K
7	sample 6 reoxidized at room temperature
8	sample 7 reoxidized at 673 K
9	15 wt% $Pt(NH_3)_4^{2+}$–NaY calcined at 573 K, slow cool
10	15 wt% $Pt(NH_3)_4^{2+}$–NaY calcined at 573 K, fast cool
11	sample 9 reduced at 673 K
12	sample 11 reoxidized at room temperature
13	sample 12 reoxidized at 573 K
14	15 wt% $Pt(NH_3)_4^{2+}$–NaY calcined at 673 K, slow cool
15	15 wt% $Pt(NH_3)_4^{2+}$–NaY calcined at 673 K, fast cool
16	15 wt% $Pt(NH_3)_4^{2+}$–NaY calcined at 673 K, reproducibility test
17	sample 14 reduced at 673 K, O_2 contaminated at 298 K
18	sample 17 reduced at 673 K
19	sample 18 reoxidized at room temperature
20	sample 19 reoxidized at 673 K
21	15 wt% $Pt(NH_3)_4^{2+}$–NaY calcined at 773 K, slow cool

Table D.2: Index of Xe adsorption isotherm data, continued.

Isotherm	Sample description
22	15 wt% $Pt(NH_3)_4^{2+}$–NaY calcined at 773 K, fast cool
23	sample 21 reduced at 673 K
24	sample 23 reoxidized at room temperature
25	sample 24 reoxidized at 773 K
26	15 wt% $Pt(NH_3)_4^{2+}$–NaY calcined at 873 K, slow cool
27	sample 26 reduced at 673 K
28	sample 27 reoxidized at room temperature
29	sample 28 reoxidized at 873 K
30	0.5 wt% $Pt(NH_3)_4^{2+}$–NaY calcined at 673 K, slow cool
31	sample 30 reduced at 673 K
32	1.0 wt% $Pt(NH_3)_4^{2+}$–NaY calcined at 673 K, slow cool
33	sample 32 reduced at 673 K
34	4.1 wt% $Pt(NH_3)_4^{2+}$–NaY calcined at 673 K, slow cool
35	sample 34 reduced at 673 K

(1)

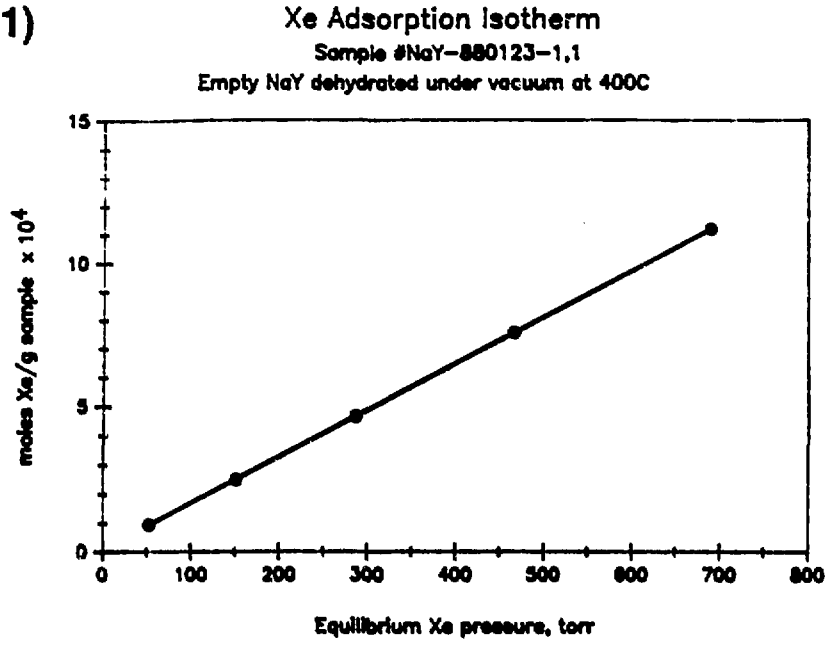
Xe Adsorption Isotherm
Sample #NaY-880123-1,1
Empty NaY dehydrated under vacuum at 400C
moles Xe/g sample x 10⁴
0
5
10
15
0
100
200
300
400
500
600
700
800
Equilibrium Xe pressure, torr

(2)

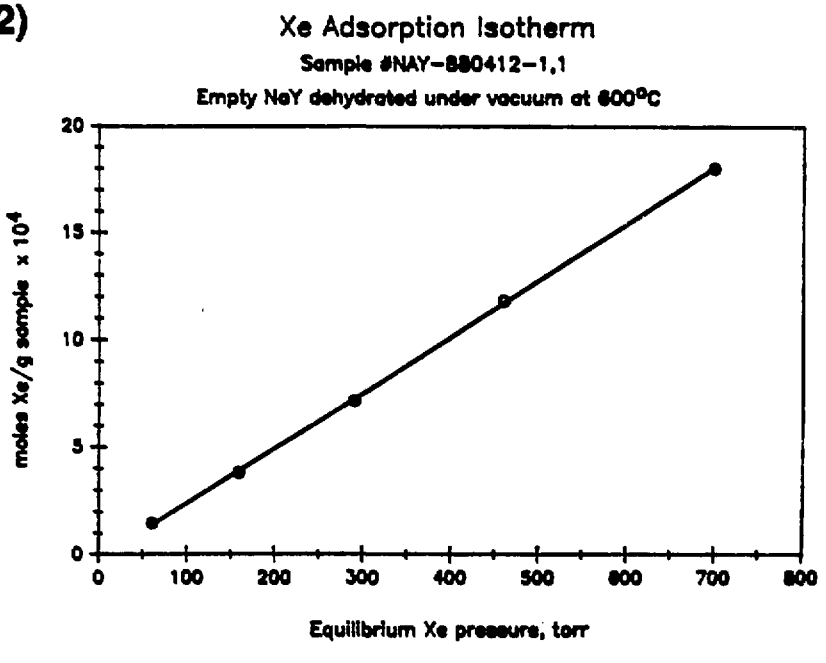
Xe Adsorption Isotherm
Sample #NAY-880412-1,1
Empty NaY dehydrated under vacuum at 600°C
moles Xe/g sample x 10⁴
0
5
10
15
20
0
100
200
300
400
500
600
700
800
Equilibrium Xe pressure, torr

(3)

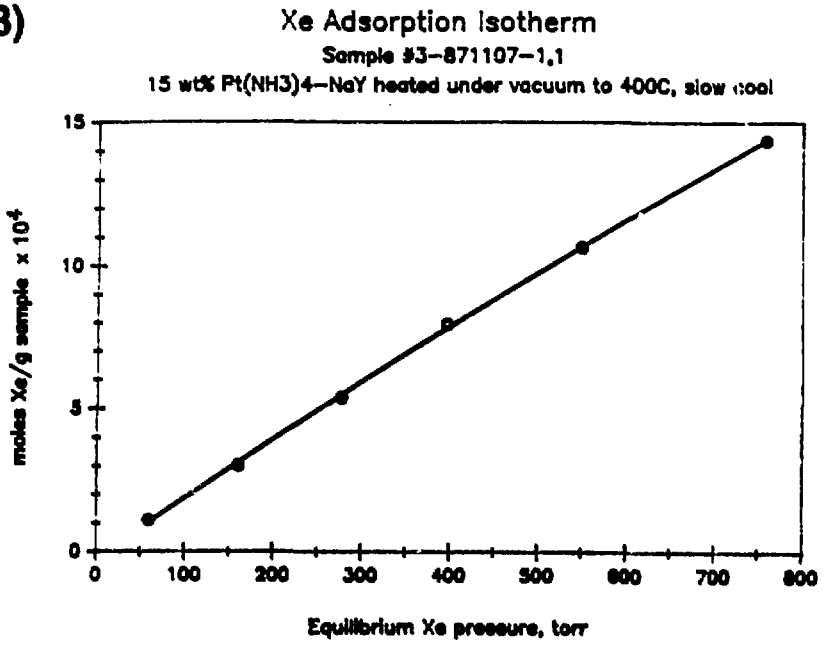
Xe Adsorption Isotherm
Sample #3-871107-1,1
15 wt% Pt(NH3)4-NaY heated under vacuum to 400C, slow cool
moles Xe/g sample x 10^4
0
5
10
15
0
100
200
300
400
500
600
700
800
Equilibrium Xe pressure, torr

(4)

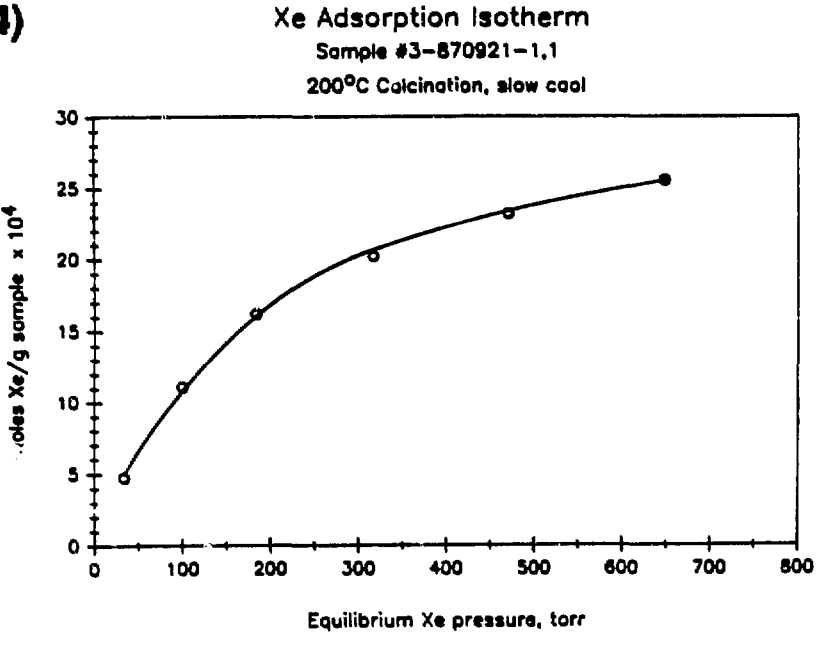
Xe Adsorption Isotherm
Sample #3-870921-1,1
200°C Calcination, slow cool
oles Xe/g sample x 10^4
0
5
10
15
20
25
30
0
100
200
300
400
500
600
700
800
Equilibrium Xe pressure, torr

(5)

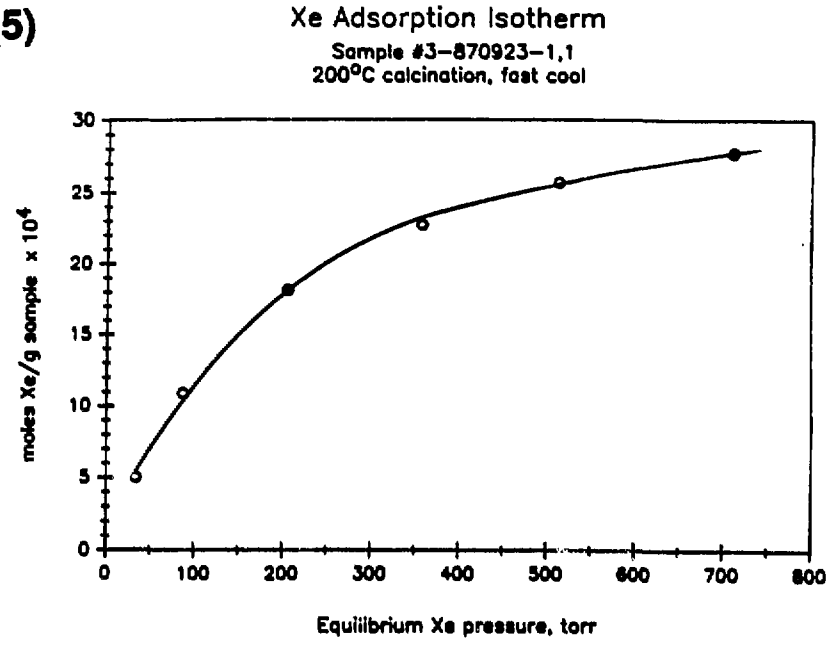
Xe Adsorption Isotherm
Sample #3-870923-1,1
200°C calcination, fast cool
moles Xe/g sample x 10⁴
0
5
10
15
20
25
30
0
100
200
300
400
500
600
700
800
Equilibrium Xe pressure, torr

(6)

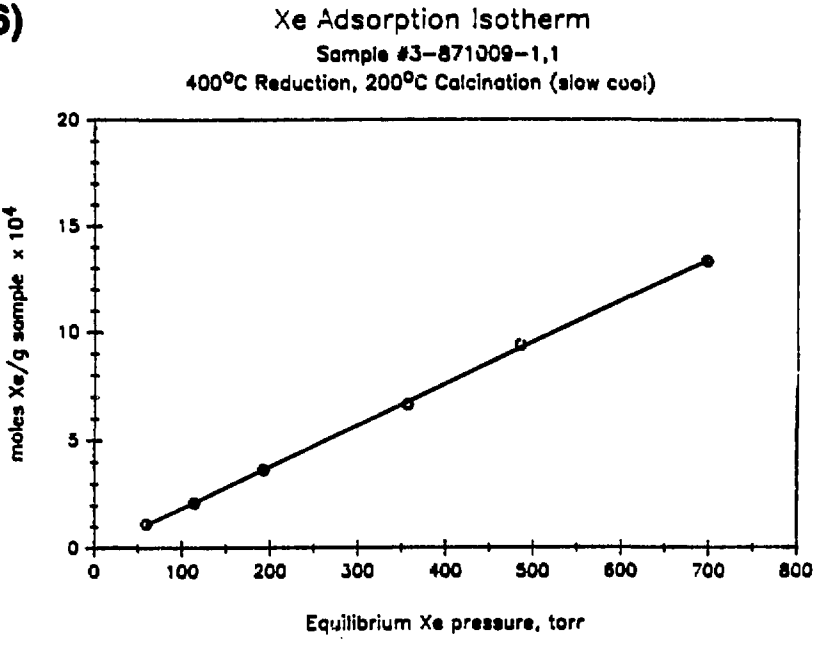
Xe Adsorption Isotherm
Sample #3-871009-1,1
400°C Reduction, 200°C Calcination (slow cool)
moles Xe/g sample x 10⁴
0
5
10
15
20
0
100
200
300
400
500
600
700
800
Equilibrium Xe pressure, torr

(7)

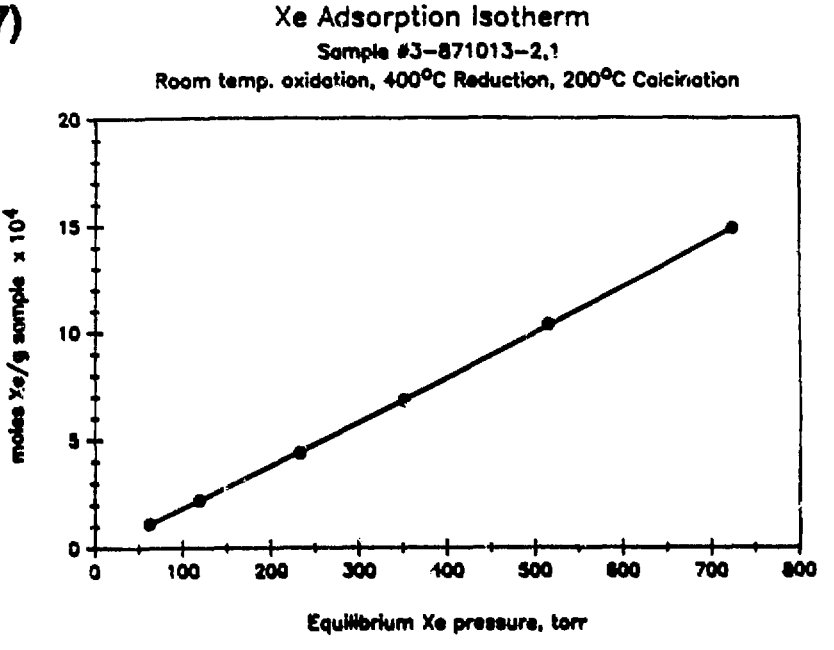
Xe Adsorption Isotherm
Sample #3-871013-2,1
Room temp. oxidation, 400°C Reduction, 200°C Calcination
moles Xe/g sample x 10⁴
0
5
10
15
20
0
100
200
300
400
500
600
700
800
Equilibrium Xe pressure, torr

(8)

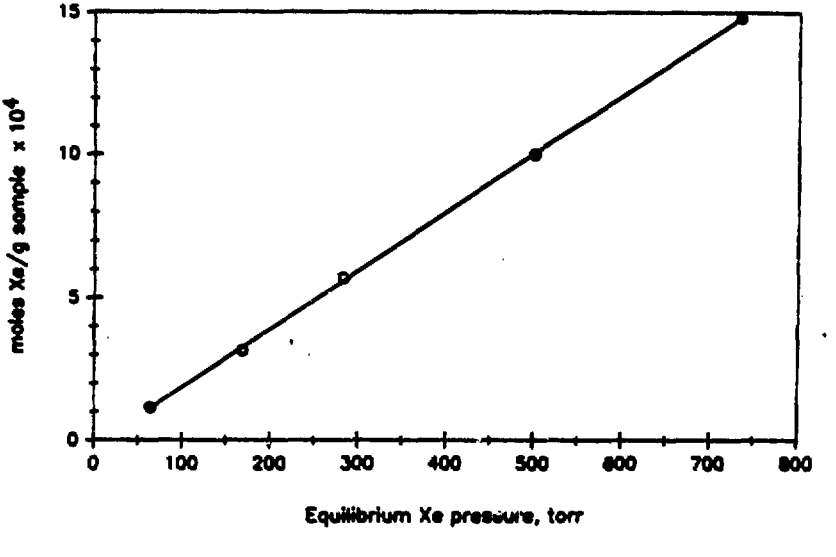
Xe Adsorption Isotherm
Sample #3-871031-1,1
200C calc./400C red.(2X)/22C oxid./400C recalcination
moles Xe/g sample x 10⁴
0
5
10
15
0
100
200
300
400
500
600
700
800
Equilibrium Xe pressure, torr

(9)

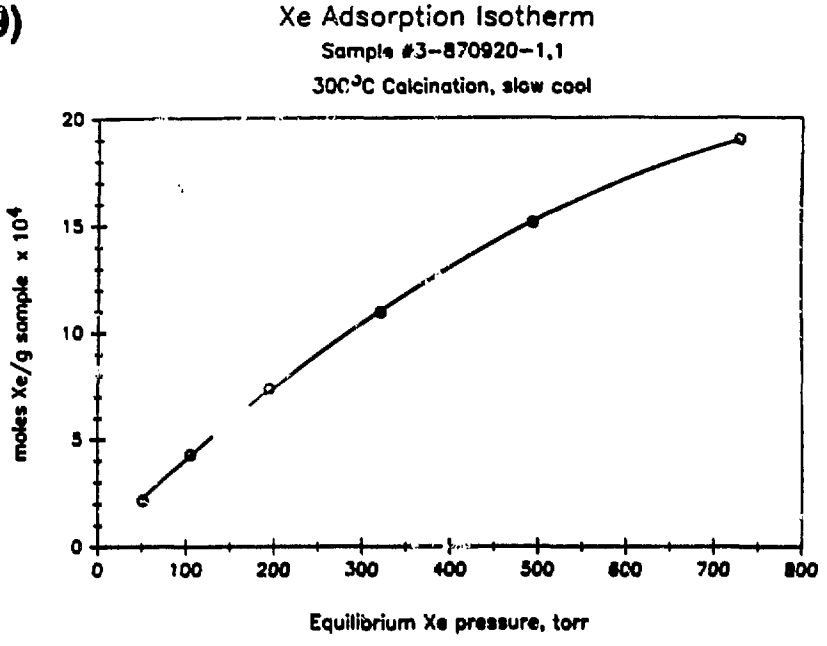
Xe Adsorption Isotherm
Sample #3-870920-1,1
300°C Calcination, slow cool
moles Xe/g sample x 10^4
0
5
10
15
20
0
100
200
300
400
500
600
700
800
Equilibrium Xe pressure, torr

(10)

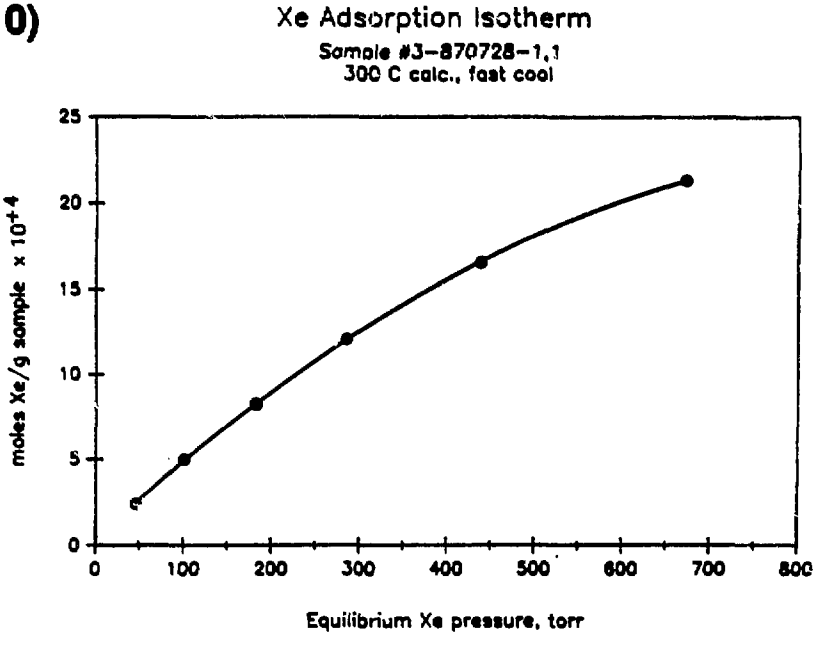
Xe Adsorption Isotherm
Sample #3-870728-1,1
300 C calc., fast cool
moles Xe/g sample x 10^+4
0
5
10
15
20
25
0
100
200
300
400
500
600
700
800
Equilibrium Xe pressure, torr

(11)

Xe Adsorption Isotherm

Sample #3-871011-1,1

400°C Reduction, 300°C Calcination (fast cool)

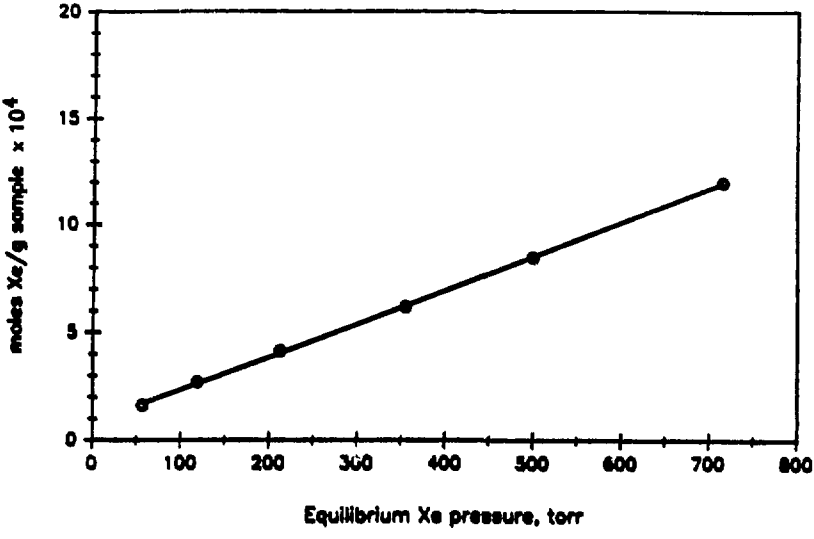

(12)

Xe Adsorption Isotherm

Sample #3-871013-2,2

Room temp. oxidation, 400°C Reduction, 300°C Calcination

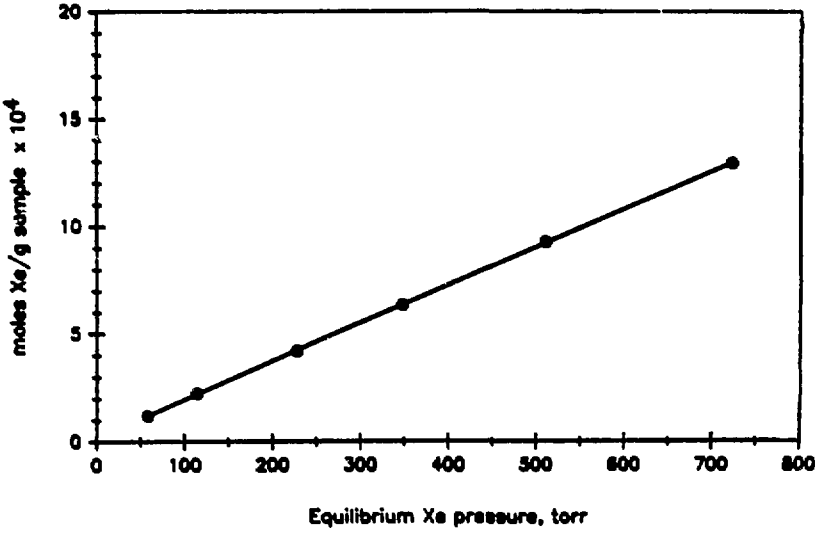

(13)

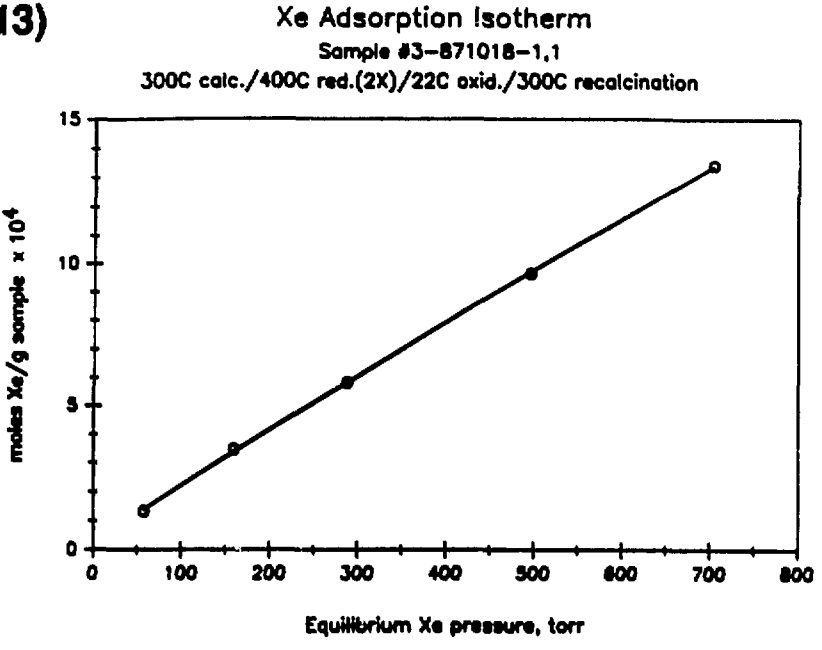
Xe Adsorption Isotherm
Sample #3-871018-1,1
300C calc./400C red.(2X)/22C oxid./300C recalcination
moles Xe/g sample x 10^4
Equilibrium Xe pressure, torr
0
5
10
15
0
100
200
300
400
500
600
700
800

(14)

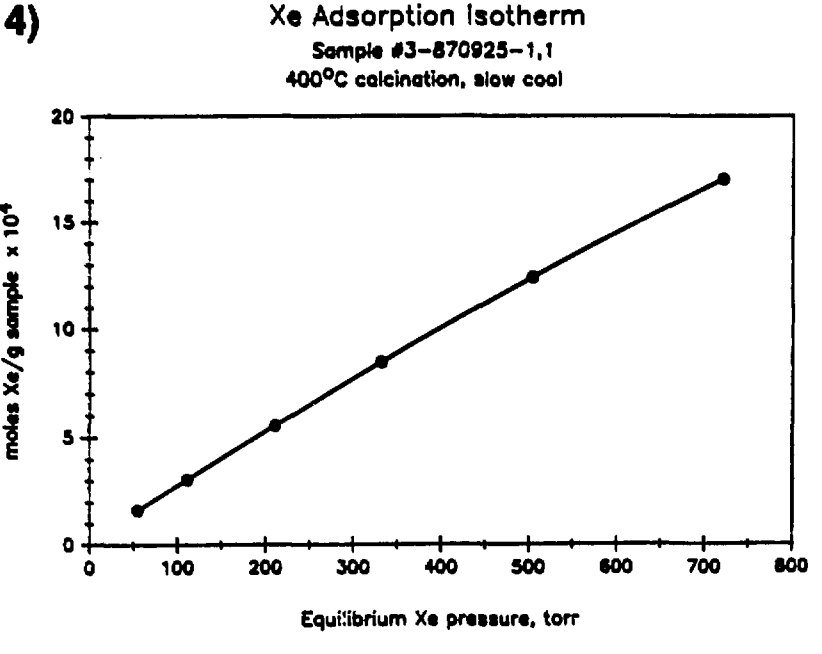
Xe Adsorption Isotherm
Sample #3-870925-1,1
400°C calcination, slow cool
moles Xe/g sample x 10^4
Equilibrium Xe pressure, torr
0
5
10
15
20
0
100
200
300
400
500
600
700
800

(15)

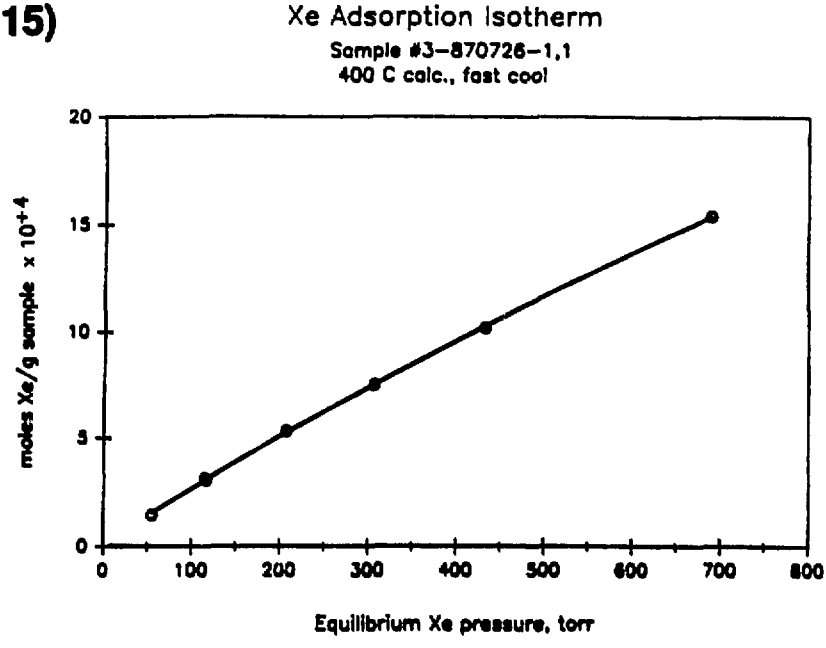
Xe Adsorption Isotherm
Sample #3-870726-1,1
400 C calc., fast cool
moles Xe/g sample x 10^+4
0
5
10
15
20
0
100
200
300
400
500
600
700
800
Equilibrium Xe pressure, torr

(16)

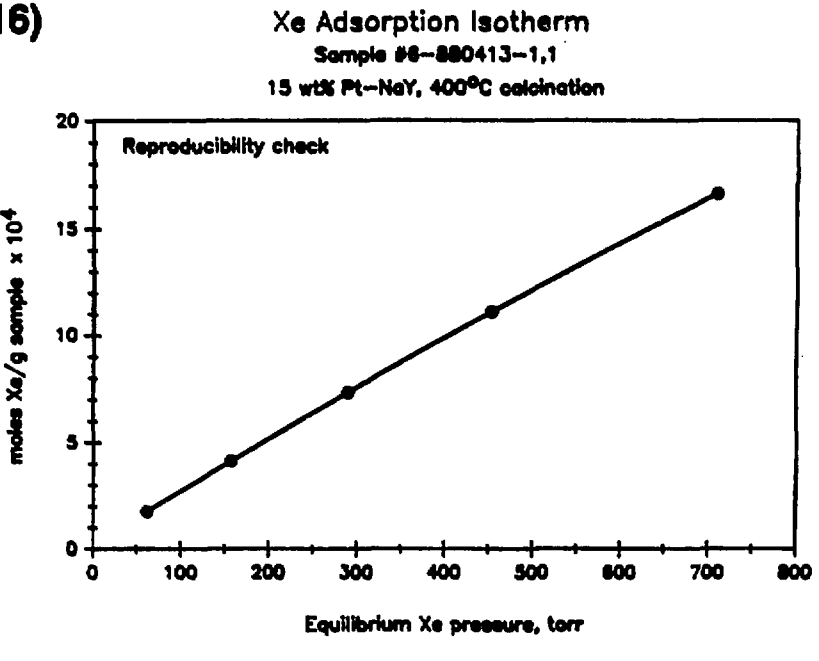
Xe Adsorption Isotherm
Sample #6-880413-1,1
15 wt% Pt-NaY, 400°C calcination
Reproducibility check
moles Xe/g sample x 10^4
0
5
10
15
20
0
100
200
300
400
500
600
700
800
Equilibrium Xe pressure, torr

(17)

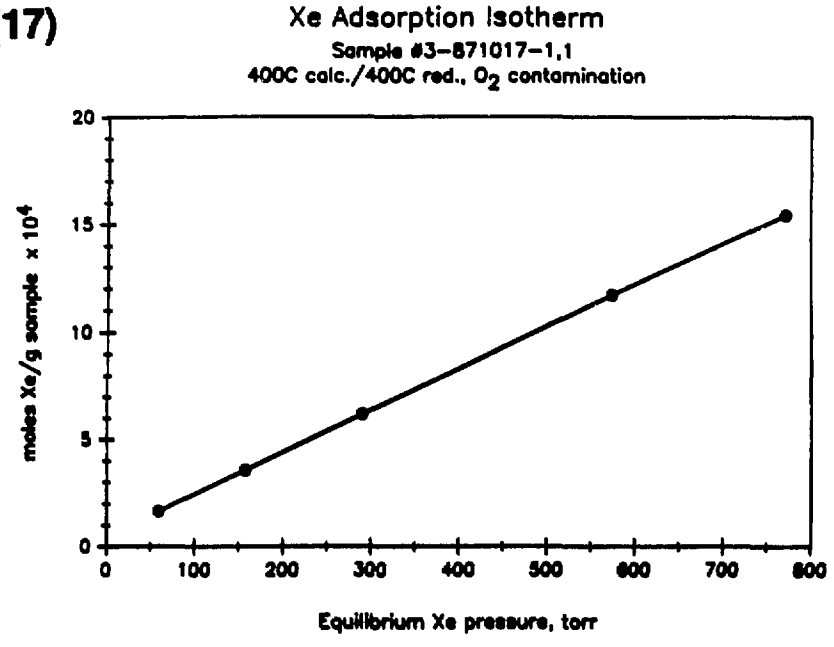
Xe Adsorption Isotherm
Sample #3-871017-1,1
400C calc./400C red., O_2 contamination
moles Xe/g sample x 10^4
0
5
10
15
20
0
100
200
300
400
500
600
700
800
Equilibrium Xe pressure, torr

(18)

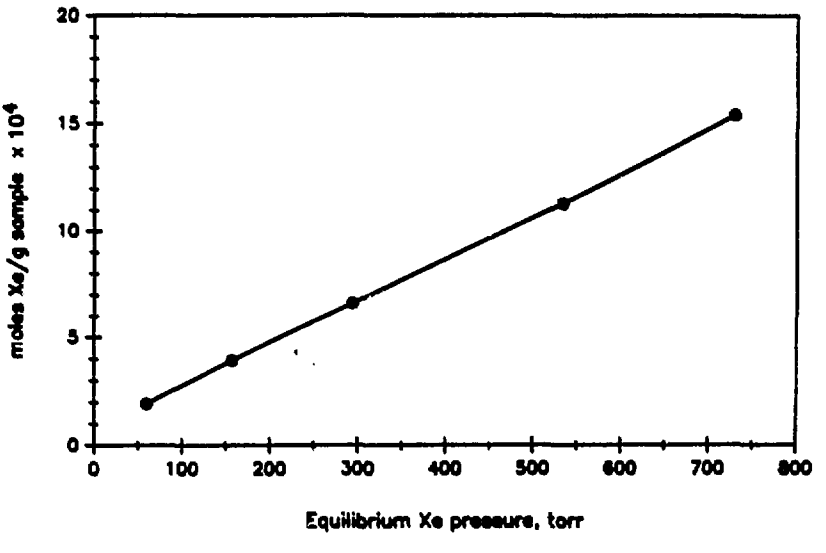
Xe Adsorption Isotherm
Sample #3-871028-1,1
400C calc./400C red. (2X)
moles Xe/g sample x 10^4
0
5
10
15
20
0
100
200
300
400
500
600
700
800
Equilibrium Xe pressure, torr

(19)

Xe Adsorption Isotherm

Sample #3-871030-1,1

400C calc./400C red. (2X)/22C oxidation

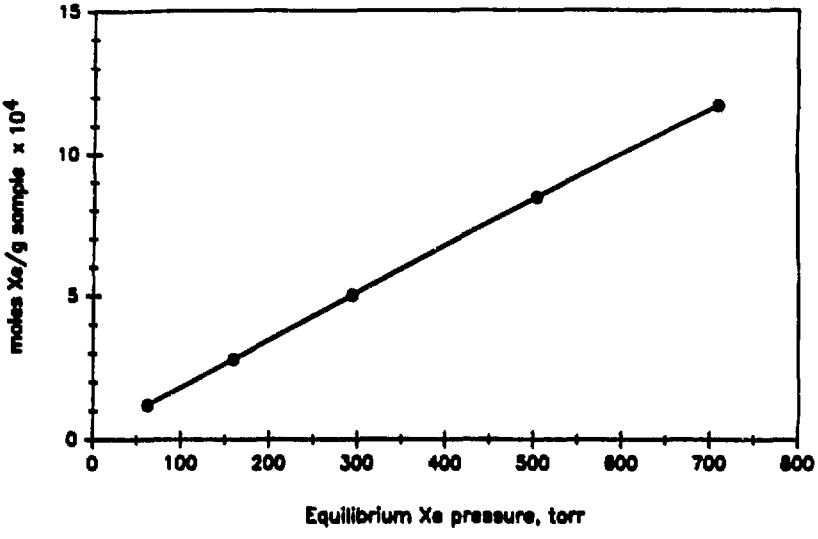

(20)

Xe Adsorption Isotherm

Sample #3-871101-1,1

400C calc./400C red. (2X)/22C oxid./400C recalcination

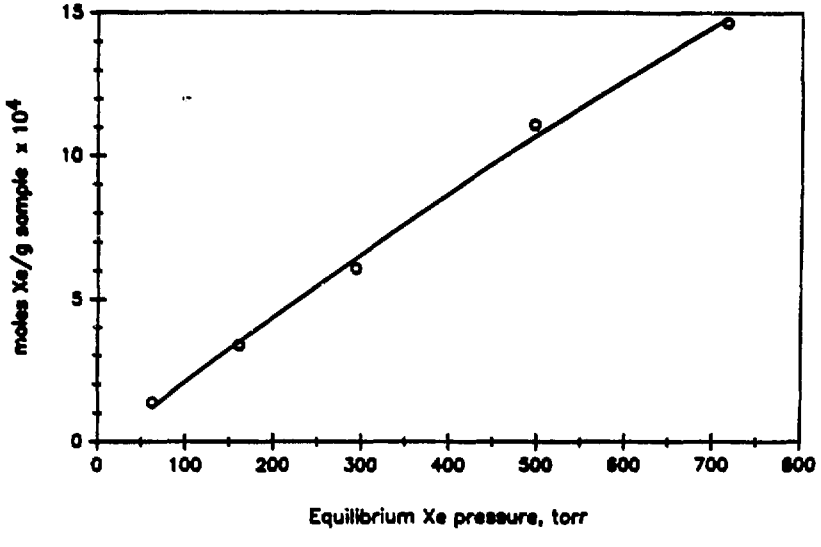

(21)

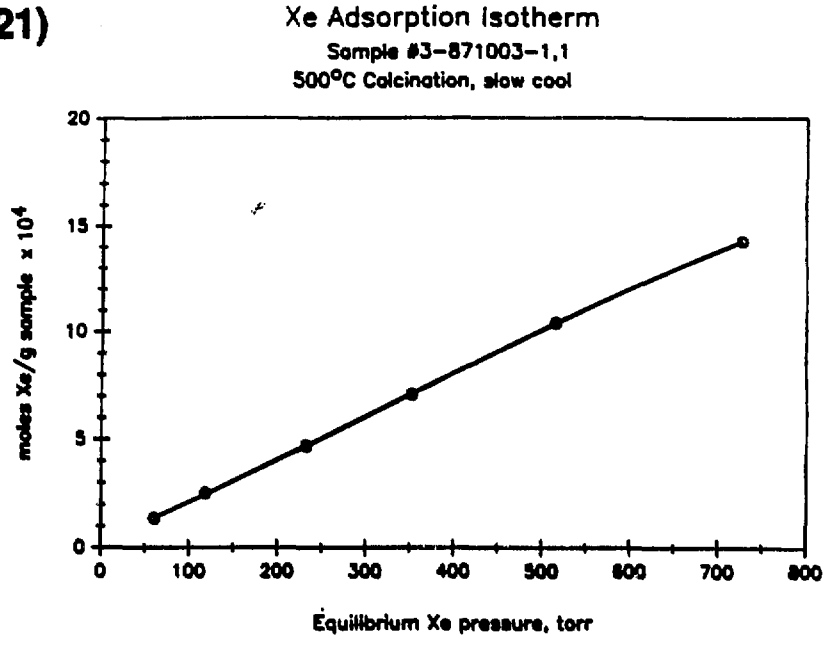
Xe Adsorption Isotherm
Sample #3-871003-1,1
500°C Calcination, slow cool
moles Xe/g sample x 10⁴
0
5
10
15
20
0
100
200
300
400
500
600
700
800
Equilibrium Xe pressure, torr

(22)

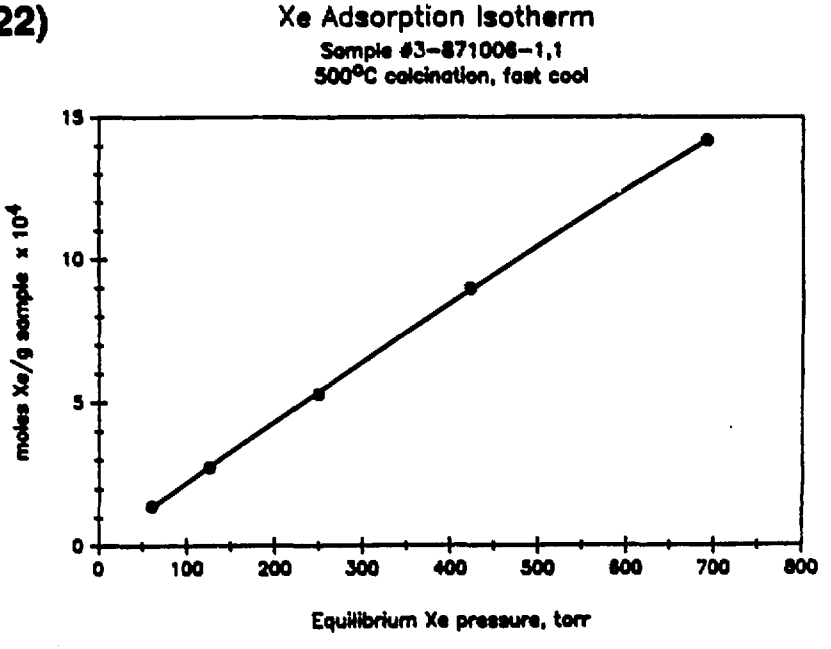
Xe Adsorption Isotherm
Sample #3-871006-1,1
500°C calcination, fast cool
moles Xe/g sample x 10⁴
0
5
10
15
0
100
200
300
400
500
600
700
800
Equilibrium Xe pressure, torr

(23)

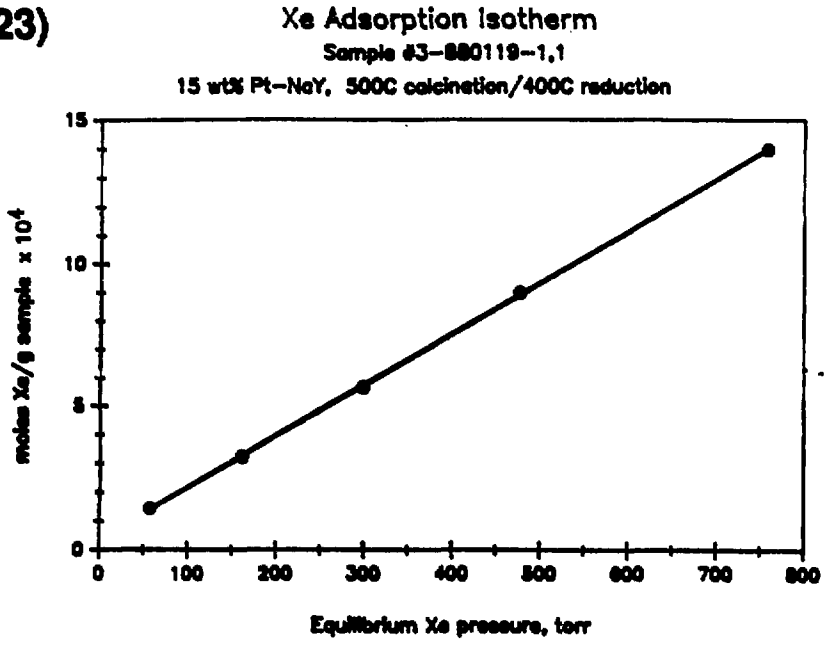
Xe Adsorption Isotherm
Sample #3-880119-1,1
15 wt% Pt-NaY, 500C calcination/400C reduction
moles Xe/g sample x 10^4
0
5
10
15
0
100
200
300
400
500
600
700
800
Equilibrium Xe pressure, torr

(24)

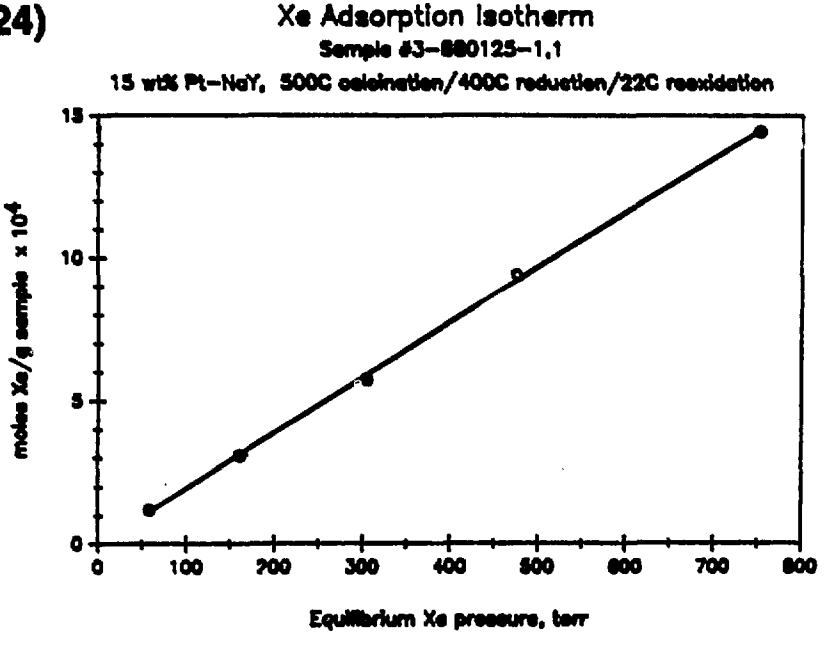
Xe Adsorption Isotherm
Sample #3-880125-1,1
15 wt% Pt-NaY, 500C calcination/400C reduction/22C reoxidation
moles Xe/g sample x 10^4
0
5
10
15
0
100
200
300
400
500
600
700
800
Equilibrium Xe pressure, torr

(25)

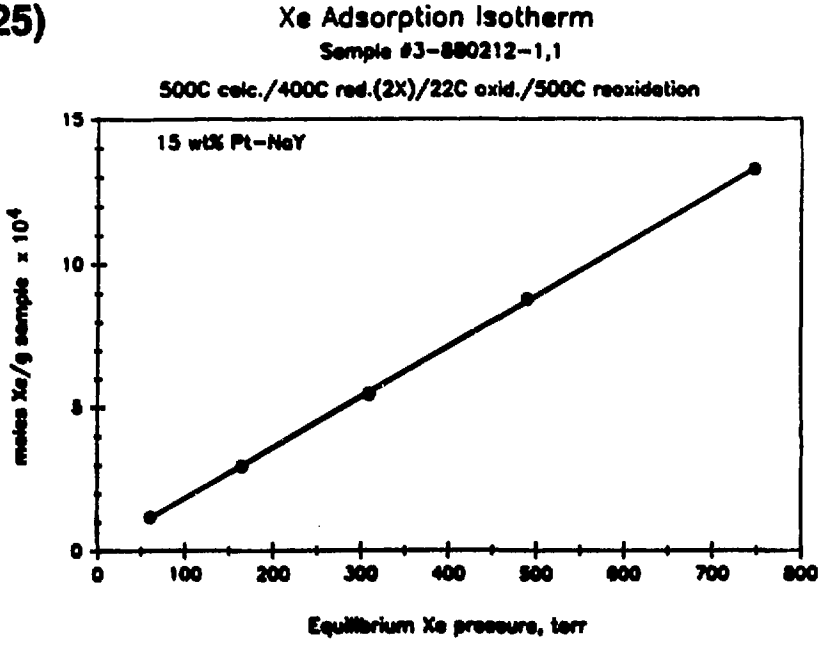
Xe Adsorption Isotherm
Sample #3-880212-1,1
500C calc./400C red.(2X)/22C oxid./500C reoxidation
15 wt% Pt-NaY
moles Xe/g sample x 10^4
0
5
10
15
0
100
200
300
400
500
600
700
800
Equilibrium Xe pressure, torr

(26)

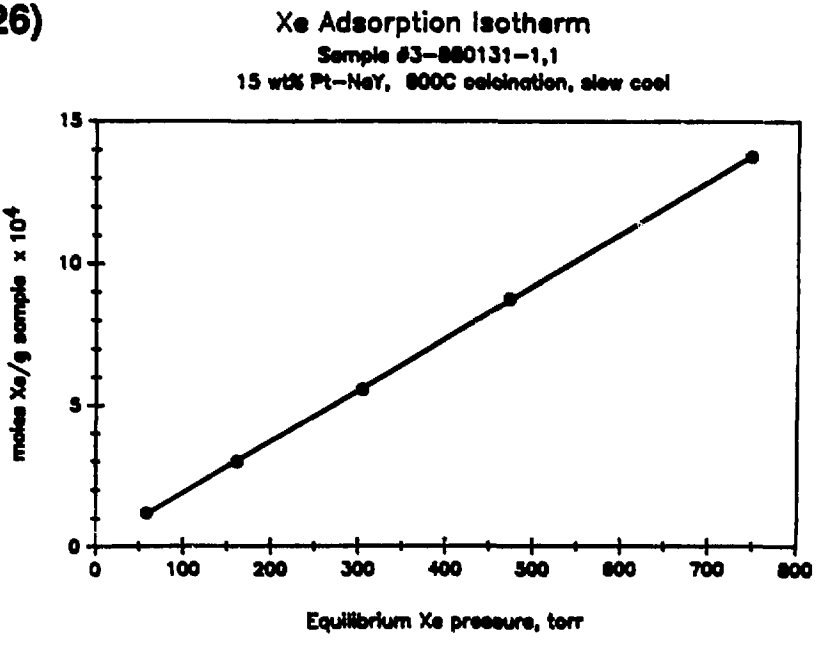
Xe Adsorption Isotherm
Sample #3-880131-1,1
15 wt% Pt-NaY, 500C calcination, slow cool
moles Xe/g sample x 10^4
0
5
10
15
0
100
200
300
400
500
600
700
800
Equilibrium Xe pressure, torr

(27)

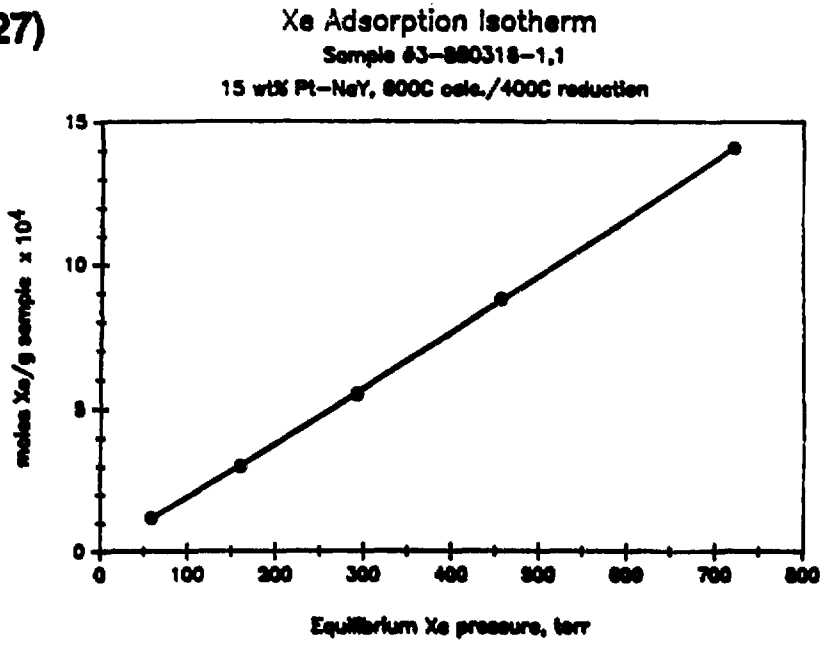
Xe Adsorption Isotherm
Sample #3-880318-1,1
15 wt% Pt-NaY, 600C calc./400C reduction
moles Xe/g sample x 10^4
15
10
5
0
0
100
200
300
400
500
600
700
800
Equilibrium Xe pressure, torr

(28)

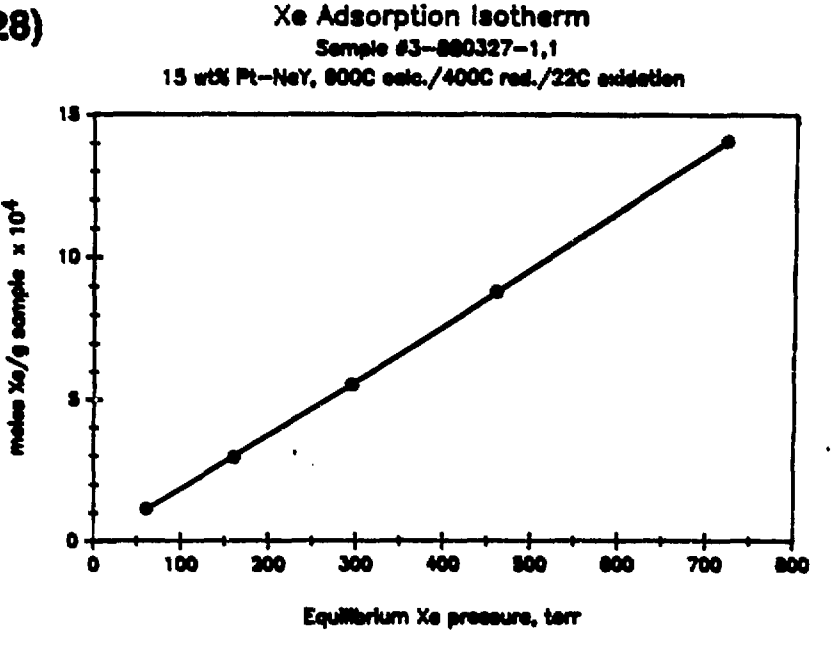
Xe Adsorption Isotherm
Sample #3-880327-1,1
15 wt% Pt-NaY, 600C calc./400C red./22C oxidation
moles Xe/g sample x 10^4
15
10
5
0
0
100
200
300
400
500
600
700
800
Equilibrium Xe pressure, torr

(29)

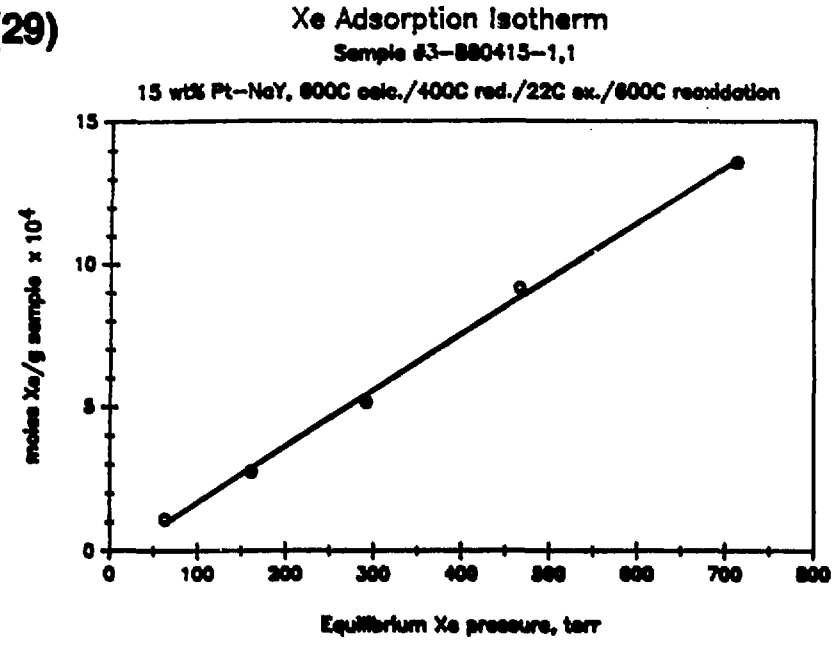
Xe Adsorption Isotherm
Sample #3–880415–1,1
15 wt% Pt–NaY, 600C calc./400C red./22C ex./600C reoxidation
moles Xe/g sample x 10⁴
15
10
5
0
0
100
200
300
400
500
600
700
800
Equilibrium Xe pressure, torr

(30)

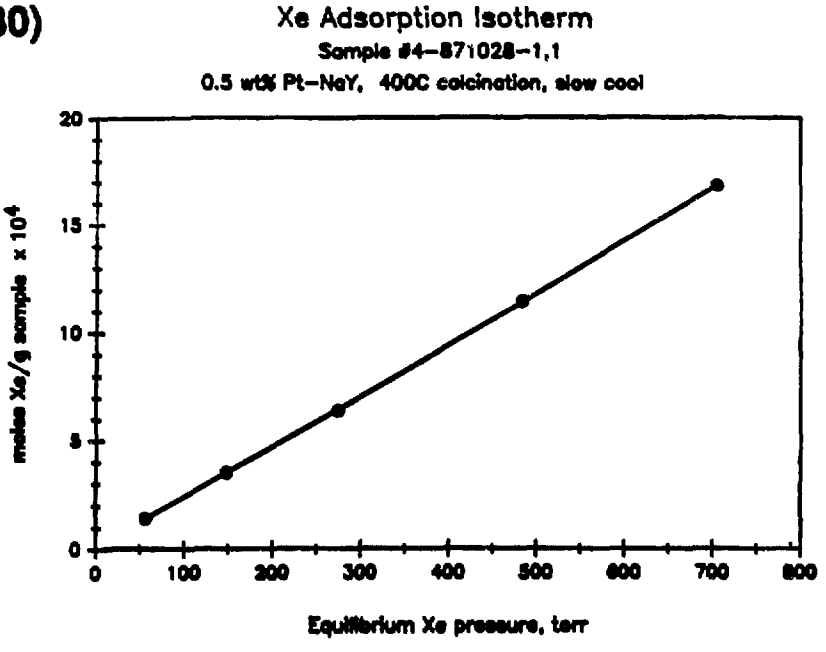
Xe Adsorption Isotherm
Sample #4–871028–1,1
0.5 wt% Pt–NaY, 400C calcination, slow cool
moles Xe/g sample x 10⁴
0
5
10
15
20
0
100
200
300
400
500
600
700
800
Equilibrium Xe pressure, torr

(31)

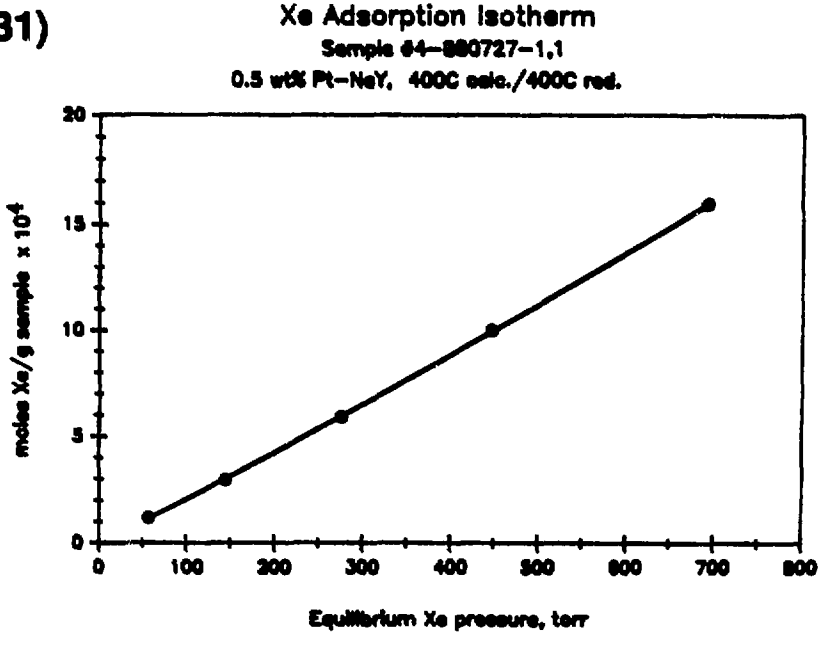
Xe Adsorption Isotherm
Sample #4–880727–1,1
0.5 wt% Pt–NaY, 400C calc./400C red.
moles Xe/g sample x 10⁴
0
5
10
15
20
0
100
200
300
400
500
600
700
800
Equilibrium Xe pressure, torr

(32)

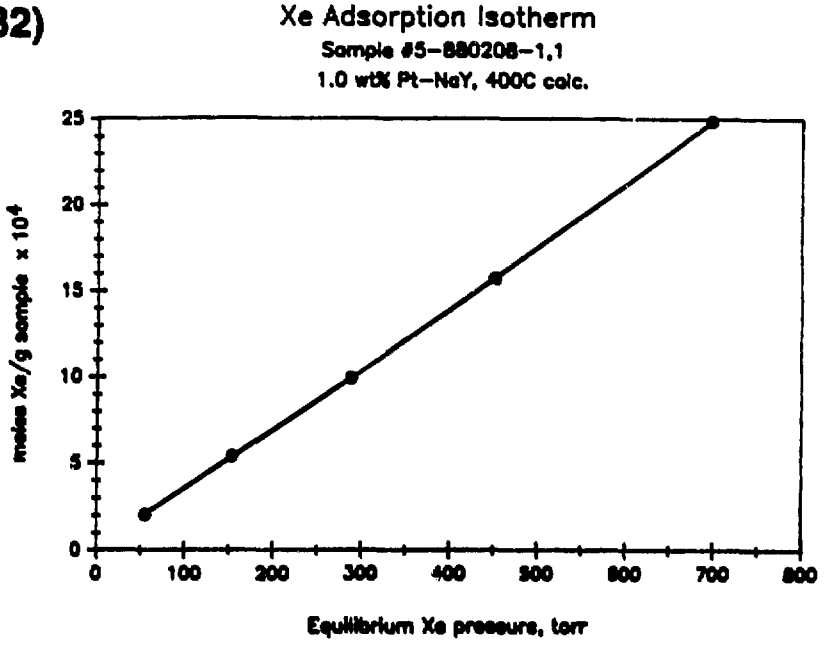
Xe Adsorption Isotherm
Sample #5-880208-1,1
1.0 wt% Pt-NaY, 400C calc.
moles Xe/g sample x 10⁴
25
20
15
10
5
0
0
100
200
300
400
500
600
700
800
Equilibrium Xe pressure, torr

(33)

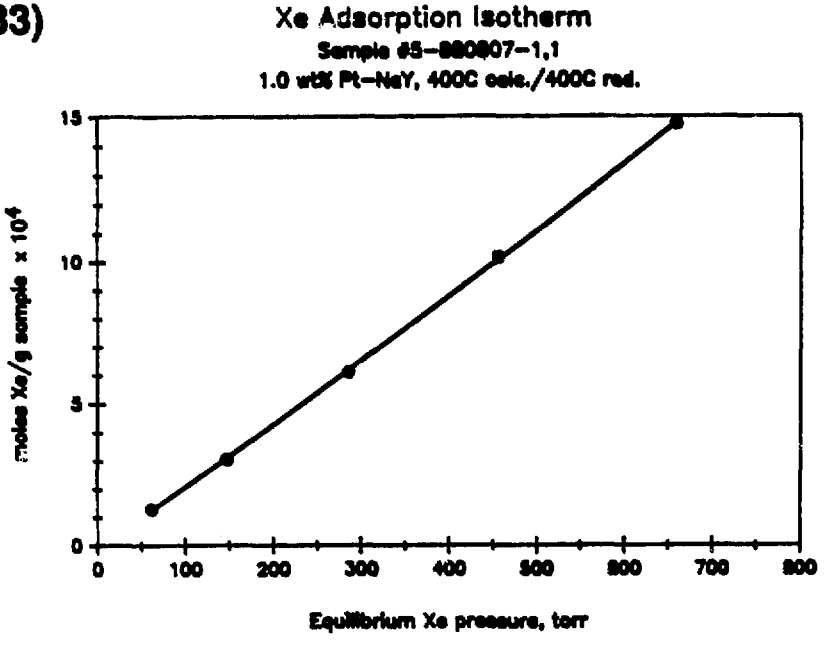
Xe Adsorption Isotherm
Sample #5-880907-1,1
1.0 wt% Pt-NaY, 400C calc./400C red.
moles Xe/g sample x 10⁴
15
10
5
0
0
100
200
300
400
500
600
700
800
Equilibrium Xe pressure, torr

(34)

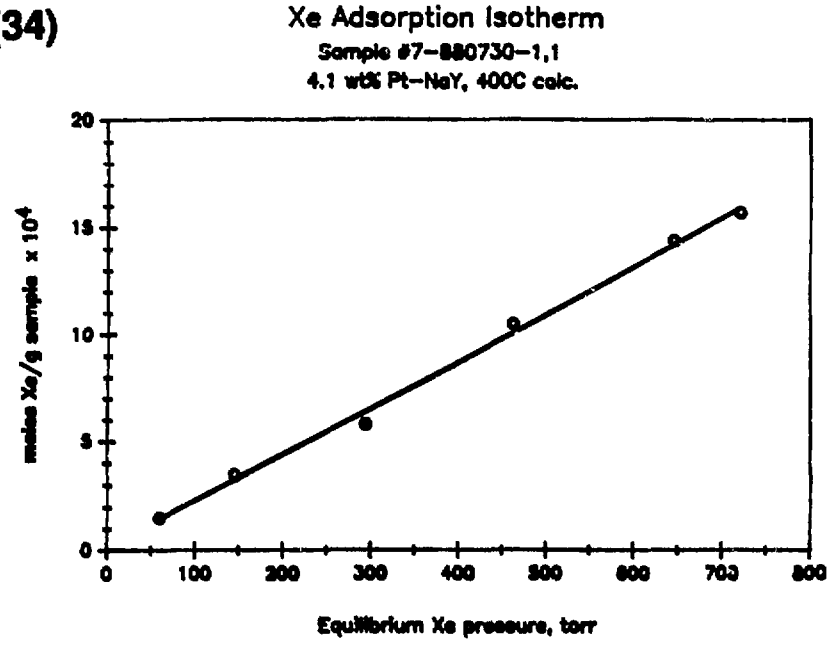
Xe Adsorption Isotherm
Sample #7-880730-1,1
4.1 wt% Pt-NaY, 400C calc.
moles Xe/g sample x 10^4
0
5
10
15
20
0
100
200
300
400
500
600
700
800
Equilibrium Xe pressure, torr

(35)

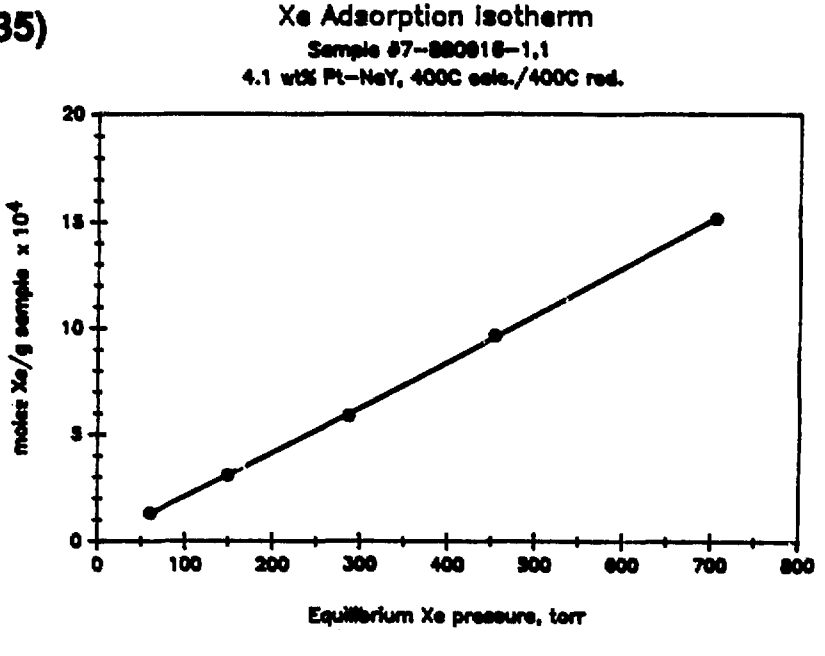
Xe Adsorption Isotherm
Sample #7-880916-1,1
4.1 wt% Pt-NaY, 400C calc./400C red.
moles Xe/g sample x 10^4
0
5
10
15
20
0
100
200
300
400
500
600
700
800
Equilibrium Xe pressure, torr

D.2 Xenon Adsorption on CaA and Silica Gel

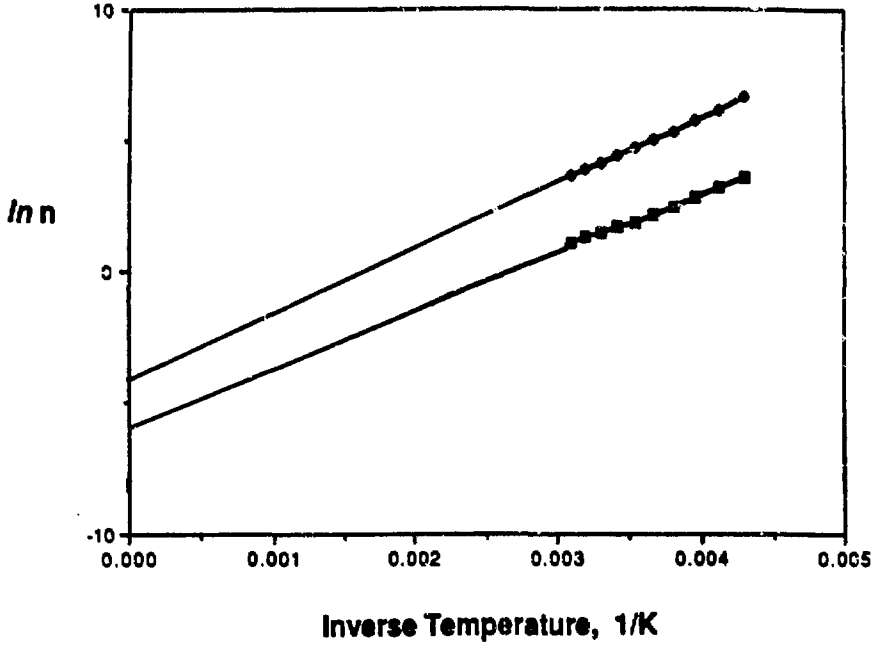

Figure D.2: Adsorption data for xenon on CaA zeolite (filled diamonds) and silica gel (open squares). The data are plotted using Equation 7.5 to estimate the enthalpic and entropic contributions to xenon adsorption. n is the amount of sorbed xenon in cm^3/g. Data taken from reference [178].

D.3 Thermodynamics of Adsorption

The local chemical potential of an adsorbed species, μ_{local}, must be equal to the chemical potential of the bulk gas, μ_{∞}, at equilibrium so that [172]:

$$\mu_{local} = \mu_{\infty} = \mu_0 + kT\ln\left(\frac{\rho_{\infty}}{kT}\right), \tag{D.2}$$

where k is Boltzmann's constant, ρ_{∞} is the density of the bulk gas (assumed to be ideal here), and μ_0 is a constant that depends only on the absolute temperature T. The local chemical potential can be expressed as

$$\begin{aligned}\mu_{local} &= \mu_{bulk}(x) + U_s(x) \\ &= \mu_0 + kT\ln\left(\frac{\rho_{local}(x)}{kT}\right) + U_s(x),\end{aligned} \tag{D.3}$$

where x is the distance from the solid surface, $\mu_{bulk}(x)$ is the bulk chemical potential for the local density $\rho_{local}(x)$, and $U_s(x)$ is the interaction potential between the adsorbate and the surface. Combining Equations D.2 and D.3 yields

$$\mu_0 + kT\ln\left(\frac{\rho_{\infty}}{kT}\right) = \mu_0 + kT\ln\left(\frac{\rho_{local}(x)}{kT}\right) + U_s(x) \tag{D.4}$$

or

$$\frac{\rho_{local}(x)}{\rho_{\infty}} = \exp\frac{-U_s(x)}{kT}. \tag{D.5}$$

At equilibrium, therefore, the local and bulk densities of the adsorbing material are related by the interaction potential between the sorbed species and the solid surface. Occluded species confined in a molecular container will be in equilibrium with other guests in the same container, but not with the bulk environment from which they are isolated.

Appendix E

Desorption and Reduction Studies of Pt–NaY

E.1 Temperature Programmed Decomposition of $Pt(NH_3)_4^{2+}$–NaX

As shown in Figure E.1, temperature programmed desorption studies [63] reflect decomposition of the metal-tetraammine complex in $Pt(NH_3)_4^{2+}$–NaX beginning at about 200 °C (473 K). The rate of NH_3 evolution reaches a maximum at slightly over 300 °C (573 K), corresponding to a maximum in the rate at which the $Pt(NH_3)_4^{2+}$ complex decomposes. Some of the ammonia is catalytically cracked by the platinum producing hydrogen and nitrogen product species. At 573 K, our results [see Chapter 4] indicate that the decomposition reaction proceeds as

$$Pt(NH_3)_4^{2+}\text{–}2Y + \frac{1}{2}O_2 \xrightarrow{573\ K} PtO\text{–}2NH_4^+Y + NH_3(g) + \frac{1}{2}N_2(g) + \frac{1}{2}H_2(g)\,. \quad \text{(E.1)}$$

At higher temperatures, ammonia desorbs from the support, leaving Brönsted acid sites to balance the anionic lattice charge. Ammonia cracking to N_2 and H_2 continues

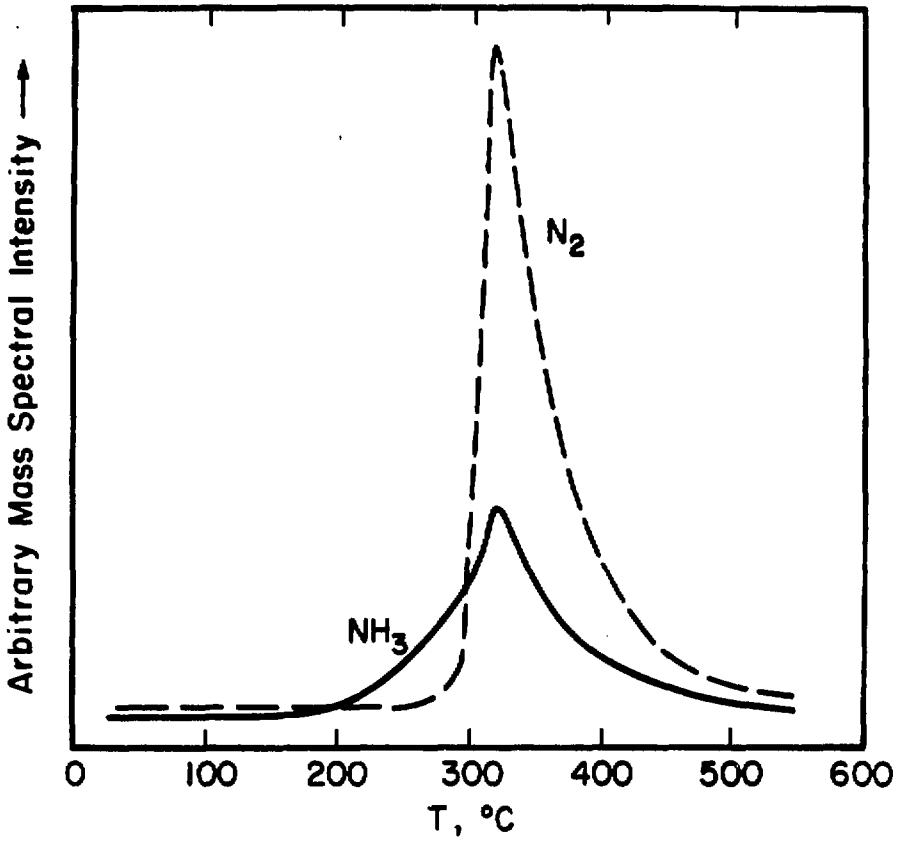

Figure E.1: Temperature programmed desorption data for the decomposition of $Pt(NH_3)_4^{2+}$ in NaX zeolite. Data taken from reference [63].

in the presence of the Pt guest species:

$$NH_4^+Y \xrightarrow{O_2,\geq 600\ K} NH_3(g) + H^+Y \tag{E.2}$$

$$NH_3(g) \xrightarrow{Pt,\geq 600\ K} \frac{1}{2}N_2(g) + \frac{3}{2}H_2(g)\,. \tag{E.3}$$

E.2 Raman Spectrum of Reduced Pt–NaY

The Raman spectrum displayed in Figure E.2 was acquired following chemisorption of hydrogen at 298 K on 15 wt% $Pt(NH_3)_4^{2+}$–NaY previously calcined at 873 K. The strong band at 632 cm^{-1} in the Raman spectrum of the calcined catalyst material [Fig. 4.1(d)] disappears in the reduced sample. As shown in Figure 4.2(b), a peak at 632 cm^{-1} reappears upon subsequent reoxidation of the reduced catalyst at 773 K. These results are consistent with assignment of bands at 610–632 cm^{-1} to Pt–O stretching frequencies, as discussed in Chapter 4.

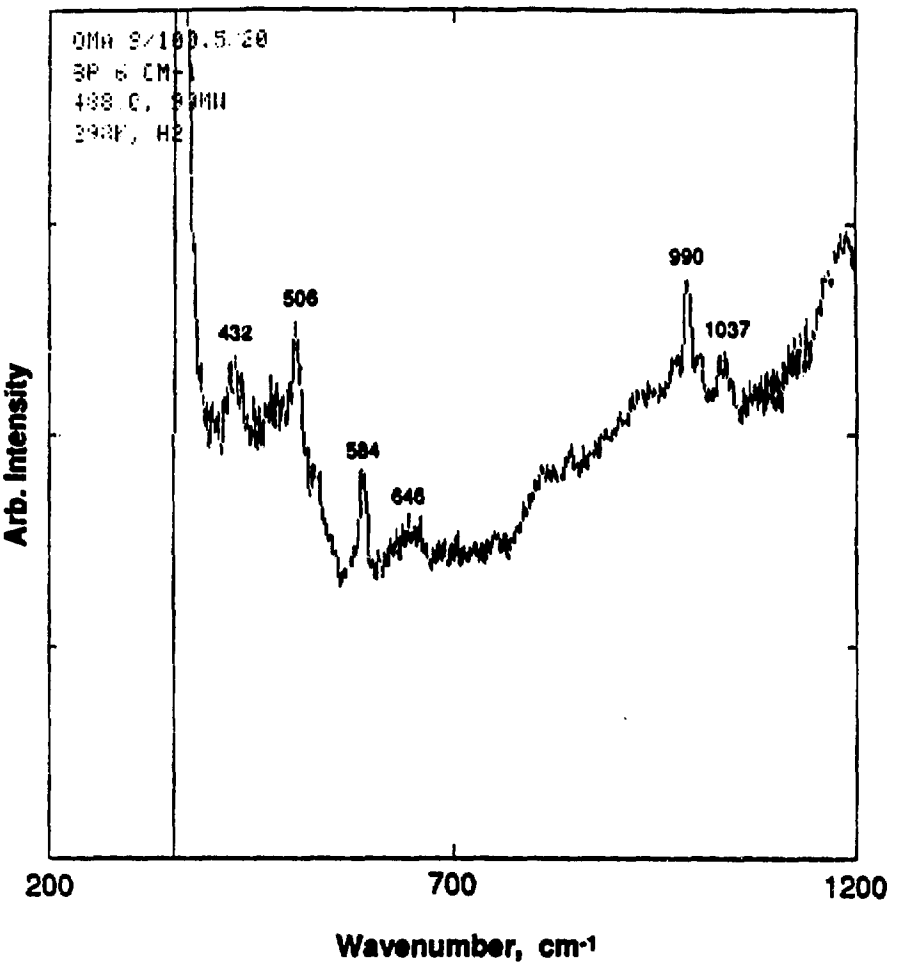

Figure E.2: Raman spectrum of 15 wt% Pt–NaY following chemisorption of hydrogen at 298 K on material previously calcined at 873 K.

E.3 Temperature Programmed Reduction Studies of Pt–NaY

TPR experiments were performed as described in Chapter 4 using the equipment configuration shown in Figure E.3. Figures E.4–E.16 which follow, correlate the composition of the reactor effluent stream with temperature, ramped linearly as a function of time. Three plots are provided for TPR experiments on 15 wt% Pt–NaY calcined at different temperatures:

1) baseline-corrected TPR profiles displaying hydrogen consumption as a function of reactor temperature;
2) plots showing H_2 baseline assignments from time-dependent temperature data and mass spectrometer traces for effluent hydrogen;

and 3) time-dependent mass spectrometer traces for hydrogen, nitrogen, ammonia, and water in the reactor effluent stream.

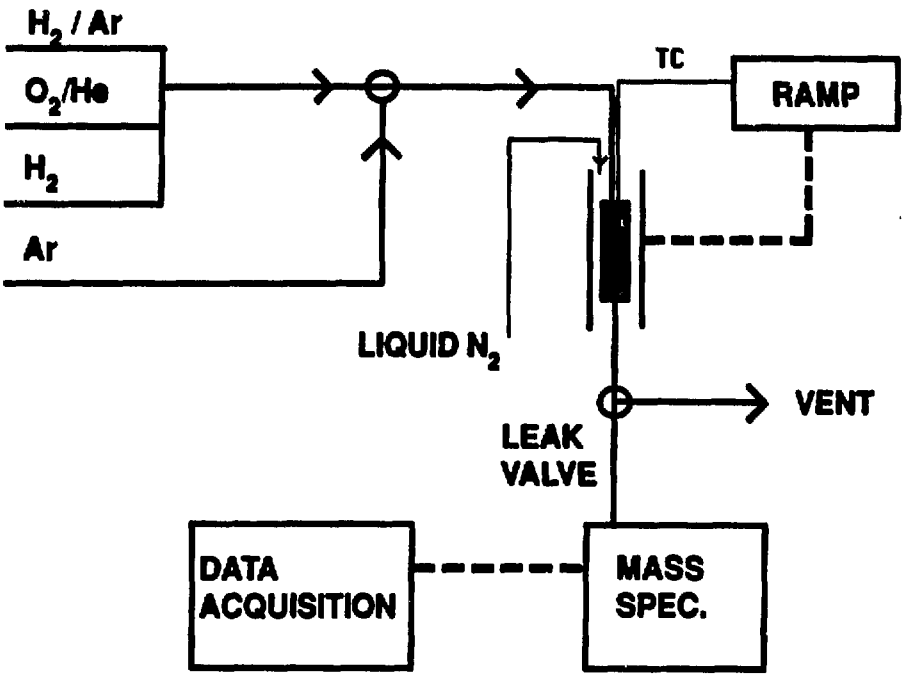

Figure E.3: Schematic diagram of the apparatus used for temperature programmed reduction experiments described in Chapter 4. Fifteen wt% Pt–NaY samples were calcined and reduced in the shaded reactor whose temperature was controlled by a programmable controller (Omega Model CN-2310) with a thermocouple input. Effluent gas species were monitored by a downstream mass spectrometer.

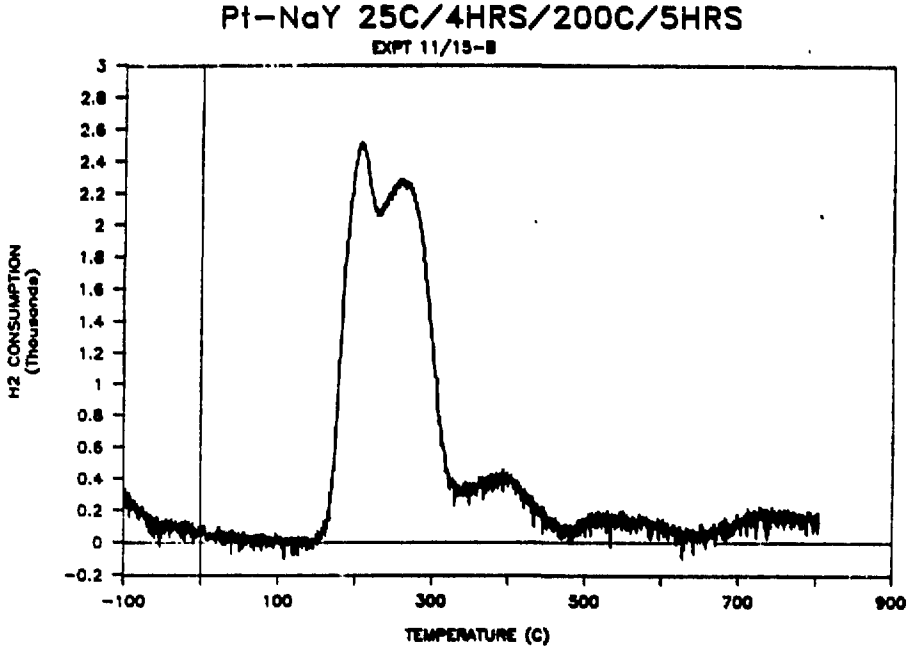

Figure E.4: Baseline-corrected TPR profile of 15 wt% Pt–NaY previously calcined at 473 K [see Fig.4.3(a)].

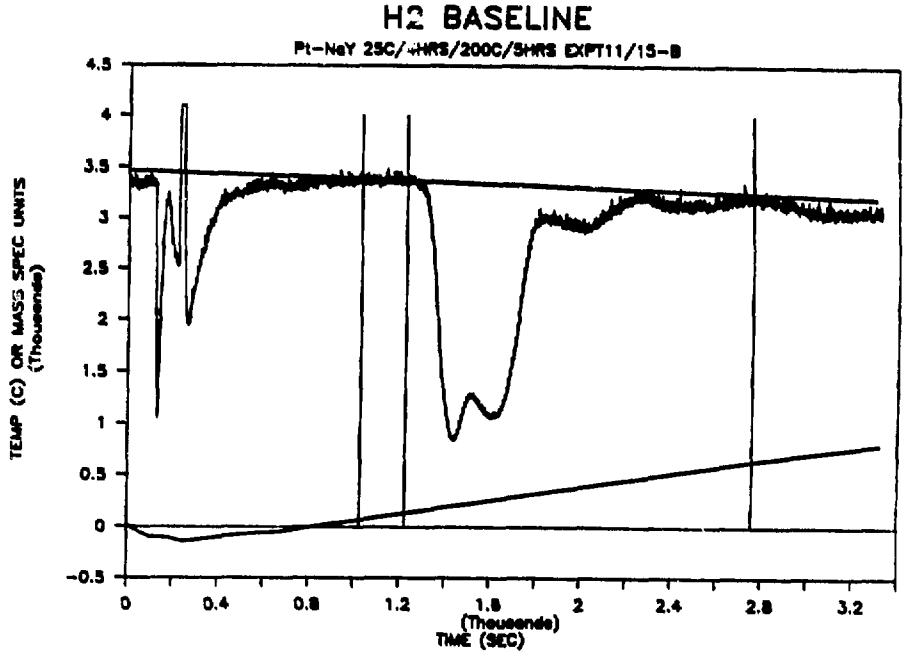

Figure E.5: Time-dependent consumption of hydrogen during temperature programmed reduction of 15 wt% Pt-NaY previously calcined at 473 K. The reactor temperature was ramped linearly (as shown) from 123 K to 1073 K. The unsettled behavior of the H_2 trace at short times arises from physisorption of hydrogen on the high surface-area sample below 200 K. The drift in the hydrogen baseline is accounted for in the profile of Figure E.4.

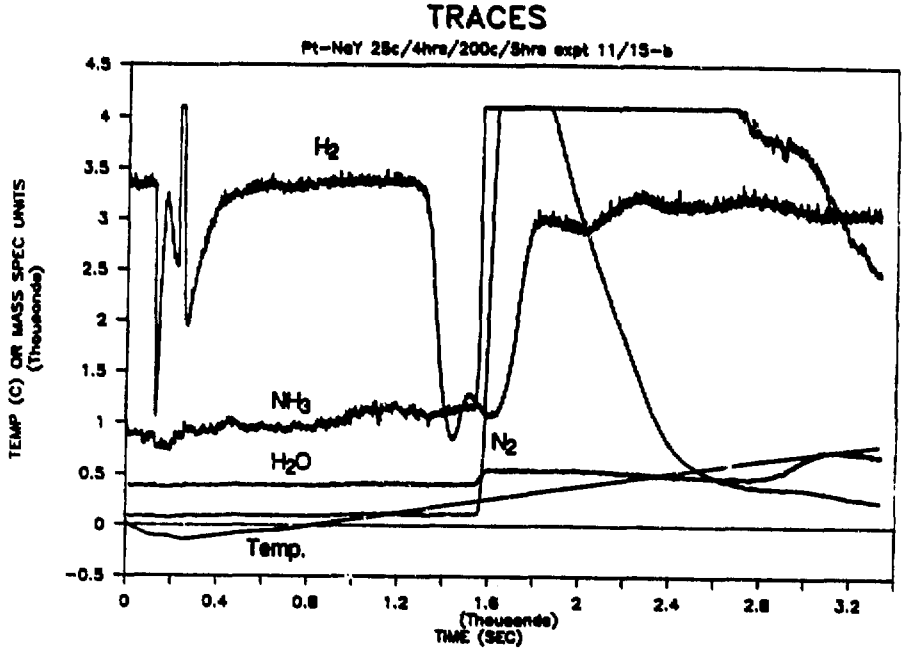

Figure E.6: Time-dependent mass spectrometer traces for H_2, N_2, NH_3, and H_2O in the reactor effluent stream during temperature programmed reduction of 15 wt% Pt–NaY previously calcined at 473 K. Large amounts of ammonia and nitrogen are evolved, consistent with decomposition of the essentially uncalcined $Pt(NH_3)_4^{2+}$ species [see Fig.E.1].

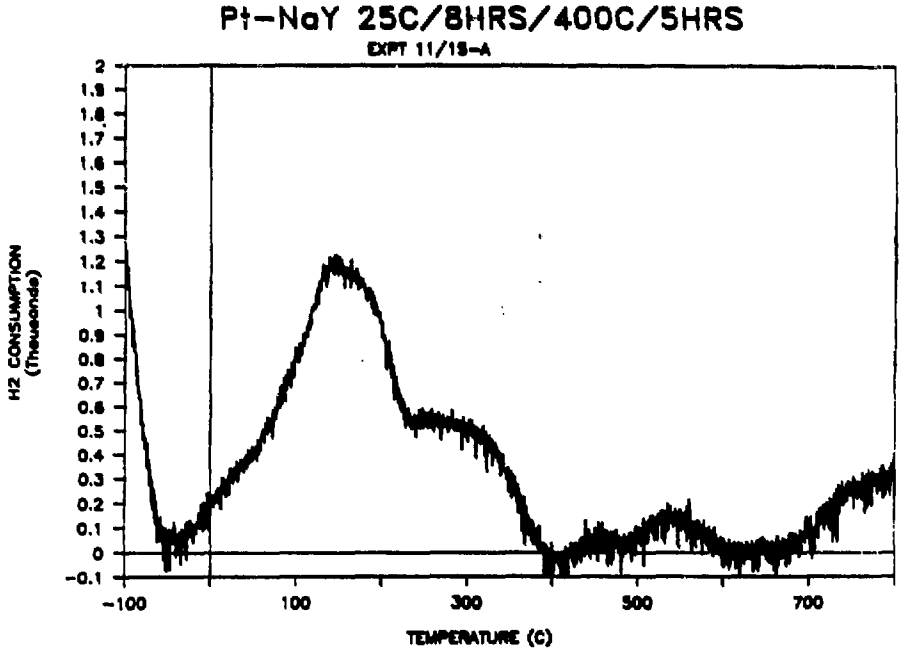

Figure E.7: Baseline-corrected TPR profile of 15 wt% Pt–NaY previously calcined at 673 K [see Fig.4.3(b)].

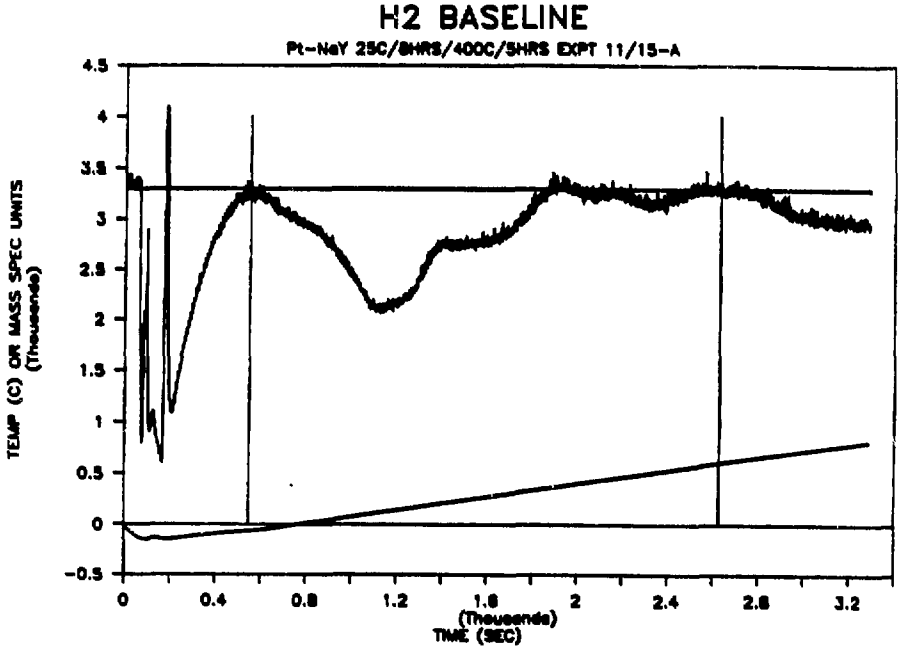

Figure E.8: Time-dependent consumption of hydrogen during temperature programmed reduction of 15 wt% Pt-NaY previously calcined at 673 K. The reactor temperature was ramped linearly (as shown) from 123 K to 1073 K. The unsettled behavior of the H_2 trace at short times arises from physisorption of hydrogen on the high surface-area sample below 200 K. The drift in the hydrogen baseline is accounted for in the profile of Figure E.7.

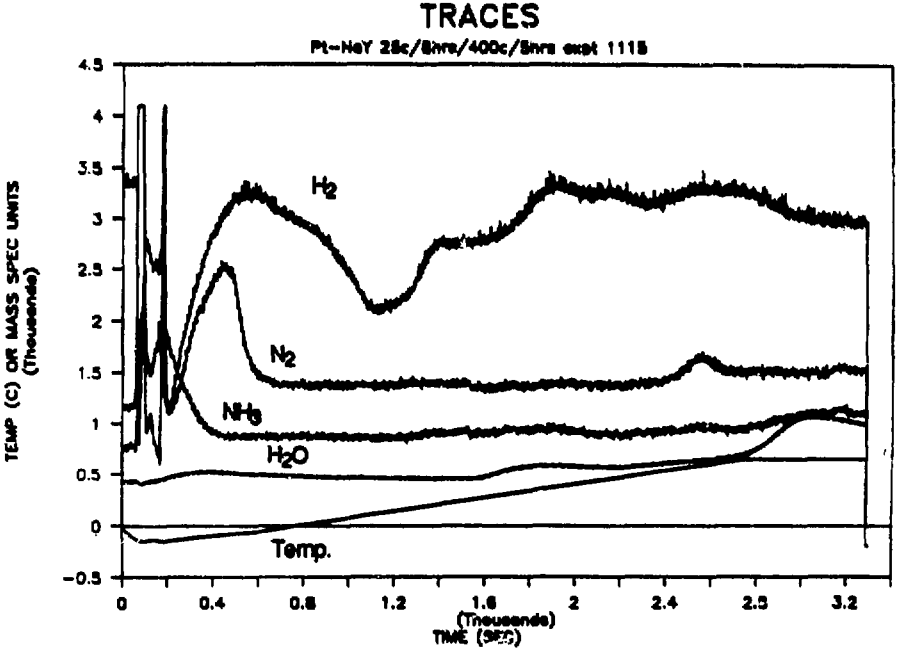

Figure E.9: Time-dependent mass spectrometer traces for H_2, N_2, NH_3, and H_2O in the reactor effluent stream during temperature programmed reduction of 15 wt% Pt–NaY previously calcined at 673 K. As a result of the higher calcination temperature, substantially less ammonia and nitrogen are evolved, consistent with essentially complete decomposition of the $Pt(NH_3)_4^{2+}$ species during calcination.

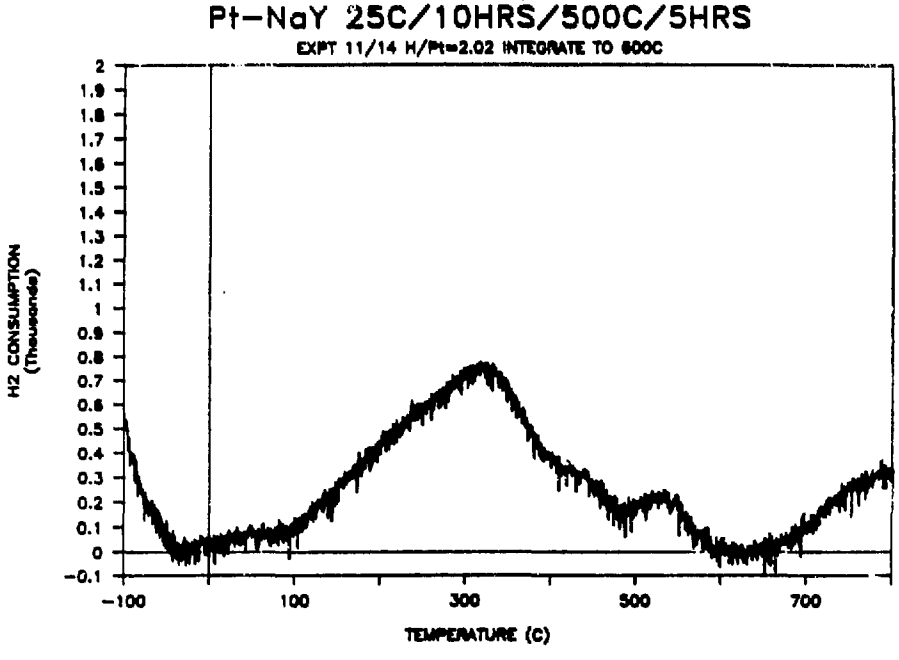

Figure E.10: Baseline-corrected TPR profile of 15 wt% Pt–NaY previously calcined at 773 K [see Fig.4.3(c)].

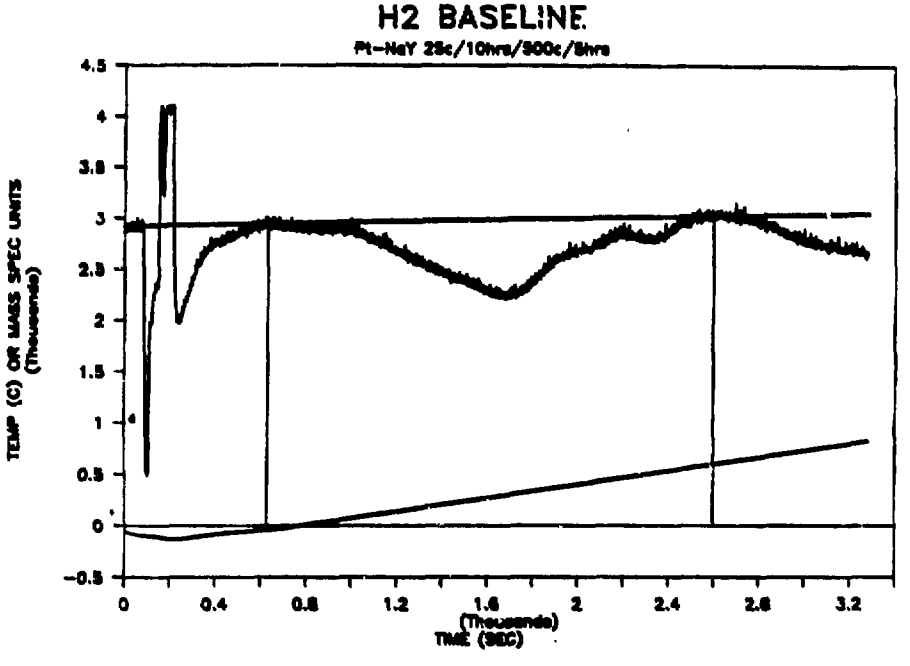

Figure E.11: Time-dependent consumption of hydrogen during temperature programmed reduction of 15 wt% Pt–NaY previously calcined at 773 K. The reactor temperature was ramped linearly (as shown) from 123 K to 1073 K. The unsettled behavior of the H_2 trace at short times arises from physisorption of hydrogen on the high surface-area sample below 200 K. The drift in the hydrogen baseline is accounted for in the profile of Figure E.10.

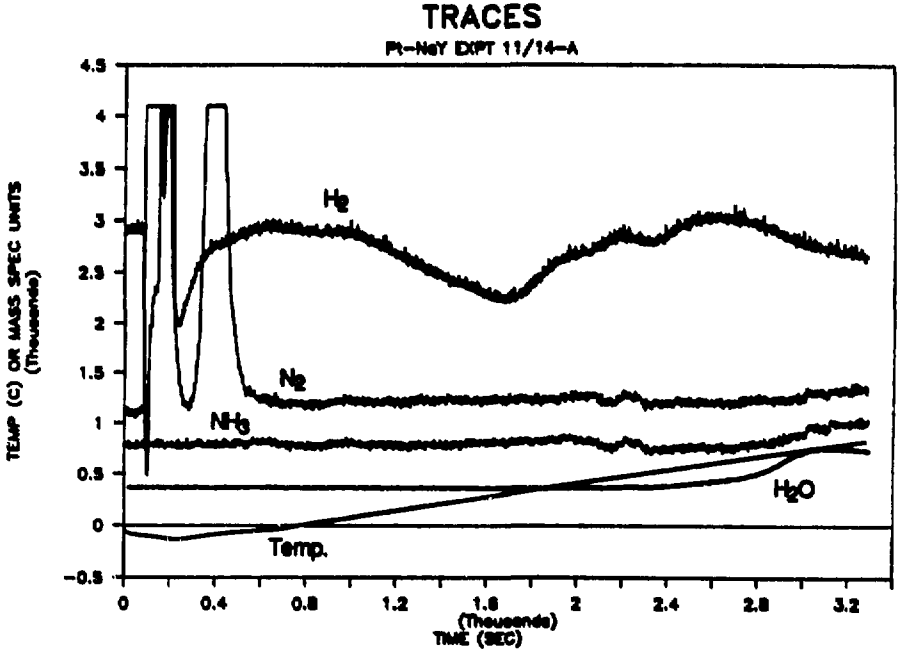

Figure E.12: Time-dependent mass spectrometer traces for H_2, N_2, NH_3, and H_2O in the reactor effluent stream during temperature programmed reduction of 15 wt% Pt–NaY previously calcined at 773 K.

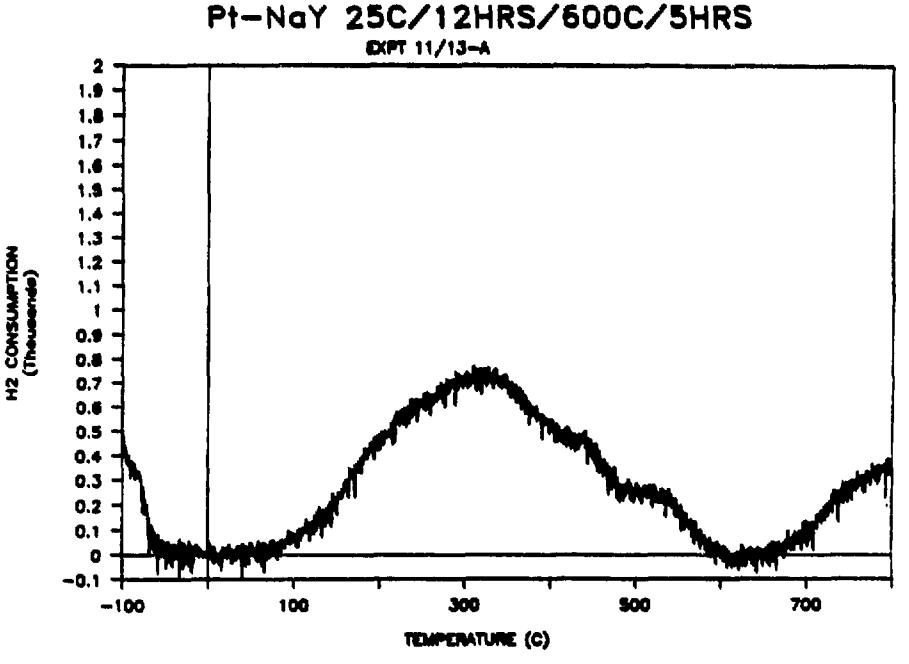

Figure E.13: Baseline-corrected TPR profile of 15 wt% Pt-NaY previously calcined at 873 K [see Fig.4.3(d)].

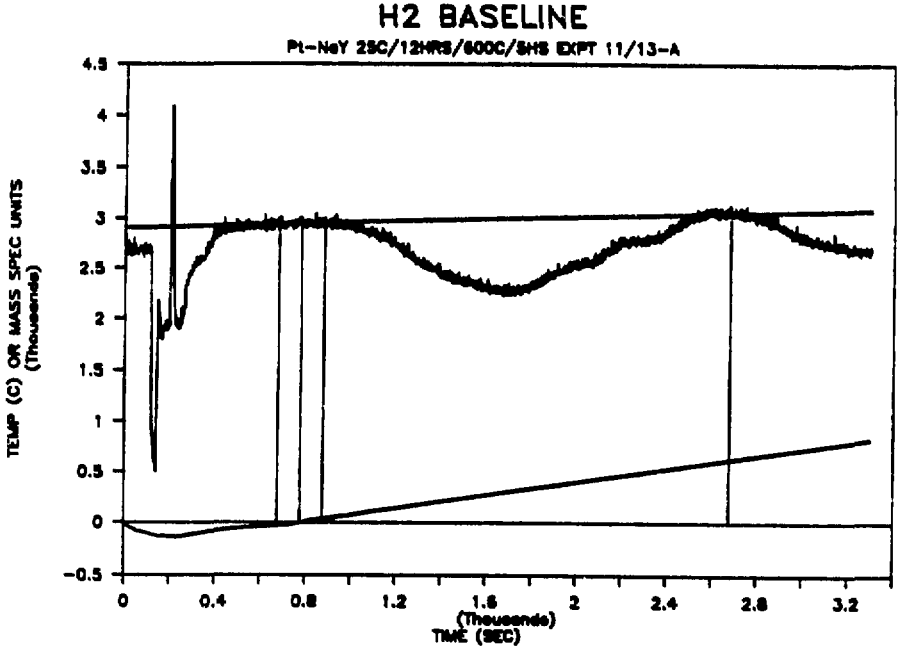

Figure E.14: Time-dependent consumption of hydrogen during temperature programmed reduction of 15 wt% Pt-NaY previously calcined at 873 K. The reactor temperature was ramped linearly (as shown) from 123 K to 1073 K. The unsettled behavior of the H_2 trace at short times arises from physisorption of hydrogen on the high surface-area sample below 200 K. The drift in the hydrogen baseline is accounted for in the profile of Figure E.13.

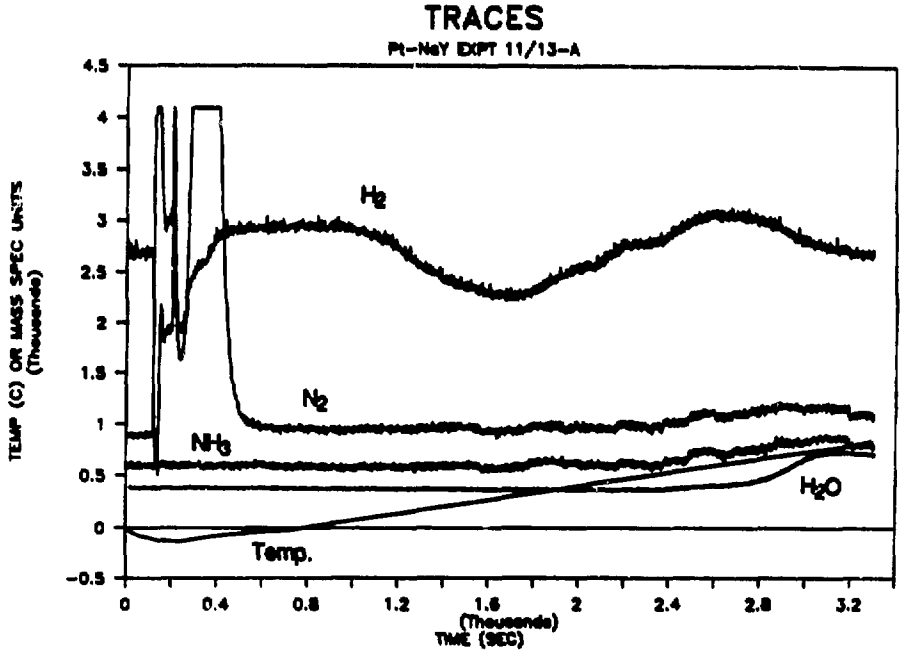

Figure E.15: Time-dependent mass spectrometer traces for H_2, N_2, NH_3, and H_2O in the reactor effluent stream during temperature programmed reduction of 15 wt% Pt–NaY previously calcined at 873 K.

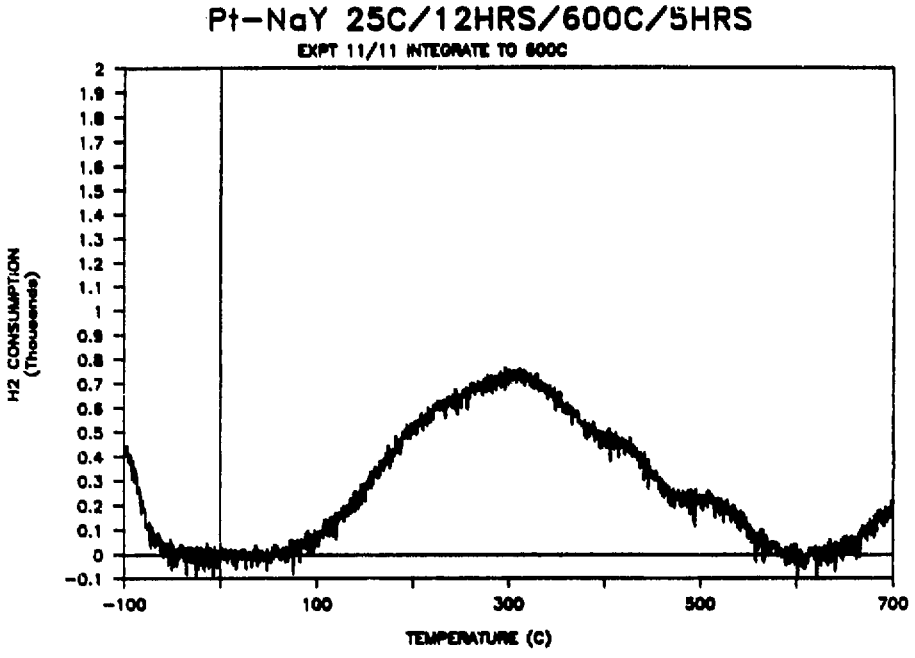

Figure E.16: Baseline-corrected TPR profile of 15 wt% Pt–NaY previously calcined at 873 K. Comparison with Figure E.13 shows good reproducibility for these calcination and reduction conditions.

E.4 Hydrogen-Chemisorption Measurements of Surface Platinum

E.4.1 Experimental Procedures

The fraction of platinum atoms occupying surface sites in reduced metal clusters accessible to diffusing hydrogen gas was determined by measuring the moles of chemisorbed H_2 at room temperature. The procedure assumes an adsorption stoichiometry of 1 H/1 Pt [66] and follows an adsorption isotherm procedure similar to that described in Appendix D.

Catalyst Reduction Procedure

1. Carefully weigh ≈0.20 g of previously calcined 15 wt% Pt–NaY. The metal loading must be known precisely to determine the fraction of platinum which occupies accessible surface sites.

2. Load the sample in a small downflow reactor of the type shown in Figure E.17. Place a small piece of quartz wool in the upstream reactor leg to prevent material from being drawn accidentally into the vacuum manifold during evacuation.

3. With stopcocks 1 and 5 closed and stopcocks 2, 3, 4, and 6 open, purge the H_2/He inlet line with ≈100 cm^3/min helium gas for 5 min.

4. Connect the reactor to the vacuum/chemisorption manifold as shown in Figure E.17. Open stopcock 4 and purge the reactor with flowing helium for 10 min.

5. Pulse H_2 intermittently into the helium stream for about one minute to avoid generating excessive heat from reaction between hydrogen and chemisorbed

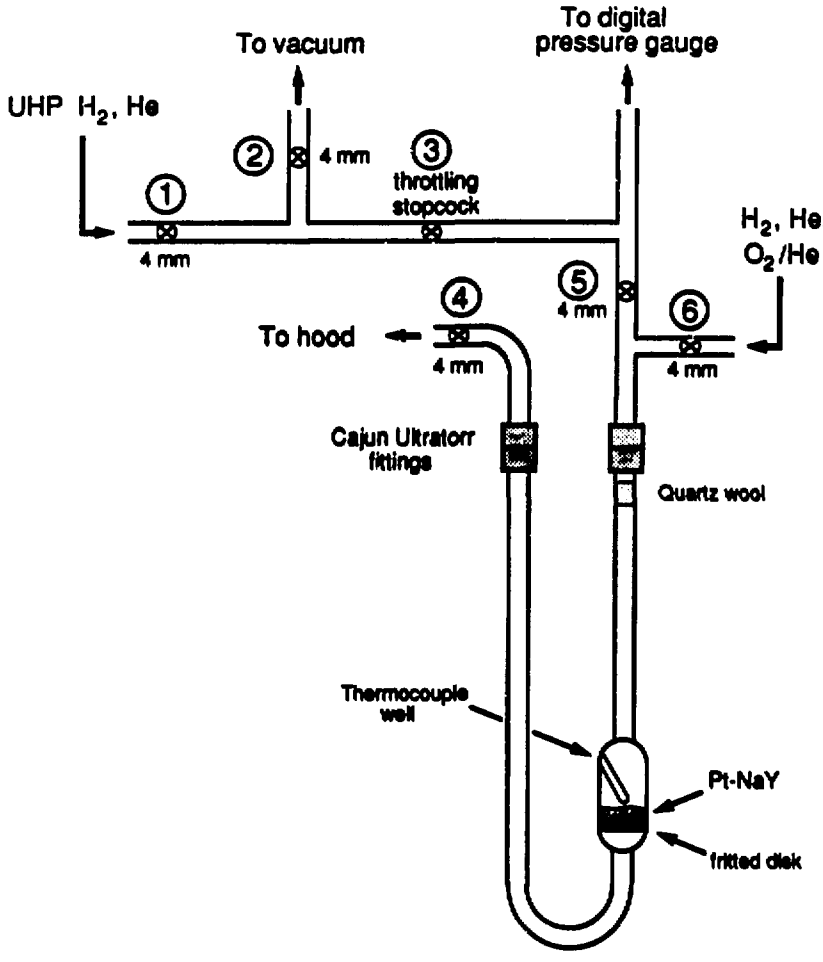

Figure E.17: Vacuum/chemisorption manifold used for measurement of surface metal fractions in reduced, supported-metal catalysts.

oxygen. Halt He flow and initiate continuous flow of ≈100 cm^3/min hydrogen gas over the sample.

6. Heat the sample in an electric heater at 100 K/h to 673 K. Reduce the catalyst in flowing hydrogen overnight at 673 K.

7. After reduction is complete, close stopcocks 4 and 6 to halt the flow of hydrogen. Slowly open stopcock 5 to evacuate the reactor. Outgas the sample at 673 K for 1 h.

8. After outgassing at 673 K, remove the heater and outgas the sample for 1.5 h as the system thermally re-equilibrates to room temperature.

Physisorption/Chemisorption of H_2

1. With the sample reduced and the reactor evacuated, close stopcocks 2 and 3. Charge ultrahigh purity (UHP) hydrogen gas to the manifold upstream of stopcock 3.

2. Using stopcock 3, throttle UHP hydrogen into the 'dosing volume' between the pressure gauge and stopcocks 3 and 5, and record the pressure P_i (≈75 torr H_2 for the first point.) The dosing volume of the vacuum manifold is known to be 43.96 cm^3 from separate H_2O volume/mass measurements.

3. Open stopcock 5 to charge UHP hydrogen to the reduced, outgassed Pt-NaY catalyst material in the reactor. Allow the chemisorption process to equilibrate for about 30 min, then close stopcock 5 and record the pressure P_f.

4. Repeat steps 2 and 3, incrementing P_i by 50 torr, until hydrogen uptake levels off at P_i ≈ 230 torr H_2.

5. Slowly open stopcocks 3 and 5 to outgas the sample once again.

6. Repeat steps 1–4 to measure physisorbed H_2 uptake by the sample. (The first cycle measures physisorbed and chemisorbed H_2 uptakes combined.)

7. Repeat steps 1–3 with ultrahigh purity helium to measure the dead volume of system.

8. Close stopcock 5. Open stopcocks 4 and 6, and purge the reactor system with flowing helium.

9. After 5 min, initiate flow of 800 ppm O_2 in helium to passivate the reduced metal catalyst. Note: this is absolutely essential to prevent explosion of the reactor as a result of violent reaction between atmospheric oxygen and chemisorbed hydrogen in the high Pt-loaded catalyst. After 10 min, halt the gas flow, remove the reactor from the vacuum/chemisorption manifold, and store the sample.

E.4.2 Hydrogen Chemisorption Data for 15 wt% Pt–NaY

Figures E.18–E.24 which follow show the isotherms for physisorption and chemisorption of hydrogen on reduced 15 wt% Pt–NaY samples previously calcined or reoxidized at different temperatures. The moles of accessible surface platinum are determined from the moles of chemisorbed hydrogen, assuming an adsorption stoichiometry of 1 H/1 Pt. The data are presented in Tables 3.1 and 3.2 in Chapter 3.

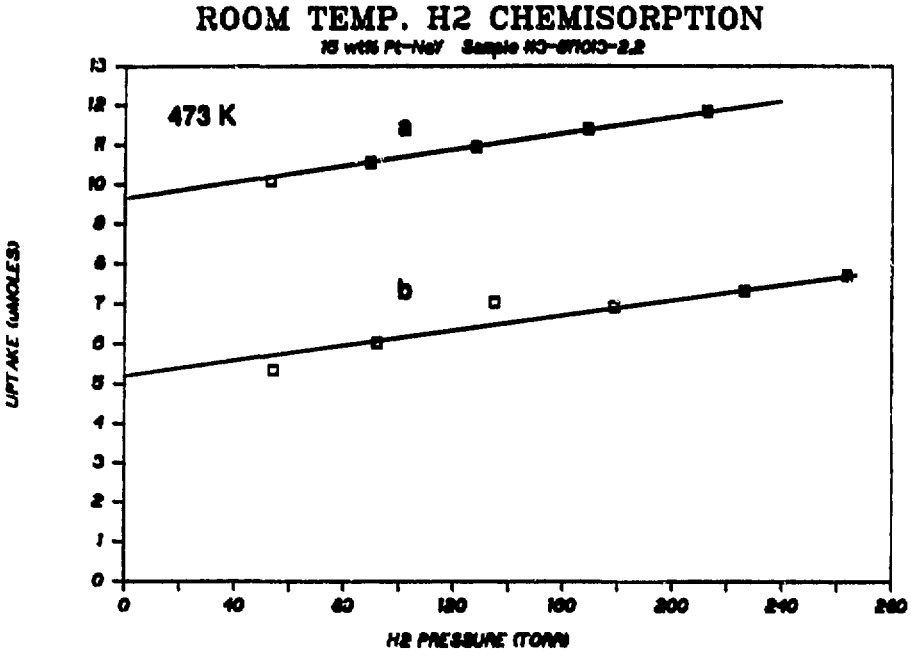

Figure E.18: Room-temperature adsorption isotherms for hydrogen on 0.1307 g of reduced 15 wt% Pt-NaY previously calcined at 473 K: (a) H_2 physisorption/chemisorption uptakes combined and (b) H_2 physisorption uptake alone. The accessible surface Pt fraction is 0.08 in this sample.

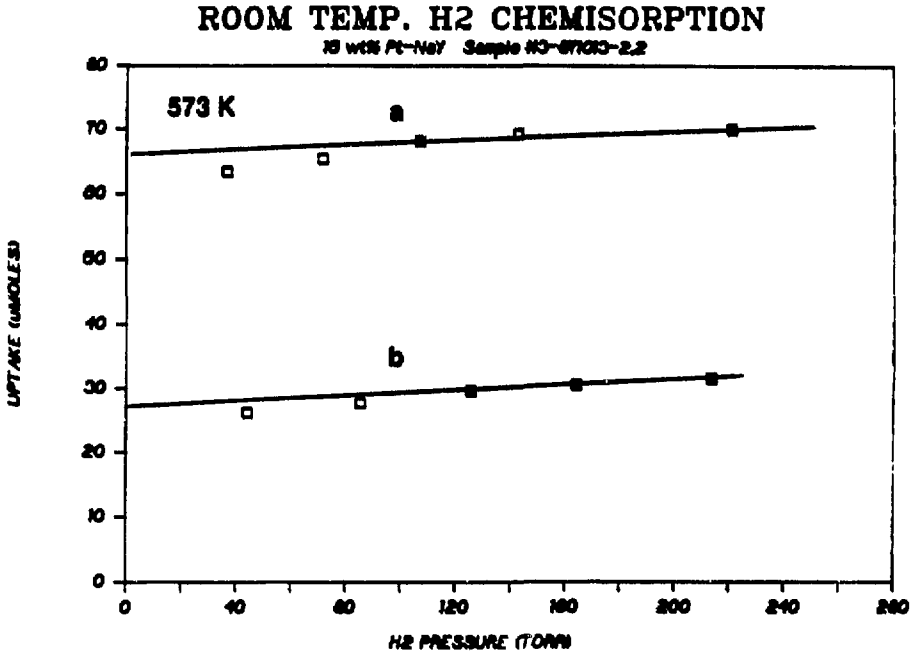

Figure E.19: Room-temperature adsorption isotherms for hydrogen on 0.1645 g of reduced 15 wt% Pt-NaY previously calcined at 573 K: (a) H_2 physisorption/chemisorption uptakes combined and (b) H_2 physisorption uptake alone. The accessible surface Pt fraction is 0.61 in this sample.

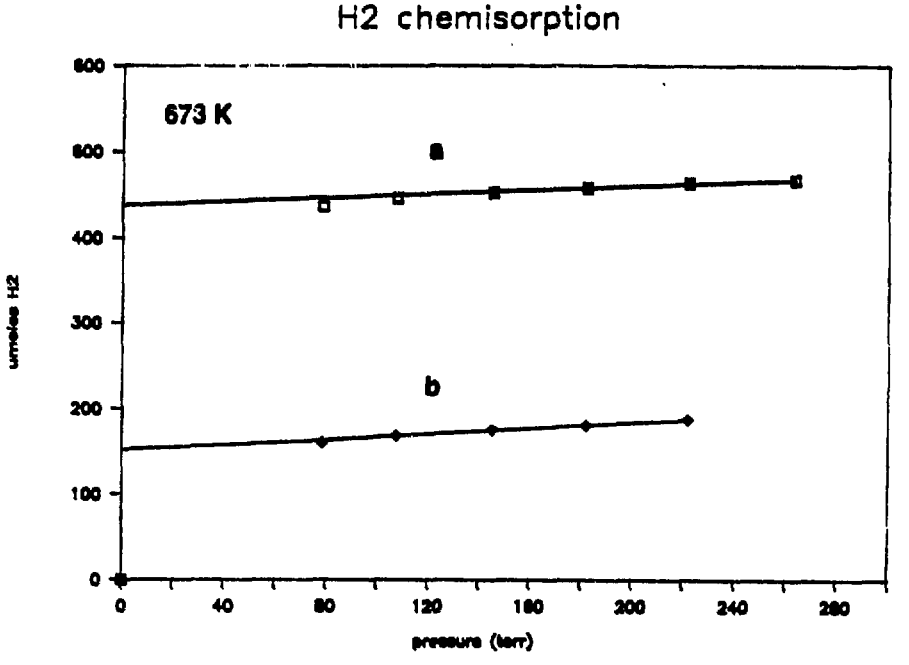

Figure E.20: Room-temperature adsorption isotherms for hydrogen on 0.2502 g of reduced 15 wt% Pt–NaY previously calcined at 673 K: (a) H_2 physisorption/chemisorption uptakes combined and (b) H_2 physisorption uptake alone. The accessible surface Pt fraction is 0.74 in this sample.

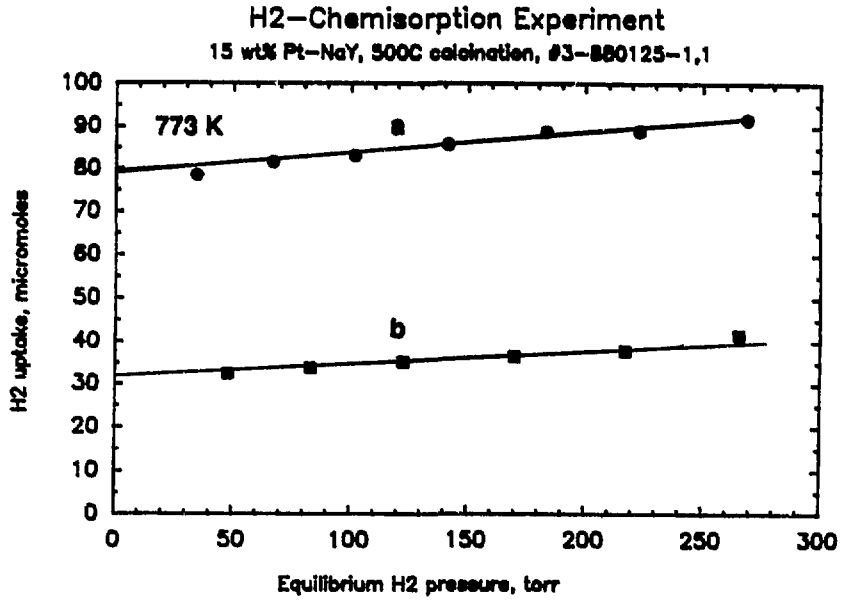

Figure E.21: Room-temperature adsorption isotherms for hydrogen on 0.2890 g of reduced 15 wt% Pt–NaY previously calcined at 773 K: (a) H_2 physisorption/chemisorption uptakes combined and (b) H_2 physisorption uptake alone. The accessible surface Pt fraction is 0.42 in this sample.

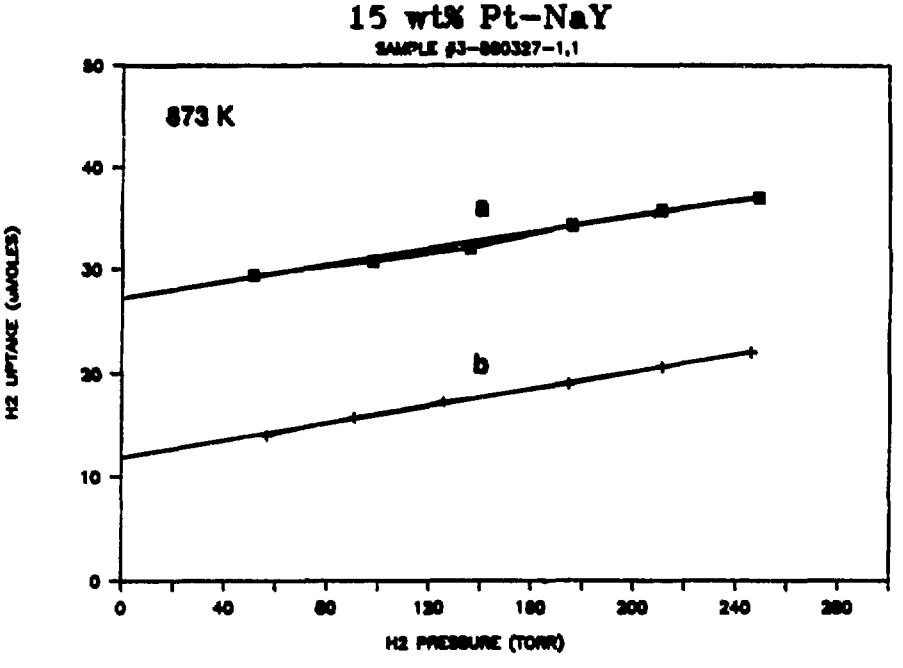

Figure E.22: Room-temperature adsorption isotherms for hydrogen on 0.2598 g of reduced 15 wt% Pt-NaY previously calcined at 873 K: (a) H_2 physisorption/chemisorption uptakes combined and (b) H_2 physisorption uptake alone. The accessible surface Pt fraction is 0.15 in this sample.

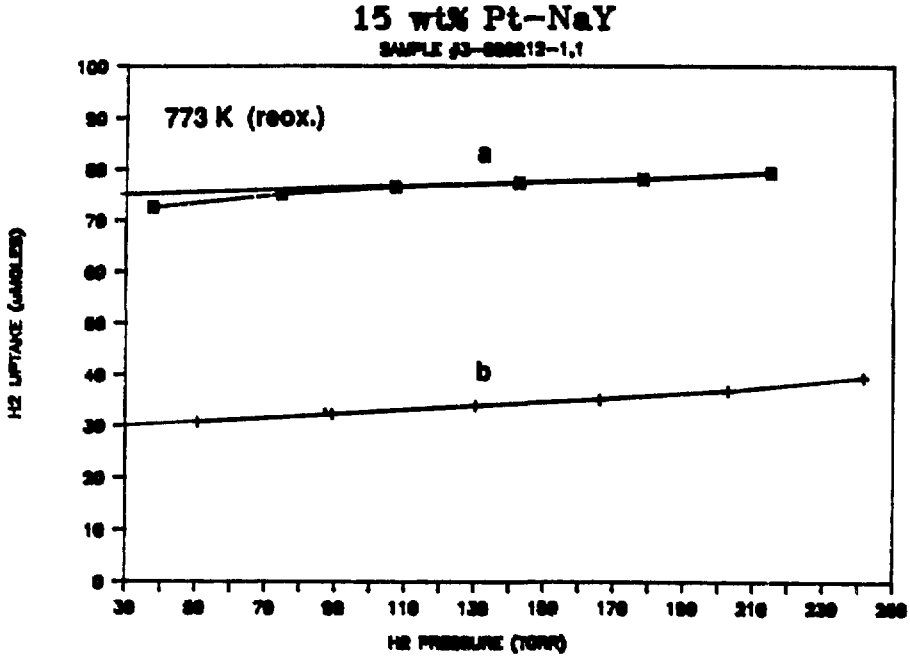

Figure E.23: Room-temperature adsorption isotherms for hydrogen on 0.2725 g of 15 wt% Pt–NaY reoxidized at 773 K following earlier calcination at 773 K and reduction at 673 K: (a) H_2 physisorption/chemisorption uptakes combined and (b) H_2 physisorption uptake alone. The accessible surface Pt fraction is 0.43 in this sample.

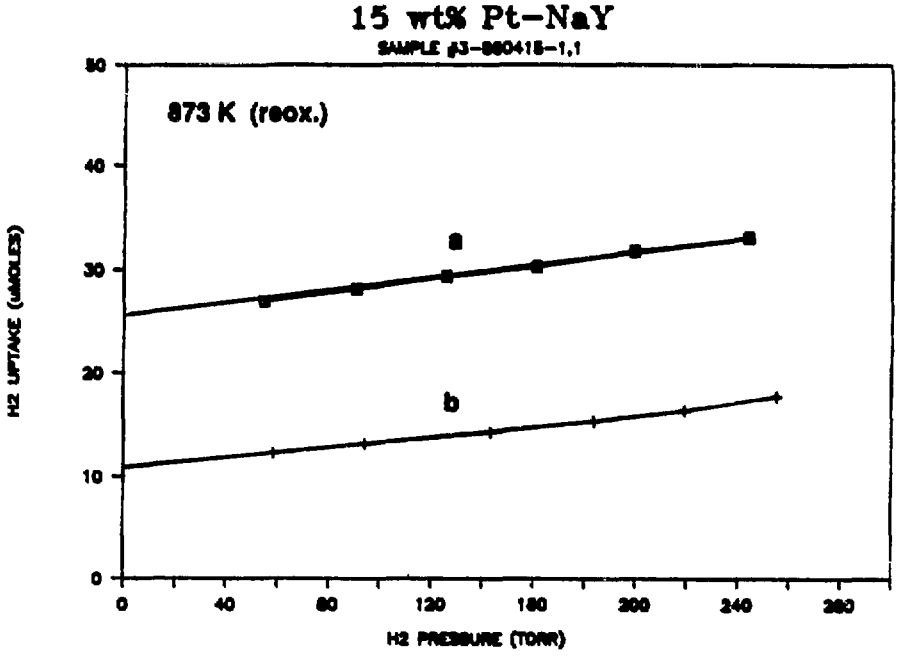

Figure E.24: Room-temperature adsorption isotherms for hydrogen on 0.2488 g of 15 wt% Pt-NaY reoxidized at 873 K following earlier calcination at 873 K and reduction at 673 K: (a) H_2 physisorption/chemisorption uptakes combined and (b) H_2 physisorption uptake alone. The accessible surface Pt fraction is 0.15 in this sample.

Appendix F

Transport of Adsorbed Guests in NaY

F.1 Liquid- Versus Vapor-Phase Guest Transport in NaY

The extremely hydrophilic nature of NaY, together with mass-transport limitations imposed on the chemisorption process by co-adsorbed guests [see Chapter 6], require that the dehydrated zeolite bed be kept in a dry environment prior to chemisorption of guest species. As described in Chapter 5, organic adsorbates were generally introduced mechanically to the top of a packed bed of dehydrated NaY zeolite crystallites at room temperature prior to heating. With a normal melting point of 440 K and a normal boiling point of 538 K, hexamethylbenzene at 523 K might be transported axially into the bed by either liquid imbibition or by diffusion as a vapor. The following experiments and calculations demonstrate that the dominant transport mechanism in the NaY macropores involves vapor-phase diffusion of HMB molecules.

F.1.1 Imbibition of Liquid Benzene

Imbibition of benzene in a packed bed of NaY zeolite crystallites can be modeled as a system of small cylindrical capillary tubes through which the liquid species is drawn. Figure F.1(a) depicts the forces present on a thin column of liquid moving within a single idealized pore. The following assumptions simplify the treatment, while maintaining the validity of the model:

1. Entr· ·ce and gravitational effects are negligible.
2. The liquid phase is incompressible. The gas phase is inviscid.
3. The contact angle, θ, between the liquid and the solid wall is 0°.
4. An infinite reservoir of liquid exists to sustain the capillary flow.
5. A parabolic velocity profile exists within the capillary tube of radius a as predicted by the Hagen-Poiseuille equation:

$$\tau_w = \frac{4\mu}{a}\langle v_z \rangle , \tag{F.1}$$

where τ_w is the shear stress at the wall, μ is the liquid viscosity, and $\langle v_z \rangle$ is the average axial velocity.

An overall force balance leads to

$$2\pi a\sigma\cos\theta = \tau_w 2\pi a\, x_f(t) , \tag{F.2}$$

where σ is the surface tension, and $x_f(t)$ is the time-dependent position of the imbibing fluid front. Substituting Equation F.1 into Equation F.2 and taking $\theta = 0°$ yields

$$\sigma a = 4\mu\langle v_z \rangle\, x_f(t) = 4\mu\frac{\mathrm{d}x_f(t)}{\mathrm{d}t}\, x_f(t) . \tag{F.3}$$

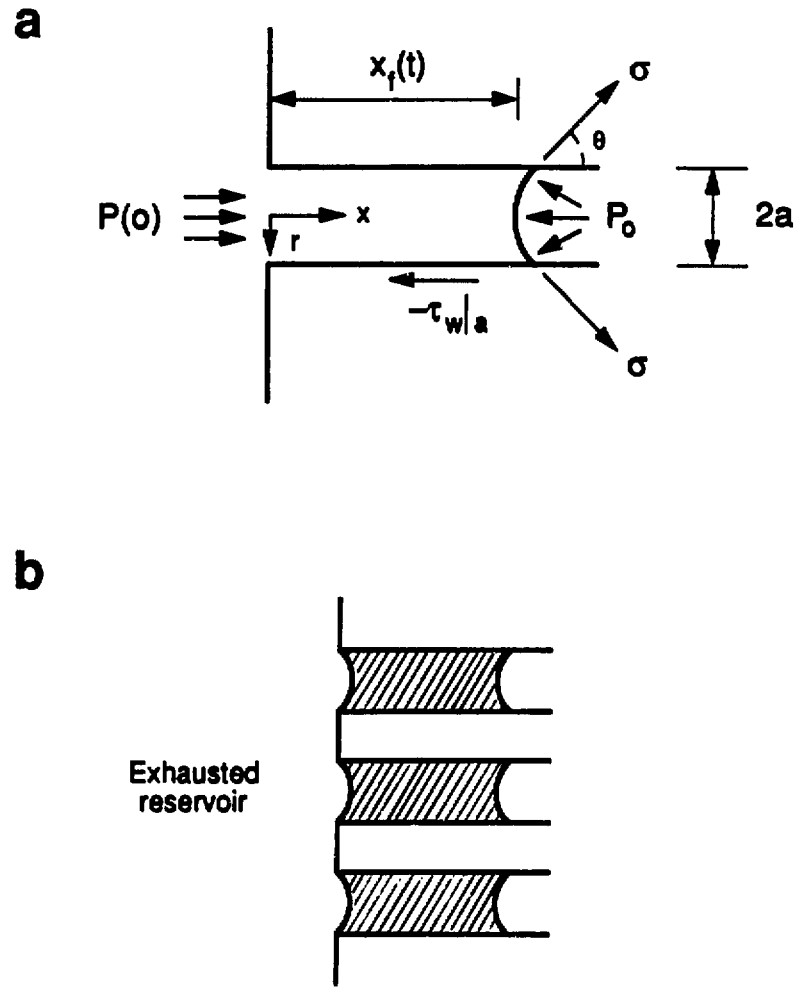

Figure F.1: (a) Dynamic force balance on a liquid thread in a cylindrical capillary tube. (b) A stationary macropore fluid distribution in thin capillaries resulting from mass-limited flow.

Integrating Equation F.3 establishes the time required for movement of the meniscus a distance $x_f(t)$ into the capillary:

$$t = \frac{2\mu x_f^2}{\sigma a}. \tag{F.4}$$

For capillary transport of benzene at 298 K through NaY macropores, the parameters in Equation F.4 acquire the values

$$\mu = 0.60\text{x}10^{-3}\ \tfrac{\text{kg}}{\text{m-s}},$$
$$\sigma = 29\text{x}10^{-3}\ \tfrac{\text{N}}{\text{m}},$$
$$a = 1\ \mu\text{m},$$
and $x_f = 0.01$ m (experimentally measured),

for which $t \approx 4$ s.

The short imbibition time computed for capillary flow of benzene in NaY macropores indicates that liquid-phase transport is occurring at room temperature. The liquid reservoir, however, (assumed to be limitless in the treatment above) is finite under the conditions of our experiments. Because the quantity of the bulk organic phase is small, the liquid reservoir is quickly exhausted after shallow penetration of the macropores at the top of the bed. As illustrated in Figure F.1(b), the meniscus formed at the trailing end of the imbibing liquid thread has a curvature opposite to that at the advancing end. With no further driving force, capillary liquid flow into the bed comes to a halt. The limited amount of bulk adsorbate, thus, leads to a stationary, imbibed fluid phase within the NaY macropores.

We observe experimentally the formation of a stable liquid phase within NaY macropores by arranging for mass-limited imbibition of benzene into a NaY packed bed. Hydrated NaY zeolite (1.16 g) was used to prevent competitive benzene adsorption within the NaY micropores. An overall loading of approximately 4 benzene

molecules per supercage requires a small volume of bulk material V_b:

$$V_b = (1.16 \text{ g wet NaY})\left(\frac{1 \text{ cm}^3}{1.92 \text{ g dry NaY}}\right)\left(\frac{1 \text{ unit cell}}{15\text{x}10^{-21} \text{ cm}^3}\right)\left(\frac{8 \text{ supercages}}{\text{unit cell}}\right) \cdot \left(\frac{4 \text{ } C_6H_6}{\text{supercage}}\right)\left(\frac{78 \text{ g } C_6H_6}{\text{mol } C_6H_6}\right)\left(\frac{1 \text{ mol } C_6H_6}{6.02\text{x}10^{23} \text{ } C_6H_6}\right)\left(\frac{1 \text{ cm}^3}{0.88 \text{ g } C_6H_6}\right)$$

$$V_b = 0.20 \text{ cm}^3 \text{ } C_6H_6 \qquad \text{(F.5)}$$

Procedure and Observations

1. Approximately 1 g of hydrated NaY zeolite was loaded into a 10-mm diameter NMR tube. The tube was tapped gently on the bench to pack the bed tightly and uniformly. (1.16 g NaY yielded a packed bed about 3.5 cm in length.)

2. Approximately 0.2 cm^3 of benzene was transferred by pipette to the top of the packed NaY bed. The macropores separating the micron-size NaY crystallites became saturated to boundary A in Figure F.2 over a period of a few seconds. The non-horizontal front boundary, on average about 0.2 cm from the top of the bed, was thereafter stationary. After 5 minutes, no tendency for further liquid penetration of the bed was observed. The volume of the macropores (50% porosity) in a 0.2 cm length of the bed is estimated to be 0.3 cm^3, corresponding closely to the amount of liquid benzene imbibed.

3. An additional 0.8 cm^3 of benzene was pipetted to the top of the packed NaY bed. The macropores became saturated down to a new stationary fluid boundary at B in Figure F.2 with no tendency for further penetration into the bed after 5 minutes.

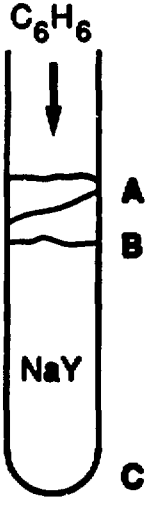

Figure F.2: Mass-limited imbibition of liquid benzene at room temperature into a packed bed of hydrated NaY zeolite. The macropores become saturated to different boundaries depending upon the amount of liquid benzene charged to the top of the bed: (A) 0.2 cm^3 C_6H_6, (B) 0.8 cm^3 C_6H_6, and (C) 3 cm^3 C_6H_6.

4. An additional 3 cm^3 of benzene was pipetted to the top of the packed NaY bed. The macropores became saturated to the bottom of the bed (C) in approximately 10 minutes as the liquid imbibed in the presence of the large benzene reservoir. Gas bubbles were liberated periodically from the bed as the liquid benzene displaced interstitial gas in the macropores. Benzene's slower than expected penetration of the bed [Eq. F.4] may arise from flow interference with exiting, displaced gases or from formation of a gelatinous slurry with the NaY powder which results in a more viscous fluid-like mixture.

For the very small quantities of benzene, 1,3,5-trimethylbenzene, and hexamethylbenzene used in the chemisorption experiments of Chapters 5 and 6, liquid-phase transport of the guest species is clearly mass-limited and occurs only within a shallow region of the bed. The adsorbate imbibes into the macropores until the supply of the liquid organic species is exhausted, that is, until an equivalent macropore volume has been filled. An overall loading of 1 HMB molecule per NaY supercage, for example, corresponds to a total adsorbate volume of 0.0954 $\frac{cm^3\ HMB}{g\ dry\ NaY}$ [Eq. F.17]. For 0.5 g dry NaY zeolite in a bed with 50% macroporosity, the HMB will consequently imbibe approximately 1.8 mm into the packed zeolite sample volume. This corresponds to about 7% of the total HMB/NaY contact volume observed after heating the system at 523 K for 2 h [Fig. 5.2]. This indicates that the dominant transport mechanism for aromatic guests within the NaY macropores must, thus, involve diffusion of the organic vapors, not capillary flow of the bulk liquids.

F.1.2 Vapor-Phase HMB Transport Experiment

To confirm that a sharp adsorption front can be produced by vapor-phase diffusion of HMB through the macropores of a packed zeolite bed, a HMB/NaY sample was

prepared in a manner that permitted only vapor-phase HMB to come in contact with the zeolite. The NaY zeolite was dehydrated overnight under vacuum (ca. 10^{-5} torr) at 723 K using the apparatus shown in Figure F.3(a). During the dehydration procedure, solid HMB was retained in the sidearm, sealed from the atmosphere, to prevent moisture contamination during mechanical addition of the bulk organic to the zeolite bed. The sidearm was immersed in an ice-water bath to minimize HMB sublimation during dehydration. After cooling the dehydrated zeolite bed to room temperature, the assembly was isolated from the vacuum rack and placed in a large diameter electric heater as shown in Figure F.3(b). The entire assembly was heated at a rate of 85 K/h to 473 K, soaked at 473 K for 2 h, and then cooled to room temperature at a rate of −85 K/h. In this way only vapor-phase HMB molecules, diffusing from the sidearm and adsorbing onto the NaY crystallites (as described in Chapter 6), were capable of reaching the zeolite bed. In Figure F.4 the ^{129}Xe NMR spectrum of xenon adsorbed on this sample reveals two well-resolved peaks at 111 ppm and 78 ppm consistent with a sharp boundary separating adsorption zones with and without HMB. Though the quantity of bulk HMB charged to the sidearm was sufficient to provide an overall loading of 0.5 HMB/supercage, the actual uptake by the zeolite bed was substantially less (≈0.15 HMB/supercage), as reflected by the low intensity of the peak at 110 ppm. While placement of heating tape around the upper teflon stopcock was designed to prevent HMB condensation in the vicinity of the fritted disk, it is likely that a significant quantity of the HMB condensed in this apparently cool region of the apparatus. Nonetheless, clear separation of the ^{129}Xe peaks provides convincing evidence that a sharp adsorption front is produced in a packed bed of NaY zeolite crystallites by vapor-phase diffusion of HMB at 473 K.

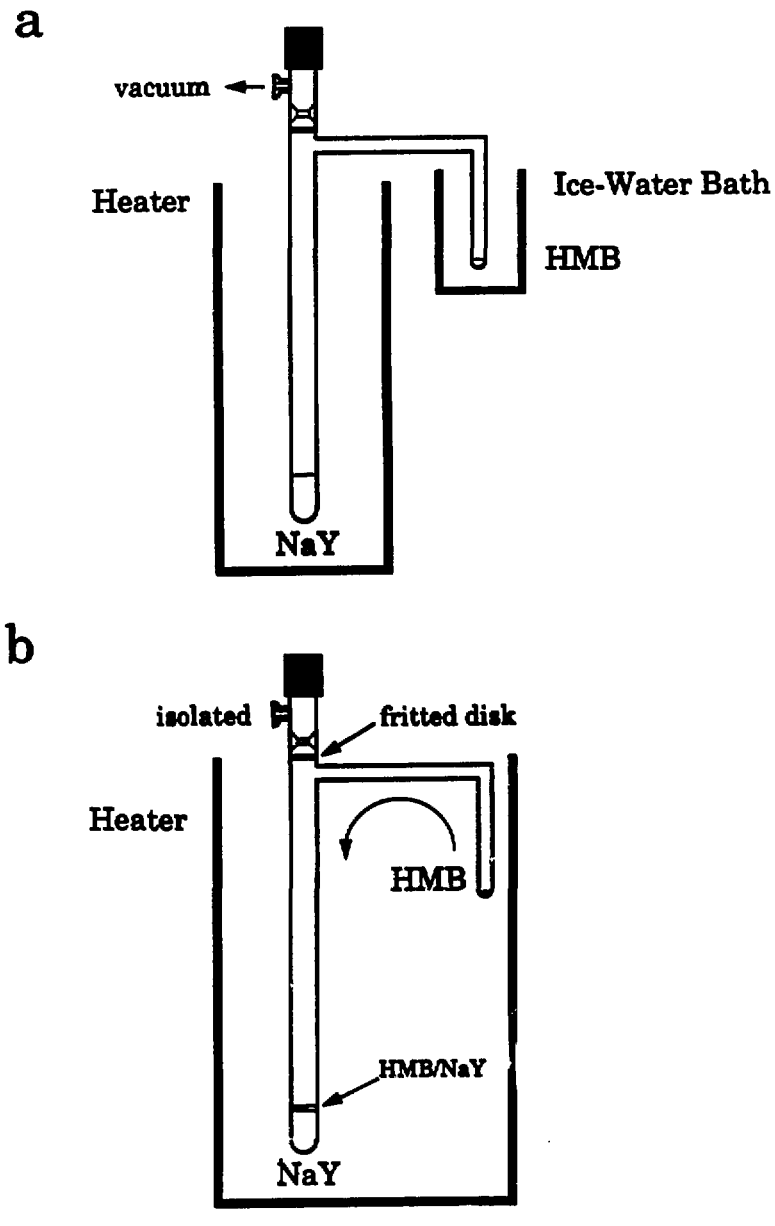

Figure F.3: Sample preparation apparatus for demonstrating vapor-phase transport of HMB through NaY macropores: (a) dehydration and (b) chemisorption configurations.

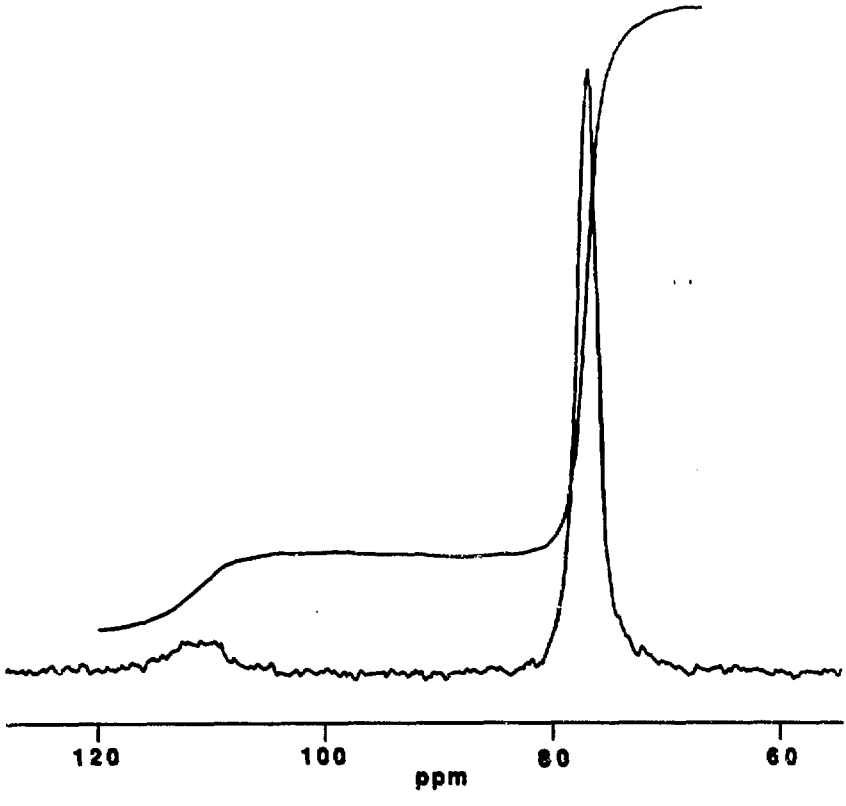

Figure F.4: Room-temperature ^{129}Xe NMR spectra of xenon (300 torr equilibrium pressure) adsorbed on dehydrated NaY zeolite containing a bulk average of $\approx$ 0.15 HMB molecules per supercage (as determined from the integrated peak areas.) The observed guest distribution resulted from strictly vapor-phase diffusion of HMB in the NaY macropores. The peak at 111 ppm arises from ^{129}Xe in supercage environments containing one adsorbed HMB guest molecule, while the resonance at 78 ppm is due to ^{129}Xe in empty NaY supercages. The two well-resolved peaks indicate the presence of a sharp adsorption front within the bed.

F.2 HMB Diffusivity in NaY

F.2.1 Intercrystalline HMB Diffusivity in Macropores

Bulk diffusivity of hexamethylbenzene.

From Bird *et al.* [183], pp. 510:

$$D_{hmb} = \frac{2}{3}\left(\frac{RT}{\pi^3 M_w}\right)^{\frac{1}{2}} \frac{1}{C_o N_A d_{hmb}^2} \tag{F.6}$$

where $R = 8.314\text{x}10^7 \frac{g \cdot cm^2}{s^2 \cdot mol \cdot K}$, gas constant;

$T = 523$ K, absolute temperature of the transport process;

$M_w = 162.28 \frac{g\ HMB}{mol}$, molecular weight of HMB;

$N_A = 6.02\text{x}10^{23}$ mol^{-1}, Avogadro's number;

$d_{hmb} = 0.82$ nm, kinetic diameter of HMB.

C_o is the vapor-phase concentration of HMB in equilibrium with the liquid reservoir at the top of the bed. At 523 K the vapor pressure of hexamethylbenzene P_{hmb} is approximately 0.1 atm so that

$$C_o = \frac{P_{hmb}}{RT} = 2.3\text{x}10^{-6} \frac{\text{mol}}{\text{cm}^3}. \tag{F.7}$$

Substituting Equation F.7 into Equation F.6 yields the bulk diffusivity of HMB at 523 K:

$$D_{hmb} = 2.1\text{x}10^{-5} \frac{\text{m}^2}{\text{s}}. \tag{F.8}$$

Knudsen diffusion of HMB in NaY macropores.

From Smith [122], pp. 452–460:

$$D_k = 97.0\, a \left(\frac{T}{M_w}\right)^{\frac{1}{2}}, \tag{F.9}$$

where a is the pore radius in meters, $\approx 1\text{x}10^{-6}$ m;

$T = 523$ K;

$M_w = 162.28 \frac{\text{g HMB}}{\text{mol}}$;

and D_k is in $\frac{\text{m}^2}{\text{s}}$;

yielding

$$D_k = 1.7\text{x}10^{-4} \frac{\text{m}^2}{\text{s}}. \tag{F.10}$$

Comparing Equations F.8 and F.10 indicates that vapor-phase transport of HMB in the NaY macropores is bulk diffusion-controlled From Sherwood *et al.* [184], pg. 42, we find that

$$D_{inter} = \frac{1}{\frac{1}{D_{hmb}} + \frac{1}{D_k}} = 1.9\text{x}10^{-5} \frac{\text{m}^2}{\text{s}}. \tag{F.11}$$

F.2.2 Intracrystalline HMB Diffusivity in Micropores

Intracrystalline transport of adsorbed aromatic guests in NaY zeolite is dealt with in detail in Chapter 6. Of interest here are the increase in intracrystalline guest diffusivity which occurs at elevated temperatures and the diminished guest diffusivity observed in the presence of co-adsorbed species. At higher temperatures, for example, transport resistances due to dipole-induced dipole interactions between the zeolite's exchangeable cations and polarizable aromatic guest species become less important [103,105,106,185]. Furthermore, elevated temperatures induce crystal lattice vibrations which decrease steric resistance to intracrystalline mass transfer. In Figure F.5 the intracrystalline diffusivity of benzene in NaX zeolite exhibits a temperature dependence consistent with an activated diffusion process described by [94,129]:

$$D_{intra}(T) = D_o e^{\frac{-E_a}{RT}}. \tag{F.12}$$

Assuming a similar functional form for the diffusivity of HMB in NaY, we can estimate the activation energy E_a which must exist for a 50 K change in temperature to produce an order of magnitude change in HMB's intracystalline diffusivity. Taking E_a and D_o to be independent of temperature, the diffusivities of HMB in NaY at temperatures T_1 and T_2 are related by

$$\frac{D_{intra,1}}{D_{intra,2}} = \frac{e^{\frac{-E_a}{RT_1}}}{e^{\frac{-E_a}{RT_2}}} = e^{\frac{-E_a}{R}\left(\frac{1}{T_1}-\frac{1}{T_2}\right)}, \tag{F.13}$$

which yields

$$E_a = \frac{R}{\left(\frac{1}{T_2}-\frac{1}{T_1}\right)} \ln\left(\frac{D_{intra,1}}{D_{intra,2}}\right). \tag{F.14}$$

Taking $R = 1.987\text{x}10^{-3}\ \frac{\text{kcal}}{\text{mol·K}}$,

$T_1 = 523$ K,

$T_2 = 573$ K,

$\left(\frac{D_{intra,1}}{D_{intra,2}}\right) = 0.1$,

permits the activation energy to be computed for diffusion of HMB in NaY under these conditions:

$$E_a = 27.4\ \frac{\text{kcal}}{\text{mol}}. \tag{F.15}$$

For comparison, the activation energy is $\approx 11\ \frac{\text{kcal}}{\text{mol}}$ for diffusion of benzene in NaX zeolite (determined from Fig. F.5). The larger activation energy estimated for HMB is consistent with greater steric resistance to diffusion of the larger HMB molecule in NaY.

Increased intracrystalline diffusivity of HMB at 573 K does not alter the shrinking-core treatment used in Chapter 6 to describe guest transport in the bidispersed NaY bed. The criterion which stipulates that guest transport in the micropores be much faster than transport in the macropores is already satisfied at 523 K. As discussed in Chapter 6, a more important factor influencing the distribution of adsorbed organic

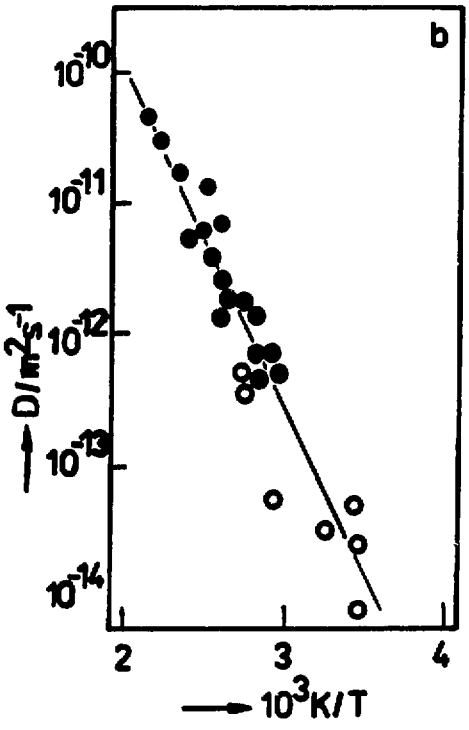

Figure F.5: Temperature dependence of the self-diffusivity of benzene in NaX zeolite at a loading of 4.8 molecules per cavity. Open circles are from NMR tracer uptake measurements; filled circles are from NMR pulsed-field gradient experiments on identical samples. Data taken from reference [186].

guests at higher temperatures is the guest concentration in the macropores, which becomes significant at 573 K [see Section 6.4.3].

Diffusion of adsorbed organic molecules in NaY zeolite has been shown to decrease dramatically in the presence of co-adsorbed water [121]. As illustrated in Figure F.6, for example, the diffusivities of ethane and n-butane decrease by up to three orders of magnitude as a function of H_2O loading in partially hydrated NaX. The diffusivities of higher molecular weight hydrocarbons in NaY are expected to be more sensitive to the presence of co-adsorbed guests because of heightened steric resistance to mass transport in general [1].

F.3 Adsorption Capacity of HMB in NaY

Intracrystalline HMB adsorption in NaY micropores.

$$\alpha = \left(\frac{1 \text{ HMB}}{\text{supercage}}\right)\left(\frac{8 \text{ supercages}}{\text{unit cell}}\right)\left(\frac{1 \text{ unit cell}}{15\text{x}10^{-21} \text{ cm}^3}\right)\left(\frac{1 \text{ cm}^3}{1.42 \text{ g dry NaY}}\right)\cdot \left(\frac{162 \text{ g HMB}}{\text{mol HMB}}\right)\left(\frac{1 \text{ mol HMB}}{6.02\text{x}10^{23} \text{ HMB}}\right)$$

$$\alpha = 0.1011 \frac{\text{g HMB}}{\text{g dry NaY}} \tag{F.16}$$

$$\alpha = 4.4\text{x}10^{-4} \frac{\text{mol HMB}}{\text{cm}^3 \text{ bed}} \tag{F.17}$$

where a macroporosity of 0.5 $\frac{\text{cm}^3 \text{ NaY}}{\text{cm}^3 \text{ bed}}$ has been used to obtain Equation F.17.
As discussed in Chapter 6 and in reference [127], a pseudo steady-state condition exists if

$$\frac{\alpha}{\phi C_o} > 10^3 . \tag{F.18}$$

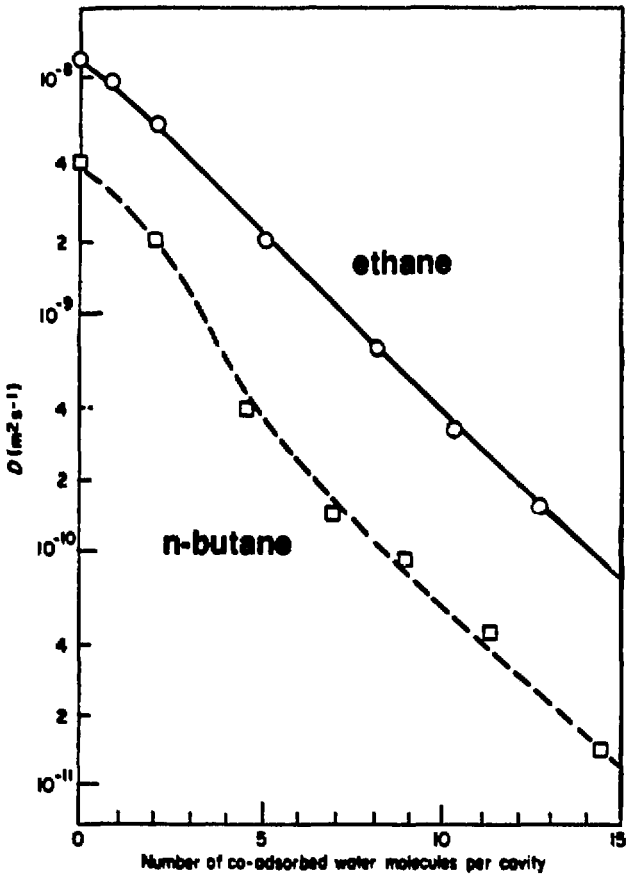

Figure F.6: Variation of the self-diffusivity of ethane (1.5 molecules/supercage) and n-butane (0.8 molecules/supercage) in NaX zeolite as a function of residual water concentration at 293 K. Data taken from reference [187].

For HMB adsorption at 523 K in a packed bed of NaY zeolite powder, this criteria is sufficiently satisfied, whereby:

$$\frac{\left(0.1011\ \frac{\text{g HMB}}{\text{g dry NaY}}\right)\left(6.17\text{x}10^{-3}\ \frac{\text{mol HMB}}{\text{g HMB}}\right)\left(1.42\ \frac{\text{g dry NaY}}{\text{cm}^3\ \text{NaY}}\right)}{\left(0.5\ \frac{\text{cm}^3\ \text{NaY}}{\text{cm}^3\ \text{bed}}\right)\left(2.3\text{x}10^{-6}\ \frac{\text{mol HMB}}{\text{cm}^3\ \text{bed}}\right)} = 770 \qquad \text{(F.19)}$$

For HMB adsorption at 573 K, however, the pseudo steady-state approximation is rendered invalid because of the higher gas-phase HMB concentration that exists in the bed. The gas-phase HMB concentration C_o is sensitive to temperature, increasing by an order of magnitude over the interval 523–573 K. Taking $P_{hmb} \approx 1$ atm at 573 K (well above the 538 K normal boiling point of HMB), C_o is computed to be $2.1\text{x}10^{-5}\ \frac{\text{mol}}{\text{cm}^3}$ using Equation F.7. The increased adsorption capacity that results from diminished kinetic barriers to sorption of a second HMB guest/supercage partially offsets the increase in C_o. This leads to

$$\frac{\alpha}{\phi C_o} \approx 140, \qquad \text{(F.20)}$$

which reflects the poorness of the pseudo steady-state approximation at 573 K.

Intercrystalline HMB adsorption in NaY macropores. The intrinsic adsorption properties of sites on the exterior surface of the 1-μm NaY crystallites will be identical to the micropore sites in the supercages, except for the absence of confinement effects and, perhaps, more numerous structural defects at the periphery of the particles. The adsorption capacities of the respective regions, therefore, scale with the available surface areas of the two regions. Intracrystalline surface areas of faujasite-type zeolites are typically in the vicinity of 800 m^2/g [188] as measured by nitrogen adsorption techniques [64]. The surface area of the macropores is readily estimated by summing the exterior surface areas of the ensemble of micron-size NaY crystallites comprising the packed bed. The exterior surface area of a single spherical

particle 1 μm in diameter is

$$S_{ext,p} = 4\pi r_p^2 = 3.1 \frac{\mu m^2}{\text{particle}}, \tag{F.21}$$

with the volume of such a particle being

$$V_p = \frac{4}{3}\pi r_p^3 = 0.5 \frac{\mu m^3}{\text{particle}}. \tag{F.22}$$

The total surface area presented by the exteriors of all the zeolite particles in the packed bed is therefore:

$$S_{ext,bed} = \phi \rho V_p S_{ext,p} = 2.1 \frac{m^2}{\text{g dry NaY}}, \tag{F.23}$$

where $\phi = 0.5 \frac{\text{cm}^3 \text{ NaY}}{\text{cm}^3 \text{ bed}}$, void fraction of the macropores;

$\rho = 1.42 \frac{\text{g dry NaY}}{\text{cm}^3 \text{ NaY}}$, density of dehydrated NaY zeolite;

and $S_{ext,p}$ and V_p are taken from Equations F.21 and F.22 above.

Hence, in a packed bed of NaY crystallites, the adsorption capacity of the micropores, thus, exceeds that of the macropores by approximately three orders of magnitude.

F.4 Adsorption of Organic Guests on Faujasite-Type Zeolites

Figures F.7 and F.8 display the highly nonlinear adsorption isotherms of benzene, n-heptane, and 1,3,5-triethylbenzene on NaX, NaY, and CaY zeolites.

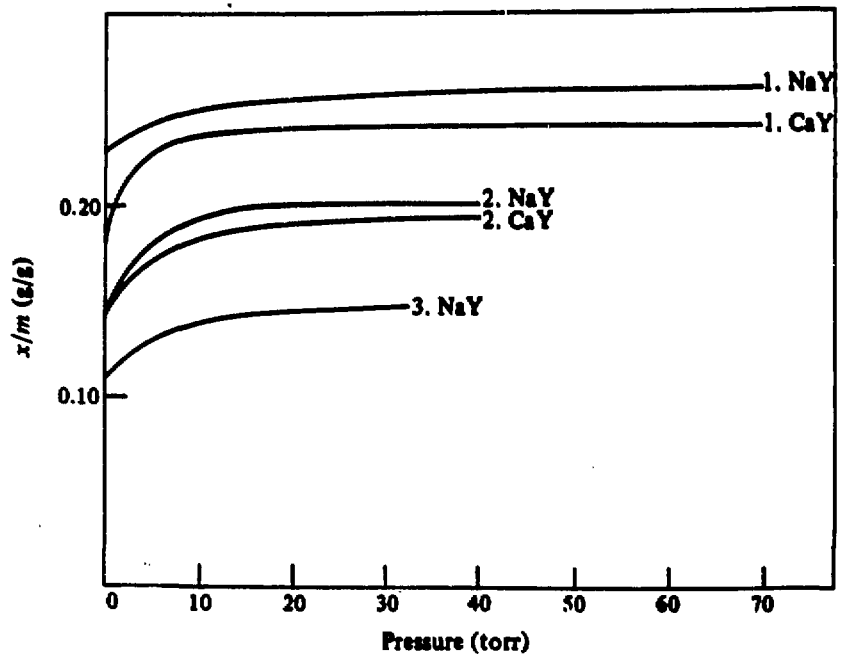

Figure F.7: Adsorption isotherms of benzene and n-heptane on NaY and CaY zeolites: (1.) benzene, 298 K; (2.) n-heptane, 298 K, (3.) n-heptane, 473 K. Data taken from reference [1], pp. 603.

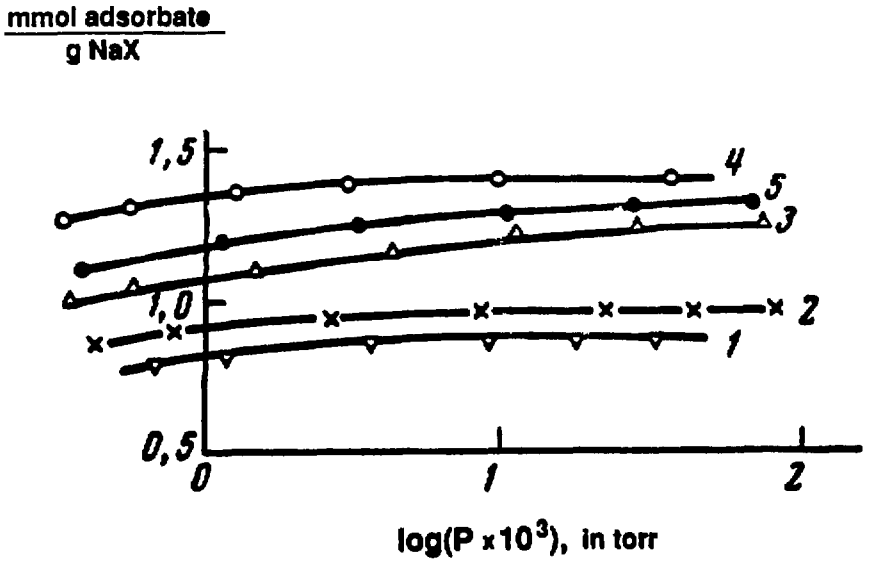

Figure F.8: Adsorption isotherms of 1,3,5-triethylbenzene (TEB) on NaX zeolite at temperatures of (1) 273 K, (2) 293 K, (3) 353 K, (4) 373 K, and (5) 423 K. Molecular sieve effects produce a kinetic barrier which restricts TEB penetration into the NaX lattice at low chemisorption temperatures. The increased TEB adsorption observed in curves (1)–(3) likely reflects transient TEB uptakes far from adsorption equilibrium. At temperatures below 373 K, equilibration times longer than those used in this study are apparently necessary to ensure adsorptive equilibrium prior to measurement of guest uptakes. At temperatures above 373 K (4)–(5), kinetic barriers to guest penetration of the zeolite are more readily overcome so that adsorptive equilibrium apparently is attained more quickly. Data taken from reference [129].

F.5 Proton NMR Spectra of HMB–NaY

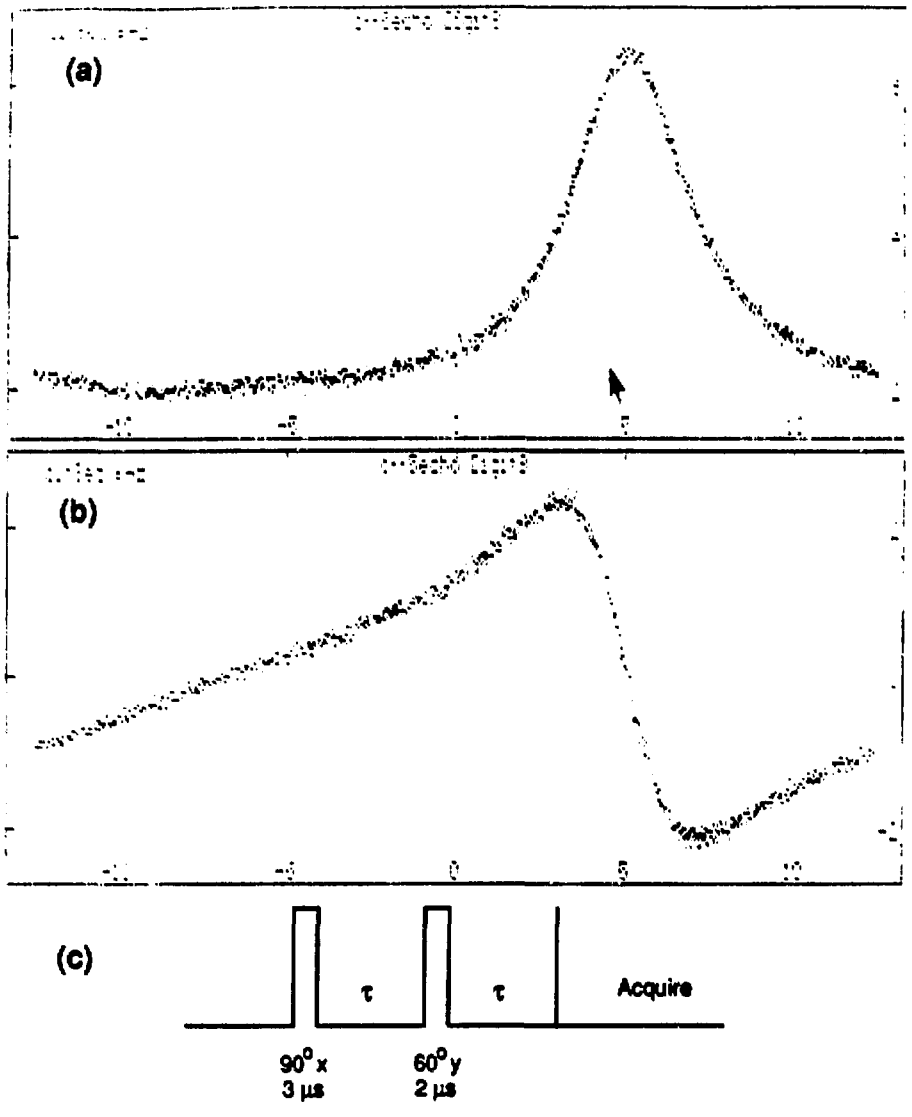

Figure F.9: Single-quantum proton NMR spectra of HMB adsorbed on NaY zeolite: (a) absorption spectrum, (b) dispersion spectrum, and (c) solid echo pulse sequence used to generate the data. The 5-kHz broad spectra preclude meaningful analysis, motivating the multiple-quantum approach discussed in Chapter 5.

Appendix G

Synthesis of ^{17}O-Enriched Mineral Precursors

G.1 Synthesis of $Si^{17}O_2$

G.1.1 Method 1: Oxidation of Silicon Tetrachloride

$$SiCl_4\,(g) + H_2{}^{17}O\,(l) \xrightarrow{298\ K} Si^{17}O_2\,(s) + 4\,HCl. \qquad (G.1)$$

This general approach was suggested by Prof. D.W. Hess (UC-Berkeley, Dept. of Chemical Engineering). Production of bulk silica (SiO_2) in such a fashion is apparently the opposite goal of methods used in the semiconductor industry for preparation of thin SiO_2 films. We have replaced the silane (SiH_4) species typically used in thin film manufacturing processes with silicon tetrachloride ($SiCl_4$), since the latter is a liquid at room temperature and therefore can be more safely handled. Nonetheless, $SiCl_4$ is toxic, reactive, and highly corrosive and, as such, must be handled only in a fume hood and with extreme care. The procedure described below proved to be a suitable means for production of contaminant-free, ^{17}O-enriched silicon

dioxide in reasonable (ca. 50%) yield.

Procedure

1. Assemble the apparatus diagrammed in Figure G.1. Begin with stopcocks 1 and 4 closed and stopcocks 2 and 3 open.

2. Heat the glassware with heating tape or a hot air blower to desorb residual water from the apparatus.

3. Evacuate the system to $\approx 10^{-3}$ torr with a mechanical pump.

4. Purge the inert-gas hose prior to connecting it to the apparatus at the location shown. Close stopcock 2 and open (slowly) stopcock 1. Charge the apparatus with dry inert gas (nitrogen or argon). Maintain positive pressure on the system, slightly above 1 atm, to prevent atmospheric moisture from entering the system when reactant species are introduced in Steps 5 and 6.

5. Remove the $H_2{}^{17}O$ reservoir flask at the 25-mm O-ring joint shown in Figure G.1. Pipette 1–2 cm^3 $H_2{}^{17}O$ into the $H_2{}^{17}O$ reservoir. Reattach the reservoir flask to the apparatus and then immerse the flask in a room-temperature water bath. The water bath mitigates any temperature increase which may result from the exothermic reaction ($\Delta H = -25.8$ $\frac{kcal}{mol}$) between water and silicon tetrachloride.

6. Remove the bellows/TC gauge assembly at the 9-mm O-ring joint also shown in Figure G.1. The stoichiometry of the reaction in Equation G.1 dictates that 3.19 cm^3 of $SiCl_4$ are required per cm^3 of $H_2{}^{17}O$. Pipette approximately two times the stoichiometric requirement of silicon tetrachloride into the $SiCl_4$ reservoir to ensure sufficient excess of this less valuable reactant. Reattach the bellows and gauge assembly to the apparatus.

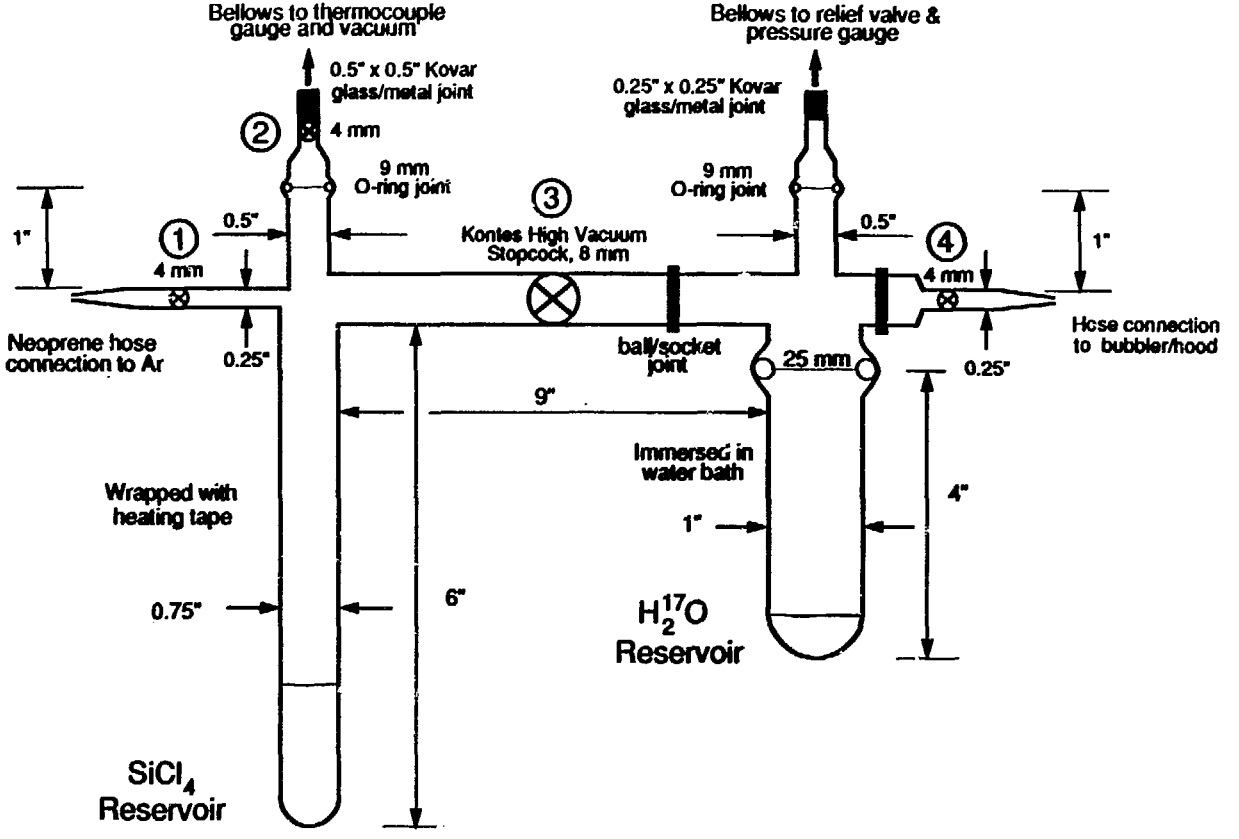

Figure H.1: Reactor apparatus for production of ^{17}O-enriched silicon dioxide.

7. Close stopcock 1 to isolate the reaction system.

8. Wrap the apparatus with heating tape. Turn on the heating tape to vaporize $SiCl_4$ (normal boiling point = 330 K). The $SiCl_4$ species will diffuse to the $H_2{}^{17}O$ reservoir flask and react at the liquid water interface. In this way the silica product is confined to a small region and is easily recovered.

9. The reaction will halt at a conversion level of about 24% due to build up of HCl in the $H_2{}^{17}O$ reservoir flask. The yield, however, can be improved by removing HCl from the reaction broth. To this end, the apparatus should be purged with inert gas by opening stopcocks 4 and 1 to flush unreacted $SiCl_4$ out of the system through a water bubbler to the fume hood exhaust. The bubbler, shown in Figure G.2, permits intimate mixing between the water and exhaust gases to ensure that no $SiCl_4$ is released to the atmosphere.

10. While the reactor apparatus is still in the fume hood and under slight positive inert gas pressure, disconnect the $H_2{}^{17}O$ reservoir flask at the 25-mm O-ring joint and syringe off the HCl by-product. The HCl is concentrated primarily in a liquid pool on top of a silica crust formed at the gas/water reaction interface. Discharge the HCl by-product into baking soda ($NaHCO_3$) to neutralize the acidity prior to disposal.

11. Break the silica crust with a glass rod and stir the silica/water gel. Add $SiCl_4$ dropwise until no further reaction occurs. The product is observed to become significantly more dense as the proportion of silica increases.

12. Reconnect the $H_2{}^{17}O$ reservoir flask to the reaction apparatus. Purge once again with inert gas as the flask is heated with a hot air blower to evaporate unreacted $SiCl_4$, together, admittedly, with any residual $H_2{}^{17}O$. Loss of a small

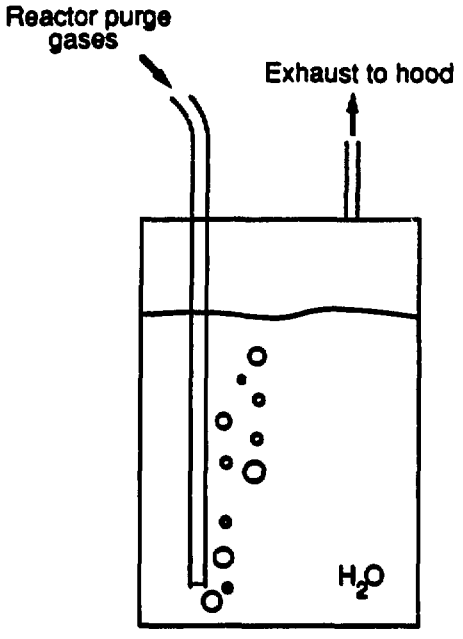

Figure G.2: Bubbler apparatus for removing unreacted $SiCl_4$ from exhaust gases.

amount of the ^{17}O-enriched water was deemed tolerable in light of the safety hazards posed by the silicon tetrachloride and the difficulty in separating the two components.

13. Disconnect the $H_2{}^{17}O$ reservoir flask at the 25-mm O-ring joint and remove the silica product. Filter and wash the silica with distilled water at room temperature to remove by-product HCl.

14. Dry the silica product at 353 K in a vacuum oven. Silica is stable and will not suffer ^{17}O–^{16}O exchange at low temperatures. The product species is actually a form of silicic acid which must be further dehydrated (more carefully in the absence of ^{16}O) at higher temperatures to remove additional water of hydration. Weighing the product at this point indicates a net yield of 50%. More

effective neutralization of the HCl by-product could improve the yield, though incorporation of a non-oxygen containing base into the process appears to be troublesome: in a trial procedure NH_3 reacted vigorously with $SiCl_4$ producing an undesirable white powder contaminant in appreciable quantity.

15. Recrystallization of pure $Si^{17}O_2$ at elevated temperatures ($\approx$ 973 K) is necessary to anneal the silica into the phase desired.

G.1.2 Method 2: Oxidation of Silicon Metal

Preparation of enriched silica by high temperature oxidation of silicon metal is infeasible because a substantial fraction of the $Si^{(0)}$ material remains as an unreacted contaminant. The reaction itself is straightforward and can be carried out in the presence of enriched oxygen gas to produce ^{17}O-enriched silica:

$$Si^{(0)}\,(s) + {}^{17}O_2\,(g) \xrightarrow{>1000\,K} Si^{17}O_2\,(s)\,. \qquad (G.2)$$

Unfortunately, as shown in Figure G.3, very long oxidation times are required at temperatures approaching 1500 K to oxidize completely silicon metal particles larger than a few microns in diameter. After thorough grinding of silicon wafers , we obtained silicon particles approximately 1–30 μm thick. The particles were pressed into a porous tablet at 10,000 psig, weighed carefully, wrapped in platinum foil, and placed in an alumina boat for heating. The tablet was then heated at 1400 K for 20 h in the presence of flowing O_2 and reweighed to determine oxygen uptake and, thus, the extent of reaction. Yields of less than 20% indicated that an appreciable fraction of unoxidized silicon remained, reflecting the diffusion-limited nature of the oxidation process.

effective neutralization of the HCl by-product could improve the yield, though incorporation of a non-oxygen containing base into the process appears to be troublesome: in a trial procedure NH_3 reacted vigorously with $SiCl_4$ producing an undesirable white powder contaminant in appreciable quantity.

15. Recrystallization of pure $Si^{17}O_2$ at elevated temperatures ($\approx$ 973 K) is necessary to anneal the silica into the phase desired.

G.1.2 Method 2: Oxidation of Silicon Metal

Preparation of enriched silica by high temperature oxidation of silicon metal is infeasible because a substantial fraction of the $Si^{(0)}$ material remains as an unreacted contaminant. The reaction itself is straightforward and can be carried out in the presence of enriched oxygen gas to produce ^{17}O-enriched silica:

$$Si^{(0)}\,(s) + {}^{17}O_2\,(g) \xrightarrow{>1000\,K} Si^{17}O_2\,(s)\,. \qquad (G.2)$$

Unfortunately, as shown in Figure G.3, very long oxidation times are required at temperatures approaching 1500 K to oxidize completely silicon metal particles larger than a few microns in diameter. After thorough grinding of silicon wafers , we obtained silicon particles approximately 1–30 μm thick. The particles were pressed into a porous tablet at 10,000 psig, weighed carefully, wrapped in platinum foil, and placed in an alumina boat for heating. The tablet was then heated at 1400 K for 20 h in the presence of flowing O_2 and reweighed to determine oxygen uptake and, thus, the extent of reaction. Yields of less than 20% indicated that an appreciable fraction of unoxidized silicon remained, reflecting the diffusion-limited nature of the oxidation process.

G.2 Synthesis of $Ca^{17}O$

G.2.1 Synthesis of $Ca(^{17}OH)_2$

$$Ca^{(0)}\ (\text{metal}) + 2\,H_2{}^{17}O\ (l) \xrightarrow{298\ K} Ca(^{17}OH)_2\ (s) + H_2\ (g) \qquad (G.3)$$

Based on the reaction stoichiometry of Equation G.3, 1.11 g of calcium metal are required per cm^3 of ^{17}O-enriched water. The synthesis must be carried out in an dry, argon-filled glove box, since $Ca^{(0)}$ passivates in air.

Procedure

1. In an argon glove box, introduce ≈ eight 6-mesh pieces of calcium metal to a vial possessing a female 24/40 standard ground glass joint.

2. Attach the 24/40 vial to a support stand and position the bottom of the vial in an ice-water bath to remove heat generated from the highly exothermic reaction ($\Delta H = -167.4\ \frac{kcal}{mol}$) between calcium metal and water. The bath condenses $H_2{}^{17}O$ vapor liberated as steam by the heat of reaction. Note: liquid nitrogen is unsatisfactory for this purpose because it not only freezes the water, but also vaporizes violently in the glove-box transfer chamber during evacuation of contaminant atmospheric gases.

3. Add $H_2{}^{17}O$ dropwise to the calcium metal pieces as shown in Figure G.4(a). Stir occasionally with a spatula.

4. When the reaction is essentially complete, cap the 24/40 reaction vial with a male 24/40 joint sealed to the 4 mm Kontes high-vacuum teflon stopcock shown in Figure G.4(b).

5. Close stopcock 5 to isolate the $Ca(^{17}OH)_2$ product in an argon atmosphere. This prevents loss of $H_2{}^{17}O$ and deters reaction with atmospheric CO_2 which

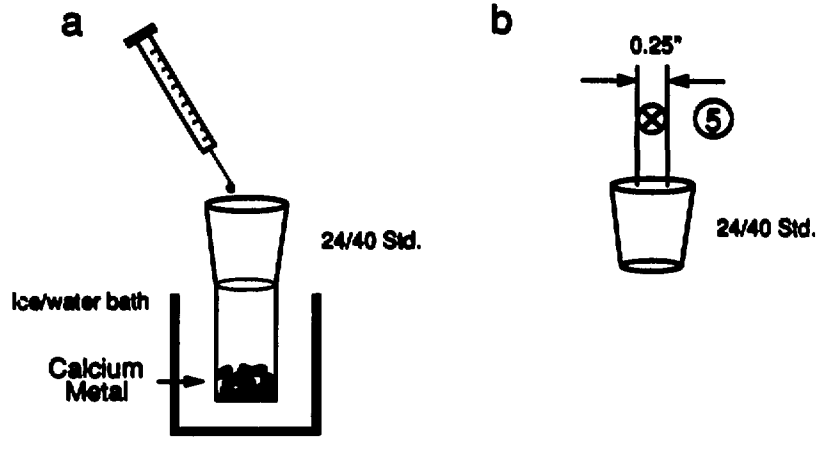

Figure G.4: Simple reaction apparatus for preparation of ^{17}O-enriched calcium hydroxide.

otherwise dilutes the ^{17}O enrichment of the final product. Calcium carbonate will be produced at room temperature ($\Delta G = -17.0 \frac{kcal}{mol}$) according to the reaction

$$Ca(^{17}OH)_2\,(s) + CO_2\,(g) \xrightarrow{298\,K} CaCO_3\,(s) + H_2{}^{17}O\,. \qquad (G.4)$$

6. Remove the closed vial assembly from the glove box for product drying and $H_2{}^{17}O$ recovery.

G.2.2 Recovery of $H_2{}^{17}O$

1. Attach the vial assembly to the Wet Product port on the vacuum rack depicted in Figure G.5.

2. Attach the recovery trap assembly illustrated in Figure G.6 to the $H_2{}^{17}O$ recovery port of Figure G.5. (The 5-cm^3 collection ampoule and the attachment with stopcock 13 should not be attached at this point but will be used later.)

3. Place heating tape around the 24/40 vial containing the $Ca(^{17}OH)_2$ product and around the vacuum rack manifold to stopcock 10. A thermocouple should be sandwiched between the glass and the tape to permit control of the drying temperature.

4. Close stopcocks 5, 6, 9, and 12, leaving 7, 8, 10, and 11 open.

5. Open stopcock 6 to evacuate the recovery assembly.

6. Immerse the U-shaped end of the recovery trap in a liquid nitrogen bath.

7. Close stopcock 6 to isolate the recovery assembly.

8. Open stopcock 5 to begin drying the product.

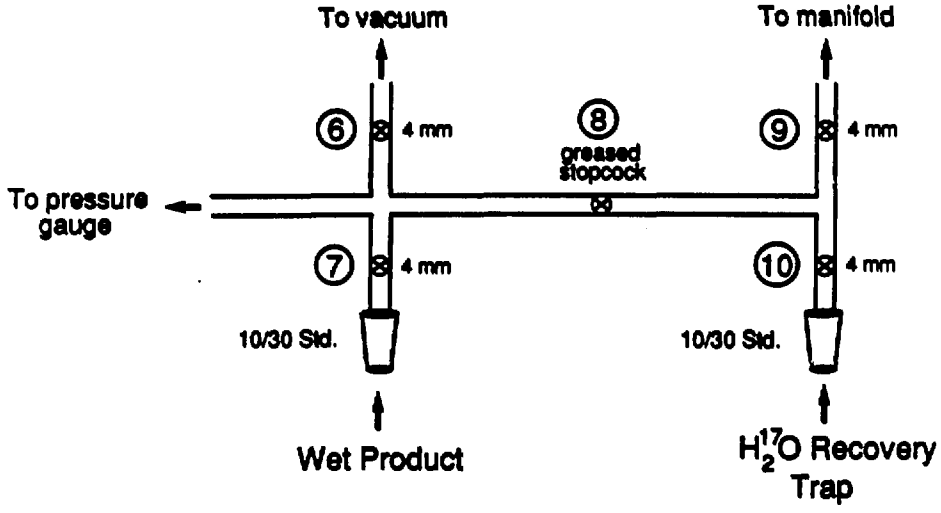

Figure G.5: Vacuum rack connections for recovery of $H_2{}^{17}O$.

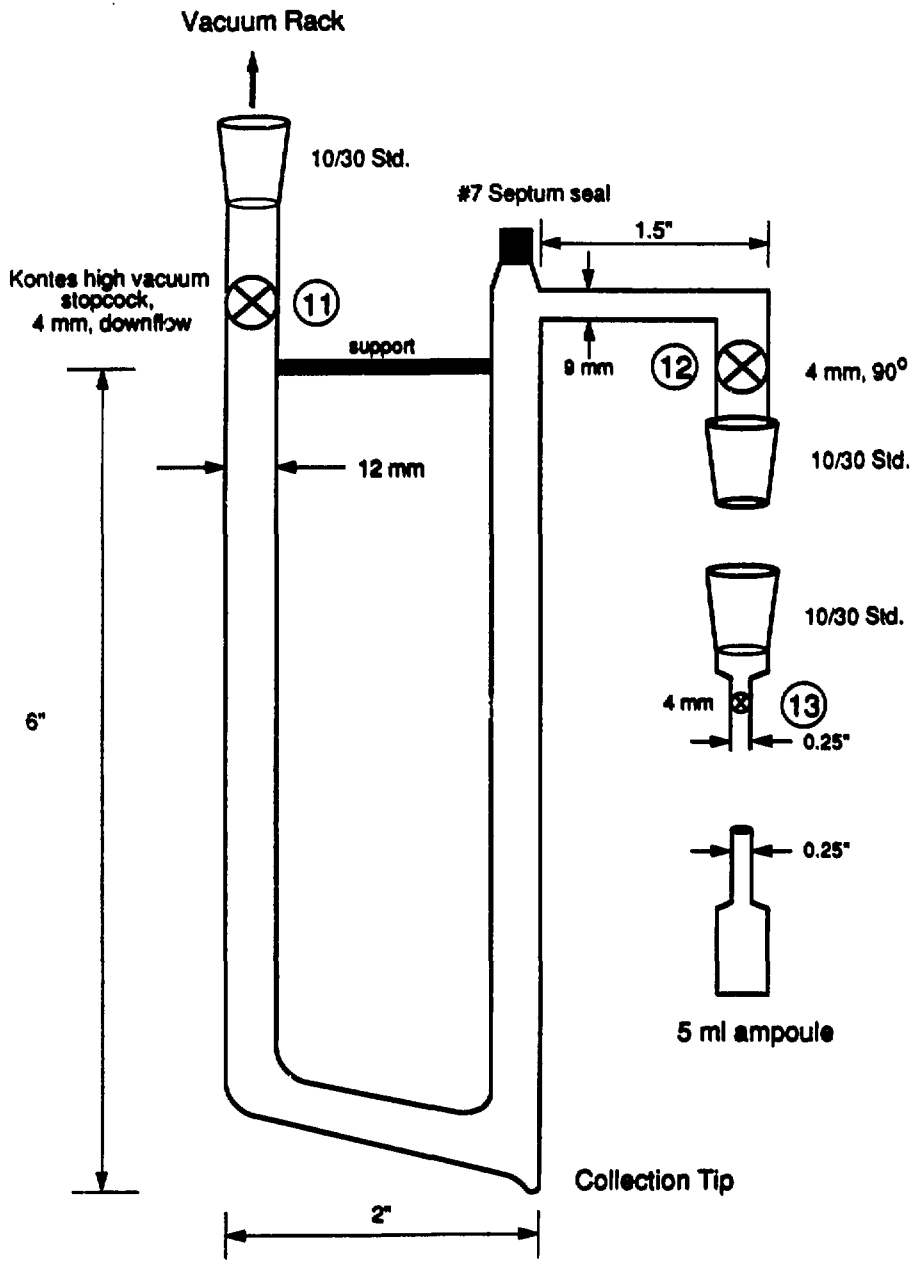

Figure G.6: $H_2{}^{17}O$ recovery trap for use during drying of solid hydroxide species.

9. Turn on the heating tape to achieve a drying temperature of 353–373 K. Note: heating the product paste encourages continued reaction between any remaining calcium metal and residual ^{17}O-enriched water.

10. When drying is complete, close stopcock 5 to isolate the dry $Ca(^{17}OH)_2$ product. Remove the vial assembly from the vacuum rack for further handling described in Section G.2.3 below.

11. With a hot-air gun chase condensed $H_2{}^{17}O$ from cold parts of the vacuum rack to the liquid nitrogen trap.

12. Close stopcock 11 to isolate the recovery trap which now contains all recoverable $H_2{}^{17}O$.

13. Remove the liquid nitrogen trap and allow the $H_2{}^{17}O$ condensate to melt. Once melting is complete, use a syringe to penetrate the septum seal and extract the $H_2{}^{17}O$ condensate from the collection tip in the recovery trap. Discharge the $H_2{}^{17}O$ into the 5-cm^3 ampoule and quickly connect the ampoule to the $H_2{}^{17}O$ recovery apparatus [Fig. G.6] with a 0.25 inch Cajun Ultratorr fitting via stopcocks 12 and 13.

14. To avoid vaporizing the water as the sample is sealed, resolidify the $H_2{}^{17}O$ by immersing the ampoule in liquid nitrogen. Sealing will be facilitated by slowly opening stopcocks 12 and 13 to produce a slight vacuum in the ampoule. ($H_2{}^{17}O$ is extremely hygroscopic and contact with the atmosphere should be minimized.)

15. With a glass-blowing torch, carefully seal the 5-cm^3 ampoule at the neck.

16. Retain the ampoule for future use. The distilled $H_2{}^{17}O$ contents should be pure and undiluted.

G.2.3 Decomposition of the Hydroxide to $Ca^{17}O$

$$Ca(^{17}OH)_2\ (s) \xrightarrow{853\ K} Ca^{17}O\ (s) + H_2{}^{17}O\ (l). \qquad (G.5)$$

1. In an argon glove box, remove the stopcock assembly from the 24/40 vial. Wipe away joint grease with a paper towel.

2. Load the dry $Ca(^{17}OH)_2$ material into the quartz calcination cell shown in Figure G.7. Place a wad of quartz wool near the top of the cell to prevent the product from being drawn into the vacuum rack. Care should be taken to avoid loss of the quartz wool into the bed upon removal of the wool. Note: originally the hydroxide was heated in a platinum crucible placed inside the quartz cell to avoid reaction with the silica in the quartz wall. The drying/decomposition, however, produced fluidization of the bed, ejecting approximately 50% of the material out of the Pt crucible into the quartz cell proper. No etching or other sign of reaction was observed between $Ca^{17}O$ and the SiO_2 cell walls at 873 K.

3. Attach the quartz cell to the vacuum rack using Apiezon grease, Type N.

4. If desired, the $H_2{}^{17}O$ decomposition product can be collected as described in Section G.2.2 above.

5. Using a programmable temperature controller, heat the hydroxide slowly from 298 K to 873 K over a period of 6 h. Soak the system at 873 K for 6 h before cooling the oxide product to room temperature. Note: the grey sample color observed after drying at 873 K likely reflects the presence of a carbon impurity since subsequent sample heating at 1273 K restores a white coloration. An

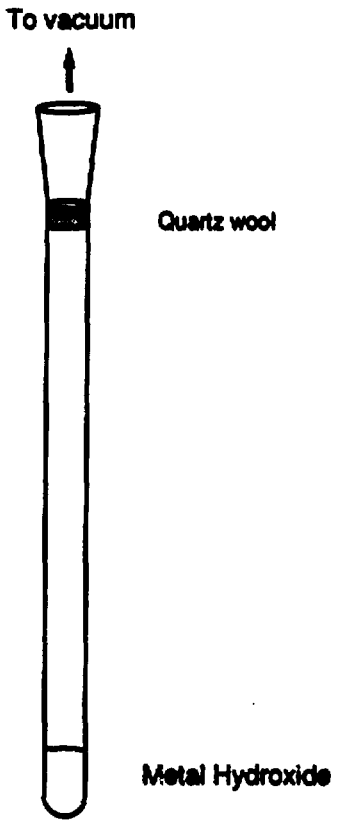

Figure G.7: Quartz cell used for decomposition of $Ca(^{17}OH)_2$ to $Ca^{17}O$ and $Mg(^{17}OH)_2$ to $Mg^{17}O$.

additional 10% loss of sample mass is also registered after heating the $Ca^{17}O$ material to 1273 K.

6. Both $Ca^{17}O$ and $Ca(^{17}OH)_2$ will react spontaneously with atmospheric CO_2 (For CaO at 298 K: $\Delta G = -32.5 \frac{kcal}{mol}$) to produce calcium carbonate with diluted ^{17}O enrichment. The ^{17}O-enriched product species should, thus, be stored under an inert atmosphere of nitrogen or argon.

G.3 Synthesis of $Mg^{17}O$

The synthesis of ^{17}O-enriched magnesium oxide involves an aqueous route since rapid passivation of the metal renders direct reaction with water infeasible. This has the inherent disadvantage of requiring much more $H_2{}^{17}O$ due to limited solubilities of the reactant species. Appropriate recovery steps are necessary to prevent waste of the expensive $H_2{}^{17}O$ solvent.

$$MgCl_2\,(aq) + 2\,K^{17}OH\,(aq) \xrightarrow{298\ K} Mg(^{17}OH)_2\,(s) + 2\,KCl\,(aq) \qquad (G.6)$$

Procedure

1. Enrich KOH in ^{17}O by dissolution and exchange in enriched $H_2{}^{17}O$. In an argon glove box, add 3.0 cm^3 $H_2{}^{17}O$ to 5.61 g KOH in a 24/40 vial [Fig. G.4(a)] to form a saturated solution at room temperature.

2. Cap the 24/40 vial with the stopcock assembly shown in Figure G.4(b). Close the stopcock to isolate the saturated KOH solution in the vial.

3. Wrap the bottom of the 24/40 vial with heating tape, sandwiching a thermocouple between the glass and the tape to monitor the KOH solution temperature

during heating.

4. Turn on the heating tape and let the solution stand for 3 days at $\approx$ 348 K.

5. Dissolve 4.8 g anhydrous $MgCl_2$ in 10.0 cm^3 $H_2{}^{17}O$ in a 25-cm^3 Erlenmeyer flask.

6. After the $K^{17}OH$ exchange is complete, add the $MgCl_2$ solution slowly to the saturated $K^{17}OH$ solution, stirring occasionally.

7. Recover the excess water as described in Section G.2.2 above. Note: The ^{17}O-enrichment of the recovered water will be somewhat less than that of the original starting material due to dilution during the KOH exchange.

8. After drying, approximately 10 g of mixed $Mg(^{17}OH)_2$ and KCl remain. Wash the solid product five times with 300 cm^3 of distilled water to remove the soluble KCl component.

9. Dry the $Mg(^{17}OH)_2$ product under vacuum at room temperature. (Mass of the product after drying: 2.57 g $Mg(^{17}OH)_2$.)

10. Decomposition of the hydroxide to $Mg^{17}O$ occurs at 623 K (use 648 K) and can be accomplished as described in Section G.2.3 above.

11. Both $Mg^{17}O$ and $Mg(^{17}OH)_2$ will react spontaneously with atmospheric CO_2 (For MgO at 298 K: $\Delta G = -17.0 \frac{kcal}{mol}$) to produce magnesium carbonate of diluted ^{17}O enrichment. The ^{17}O-enriched product species should, thus, be stored in an inert atmosphere of nitrogen or argon.

G.4 Uses of Precursor Materials

A variety of ^{17}O-enriched silicate minerals have been produced by heating mixtures of $Si^{17}O_2$, $Ca^{17}O$, and $Mg^{17}O$ at high temperatures (ca. 1300 K). We thank Prof. J. Stebbins (Stanford Univ., Dept. of Geology) for preparation of the mineral compounds cristobalite ($Si^{17}O_2$), diopside ($CaMgSi_2^{17}O_6$), forsterite ($Mg_2Si^{17}O_4$), larnite ($Ca_2Si^{17}O_4$), and wollastonite ($CaSi^{17}O_3$) using the ^{17}O-enriched precursor species whose synthesis has been outlined above. New double rotation and dynamic-angle spinning NMR experiments for the first time resolve distinct ^{17}O sites in these materials by removing anisotropic effects associated with second-order quadrupolar interactions [189,190].

Bibliography

[1] Breck, D.W., **Zeolite Molecular Sieves**, Krieger: Malabar, Florida (1982).

[2] Barrer, R.M., **Zeolites and Clay Minerals as Sorbents and Molecular Sieves**, Academic Press: New York (1978).

[3] Minachev, Kh. and Isakov, Ya.I., "Catalytic Properties of Metal-Containing Zeolites," **Zeolite Chemistry and Catalysis**, Rabo, J.A., ed., American Chemical Society: Washington, D.C., 552–611 (1976).

[4] Bolton, A.P., "Molecular Sieve Zeolites," **Experimental Methods in Catalysis Research**, vol. 2, Anderson, R.B. and Dawson, P.T., eds., Academic Press: New York, 1–42 (1976).

[5] **Proceedings of the Symposium on Zeolites, Szeged, Hungary, 11 to 14 September 1978**, *Acta Physica et Chemica* **24**(1–2), 1–354 (1978).

[6] Jacobs, P.A., **Carboniogenic Activity of Zeolites**, Elsevier: Amsterdam (1977).

[7] Jacobs, P.A., *et al.*, eds., **Metal Microstructures in Zeolites: Preparation, Properties, Applications**, *Studies in Surface Science and Catalysis 12*, Elsevier: Amsterdam, (1982).

[8] Jacobs, P.A., Jaeger, N.I., Jírů, P., Kazansky, V.B., and Schulz-Ekloff, G., eds., **Structure and Reactivity of Modified Zeolites**, *Studies in Surface Science and Catalysis 18*, Elsevier: Amsterdam, (1984).

[9] Jacobs, P.A. and van Santen, R.A., eds., **Zeolites: Facts, Figures, Future**, *Studies in Surface Science and Catalysis 49*, Elsevier: Amsterdam, (1989).

[10] Dalla-Betta, R.A. and Boudart, M., "Well-Dispersed Platinum on Y Zeolite: Preparation and Catalytic Activity," Proceedings of the Fifth International Congress on Catalysis, Miami, 20 to 26 July 1972, **Catalysis**, Hightower, J.W., ed., North-Holland: Amsterdam, vol. 2, 1329–1341 (1973).

[11] Gallezot, P., "The State and Catalytic Properties of Platinum and Palladium in Faujasite-type Zeolites," *Catalysis Reviews – Science and Engineering* **20**(1), 121–154 (1979).

[12] Weitkamp, J., Jacobs, P.A., and Ernst, S., "Shape Selective Isomerization and Hydrocracking of Naphthenes over Pt/HZSM-5 Zeolite," **Structure and Reactivity of Modified Zeolites**, Jacobs, P.A., Jaeger, N.I., Jírů, P., Kazansky. V.B., and Schulz-Ekloff, G., eds., Elsevier: Amsterdam, 279–290 (1984).

[13] Martens, J.A. and Jacobs, P.A., "Shape-Selective Effects on the Metal Catalyzed Reactions of Prehnitene over Zeolites," **Structure and Reactivity of Modified Zeolites**, *Studies in Surface Science and Catalysis 18*, Jacobs, P.A., Jaeger, N.I., Jírů, P., Kazansky, V.B., and Schulz-Ekloff, G., eds., Elsevier: Amsterdam, 189–199 (1984).

[14] Arai, H. and Tominaga, H., "The Influence of Platinum Particle Size on the Activity and Selectivity of Reforming Catalysts," **New Horizons in Catalysis**,

Studies in Surface Science and Catalysis 7B, Seiyama, T. and Tanabe, K., eds., Elsevier: Amsterdam, 1446–1447 (1981).

[15] Bragin, O.V., Vasina, T.V., Isakov, Ya.I., Palishkina, N.V., Preobrazhensky, A.V., Nefedov, B.K., and Minachev, Kh.M., "Aromatization of Ethane on Metal-Zeolite Catalysts," **Structure and Reactivity of Modified Zeolites**, *Studies in Surface Science and Catalysis 18*, Jacobs, P.A., Jaeger, N.I., Jírů, P., Kazansky, V.B., and Schulz-Ekloff, G., eds., Elsevier: Amsterdam, 273–278 (1984).

[16] Corma, A., Miranda, M.A., and Perez-Pariente, J., "Influence of Metal Dispersity on the Decay of a Platinum/NaY Zeolite Catalyst in the Dehydrogenation of Methylcyclohexane," *Reaction Kinetics and Catalysis Letters* **23**(1–20), 153–158 (1983).

[17] Engelen, C.W.R., Wolthuizen, J.P., and Van Hooff, J.H.C., "Reactions of Propane over a Bifunctional Platinum/H-ZSM-5 Catalyst," *Applied Catalysis* **19**(1), 153–163 (1985).

[18] Jacobs, P.A., Tielen, M., and Martens, J., "Comparison of Acid- to Metal-Catalysed Conversion of n-Decane and Cyclodecane on ZSM-5 and Faujasite-Type Zeolites," *Journal of Molecular Catalysis* **27**(1), 11–23 (1984).

[19] Meriaudeau, P., Sapaly, G., and Naccache, C., "On the Role of Ga, Pt, PtCu and PtGa in HZSM-5 for the Cyclisation of Propane into Aromatics," **Zeolites: Facts, Figures, Future**, *Studies in Surface Science and Catalysis 49*, Jacobs, P.A. and van Santen, R.A., eds., Elsevier: Amsterdam, 1423–1429 (1989).

[20] Naccache, C., Kaufherr, N., Dufaux, M., Bandiera, J., and Imelik, B., "Platinum Catalysts Supported on Zeolite. Hydrogenation of Cyclopropane and Hydrogenolysis of Ethane," **Molecular Sieves–II**, Katzer, J.R., ed., American Chemical Society: Washington, D.C., 538–548 (1977).

[21] Chow, M., Park ,S.H., and Sachtler, W.H.M., "Ring Enlargement and Ring Opening over Mono- and Bifunctional Catalysts," *Applied Catalysis* **19**(1), 349–364 (1985).

[22] Gallezot, P., Datka, J., Massardier, J., Primet, M., and Imelik, B., "Unusual Catalytic Behavior of Very Small Platinum Particles Encaged in Y Zeolites," **Proceedings of the 6th International Congress on Catalysis, 1976**, Royal Chemical Society: London, 696–707 (1977).

[23] Rabo, J.A., Schomaker, V., and Pickert, P.E., "Sulfur Resistant Isomerization Catalyst. Study of Atomic Platinum Dispersions on a Zeolite Support," **Proceedings of the 3rd International Congress on Catalysis, 1964**, vol. 2, North Holland: Amsterdam, 1264–1275 (1965).

[24] Gallezot, P., Alarcon, A., Dalmon, J.A., Renouprez, A.J., and Imelik, B., "Location and Dispersion of Platinum in PtY Zeolites," *Journal of Catalysis* **39**, 334–349 (1975).

[25] For example: (a) Gallezot, P., Coudurier, G., Primet, M., and Imelik, B., "Adsorption and Decomposition of Metal Carbonyls Loaded in Y-type Zeolites," **Molecular Sieves–II**, Katzer, J.R., ed., American Chemical Society: Washington, D.C., 144–155 (1977); (b) Bailey, D.C. and Langer, S.H., "Immobilized Transition-Metal Carbonyls and Related Catalysts," *Chemical Reviews* **81**, 110–148 (1981); (c) Evans, J., "The Relationship between Metal Carbonyl Clusters

and Supported Metal Catalysts," *Chemical Society Reviews* **10**, 159–180 (1981); (d) Tatsumi, T., Odajima, H., Yamaguchi, K., and Tominaga, H., "Carbon Monoxide Hydrogenation Catalyzed by Zeolite-Supported Ruthenium Carbonyl Clusters in the Presence of Methyl Iodide," **Zeolites: Fac s, Figures, Future,** *Studies in Surface Science and Catalysis 49*, Jacobs, P.A. and van Santen, R.A., eds., Elsevier: Amsterdam, 1301–1310 (1989).

[26] Jacobs, P.A., "Mechanisms of Formation and Stabilization of Metals in the Pore Structure of Zeolites," **Metal Microstructures in Zeolites: Preparation, Properties, Applications**, *Studies in Surface Science and Catalysis 12*, Jacobs, P.A., *et al.*, eds., Elsevier: Amsterdam, 71–85 (1982).

[27] Ribeiro, F.R. and Marcilly, C., "Influence of Platinum on the Structural Stability of $[Pt(NH_3)_4NH_4Y]$ and $[Pt(NH_3)_4NH_4M]$ Zeolites during Calcination," Proceedings of the Fifth International Symposium on Heterogeneous Catalysis, Varna, USSR, *Geterogennyi Kataliz Trudy Mezhdunarounogd Sympozima*, **5**, 383–387 (1983).

[28] Foger, K. and Anderson, J.R., "Reactions of Neopentane and Neohexane on Platinum/Y-Zeolite and Platinum/Silica Catalysts," *Journal of Catalysis* **54**(3), 318–335 (1978).

[29] Uytterhoeven, J.B., "Metallic Clusters in Zeolites," *Acta Physica et Chemica*, 53–69 (1978).

[30] Braun, G., Fetting, F., Haelsig, C.P., and Gallei, E., "The State of Platinum in Zeolitic Catalysts," *Acta Physica et Chemica*, 93–97 (1978).

[31] Gallezot, P., "Catalytic Activity of Very Small Particles of Platinum and Palladium Supported in Y-type Zeolite," **Catalysis by Zeolites**, *Studies in Surface Science and Catalysis 5*, Imelik, B. et al., eds., Elsevier: Amsterdam, 227–234 (1980).

[32] Jaeger, N., Ryder, P., Schulz-Ekloff, G., **Structure and Reactivity of Modified Zeolites**, *Studies in Surface Science and Catalysis 18*, Jacobs, P.A., Jaeger, N.I., Jírů, P., Kazansky, V.B., and Schulz-Ekloff, G., eds., Elsevier: Amsterdam, 299–311 (1984).

[33] Felthouse, T.R. and Murphy, J.A., "Zeolite-Encapsulated Platinum Catalysts: Preparation, Characterization by Transmission Electron Microscopy, and Their Shape Selective Behavior toward Various Nitrogen Base Poisons during the Catalytic Oxidation of Aqueous Formaldehyde," *Journal of Catalysis* **98**, 411–433 (1986).

[34] Tzou, M.S., Jiang, H.J., and Sachtler, W.M.H., "Genesis and Catalysis of Metal Particles in Zeolites," *Reaction Kinetics and Catalysis Letters* **35**(1–2), 207–217 (1987).

[35] Ito, T. and Fraissard, J., "^{129}Xe NMR Study of Xenon Adsorbed on Y Zeolites," *Journal of Chemical Physics* **76**(11), 5225–5229 (1982).

[36] de Menorval, L.C., Fraissard, J., and Ito, T., "Nuclear Magnetic Resonance Study of Xenon Adsorbed of Metal-NaY Zeolites," *Journal of the Chemical Society, Faraday Transactions 1*, **78**, 403–410 (1982).

[37] Fraissard, J., Ito, T., de Menorval, L.C., and Spinguel-Huet, M.A., "Nuclear Magnetic Resonance Study of Xenon Adsorbed on Metal-NaY Zeolites (Size

of Metal Particles and Chemisorption)," **Metal Microstructures in Zeolites: Preparation, Properties, Applications**, *Studies in Surface Science and Catalysis 12*, Jacobs, P.A. *et al.*, eds., Elsevier: Amsterdam, 179–189 (1982).

[38] Ito, T., de Menorval, L.C., and Fraissard, J.P., "Nuclear Magnetic Resonance Study of Xenon Adsorbed on Metal-NaY Zeolites," *Journal de Chimie Physique* **80**, 573–578 (1983).

[39] Ito, T. and Fraissard, J., "^{129}Xe Nuclear Magnetic Resonance Study of Xenon Adsorbed on Zeolite NaY Exchanged with Alkali-Metal and Alkaline-Earth Cations," *Journal of the Chemical Society, Faraday Transactions 1* **83**, 451–462 (1987).

[40] (a) Ripmeester, J.A. and Davidson, D.W., "^{129}Xe Nuclear Magnetic Resonance in the Clathrate Hydrate of Xenon," *Journal of Molecular Structure* **75**, 67–72 (1981); (b) Ripmeester, J.A., "Nuclear Shielding of Trapped Xenon Obtained by Proton-Enhanced Magic-Angle Spinning ^{129}Xe NMR Spectroscopy," *Journal of the American Chemical Society* **104**, 289–290 (1982); (c) Ripmeester, J.A., "Characterization of Void Spaces in Mordenites by Means of ^{129}Xe NMR," *Journal of Magnetic Resonance* **56**, 247–253 (1984).

[41] Ryoo, R., Liu, S.B., de Menorval, L.C., Takegoshi, K., Chmelka, B., Trecoske, M., and Pines, A., "Distribution of Hexamethylbenzene in a Zeolite by Xenon-129 and Multiple-Quantum NMR," *Journal of Physical Chemistry* **91**, 6575–6577 (1987).

[42] Scharpf, E.W., Crecely, R.W., Gates, B.C., and Dybowski, C., "Characterization of NiNa-Y Zeolite by ^{129}Xe NMR Spectroscopy," *Journal of Physical Chemistry* **90**, 9–11 (1986).

[43] Shoemaker, R. and Apple, T., "Redox Behavior of Ruthenium in Zeolite Y," *Journal of Physical Chemistry* **91**, 4024–4029 (1987).

[44] Davis, M.E., Saldarriaga, C., Montes, C., and Hanson, B.E., "Characterization of $AlPO_4$ and SAPO Molecular Sieves by ^{129}Xe NMR Spectroscopy," *Journal of the American Chemical Society* **92**, 2557–2560 (1988).

[45] Samant, M.G., de Menorval, L.C., Dalla-Betta, R.A., and Boudart, M., "Nuclear Magnetic Resonance of Xenon Occluded in Na-A Zeolite," *Journal of Physical Chemistry* **92**, 3937–3938 (1988).

[46] Fyfe, C.A., **Solid State NMR for Chemists**, C.F.C. Press: Guelph, Ontario, Canada (1983).

[47] Mehring, M., **Principles of High Resolution NMR in Solids**, Springer-Verlag: Berlin (1983).

[48] Klinkenburg, P.F.A., "Tables of Nuclear Shell Structure," *Reviews of Modern Physics* **24**(2), 63–73 (1952).

[49] (a) Jameson, A.K., Jameson, C.J., Gutowsky, H.S., "Density Dependence of ^{129}Xe Chemical Shifts in Mixtures of Xenon and Other Gases," *Journal of Chemical Physics* **53**(6), 2310–2321 (1970); (b) Jameson, C.J., Jameson, A.K., Cohen, S.M., "Temperature and Density Dependence of ^{129}Xe Chemical Shift in Xenon Gas," *Journal of Chemical Physics* **59**(8), 4540–4546 (1973); (c) Jameson, C.J., Jameson, A.K., Cohen, S.M., "Temperature and Density Dependence of ^{129}Xe Chemical Shift in Rare Gas Mixtures," *Journal of Chemical Physics* **62**(10), 4224–4226 (1975).

[50] Reagan, W.J., Chester, A.W., and Kerr, G.T., "Studies of the Thermal Decomposition and Catalytic Properties of Some Platinum and Palladium Ammine Zeolites," *Journal of Catalysis* **69**, 89–100 (1981).

[51] Somorjai, G.A., **Chemistry in Two Dimensions: Surfaces**, Cornell University Press: Ithaca (1981) pp. 178.

[52] Abragam, A. **Principles of Nuclear Magnetism**, Clarendon Press: Oxford (1961).

[53] Carrington, A. and McLachlan, A.D., **Introduction to Magnetic Resonance**, Harper and Row: New York (1967) pp. 207.

[54] Ito, T., de Menorval, L.C., Guerrier, E., and Fraissard, J.P., *Chemical Physics Letters* **111**, 271–274 (1984).

[55] Ripmeester, J.A., "Characterization of Void Spaces in Mordenites by Means of ^{129}Xe NMR," *Journal of Magnetic Resonance* **56**, 247–253 (1984).

[56] Johnson, D.W. and Griffiths, L., "Application of Xenon-129 N.M.R. to the Characterization of Zeolites," *Zeolites* **7**, 484–487 (1987).

[57] Bansal, N. and Dybowski, C., "Effects of Replacing Sodium by Nickel Ions in Y-Zeolite: Evidence from Xenon-129 NMR Spectroscopy," *Journal of Physical Chemistry* **92**(8), 2333–2337 (1988).

[58] Fraissard, J., Ito, T., and de Menorval, L.C., "Nuclear Magnetic Resonance Study of Xenon Adsorbed on Zeolites. Application to Catalysis Research," **Eighth International Congress on Catalysis, Berlin, 2 to 6 July 1984**, vol. 3, Verlag-Chemie: Weinheim, Germany, 25–35 (1984).

[59] Chmelka, B.F., Ryoo, R., Liu, S.B., de Menorval, L.C., Radke, C.J., Petersen, E.E., and Pines, A., "Probing Metal Cluster Formation in NaY Zeolite by ^{129}Xe NMR," *Journal of the American Chemical Society* **110**, 4465–4467 (1988).

[60] Gallezot, P., Mutin, I., Dalmai-Imelik, G., and Imelik, B., "Electron Microscopy Study of Platinum Dispersion in Y Zeolites," *Journal de Microscopie et Spectroscopie Electronique*, **1**, 1–6 (1976).

[61] Kleine, A., Ryder, P.L., Jaeger, N., and Schulz-Eckloff, G., "Electron Microscopy of Pt, Pd and Ni Particles in a NaX Zeolite Matrix," *Journal of the Chemical Society, Faraday Transactions 1* **82**, 205–212 (1986).

[62] Zandbergen, H.W., Engelen, C.W.R., and van Hooff, J.H.C., "Electron Microscopic Study of Defects and Metal Particles in Zeolites," *Applied Catalysis* **25**, 231–238 (1986).

[63] Exner, D., Jaeger, N., Möller, K., and Schulz-Ekloff, G., "Thermal Analysis of the Decomposition Mechanism of Platinum and Palladium Tetrammine Faujasite X," *Journal of the Chemical Society, Faraday Transactions 1* **78**, 3537–3544 (1982).

[64] Emmett, P.H. and Brunauer, S., "The Use of Low-Temperature van der Waal Adsorption Isotherms in Determining the Surface Area of Iron Synthetic Ammonia Catalysts," *Journal of the American Chemical Society* **59**(310), 1553–1564, (1937).

[65] Karnaukhov, A.P., "The Problem of the Chemisorptive Determination of the Degree of Dispersion of Metals on Carriers," *Kinetics and Catalysis* **12**(6), part

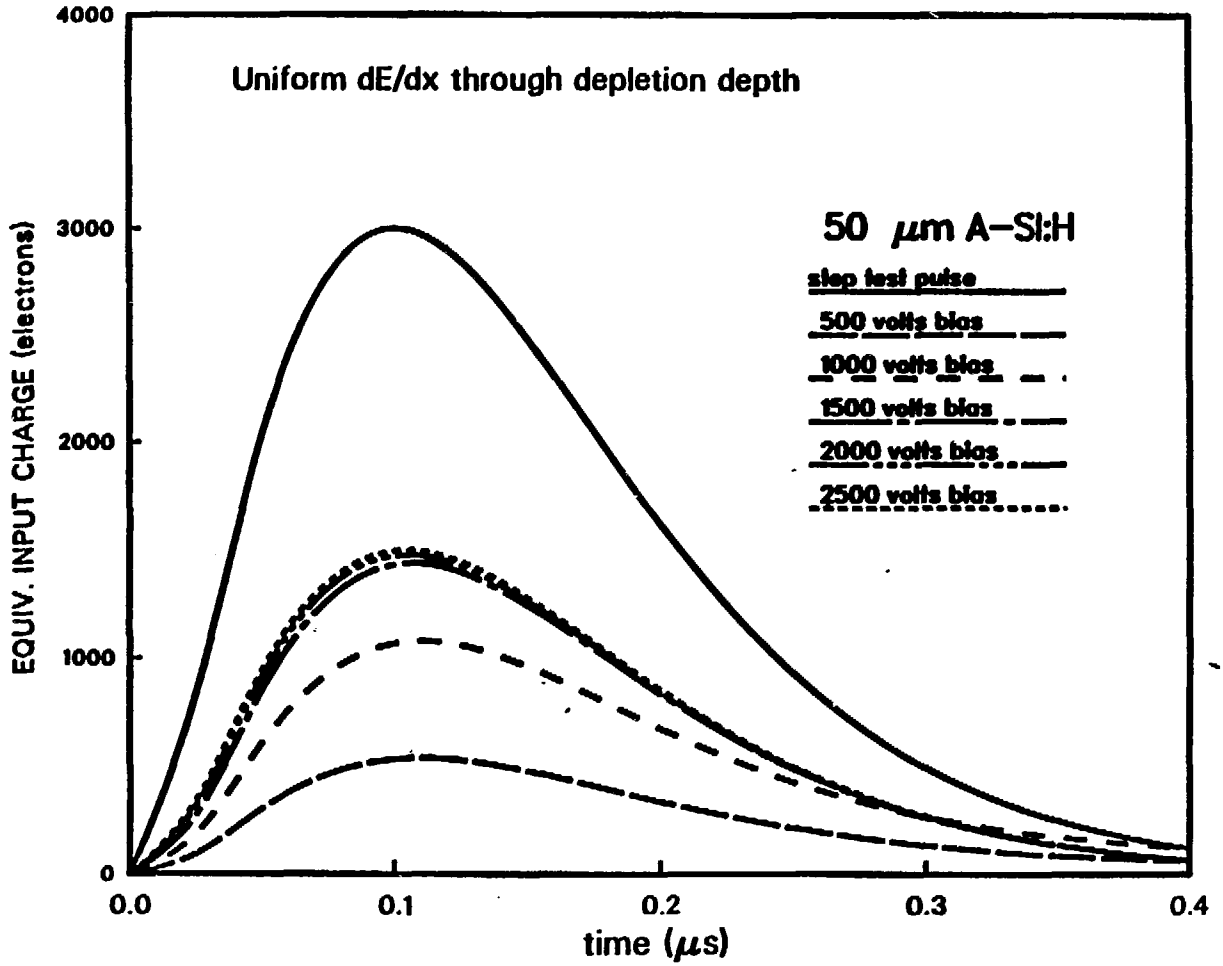

Figure 6.6.a : Output signal (in equivalent input charge units) as a function of time for a shaping time of 100 ns; different biases are applied on a 50 μm detector. The step test pulse corresponds to infinite mobility of charge in the detector, and total collection in zero time.

sorption Fine Structure (EXAFS) Spectroscopy," *Surface Science* **81**, L631–L634 (1979).

[74] Domínguez, J.M. and Yacamán, M.J., "The Structure and Selectivity of Supported Metal Particles," **Growth and Properties of Metal Clusters**, *Studies in Surface Science and Catalysis 4*, Bourdon, J., ed., Elsevier: Amsterdam, 493–503 (1980).

[75] Gault, F.G., Garin, F., and Mairo, G., "Skeletal Rearrangements of Hydrocarbons on Metals with various Particle Sizes," **Growth and Properties of Metal Clusters**, *Studies in Surface Science and Catalysis 4*, Bourdon, J., ed., Elsevier: Amsterdam, 451–466 (1980).

[76] Gallezot, P., "Structure of Platinum Aggregates Encaged in Y-type Zeolite. Effect of CO Adsorption and CO–H_2 Co-adsorption," *Zeolites* **2**, 103–108 (1982).

[77] Khanna, S.N., Bucher, J.P., Buttet, J., and Cyrot-Lackmann, F., "Stability and Lattice Contraction of Small Platinum Particles," *Surface Science* **127**, 165–174 (1983).

[78] Ratnasamy, P., Leonard, A.J., Rodrique, L., and Fripiat, J.J., "Structure and Surface Properties of Supported Platinum Catalysts," *Journal of Catalysis* **29**, 374–384 (1973).

[79] Gallezot, P., Bienenstock, A.I., and Boudart, M., "The Atomic Structure of Platinum Clusters," *Nouveau Journal de Chimie* **2**(3), 263–266 (1978).

[80] Burton, J.J., "Configuration, Energy, and Heat Capacity of Small Spherical Clusters of Atoms," *Journal of Chemical Physics* **52**(1), 345–352 (1970).

[81] Fripiat, J.G., Chow, K.T., Boudart, M., Diamond, J.B., and Johnson, K.H., "The Structure and Bonding of Lithium Clusters," *Journal of Molecular Catalysis* **1**, 59–72 (1975/76).

[82] Gandhi, S., **VLSI Fabrication Principles**, Wiley: New York (1983) pp. 386–389.

[83] Wang, T., Lee, C., and Schmidt, L.D., "Shape and Orientation of Supported Pt Particles," *Surface Science* **163**, 181–197 (1985).

[84] Chmelka, B. F., de Menorval, L. C., Csencsits, R., Ryoo, R., Liu, S. B., Radke, C. J., Petersen, E. E., and Pines, A., "Calcination-Dependence of Platinum Cluster Formation in NaY Zeolite: A Xenon-129 NMR Study," **Structure and Reactivity of Surfaces**, *Studies in Surface Science and Catalysis 48*, Morterra, C., Zecchina, A., and Costa, G., eds., Elsevier: Amsterdam, 269–278 (1989).

[85] Roozeboom, F., Mittelmeijer-Hazeleger, M.C., Moulijn, J.A., Medema, J., de Beer, V.H.J., and Gellings, P.J., "Vanadium Oxide Monolayer Catalysts. 3. A Raman Spectroscopic and Temperature-Programmed Reduction Study of Monolayer and Crystal-Type Vanadia on Various Supports," *Journal of Physical Chemistry* **84**(21), 2783–2791 (1980).

[86] Roozeboom, F., Robson, H.E., and Chan, S.S., "Laser Raman Study on the Crystallization of Zeolites A, X, and Y," *Zeolites* **3**, 321–328 (1983).

[87] Dutta, P.K., Shieh, D.C., and Puri, M., "Raman Spectroscopic Study of the Synthesis of Zeolite Y," *Journal of Physical Chemistry* **91**, 2332–2336 (1987).

[88] Chan, S.S. and Bell, A.T., "Characterization of the Preparation of Pd/SiO_2 and Pd/La_2O_3 by Laser Raman Spectroscopy," *Journal of Catalysis* **89**, 433–441 (1984).

[89] James, D.W. and Nolan, M.J., "Vibrational Spectra of Substituted Platinum(IV) Ammine Complexes," *Journal of Raman Spectroscopy* **1**, 271–284 (1973).

[90] Goncharenko, G.I., Lazarev, V.B., and Shaplygin, I.S., "The Infrared Spectra of Simple Oxides of the Platinum Metals," *Russian Journal of Inorganic Chemistry* **30**(12), 1723–1726 (1985).

[91] Cheng, C.P., Ludowise, J.D., and Schrader, G.L., "Controlled-Atmosphere Rotating Cell for In Situ Studies of Catalysts Using Laser Raman Spectroscopy," *Applied Spectroscopy* **34**(2), 146–150 (1980).

[92] Freeman, jr., D.C. and Stamires, D.N., "Electrical Conductivity of Synthetic Crystalline Zeolites," *Journal of Chemical Physics* **35**(3), 799–806 (1961).

[93] Went, G.T. and Bell, A.T., in preparation.

[94] CRC Press, **Handbook of Chemistry and Physics**, 62nd ed., (1981) pp. B-129.

[95] Park, S.H., Tzou, M.S., and Sachtler, W.M.H., "Temperature Programmed Reduction and Re-oxidation of Platinum in Y-Zeolites," *Applied Catalysis* **24**, 85–98 (1986).

[96] Chmelka, B.F., Rosin, R.R., Went, G.T., Bell, A.T., Radke, C.J., and Peteresen, E.E., "The Chemistry of Pt–NaY Zeolite Preparation," **Zeolites: Facts,**

Figures, Future, *Studies in Surface Science and Catalysis 49*, Jacobs, P.A. and van Santen, R.A., eds., Elsevier: Amsterdam, 995–1004 (1989).

[97] Amaro, A.A. and Seff, K., "Crystal Structure of an Acetylene Sorption Complex of Zeolite 4A," *Journal of Physical Chemistry* **77**(7), 906–910 (1973).

[98] Cohen de Lara, E., "Temperature Dependence of the Mobility of Adsorbed Molecules–Infrared Study," **Proceedings of the Fifth International Conference on Zeolites**, Rees, L.V.C., ed., Heyden: London, 414–423 (1980).

[99] See for example: (a) Renouprez, A.J., Jobic, H., and Oberthür, R.C., "Aggregation of Benzene on Na-Y Zeolites–A Small Angle Neutron Scattering Study," *Zeolites* **5**(4), 222–224 (1985); (b) Stockmeyer, R., "Methane in Zeolites A and X Studied by Neutron Scattering: A Solid or Fluid Phase at Ambient Temperature?" *Zeolites* **4**(1), 81–86 (1984); (c) Kahn, R., Cohen de Lara, E., Thorel, P., and Ginoux, J.L., "Adsorption Sites in Na-A Zeolites. Neutron Diffraction Study of NaA-Methane and NaA-Acetylene Systems," *Zeolites* **2**(4), 260–266 (1982); (d) Wright, P.A., Thomas, J.M., Ramdas, S., and Cheetham, A.K., "Locating the Sites of Adsorbed Species in Heterogeneous Catalysts: A Rietveld Neutron Powder Profile Study of Xenon in Zeolite-Rho," *Journal of the Chemical Society, Chemical Communications* 1338–1339 (1984); (e) Taylor, J.C., "Locations of Deuterobenzene Molecules in the Synthetic Zeolite ZSM-5 at 77 K by Powder Neutron Diffraction," *Zeolites* **7**, 311–318 (1987).

[100] (a) Klinowski, J., "Nuclear Magnetic Resonance Studies of Zeolites," *Progress in Nuclear Magnetic Resonance Spectroscopy*, **16**, 237–309 (1984); (b) Thomas, J.M. and Klinowski, J., "The Study of Aluminosilicate and Related Catalysts by High-Resolution Solid-State NMR Spectroscopy," *Advances in Catalysis* **33**,

199–374 (1985).

[101] Engelhardt, G. and Michel, D., **High-Resolution Solid State NMR of Silicates and Zeolites**, Wiley: New York, (1987).

[102] Resing, H.A., "NMR Relaxation of Adsorbed Molecules with Emphasis on Adsorbed Water," *Advances in Molecular Relaxation Processes* **3**, 199–226 (1972).

[103] Geschke, D. and Pfeifer, H., "Comparison of the Adsorption States of Water and Simple Aromatics on Faujasite-Type Zeolites," *Zeitschrift für Physikalische Chemie, Leipzig* **257**(2), 365–372 (1976).

[104] Basler, W.D., Lechert, H., and Weyda, H., "Molecular Motion of Aromatics in Zeolites of Different Channel Dimensions Studied by Nuclear Magnetic Resonance," *Catalysis Today* **3**, 31–40 (1988).

[105] Hoffmann, W.D., "Study of the Specific Adsorption of Benzene on NaX and NaY Zeolite by Measuring the Second Moment of Proton Resonance," *Zeitschrift für Physikalische Chemie, Leipzig* **257**(2), 315–320 (1976).

[106] Lechert, H. and Wittern, K.P., "Nuclear Magnetic Resonance Studies of the Arrangement of Benzene Molecules in the Cavities of the Zeolite NaX," *Bunsengesellschaft für Physikalische Chemie, Berichte* **82**(10), 1054–1060 (1978).

[107] Eckman, R.R. and Vega, A.J., "Deuterium NMR Study of Organic Molecules Adsorbed by Zeolites," *Journal of the American Chemical Society* **105**, 4841–4842 (1983).

[108] Kärger, J., Pfeifer, H., and Heink, W., "Principles and Applications of Self-Diffusion Measurements by Nuclear Magnetic Resonance," **Advances in Magnetic Resonance**, Waugh, J., ed., Academic Press: San Diego, 2–89 (1988).

[109] For ^{129}Xe NMR studies of xenon adsorbed in zeolites: (a) Ito, T. and Fraissard, J., "^{129}Xe NMR Study of Xenon Adsorbed on Y Zeolites," *Journal of Chemical Physics* **76**(11), 5225–5229 (1982); (b) Ito, T., de Menorval, L.C., Guerrier, E., and Fraissard, J., "NMR Study of ^{129}Xe Adsorbed on L, Z, and ZSM Zeolites," *Chemical Physics Letters* **111**(3), 271–274 (1984); (c) Springuel-Huet, M.A., Ito, T., and Fraissard, J., "Adsorption of Xenon: A New Method for Studying the Crystallinity of Zeolites," **Structure and Reactivity of Modified Zeolites**, *Studies in Surface Science and Catalysis 18*, Jacobs, P.A., Jaeger, N.I., Jírů, P., Kazansky, V.B., and Schulz-Ekloff, G., eds., Elsevier: Amsterdam, 13–21 (1984).

[110] For ^{129}Xe NMR studies of xenon adsorbed in metal-loaded zeolites: (a) Fraissard, J., Ito, T., and de Menorval, L.C., "Nuclear Magnetic Resonance Study of Xenon Adsorbed on Zeolites. Application to Catalysis Research," **Proceedings of the Eighth International Zeolite Conference**, vol. 3, Verlag-Chemie: Weinheim, 25–35 (1984); (b) de Menorval, L.C., Fraissard, J., and Ito, T., "Nuclear Magnetic Resonance Study of Xenon Adsorbed of Metal-NaY Zeolites," *Journal of the Chemical Society, Faraday Transactions 1* **78**, 403–410 (1982); (c) de Menorval, L.C., Fraissard, J., Ito, T., and Primet, M., "Carbon Monoxide Chemisorption on a Pt-NaY Catalyst," *Journal of the Chemical Society, Faraday Transactions 1* **81**, 2855–2865 (1985).

[111] de Menorval, L.C., Raftery, D., Liu, S.B., Takegoshi, K., Ryoo, R., and Pines, A., "Investigations of Adsorbed Organic Molecules in NaY Zeolite by Xenon-129 NMR," *Journal of Physical Chemistry*, in press.

[112] Derouane, E.G. and Davis, M.E., "On the Polarizability of Molecular Sieves: ^{129}Xe NMR Chemical Shifts and Sorption Energetics," *Journal of Molecular Catalysis* **48**(1), 37–41 (1988).

[113] (a) Pines, A., "Lectures on Pulsed NMR," **Proceedings of the 100th School of Physics "Enrico Fermi"**, Maraviglia, B., ed., North-Holland: Amsterdam, 43–120 (1988); (b) Munowitz, M. and Pines, A., "Multiple-Quantum Nuclear Magnetic Resonance Spectroscopy," *Science* **233**, 525–531 (1983).

[114] (a) Baum, J. and Pines, A., "NMR Studies of Clustering in Solids," *Journal of the American Chemical Society* **108**(24), 7447–7454 (1986); (b) Munowitz, M., Pines, A., and Mehring, M., "Multiple-Quantum Dynamics in NMR: A Directed Walk Through Liouville Space," *Journal of Chemical Physics* **86**(6), 3172–3182 (1987); (c) Shykind, D.N., Baum, J., Liu, S.B., Pines, A., and Garroway, A.N., "Phase-Incremented Multiple-Quantum NMR Experiments," *Journal of Magnetic Resonance* **76**, 149–154 (1988).

[115] Munowitz, M., **Coherence and NMR**, Wiley: New York (1988).

[116] Gedeon, A., Ito, T., and Fraissard, J., "Study of the H_2O/NaY System: An Example of the Application of ^{129}Xe NMR of the Xenon Probe to the Investigation of the Location of Adsorbed Phases," *Zeolites* **8**(5), 376–380 (1988).

[117] Fominykh, L.F., Shaburo, I.S., and Artem'eva, A.F., "Thermal Study of the Desorption of Benzene and n-Heptane from NaX Zeolites," *Neftepererabotka i Neftekhimiia (Moscow, RSFSR)* **7**, 39–40 (1974).

[118] Reid, R.C., Prausnitz, J.M., and Sherwood, T.K., **The Properties of Gases and Liquids**, McGraw-Hill: New York (1977).

[119] Kaplan, J.I. and Fraenkel, G., **NMR of Chemically Exchanging Systems**, Academic Press: New York (1980).

[120] Freeman, R., **A Handbook of Nuclear Magnetic Resonance**, Wiley: New York (1987).

[121] Kärger, J. and Pfeifer, H., "N.M.R. Self-Diffusion Studies in Zeolite Science and Technology," *Zeolites* **7**, 90–107 (1987).

[122] Smith, J.M., **Chemical Engineering Kinetics**, McGraw-Hill: New York (1981).

[123] Kondis, E.F. and Dranoff, J.S., "Kinetics of Isothermal Sorption of Ethane on 4A Molecular Sieve Pellets," *Industrial and Engineering Chemistry, Proc. Des. Develop.* **10**(1), 108–114 (1971).

[124] Kärger, J., Pfeifer, H., Rauscher, M., Bülow, M., Samulevič, N.N., and Žandov, S.P., "Comparative NMR and Uptake Studies of Molecular Transport of Ethane in 5A Zeolites after Different Sample Treatments," *Zeitschrift für Physikalische Chemie, Leipzig* **262**, 567–576, (1981).

[125] Chmelka, B. F., Pearson, J. G., Liu, S.B., Ryoo, R., de Menorval, L.C., Trecoske, M., and Pines, A., in preparation.

[126] Ruckenstein, E., Vaidyanathan, A.S., and Youngquist, G.R., "Sorption by Solids with Bidisperse Pore Structures," *Chemical Engineering Science* **26**, 1305–1318 (1971).

[127] Froment, G.F. and Bischoff, K.B., **Chemical Reactor Analysis and Reactor Design**, Wiley: New York (1979), pp. 242–259.

[128] Dubinin, M.M., Nikolaev, K.M., Polyakov, N.S., and Seregina,N.I., "Investigation of Adsorption of Vapors of Substances with Relatively Big Molecules. 2. Study of Activated Character of Adsorptions on Active Charcoals," *Akademiia Nauk SSSR, Izvestia, Seriia Khimicheskaia* **1971**(9), 1871–1876 (1971).

[129] Dubinin, M.M., Nikolaev, K.M., Polyakov, N.S., Seregina,N.I., and Tokarev, Yu.A., "Study of of Vapour Adsorption of Various Organic Substances. 3. Characteristics of the Microporous Structure of Adsorbents in Case of Activated Nature of Adsorption," *Akademiia Nauk SSSR, Izvestia, Seriia Khimicheskaia* **1974**(9), 1479–1484 (1974).

[130] Bischoff, K.B., "Accuracy of the Pseudo Steady State Approximation for Moving Boundary Diffusion Problems," *Chemical Engineering Science* **18**, 711–713 (1963).

[131] Bischoff, K.B., "Further Comments on the Pseudo Steady State Approximation for Moving Boundary Diffusion Problems," *Chemical Engineering Science* **20**, 783–784 (1963).

[132] Luss, D., "On the Pseudo Steady State Approximation for Gas Solid Reactions," *The Canadian Journal of Chemical Engineering* **46**, 154–156 (1965).

[133] Theofanous, T.G. and Lim, H.C., "An Approximate Analytical Solution for Non-Planar Moving Boundary Problems," *Chemical Engineering Science* **26**, 1297–1300 (1971).

[134] Sohn, H.Y. and Szekely, J., "Structural Model for Gas-Solid Reactions with a Moving Boundary. III. General Dimensionless Representation of the Irreversible Reaction between a Porous Solid and a Reactant Gas," *Chemical Engineering*

Science **27**(4), 763–778 (1972).

[135] Sohn, H.Y. and Szekely, J., "The Effect of Intragrain Diffusion on the Reaction between a Porous Solid and a Gas," *Chemical Engineering Science* **29**, 630–634 (1974).

[136] Barrer, R.M. and Coughlan, B., "Influence of Crystal Structures upon Zeolitic Carbon Dioxide. Part I: Isotherms and Selectivity," **Molecular Sieves**, Society of Chemical Industry: London, 241–251 (1968).

[137] Anderson, M.W., Klinowski, J., and Thomas, J.M., "Zeolites Treated with Silicon Tetrachloride Vapour," *Journal of the Chemical Society, Faraday Transactions 1* **82**, 2851–2862 (1986).

[138] Kiselev, A.V., Lopatkin, A.A., and Shul'ga, A.A., "Molecular Statistical Calculation of Gas Adsorption by Silicalite," *Zeolites* **5**(4), 261–267 (1985).

[139] Arusmov, B.G., Vosachek, B., and Kiselev, A.B., *Zhurnal Fizicheskoĭ Khimii* **43**(1), 292-298 (1969).

[140] Fomkin, A.A and Serpinskii, V.V., and Bering, B.P., "Adsorption of Xenon on NaX Zeolite in a Wide Range of Pressures and Temperatures *Akademiia Nauk SSSR, Izvestia, Seriia Khimicheskaia* **6**, 1244-1248 (1975).

[141] Barrer, R.M., "Specificity in Physical Adsorption," *Journal of Colloid and Interface Science* **21**(4), 415–434 (1966).

[142] Ruthven, D.M., **Principles of Adsorption and Adsorption Processes**, Wiley: New York (1984).

[143] Kiselev, A.V., "Investigations of the Adsorption in Zeolites at Zero Filling," **Proceedings of the Fifth International Conference on Zeolites**, Rees, L.V.C., ed., Heyden: London, 400–413 (1980).

[144] Bezus, A.G., Dobrova, E.S., Kats, V.M., Kiselev, A.V., Lopatkin, A.A., and Si, P.Q., "Thermodynamic Characteristics of the Adsorption of Noble Gases by Zeolite NaX," *Kolloidn. Zhurnal* **37**(6), 1045–1052 (1975).

[145] Kiselev, A.V. and Du, P.Q., "Molecular Statistical Calculation of the Thermodynamic Adsorption Characteristics of Zeolites Using the Atom-Atom Approximation," *Journal of the Chemical Society, Faraday Transactions 2* **77**, 1–15 (1981).

[146] Pickett, S.D., Nowak, A.K., Thomas, J.M., and Cheetham, A.K., "Computer Simulation of the Adsorption and Diffusion of Benzene in Silicalite, Theta-1 and a New Zeolite, EU-1," *Zeolites* **9**(2), 129–135 (1989).

[147] Miertuš, S. and Miertušová, J., "Theoretical and Experimental Study of the Sorption Processes of Gases on NaY Zeolites," *Journal of Chromatography* **286**, 31–36 (1984).

[148] Soto, J.L. and Myers, A.L., "Monte Carlo Studies of Adsorption by Molecular Sieves," *Molecular Physics* **42**(4), 971–983 (1981).

[149] Rybolt, T.R., Mitchell, R.L., and Waters, C.M., "Monatomic Gas Adsorption and the Structure of the 5A and 13X Zeolites," *Langmuir* **3**(3), 326–331 (1987).

[150] Yashonath, S., Thomas, J.M., Nowak, A.K., and Cheetham, A.K., "The Siting, Energetics, and Mobility of Saturated Hydrocarbons inside Zeolitic Cages: Methane in Zeolite Y," *Nature* **331**, 601–604 (1988).

[151] Aziz, R.A. and Slaman, M.J., "On the Xe–Xe Potential Energy Curve and Related Properties," *Molecular Physics*, **57**(4), 825–840 (1986).

[152] Rabo, J., presented at the *North American Catalysis Society Meeting*, Dearborn, Michigan (1989).

[153] (a) Derouane, E.G., Andre, J.M., and Lucas, A.A., "A Simple van der Waals Model for Molecule-Curved Surface Interactions in Molecular-Sized Microporous Solids," *Chemical Physics Letters* **137**(4), 336–340 (1987); (b) Derouane, E.G. and Nagy, J.B., "Surface Curvature Effects on the NMR Chemical Shift for Molecules Trapped in Microporous Solids," *Chemical Physics Letters* **137**(4), 341–344 (1987); (c) Derouane, E.G., presented at the *North American Catalysis Society Meeting*, Dearborn, Michigan (1989).

[154] van Megen, W.J. and Snook, I.K., "Solvation Forces in Simple Dense Fluids. II. Effect of Chemical Potential," *Journal of Chemical Physics* **74**(2), 1409–1411 (1981).

[155] Magda, J.J., Tirell, M., and Davis, H.T., "Molecular Dynamics of Narrow, Liquid-Filled Pores," *Journal of Chemical Physics* **83**(4), 1888–1901 (1985).

[156] Vanderlick, T.K., Scriven, L.E., and Davis, H.T., "Molecular Theories of Confined Fluids," *Journal of Chemical Physics* **90**(4), 2422–2436 (1989).

[157] Israelachvili, J.N., **Intermolecular and Surface Forces**, Academic Press: New York (1985).

[158] Streever, R.J. and Carr, H.Y., "Nuclear Magnetic Resonance of ^{129}Xe in Natural Xenon," *Physical Review* **121**(1), 20–25 (1961).

[159] Torrey, H.C., "Chemical Shift and Relaxation of ^{129}Xe in Xenon Gas," *Physical Review* **130**(6), 2306–2312 (1963).

[160] Hunt, E.R. and Carr, H.Y., "Nuclear Magnetic Resonance (N.M.R.) of ^{129}Xe in Natural Xenon," *Physical Review* **130**(6), 2302–2305 (1963).

[161] For example: (a) Davis, M.E., Saldarriaga, C., Montes, C., and Hanson, B.E., "Characterization of $AlPO_4$ and SAPO Molecular Sieves by ^{129}Xe NMR Spectroscopy," *Journal of the American Chemical Society* **92**, 2557–2560 (1988); (b) Ito, T., Fraissard, J., Nagy, J.B., Dewaele, N., Gabelica, Z., Nastro, A., and Derouane, E.G., "^{129}Xe-NMR Studies of Type NaY, ZSM-5, ZSM-20 Zeolite Crystallization," **Zeolites: Facts, Figures, Future**, *Studies in Surface Science and Catalysis 49*, Jacobs, P.A. and van Santen, R.A., eds., Elsevier: Amsterdam, 579–588 (1989).

[162] Kärger, J., Pfeifer, H., and Fraissard, J., "Estimate of the Translational Mobility of Xenon in Modified Pt–NaY Catalysts by ^{129}Xe NMR Lineshape Analysis," *Zeitschrift für Physikalische Chemie, Leipzig* **268**(1), 195–199 (1987).

[163] (a) Lee, F., Gabe, E., Tse, J.S., and Ripmeester, J.A., "Crystal Structure, CP/MAS ^{129}Xe, ^{13}C NMR of Local Ordering in Dianin's Compound Clathrates," *Journal of the American Chemical Society* **110**, 6014–6019 (1988); (b) Ripmeester, J.A., Ratcliffe, C.I., and Tse, J.S. "The Nuclear Magnetic Resonance of ^{129}Xe Trapped in Clathrates and Some Other Solids," *Journal of the Chemical Society, Faraday Transactions 1* **84**(11), 3731–3745 (1988).

[164] Harris, R.K., **NMR Spectroscopy**, Pitman: London, (1983).

[165] Kahn, R., Cohen de Lara, E., Thorel, P., and Ginoux, J.L., "Adsorption Sites in Na-A Zeolites. Neutron Diffraction Study of NaA-Methane and NaA-Acetylene Systems," *Zeolites* **2**(4), 260–266 (1982).

[166] Stockmeyer, R., "Methane in Zeolites A and X Studied by Neutron Scattering: A Solid or Fluid Phase at Ambient Temperature?" *Zeolites* **4**(1), 81–86 (1984).

[167] Bakaev, V.A., "On the Statistical Thermodynamics of Adsorption Equilibrium in the Case of Zeolites," *Doklady Akademii Nauk SSSR* **167**(2), 369–372 (1966).

[168] Demarquay, J. and Fraissard, J., "^{129}Xe NMR of Xenon Adsorbed on Zeolites. Relationship between the Chemical Shift and the Void Space," *Chemical Physics Letters* **136**(3-4), 314–318 (1987).

[169] de Menorval, L. C., unpublished results.

[170] Kreyszig, E., **Advanced Engineering Mathematics**, Wiley: New York (1983) pp. 922-923.

[171] Ahrens-Botzong, V. R., Hess, P., and Schäfer, K., "Messung der physikalischen Adsorption von Xenon an Quarzglas," *Berichte Bunsen-Gesellschaft* **76**(5), 460-462 (1972).

[172] Smith, J.M. and van Ness, H.C., **Introduction to Chemical Engineering Thermodynamics**, 3rd edition, McGraw-Hill: New York, (1975) pp. 294–295.

[173] Atkins, P.W., **Physical Chemistry**, W. H. Freeman and Co.: San Francisco (1982) pp. 182–184.

[174] Perry, R.H. and Chilton, C.H, eds., **Chemical Engineers' Handbook**, McGraw-Hill: New York, (1973).

[175] Fraissard, J., Ito, T., Springuel-Huet, M., and Demarquay, J., "Adsorption of Xenon: A New Method for Studying Zeolites," **New Developments in Zeolite Science and Technology**, *Studies in Surface Science and Catalysis 28*, Murakami, Y., ed., Elsevier: Amsterdam, 393–400 (1986).

[176] Cohen de Lara, E., Kahn, R., Goulay, A.M., Lebars, M., "Molecular Dynamics by Numerical Simulation of Methane in NaA Zeolite," in **Zeolites: Facts, Figures, Future**, *Studies in Surface Science and Catalysis 49*, Jacobs, P.A. and van Santen, R.A., eds., Elsevier: Amsterdam, 753–762 (1989).

[177] Springuel-Huet, M.A., Demarquay, J., Ito, T., and Fraissard, J., "Xenon-129 NMR of Xenon Adsorbed on Zeolites: Determination of the Dimensions of the Void Space from the Chemical Shift δ(Xenon-129)," **Innovations in Zeolite Materials Science**, *Studies in Surface Science and Catalysis 37*, Grobet, P.J., *et al.*, eds., Elsevier: Amsterdam, 183–189 (1988).

[178] Razga, J., "Adsorption of Krypton and Xenon on Solid Materials," *Jaderna Energie* **21**(12), 455–456 (1975).

[179] Fomkin, A.A., "Fluid Adsorption in Zeolites at High Pressure," **Zeolites: Facts, Figures, Future**, *Studies in Surface Science and Catalysis 49*, Jacobs, P.A. and van Santen, R.A., eds., Elsevier: Amsterdam, 953–962 (1989).

[180] Csencsits, R. and Gronsky, R., "Damage of Zeolite Y in the TEM and Its Effects on TEM Images," *Ultramicroscopy* **23**, 421–432 (1987).

[181] Bursill, L.A., Lodge, E.A., and Thomas, J.M., "Zeolitic Structures Revealed by High-Resolution Electron Microscopy," *Nature* **286**, 111–113 (1980).

[182] Ward, J.W., "The Nature of Active Sites on Zeolites," *Journal of Catalysis* **10**, 34–46 (1968).

[183] Bird, R.B., Stewart, W.E., and Lightfoot, E.N., **Transport Phenomena**, Wiley: New York (1960).

[184] Sherwood, T.K., Pigford, R.L., and Wilke, C.W., **Mass Transfer**, McGraw-Hill: New York (1975).

[185] Lechert, H. and Hennig, H.J., "Temperature Behavior of the Proton Resonance of Adsorbed Benzene in the Holes of Synthetic Zeolites of the Faujasite Type," *Zeitschrift für Naturforschung, Teil A*, **29**(7), 1065–1070 (1974).

[186] Förste, C., Kärger, J., and Pfeifer, H., "Self-Diffusion by NMR Tracer Uptake Measurements," **Zeolites: Facts, Figures, Future**, *Studies in Surface Science and Catalysis 49*, Jacobs, P.A. and van Santen, R.A., eds., Elsevier: Amsterdam, 907–914 (1989).

[187] Germanus, A., Kärger, J., and Pfeifer, H., "Self-Diffusion of Paraffins and Olefins in Zeolite Na-X Under the Influence of Residual Water Molecules," *Zeolites* **4**(2), 188–190 (1984).

[188] Newsam, J.M., "The Zeolite Cage Structure," *Science* **231**, 1093–1099 (1986).

[189] Chmelka, B.F., Mueller, K.T., Pines, A., Stebbins, J., Wu, Y., and Zwanziger, J.W., "Oxygen-17 NMR in Solids by Dynamic-Angle Spinning and Double Rotation," *Nature* **339**, 42–43 (1989).

[190] Mueller, K.T., Sun, B.Q., Chingas, G.C., Zwanziger, J.W., Terao, T., and Pines, A., "Dynamic-Angle Spinning of Quadrupolar Nuclei," *Journal of Magnetic Resonance*, in press.